UNIVERSITY OF CALIFORNIA,
IRVINE

Using *In Vivo* Models to Understand Melanogenesis

DISSERTATION

submitted in partial satisfaction of the requirements
for the degree of

DOCTOR OF PHILOSOPHY

in Biomedical Sciences

by

Jessica Leigh Flesher

Dissertation Committee:
Professor Anand K. Ganesan, Chair
Professor Xing Dai
Associate Professor Maksim V. Plikus
Assistant Professor Kai Kessenbrock

2020

DEDICATION

To

My parents, David and Sarah,
For always believing in me and giving me every opportunity to succeed;

My brothers, Andrew and Daniel,
For always pushing me and never once questioning whether I could;

My sisters, Susanna and Virginia,
For always inspiring me to be a good role model and
Helping me express my frustration through creative outlets;

And my Grandma Ann,
For always being an excited ear to hear about my experiences and share in my joy.

If you find it's me your missing
If you're hoping I'll return
To your thoughts I'll soon be listening
In the road I'll stop and turn
Then the wind will set me racing
As my journey nears its end
And the path I'll be retracing
When I'm homeward bound again

Bind me not to the pastures
Chain me not to the plow
Set me free to find calling
And I'll return to you somehow

"Homeward Bound" by Marta Keen, 1991

TABLE OF CONTENTS

LIST OF FIGURES

LIST OF TABLES

LIST OF ABBREVIATIONS

7-DHC	7-Deydrocholesteerol
αMSH	Alpha Melanocyte Stimulating Hormone
AP	Adaptor Protein Complex
ASIP	Agouti Signaling Protein
ATG	Autophagy Related Protein
ATP	Adenosine Triphosphate
ATP7A	ATPase Copper Transporting Alpha
bHLH	Basic Helix-Loop-Helix
BLOC	Biogenesis of Lysosome Related Organelle Complex
BLOS	Biogenesis of Lysosome Related Organelle Complex 1 Subunit
BTZ	1,4-Benzothiazine
BTZCA	1,4-Benzothiazine-3-Carboxylic Acid
cAMP	Cyclic Adenosine Monophosphate
CAS9	CRISPR Associated Protein 9
ChIP	Chromatin Immunoprecipitation
CNO	Cappuccino
CNS	Central Nervous System
CREB	cAMP Response Element-Binding Protein
CRISPR	Clustered Regularly Interspaced Short Palindromic Repeats
DCT	Dopachrome Tautomerase
DHI	5,6-Dihydroxyindole
DHICA	5,6-Dihydroxyindole-2-Carboxylic Acid
DMSO	Dimethyl Sulfoxide
DNA	Deoxyribonucleic Acid
DTBP1	Dystrobrevin Binding Protein 1
E	Embryonic Day

EDN3	Endothelian 3
EDNRB	Endothelian Receptor B
EEA1	Early Endosome Antigen 1
EGFP	Enhanced Green Fluorescent Protein
EM	Electron Microscopy
ER	Endoplasmic Reticulum
ESCRT	Endosomal Sorting Complexes Required for Transport
FIG4	FIG4 Phosphoinositide 5-Phosphatase
GDP	Guanine Diphosphate
GEF	Guanine Nucleotide Exchange Factor
GTP	Guanine Triphosphate
H&E	Hematoxylin & Eosin
HPS	Hermansky-Pudlak Syndrome
IPE	Iris Pigment Epithelium
KIT	KIT Proto-Oncogene, Receptor Tyrosine Kinase
LAMP1	Lysosomal Associated Membrane Protein 1
L-DOPA	L-3,4-Dihydroxyphenylalanine
MART1	Melanoma Antigen Recognized by T Cells 1
MATP	Membrane-Associated Transporter Protein
MC1R	Melanocortin 1 Receptor
MFSD12	Major Facilitator Superfamily Domain Containing 12
mi	Microphthalmia
mi-bw	Microphthalmia Black-Eyed White
mi-rw	Microphthalmia Red-Eyed White
mi-vga9	Microphthalmia Transgenic Insertion 9
MiT/TFE	Microphthalmia Transcription Factor Family
MITF	Microphthalmia Associated Transcription Factor
MLANA	Melan-A, MART1 Gene

MVE	Multivesicular Endosome
OA1	Ocular Albinism 1
OCA2	Oculocutaneous Albinism 2
P	Postnatal Day
PAX3	Paired Box Gene 3
PI	Phosphoinositide
PI(3)P	Phosphoinositol 3-Phosphate
$PI(3,5)P_2$	Phosphoinositol 3,5-Bisphosphate
PI(5)P	Phosphoinositol 5-Phosphate
PIKFYVE	1-Phosphatidylinositol 3-Phosphate 5-Kinase
PLDN	Pallidin
PMEL	Premelanosome Protein
POMC	Proopiomelanocortin
PROPPIN	Beta-Propellers that Bind Polyphosphoinositides
RAB	RAB Family of GTPases
RAR	Retinoic Acid Receptor
RARE	Retinoic Acid Response Element
RNA	Ribonucleic Acid
RNAi	Ribonucleic Acid Interference
ROS	Reactive Oxygen Species
RPE	Retinal Pigment Epithelium
RT-qPCR	Reverse Transcriptase Quantitative Polymerase Chain Reaction
RXR	Retinoic X Receptor
SAD	Seasonal Affective Disorder
SD	Standard Deviation
SE	Standard Error
SLC24A2	Solute Carrier Family 24 Member 2
SLC45A2	Solute Carrier Family 45 Member 2, MATP Gene

SNAI2	Snail Family Transcriptional Repressor 2
SNAPN	SNAP Associated Protein
SNP	Single Nucleotide Polymorphism
SOX10	SRY-Box Transcription Factor 10
TPC2	Two Pore Segment Channel 2
TRP63	Transformation Related Protein 63, p63 Gene
UV	Ultraviolet
VAC14	VAC14 Component of PIKFYVE Complex
WIPI1	WD Domain, Phosphoinositide Interacting 1
WS	Waardenburg Syndrome

ACKNOWLEDGEMENTS

While the following pages are the culmination of many hours of my graduate work, I could not have accomplished all I have without the mentorship, friendship, and support from the individuals who have taken part in this journey with me. First, I would like to thank **Dr. Anand Ganesan**, who has been an amazing mentor and advocate. He encouraged me to grow as a scientist through discussions and to utilize all available resources to follow where the research led. Beyond the research, Anand provided a solid sounding board for my future, all while introducing me into the wonderful world of pigment cell biology.

My committee members **Drs. Xing Dai, Maksim Plikus,** and **Kai Kessenbrock** have time and again helped me look through a different lens. Whether taking a step back to look at the research outside of pigment cell biology or in discussion of my goals for the future. **Drs. Klemens Hertel** and **Angela Fleischman** provided amazing mentorship during my rotations and have been great resources. **Dr. Marian Waterman** has been a wealth of advice and support as a colleague and collaborator. As leaders and mentors of the Cancer Biology and Therapeutics Training Grant, **Drs. David Fruman** and **Aimee Edinger** have taught me about the importance of mentorship and building community beyond the requirements.

The people of the Ganesan Laboratory have been my day-to-day mentors and coconspirators for much of the last few years. Starting during my rotation, **Dr. Elyse Patterson-Coleman** gave me my first glimpse into life during graduate school and provided me with lots of guidance as a new graduate student. **Dr. Sohail Jahid** was an amazing sounding board from day one, sharing her experience and expertise while also being a great confidant, even after moving on from the lab. As a fellow graduate student, **Dr. Rolando Ruiz-Vega** constantly asked me the hard questions, highlighted the strengths of collaboration with others to share expertise, and has been a

fount of wisdom for my questions. **Chi-Fen Chen** has been a constant throughout my time in the Ganesan lab, providing me with scientific advice, a helping hand, and conversation as the lab has changed over time. **Priya Vasudeva** was an essential help through the transition into my second year of graduate school, helping with experiments and decompressing after long days of work. **Dr. Jessica Shiu**, while adding to the confusion of lab, has been a great resource for bouncing off ideas and helping me prepare to transition into the future. **Francisco Espita** taught me the basic for working with mice which became such an essential part of my graduate research. **Dr. Pezhman Mobasher** provided a unique perspective from his experiences in clinical research. **Dr. Marc Liggins** helped me grow as a collaborator as I took over from his graduate work, while newer members, **Dr. Linh Voung** and **Terry Nugyen**, have been enthusiastic as they take over some of my projects despite the challenges of the last few months.

I have spent the last few years mentoring high school students, undergraduates, and graduate students in the lab. While I have striven to share my expertise in scientific research, they have all taught me patience and how to cater my mentorship style to my mentee. Beyond the lab, I have interacted with many talented high school students through the UCI Cancer Research Institute Youth Science Fellowship Program (YSFP) who have always inspired me with their motivation and dedication to learning what goes on behind the scenes of cancer research.

I have been supported by the UCI Community in many ways. **Nita Driscoll, Krystina Jarema**, and the Cancer Research Institute have been an immense help as a researcher and trainee always going the extra mile to help me understand the system and decompress. Their assistance with outreach for the YSFP and support through the foundation and continuation of the Oncoslayers, a UCI Anti-Cancer Challenge team, have been an integral component of my graduate experience. As a part of the Cellular and Molecular Biosciences umbrella program, the

Department of Biological Chemistry, the Cancer Research Institute, and the UCI Skin Club, I am appreciative of the diverse research interests that allowed me to understand advancing techniques regardless of the system, set the framework for collaborations within the university, and provide constructive criticism for discussion of research in progress. **Leora Fellus** and the staff of the School of Medicine Graduate Studies created fun events that helped develop a sense of community. Also, the Department of Dermatology and Center for Complex Biological Systems have been helpful in making sure we had the reagents needed for research.

The core facilities at UCI have allowed me the opportunity to use cutting edge techniques with the help of amazing colleagues without leaving campus. **Dr. Melanie Oakes** has been an amazing resource for next generation techniques, but also an amazing friend during the shelter-in-place willing to provide advice and a willing ear as I transition out of graduate school and prepare for my next steps in the middle of a pandemic. Melanie, **Dr. Jenny Wu**, and the Genomics High Throughput Facilities staff have made the genomics experiments in my research possible and provided the necessary support when I had any questions. **Dr. Grant MacGregor, Jonathan Neumann**, and the Transgenic Mouse Facility have been an amazing resource for mouse model studies, including the generation of novel strains. My research was also completed with the help of **Michaela Marshall** and **Eric Pearlman**; **Jennifer Atwood** at the Institute for Immunology Flow Core; **Dr. Rob Edwards** and the UCI Pathology Core; **Ilse Sears-Kraxberger** and **Oswald Steward**; **Dr. Mihaela Balu, Dr. Alexander Fast,** and **Griffin Lentsch** at the Beckman Laser Institute.

Though my highs and lows, I have been extremely appreciative of my fellow graduate students. **Amber Habowski**, more than anyone, has been an outlet for the little joys and the overwhelming frustrations in research after a long day in lab. She was also an amazing

collaborator for research and outreach, always willing to lend either an ear or a helping hand. To the rest of my compatriots in the Biological Chemistry, the School of Medicine, and Cellular and Molecular Biosciences, thank you for the advice and commiseration throughout this journey.

I have been fortunate to receive financial support for my graduate education from the Gazzaniga Family, the UCI Cancer Biology and Therapeutics training grant, the UCI School of Medicine, and the UCI Anti-Cancer Challenge.

While I have long been interested in science, I have been very fortunate to have many teachers and mentors along the way who have cultivated my interest. From the encouragement with photography lessons after finishing in class work in **Mr. Stanford's** seventh grade science class to my online excursion into marine science with **Fawn Custer** and A.P. Biology with **Bernadette Hoover**, I had all of the necessary tools to succeed as an undergraduate. At Oregon State University, the vested interest of **Drs. Indira Rajagopal** and **Kevin Ahern** helped me get my start in scientific research with **Dr. Virginia Weis**. **Camille Paxton, Angela Poole, Shelia Kitchen,** and the rest of the Weis laboratory gave me my first glimpse of the hard work and rewards with scientific research and the confidence to continue on in graduate school.

Life cannot be just one sided and I have been blessed to find a musical outlet at St. Mark Presbyterian Church. **Dr. Mark Davis, Ron Levy, Cathy Green, Ernie Nunez, Bart McHenry, Deborah and Lou Savage** have made me a welcome part of the Saturday worship service, teaching me improvisation, sharing a love of great music, and tolerating my constant references to science. All of the members at St. Mark have supported me with their fellowship as I worked through graduate school.

Lastly, I have to thank my family. My parents, **David** and **Sarah Flesher**, who were given a daughter with a hearing disorder and never questioned whether it was possible for me to achieve

whatever I set my mind to. Through my struggles, they have supported me and given me every opportunity to succeed. My siblings **Andrew, Virginia, Daniel,** and **Susanna** have been outlets for my frustrations, celebrated my joys, and shared their puppies when they could. My grandma **Ann Flesher** and uncle **Stephen Flesher** have always been excited for news and all of my updates during this adventure, as well as the rest of my extended family who have checked in and engaged in all of my triumphs.

I look forward to taking the next steps in my career and I am confident that my foundation in science will be firmly planted on the basis of what I have learned. Thank you everyone for your support.

CURRICULUM VITAE

Jessica Leigh Flesher

EDUCATION

University of California, Irvine, Irvine, CA June 2020

Ph.D. in Biomedical Sciences, Ganesan Laboratory, Department of Biological Chemistry
Dissertation: Using *In Vivo* Models to Understand Melanogenesis

Oregon State University, Corvallis, OR June 2013

Honors B.S. in Biology, Marine Biology Option, s*umma cum laude*, Undergraduate Research Fellow
Honors Thesis: Is there a change in expression of apoptosis and autophagy genes in *Aiptasia* sp. after thermal stress? Available: http://hdl.handle.net/1957/40251

RESEARCH EXPERIENCE

Ganesan Laboratory, Dept. of Biological Chemistry, University of California, Irvine, Irvine, CA
Graduate Student Researcher, Fall 2014 – present
Focus: Using *In Vivo* Models to Understand Melanogenesis

Weis Laboratory, Dept. of Zoology, Oregon State University, Corvallis, OR
Undergraduate researcher, 2011-2013
Focus: Characterize cellular pathways that result in coral bleaching of anemones

RESEARCH SKILLS

Mouse husbandry; collection and analysis of mouse tissues; PDX tumor models; bioinformatics (Linux, python, R), single-cell and bulk RNA-seq analysis; primary mouse cultures; binding assays; western blot analysis; flow cytometry; IHC/IF staining; luciferase assays; cell culture; animal husbandry of sea anemone, *Aiptasia* sp.; *Symbiodinium* sp. extraction from *Aiptasia* and culture; PCR and gel electrophoresis; cloning; RNA extraction and purification; cDNA synthesis; qRT-PCR; primer design; laboratory maintenance

PUBLICATIONS

*,† - indicate co-authors

Flesher, J.L., E.K. Patterson-Coleman, P. Vasudeva, R. Ruiz, M. Marshall, E. Pearlman, G.R. MacGregor, J. Neumann, A.K. Ganesan. (2020) "Delineating the Role of MITF Isoforms in Pigmentation and Tissue Homeostasis". *PCMR*. doi: 10.1111/pcmr.12828. PMID 31562697.

Liggins, M.C.*, **J.L. Flesher***, S. Jahid, P. Vasudeva, V. Eby, S. Takasuga, J. Sasaki, T. Sasaki, R.E. Boissy, A.K. Ganesan. (2018) "PIKfyve regulates melanosome biogenesis". *PLoS Genet.* https://doi.org/10.1371/journal.pgen.1007290. PMID 29584722.

Habowski, A.N., **J.L. Flesher**, J.M. Bates, C. Tsai, R. Zhao, K. Martin, A.K. Ganesan, R.A. Edwards, Y. Shi, K.J. Hertel, M.L. Waterman. "RNA Processing is an Immediate Early Event in Colon Stem Cell Differentiation". Accepted *Communications Biology*.

Jahid, S.*, J.A. Ortega*, **J.L. Flesher***, G. La Sala, J. Manigrasso, N. Brindani, M.A. La Serra, J.M. Arencibia, S.M. Bertozzi, M. Summa, R. Bertorelli, A. Armirotti, S.J. Hachey, C. Chen, C.C.W Hughes, R.A. Edwards, M. De Vivo†, A.K. Ganesan†. "Structure-based Design of Selective RHOJ/CDC42 Effector Interaction Inhibitors for the Treatment of Cancer". Manuscript submitted for publication.

Mobasher, P., J. Shiu, **J.L. Flesher**, G. Lentsch, A.K. Ganesan. "Evaluating the Efficacy of the Melanocyte Keratinocyte Transplantation Procedure in the Treatment of Vitiligo: A comparative study of two different harvesting techniques". Manuscript submitted for publication.

ABSTRACTS

Flesher, J.L., S. Jahid, J.A. Ortega, G. La Sala, N. Brindani, J.M. Arencibia, J. Manigrasso, S. Hachey, C. Chen, C. Hughes, M. De Vivo, A.K. Ganesan. Structure-based Design of CDC42/RHOJ Effector Inhibitors for the Treatment of Cancer. Bar Harbor, ME, USA: PanAmerican Society for Pigment Cell Research Annual Meeting 2019.

Flesher, J.L., E.K. Paterson, P. Vasudeva, R. Ruiz-Vega, G.R. MacGregor, J. Neumann, A.K. Ganesan. Delineating the Role of MITF Isoforms in Pigmentation and Tissue Development. Salishan Resort, OR, USA: Joint Montagna Symposium on the Biology of Skin and PanAmerican Society for Pigment Cell Research Conference 2018.

Flesher, J.L., E.K. Paterson, P. Vasudeva, G.R. MacGregor, J. Neumann, A.K. Ganesan. Delineating the Role of MITF Isoforms in Melanogenesis. Denver, CO, USA: International Pigment Cell Conference 2017.

Movassat, M., **J. Flesher**, K. J. Hertel. Splicing repression results in changes to U1 snRNP complex integrity at the 5' splice site. Cold Spring Harbor, NY, USA: Eukaryotic mRNA Processing, Cold Spring Harbor Laboratory Meeting 2015.

PRESENTATIONS

Flesher, J.L. Structure-based Design of CDC42/RHOJ Effector Inhibitors for the Treatment of Cancer.
UCI Skin Club, Irvine, CA, October 21, 2019
PanAmerican Society for Pigment Cell Research Annual Meeting 2019, Bar Harbor, ME, October 4, 2019.

Flesher, J.L. Delineating the Role of MITF Isoforms in Pigmentation and Tissue Development.
Department of Biological Chemistry Seminar Series, Irvine, CA, June 5, 2019.
T32 Cancer Biology Retreat, Los Angeles, CA, April 13, 2019.
UCI Skin Club, Irvine, CA, October 29, 2018
Joint Montagna Symposium on the Biology of Skin and PanAmerican Society for Pigment Cell Research, Salishan Resort, OR, USA, October 19, 2018
Department of Biological Chemistry Seminar Series, Irvine, CA, May 30, 2018

Flesher, J.L. Pigmentation: Hidden in Plain Sight. TEDx Newport Beach invited speaker, Newport Beach, CA, March 20, 2018.

Flesher, J.L. Delineating the Role of MITF Isoforms in Melanogenesis.
UCI Cancer Biology Research in Progress Talk, Irvine, CA, February 12, 2018.
UCI Skin Club, Irvine, CA, October 16, 2017.
International Pigment Cell Conference 2017, Denver, CO, USA, August 27, 2017.
UCI Skin Club, Irvine, CA, March 6, 2017.

Flesher, J.L. Pigmentation Schmigmentation: Looking Skin Deep. St. Mark Presbyterian Church, Adult Discipleship Commission invited speaker, Newport Beach, CA, January 7, 2018.

Flesher, J.L. Transgenic approaches to study mouse pigmentation. University of California, Irvine 2017 Cancer Biology & Therapeutics Training Grant Retreat, Pasadena, CA, April 22, 2017.

Flesher, J.L. Looking for Grey. University of California, Irvine Scientific Communication Skills, Irvine, CA, May 25, 2016. Available: https://www.youtube.com/watch?v=SMSSRUaiIzk

Flesher, J.L. WIPI1: a novel regulator of melanogenesis. University of California, Irvine Skin Club, Irvine, CA, May 16, 2016.

Flesher, J.L. Is there a change in apoptosis and autophagy genes in *Aiptasia* sp. after thermal stress? Oregon State Univeristy Honors Thesis Defense, Corvallis, OR, May 13, 2013.

Flesher, J.L., D. Aguilar, K. Belica. Macroagal feeding preference of the gumboot chiton, *Cryptochiton stelleri*. Oregon State University Hatfield Marine Science Center Marine Biology Symposium, Newport, OR, June 8, 2012.

Flesher, J.L. Change in the genetic expression of apoptotic and autophagic proteins after thermal stress in *Aiptasia pallida*. Oregon State University/Howard Hughes Medical Institute Summer Undergraduate Research Symposium, Corvallis, OR, September 20, 2011. Available: http://www.youtube.com/watch?v=qFL7JUOym34

POSTERS

Flesher, J.L., S. Jahid, J.A. Ortega, G. La Sala, N. Brindani, J.M. Arencibia, J. Manigrasso, S. Hachey, C. Chen, C. Hughes, M. De Vivo, A.K. Ganesan. Structure-based Design of CDC42/RHOJ Effector Inhibitors for the Treatment of Cancer.
3rd Annual Skin Symposium, UCI, January 24, 2020.
School of Medicine Grad Day 2019, UCI, October 11, 2019.
PanAmerican Society for Pigment Cell Research Annual Meeting 2019, Bar Harbor, ME, USA, October 3, 2019.

Flesher, J.L., E.K. Paterson, P. Vasudeva, R. Ruiz-Vega, G.R. MacGregor, J. Neumann, A.K. Ganesan. Delineating the Role of MITF Isoforms in Pigmentation and Tissue Development.
3rd Annual Skin Symposium, UCI, January 24, 2020.
The 2019 UCI Campus-Wide Symposium on Basic Cancer Research, UCI, May 3.
Joint Montagna Symposium on the Biology of Skin and PanAmerican Society for Pigment Cell Research Conference 2018, Salishan Resort, OR, USA, October 19, 2018.

Flesher, J.L., P. Mobasher, A.K. Ganesan. Unique Cell Types Revealed in Vitiligo Skin with Single Cell RNA Sequencing. **2019 Systems Biology Retreat**, Los Angeles, CA, USA, March 29-30, 2019.

Flesher, J.L., E.K. Paterson, P. Vasudeva, G.R. MacGregor, J. Neumann, A.K. Ganesan. Delineating the Role of MITF Isoforms in Melanogenesis.
School of Medicine Grad Day 2018, UCI, October 12, 2018.
The 2018 UCI Skin Symposium, UCI September 14, 2018.
The 2018 UCI Campus-Wide Symposium on Basic Cancer Research, UCI, May 5, 2018.
2017 CABTRAC Annual Retreat, Stevenson, Washington, October 29-31, 2017.
School of Medicine Grad Day, UCI, September 28, 2017.
International Pigment Cell Conference 2017, Denver, CO, USA, August 27-29, 2017.
The 2017 UCI Campus-Wide Symposium on Basic Cancer Research, UCI, May 6, 2017.
2017 Skin Symposium UCI, February 23, 2017.

Flesher, J.L., C.W. Paxton, A.Z. Poole, S.A. Kitchen, V.M. Weis. Is there a change in apoptosis and autophagy genes in *Aiptasia* sp. after thermal stress?
2013 Center for Genome Research and Biocomputing Conference, OSU, June 3, 2013.
Celebrating Undergraduate Excellence, OSU, May 21, 2013
University Honors College Thesis Fair, OSU, May 17, 2013

RESEARCH FUNDING

UCI Center for Complex Biological Systems and UCI Skin Biology Center 2019 Opportunity Award
T32 Training Program in Cancer Biology and Therapeutics through the UCI Cancer Institute, January 2017 – December 2018
University Honors College Experience Scholarship, 2012
Howard Hughes Medical Institute Summer Undergraduate Research Program at OSU, 2011
Undergraduate Research, Innovation, Scholarship, and Creativity: Start, 2011

AWARDS

PanAmerican Society of Pigment Cell Research Travel Award	October 2019
UCI Anti-Cancer Challenge Travel Award	October 2019
School of Medicine Travel Award	October 2019
Gazzaniga Family Medical Research Award	November 2018
PanAmerican Society of Pigment Cell Research Travel Award	October 2018
UCI School of Medicine Travel Award	October 2018
PanAmerican Society of Pigment Cell Research Travel Award	August 2017
UCI School of Medicine Travel Award	August 2017
Bob & LaRae Parry Environmental Scholarship, St. Mark Presbyterian Church (USA)	July 2017
School of Medicine Individual Fellowship Application Incentive, UCI	January 2016
Alex Riazance Scholarship, OSU	2012-2013
Barry M. Goldwater Scholarship and Excellence in Education Program, OSU Nominee	2012
Merrill Family Fund Scholarship, OSU	2011-2013
Andy Aitkenhead Memorial Scholarship, OSU	2010-2013
Science Scholars Scholarship, OSU	2010-2012
Provost Scholar, OSU	2009-2013

PROFESSIONAL SOCIETIES

PanAmerican Society for Pigment Cell Research, 2017 – present.
American Association for Cancer Research, 2019 – present.

TEACHING EXPERIENCE

University of California, Irvine, School of Biological Sciences, Irvine, California

Teaching Assistant, Cancer Systems Biology Short Course, Jan 2019.
Teaching Assistant, Center for Complex Biological Systems Bootcamp, Aug 2018.
Teaching Assistant, Cancer Systems Biology Short Course, May 2018.
Teaching Assistant, Biology: DNA to Organisms, Sept 2016 – Dec 2016.
Teaching Assistant, Biology: Organisms to Ecosystems, Jan 2016 – March 2016.
Student Leader, Cellular and Molecular Biosciences journal club to prepare first year graduate students for preliminary exams, Jan 2016 – May 2016.

MENTORING EXPERIENCE

University of California, Irvine

Graduate Students: **Yingxin Cao** (April 2019 – June 2019); **Leanne Hildebrand** (Jan 2019 – Feb 2019); **Emily Neubert** (Sept 2018 – Dec 2018)

Undergraduate Students: **Celine Saade** (Sept 2018 – present); **Zachary Springs** (Sept 2018 – Sept 2018); **Madeline McCanne** (May 2019 – Aug 2019; June 2017 – Aug 2017 in HS); **Jason Wu** (April 2018 – Dec 2018); **Trung Tran** (Sept 2017 – June 2018); **Shyam Chandrasekar** (June 2016 – Sept 2016)

High School Students: **Katrina Huynh** (June 2019 – Aug 2019); **Alexa Herbel** (June 2018 – Aug 2018); **Sahil Telang** (June 2016 – Sept 2017)

COMMUNITY INVOLVEMENT

The Oncoslayers team for the UCI Anti-Cancer Challenge,	2017 – 2020
Team Captain	2017 – 2019
Synerjazz, worship band at St. Mark Presbyterian Church	2015 – 2020
UCI Cancer Research Institute Youth Science Fellows Program,	2016 – 2019
Graduate Student Organizer	2017 – 2019
The 2019 UCI Anti-Cancer Challenge, Volunteer	June 8, 2020
The 2018 UCI Anti-Cancer Challenge, Volunteer	May 19, 2018
Department of Biological Chemistry Student Representative,	2017 – 2018
GPS-BIOMED Peer-led Seminar: Mentoring Students & Getting Involved in Outreach,	
Invited speaker	September 27, 2017
The UCI Anti-Cancer Challenge Weekend, Volunteer	June 10 – 11, 2017
Ganesan Laboratory Tour, February 23, 2017	February 23, 2017
UCI Tumor Suppressors, Relay for Life, Team member	February 2016 – April 2016
Ganesan Laboratory Tour for middle school students,	November 4, 2015
Leukemia and Lymphoma Society Light the Night, Volunteer	September 19, 2015
Leukemia and Lymphoma Society UCI Laboratory Tour	April 2, 2015
Rock the Socks, video campaign for Leukemia and Lymphoma Society,	
Cancer Researcher	February 21, 2015
United Methodist Volunteers in Mission, Galena, AK flood repair	Fall 2013
Oregon State University Bands, piccolo and flute	2009 – 2013
Marching Band Piccolo Section Leader	2011 – 2013
Marine Science Day, Hatfield Marine Science Center, Volunteer	May 2012

REFERENCES

Anand K. Ganesan, MD, PhD
Professor
University of California, Irvine
202 Sprague Hall
Irvine, CA 92697
(949)-824-2926
aganesan@uci.edu

Xing Dai, PhD
Professor
University of California, Irvine
D250 Medical Sciences I
Irvine, CA 92697
(949)-824-3103
xdai@uci.edu

Maksim Plikus, PhD
Associate Professor
University of California, Irvine
3108 Gross Hall
Irvine, CA 92697
(949)-824-1260
plikus@uci.edu

Additional details are available upon request

ABSTRACT OF THE DISSERTATION

Using *In Vivo* Models to Understand Melanogenesis

by

Jessica Leigh Flesher

Doctor of Philosophy in Biomedical Sciences

University of California, Irvine, 2020

Professor Anand K. Ganesan, Chair

The diversity of hair and skin color is a direct result of melanin synthesis occurring in melanocytes. Melanogenesis is a set of highly regulated processes that occur in a specialized organelle called the melanosome. Two components that are essential for melanogenesis to occur are 1) transcriptional regulation of the genes required for pigment production by MITF, and 2) proper trafficking of proteins and enzyme components to the melanosomes. While extensive studies have identified over 100 genes, there are still gaps in understanding how *MITF* isoforms alter melanogenesis-specific gene expression and how proteins control the formation of the melanosome. While these two parts of melanogenesis are distinct, *in vivo* models are a standard way to understand how these pathways contribute to melanogenesis as a whole. We recently identified *Pikfyve*, a gene that encodes a phosphoinositide kinase, as a regulator of melanogenesis. Conditional loss of *Pikfyve* in murine melanocytes causes greying of the coat. Isolation and culture of melanocytes from *Pikfyve* mice revealed defects in melanosome maturation due to failure of protein trafficking to the melanosome, defining a new lipid signaling pathway that controls the early stages of melanogenesis. Another phosphoinositide binding protein, *Wipi1,* subtly alters pigmentation after constitutive loss in mice, with more pronounced phenotypes occurring at the cellular level. In addition to this work, we completed additional studies trying to understand which

Mitf isoform regulates melanogenesis and when and where it does. As *Mitf-A* and *Mitf-M* are the primary *Mitf* isoforms in melanocytes, we used CRISPR/Cas9 technology to generate both *Mitf-A* and *Mitf-M* isoform-specific knockout mice. While loss of *Mitf-A* had only subtle impacts on pigmentation, loss of *Mitf-M* drastically alters pigmentation in the hair, skin, and eyes due to loss of melanocytes in adults. Intriguingly, *Mitf-M* knockout mice also have enlarged kidneys, revealing new roles for this transcription factor in other tissues. Moreover, we have recently revealed that some Mitf-M knockout mice can develop spontaneous repigmentation on parts of their body, a mechanism that is a result of spontaneous reactivation of melanocytes. Taken together, these studies outline an approach that can be used to better understand how melanogenesis is specified in both place (intracellularly and in the organism) and time (development and hair stage).

CHAPTER 1

Melanocytes, Pigmentation, and Human Health

Jessica L. Flesher and Anand K. Ganesan

ABSTRACT

Melanocytes are responsible for pigmentation variation found in humans and other mammals. Within the epidermis, these specialized cells are responsive to environmental triggers and localized cell-to-cell signaling provides inductive signals for melanogenesis. Mutations in melanocyte-specific genes account for much of the variation in skin and hair color in human populations and other species, but can also lead to psychologically damaging and deadly diseases. An invaluable tool in understanding melanocyte biology and the underlying process of melanogenesis are mouse models. By manipulating the expression of key genes, we can better understand how melanogenesis is regulated *in vivo*.

A CANVAS FOR PIGMENTATION

As the most exposed surface, skin provides many vital functions for an organism. Skin prevents desiccation and infection, heals following injury, provides an anchor for secondary structures, and is a canvas for the wide range of pigmentation patterns found in the animal kingdom (*1*). In mammals, the skin is composed of three layers. The uppermost and cellularly dense layer is the epidermis (*2*). While the epidermis has numerous cell types, it is predominantly composed of keratinocytes and separated from the rest of the skin layers by a basement membrane (*2*, *3*). Next, the dermis provides the underlying structure (*2*) and contains blood vessels that feed the epidermis. Additionally, hair follicles and sweat glands that are continuous with the epidermis extend into the dermis during their formation (*3*). The hypodermis, or fat layer, is the lowest layer of the skin. Depending on the body region, the hypodermis consists of loose connective tissue to allow for the skin to glide or provides pockets of adipose for insulation (*2*). While all the layers

of the skin contribute to the organs function, the dynamic epidermis and continuous hair follicles are responsible for the most visually apparent feature of skin, pigmentation.

The range of mammalian hair and skin colors and patterns is due to specialized cells called melanocytes. In human skin, melanocytes are found in the basal layer of the interfollicular epidermis and within the bulge and bulb of the hair follicle (*4*). The basement membrane of human epidermis contains approximately one melanocyte for every ten keratinocytes (*4*). The location of melanocytes can vary between species. Mice and other mammals have an abundance of follicular melanocytes, but lack melanocytes residing in the epidermis on the main trunk of the body (*5*). In contrast, humans have melanocytes in the epidermis and in the hair, which are sparsely localized on body regions other than the scalp (*6*). The number of melanocytes can also vary by body region. The scalp, palms of hands and soles of feet generally have fewer active melanocytes than found in the skin of the trunk, arms, or legs (*7*, *8*). When the normal distribution of melanocytes is lost and melanocytes overgrow this leads to the formation of melanocytic moles (aka nevi) and malignant melanomas (*9*). The main contributor to the different shades of skin and hair color is the amount and type of the melanin pigments that are produced and packaged into organelles by melanocytes. These pigment units are delivered to keratinocytes in the epidermis or growing hair follicles (*10*).

During normal development melanocyte precursors called melanoblasts have to migrate from the neural crest to reach the skin. Commitment to the melanocyte lineage requires the activation of key transcription factors and lineage markers that is initiated in the early embryo. Murine neural crest cells start to differentiate into migratory precursors at embryonic day (E) 8 through the induction of *Pax3* and *Zic1* (*11*). Bipotent progenitors of melanoblasts and glial cells are further specified by the expression of *Sox10* and *Snai2* at E8.5 (*11*, *12*). Expression of *Mitf*, *Kit*, and *Ednrb* starting at E9.5 commit cells to the melanocyte lineage (*12*) with detectable

melanoblasts by E10.5 (*13*). Pools of melanocytes in the skin originate from melanoblasts derived from the cervical and trunk regions of the neural crest (*14*), but melanocytes are also found in the ear, eye, brain, and heart. Melanoblasts from the cranial neural crest populate the stria vascularis, the vascularized portion of the cochlea in the ear and the uvea (iris stroma and choroid) of the eye (*13*, *15*, *16*). The other pigmented cells of the eye, the iris pigment epithelium (IPE) and retinal pigment epithelium (RPE), produce melanin in an MITF-dependent manner, but are derived from the neuroepithelium rather than the neural crest (*17*). Originating from the cephalic neural crest, melanocytes have been identified in the leptomeniges and the sympathetic cephalic ganglia of the brain (*18*, *19*). Melanocytes have also been identified in the valves and septa of the heart that originate from cardiac neural crest cells (*11*, *19*). Despite the different locations of the cells, the production of the pigment melanin is a defining characteristic.

AN OVERVIEW OF MELANOGENESIS

The production of melanin plays a very important role in the skin apart from outward appearance. Melanin protects skin cells from harmful damage by ultraviolet (UV) radiation. UV induces DNA damage which activates p53 as part of the repair pathways in keratinocytes and melanocytes (*20*). As part of this response, p53 upregulates POMC (*21*) which is cleaved by multiple proprotein convertases releasing alpha-melanocyte stimulating hormone (αMSH) (*22*). The αMSH is recognized by the g-protein coupled melanocortin 1 receptor (MC1R) and sets off a adenylate cyclase dependent signaling cascade that leads to the activation and translocation of CREB into the nucleus (*23*). Phosphorylation of CREB can also be stimulated by endothelins, which bind the endothelin receptor type B (EDNRB) and activate the MAPK signaling cascade

(*24*). Among the CREB target genes in melanocytes is the *Microphthalmia associated transcription factor* (*MITF*).

MITF acts as the master regulator of melanogenesis. While αMSH/MC1R stimulated *MITF* upregulation, canonical WNT signaling through the frizzled receptors allows β-catenin/LEF1 binding to the *MITF* promoter (*24*). MITF activity is also regulated post-translationally. Signaling through c-Kit is required for ERK2 phosphorylation of $MITF^{Ser73}$, while Ser409 is phosphorylated by the p90 ribosomal S6 kinase (p90RSK) (*23*). Sumoylation of MITF also occurs at Lys182 and Lys316 which promotes MITF activity on promoters with multiple MITF binding sites (*25*). Activated MITF turns on transcription of a number of target genes involved in motility (*c-Met*), survival (*BCL2, HIF1A*), proliferation (*CDK2, CDK4, p16, Rb, p21*), and melanogenesis (*TYR, TYRP1, PMEL, MLANA, DCT*) (*23*, *26*). The upregulation of melanogenesis-specific genes is necessary to provide the correct conditions for melanin synthesis to occur.

Melanocytes sequester melanin synthesis and reactive oxygen species (ROS) intermediates within organelles called melanosomes. Melanosomes, like lysosomes and other lysosome-related organelles, are derived from endosomes, have a low pH, and contain some lysosomal resident proteins (*27*). There are four distinct stages of melanosomes characterized by both protein components and melanin deposition (*24*). Stage I melanosomes resemble early endosomes marked by MART1 (melanoma antigen recognized by T-Cells 1) (*28*) and OA1 (ocular albinism 1) (*24*) with intraluminal vesicles containing PMEL (premelanosome protein) (*27*). PMEL is first sent to the cellular membrane and must undergo clathrin-dependant endocytosis facilitated by adaptor protein complex 2 (AP-2) in order to make its way to stage I melanosomes (*27*). In stage I melanosomes, PMEL is cleaved to form long amyloid fibrils characteristic of Stage II

melanosomes, this also corresponds with the morphological change to ellipsoidal, eumelanic melanosomes (*24*). During this step, the kiss-and-run action of melanosomes with nearby lysosomes leads to the delivery of necessary proteins required for PMEL cleavage and the acidic environment for melanin synthesis (*29*).

Melanosomes continue to progress with the delivery of catalytic enzymes including tyrosinase (TYR), tyrosinase-related protein 1 (TYRP1), and dopachrome tautomerase (DCT). Following post-translational modification in the Golgi, these membrane bound proteins are trafficked to endosomes and multivesicular bodies and sorted into the appropriate vesicles for trafficking to the melanosome (*27*). Vesicle trafficking of both TYR and TYRP1 from the *trans*-Golgi network relies on the activity of RAB32 and RAB38, two functionally redundant RAS GTPases (*30*). Like other GTPases, the activity of RAB32 and RAB38 is regulated by guanine nucleotide exchange factors (GEFs) that coordinate the release of guanosine diphosphate (GDP) to allow for guanosine triphosphate (GTP) binding and activation (*30*). BLOC-3 (biogenesis of lysosomal related organelles complex 3) is composed of two subunits, HPS1 (Hermasky-Pudlak syndrome protein 1) and HPS4, that function as a RAB32 and RAB38 GEF and facilitate melanosome localization (*31*). From early endosomes, TYRP1 and some TYR containing vesicles are trafficked to intermediate endosomes and endosomal tubules in a process requiring BLOC-1 (*32*) which is made up of BLOS1 (Biogenesis of lysosome-related organelles complex 1 subunit 1), BLOS2, BLOS3, SNAPN (Snapin) (*33*), PLDN (Pallidin), MUTED (*34*), CNO (Cappuccino) (*35*), and DTBP1 (Dysbindin) (*36*). This trafficking mechanism also relies on the AP-1 complex for sorting TYR and TYRP1 into the tubules and positioning the cargo for delivery to melanosomes (*37*). Fusion of endosomal tubules containing melanosomal proteins requires BLOC-2 composed of HPS3, HPS5 and HPS6 (*38*, *39*). Cells without the required AP-1, BLOC-1, or BLOC-2 have

mislocalization of TYRP1 to the Golgi and the cell membrane, while some TYR containing membranes are also delivered to the cell membrane (*27*, *37*, *38*). The majority of TYR containing vesicles are trafficked in a nonredundant manner from multivesicular bodies (MVBs) through recruitment by AP-3 (*40*). After delivery of the enzymatic proteins, melanosomes advance to Stage III, characterized by melanin deposition on PMEL fibrils (*27*). TYR catalytic activity relies on copper, which is transported into melanosomes by ATP7A (ATPase copper transporting alpha) (*41*). ATP7A is trafficked to stage III melanosomes in a BLOC-1 dependent manner (*42*). Melanin synthesis continues until melanosomes are fully pigmented and enter Stage IV (*27*). Melanosomes are themselves trafficked along microtubules to reach cellular dendritic "fingers" by microtubule-associated motor proteins (*24*). LC3B (microtubule-associated protein 1 light chain 3 beta) coordinates the assembly of motor proteins to the melanosome (*43*). Regulation of LC3 is controlled through conjugation to phophatidylethanolamine on the melanosome membrane and is removed by ATG4B (autophagy related protein 4 beta) as the melanosomes reach the actin network (*43*). Melanosomes then interact with the actin network in dendrites and dock to the plasma membrane in processes that require RAB27A (*24*).

Stage IV melanosomes are transferred to neighboring keratinocytes. Each melanocyte can interact with 30-50 neighboring keratinocytes to deliver melanosomes to the basal and suprabasal layers of the epidermis (*4*, *44*). In keratinocytes, melanosomes are trafficked towards the nucleus, where they form a cap on the apical side of the nucleus to prevent further DNA damage from UV irradiation (*45*). Key steps of melanogenesis are illustrated in Figure 1.1. Melanin is retained as keratinocytes differentiate, and degraded during terminal differentiation (*45*) through autophagy (*46*). While melanogenesis can be stimulated by UV radiation, the amount of tanning that occurs is dependent on the complexion of an individual as described by the Fitzpatrick phototype scale

(*44*). The range of pigmentation from phototypes I to VI is a result of mutations in the regulatory regions and genes that alter melanin synthesis.

VARIATION IN HUMAN PIGMENTATION

Melanins can be divided into two categories: brown to black eumelanin and yellow to red pheomelanin (*47*). The first steps of melanin synthesis requires TYR to catalyze the conversion of L-tyrosine to L-DOPA, the rate-limiting step of melanogenesis, and subsequently into dopaquinone (*23*). Eumelanins are produced through the cyclization of dopaquinone into dopachrome which can be modified by TYR into 5,6-dihydroxyindole (DHI) or converted by TYRP1 or DCT into 5,6-dihydroxyindole-2-carboxylic acid (DHICA), the two eumelanin subunits (*48*). For the production of pheomelanins, the sulfhydryl group of cysteine reacts with dopaquinone to form cysteinyl-DOPA which is further converted into the pheomelanins 1,4-benzothiazine (BTZ) and 1,4-benzothiazine-3-carboxylic acid (BTZCA) (*47*). The individual monomers of melanin alter how tightly the polymeric melanin can be deposited onto PMEL fibrils which, in turn, affects the shape of melanosomes (*49*) and how much photoprotection they confer (*50*). Eumelanin, as illustrated in Figure 1.1, prevents DNA damage through absorption of UVB rays (280 – 320nm) that penetrate into the epidermis of the skin (*44*). However, pheomelanin provides no protection against UVB irradiation and can amplify oxidative stress from UVA rays (320 – 400nm) that travel into the dermis of the skin (*44*, *51*). Through the irradiation of pheomelanin, UVA produces a superoxide anion that increases DNA damage through the production of reactive oxygen species (ROS) (*51*, *52*). Different hair colors and skin phototypes are a result of the balance between eumelanin and pheomelanin synthesis.

Variation in human pigmentation is caused by genetic mutations that regulate steps of melanogenesis. The recessive inheritance of red hair has led to the identification of multiple mutations residing in the *MC1R* gene that lead to a reduction or loss of function of the receptor (*53*) which triggers the production of pheomelanin. African-American populations have an ancestral single nucleotide polymorphism (SNP) within the *Agouti signaling protein* (*ASIP*) gene region that is associated with darker skin tones (*54*). ASIP is a known antagonist of the MC1R receptor, triggering pheomelanin synthesis and patterning of hair in some species (*55*). Additional studies have identified SNPs associated with *SLC24A2* (*Solute Carrier Family 24 Member 5*) that confer lighter skin in individuals of European descent (*56*) and *MFSD12* (*major facilitator superfamily domain containing 12*) in African populations that increase the amount of melanin (*57*). These observations illustrate how pigment variation is genetically encoded, even amongst a population that has very similar skin tones.

In areas with high levels of UV, like the tropics, protection from UV-induced DNA damage can explain the prevalence of darker skin shades. Individuals with more melanin and darker skin tones (Fitzpatrick phototypes V-VI) have more UV protection, increased ability to tan, and reduced risk for skin cancer (*44*). Lighter skin tones (phototypes I-II) have less melanin, decreased UV protection, reduced tanning potential, and an increased risk for skin cancer (*44*), resulting in higher rates of skin cancer for tropical and subtropical climates with large Caucasian populations including regions of Australia and southern latitudes of the United States (*58*). The leading theory for the evolution of lighter skin tones present in ancestral European and Asian populations is related to vitamin D synthesis (*59*). An essential step in vitamin D synthesis is the conversion of 7-dehydrocholesterol (7-DHC) to vitamin D_3 by basal keratinocytes in a process dependent on UVB radiation (*60*). Near the equator, the high levels of UV light year-round allow for enough

vitamin D synthesis even with high levels of melanin blocking some of the UVB. Closer to the poles, the total amount of UV radiation is drastically reduced due to cloud cover and the angle of the sun hitting the Earth (*61*). This is consistent with historical data showing how skin pigmentation varies across different latitudes (*62*). Retaining the ability to produce vitamin D is important for bone health, since Vitamin D deficiency causes rickets (*60*). Vitamin D levels can influence mental health as vitamin D supplements have been used to treat seasonal affective disorder (SAD) (*63*) in order to improve patient wellness during winter months (*64*). While pigmentation plays an important role in skin cancer risk, its influence on other facets of human health is incompletely understood.

HUMAN PIGMENTARY DISEASES AND MOUSE MODELS

The accumulation of mutations, either through direct UV-induced damage, amplified ROS induction, or aging can lead to skin cancer, the most commonly diagnosed group of cancers in the United States. The main risk factors for any type of skin cancer are the amount of exposure to UV radiation and the amount of melanin present in the skin where individuals with mostly pheomelanin have the highest risk (*65*). Melanocytes can also transform into the deadliest form of skin cancer, melanoma, responsible for 70-80% of all skin cancer related deaths (*66*). Cutaneous melanomas have a high burden of somatic mutations that have a signatures attributed to UV damage and age (*67*). While use of sunscreen has grown, melanomas are still frequent with increasing numbers in younger individuals due to use of tanning beds (*44*). Additional factors contribute to melanoma formation, since the most common oncogenic driver mutation, $BRAF^{V600E}$, does not share the classic UV signature. Targeted therapy for the BRAF mutation and immunotherapy that recognizes neoantigens from highly mutated tumors have been effective for

a subset of melanoma patients (*68*). Additionally, the presence of a $BRAF^{V600E}$ mutation is not sufficient to trigger melanoma formation, since this mutation is found in the majority of benign nevi, or moles, with additional mutations required to progress past initial growth arrest to form melanoma (*69*). To better understand how melanomas form and the complex relationship with other tumor suppressors and oncogenes, *Tyr* inducible Cre mouse models have been developed including two different $Braf^{V600E}$ models, $Braf^{V600E}$ alone (*70*) and in combination with *Pten* loss (*71*, *72*), and an $Nras^{Q61K}$ model with *Cdkn2a* loss (*73*) The complicated nature of melanocytes as the cell of origin continues to provide insight into how melanomas start and grow.

Overactive melanocytes can also impact health through the upregulation of melanin production. One common form of hyperpigmentation is melasma, a localized increase in pigmentation on the face, commonly associated with pregnancy (*74*). Melasma is prevalent in about 1% of the general population (*74*) with approximately 90% of cases found in women (*75*). While topical, oral, and minimally invasive surgical procedures exist, many effective treatments cause unwanted side effects that can vary from irritation to burns on the skin (*74*). UV exposure can exacerbate symptoms, so an important aspect of treatment is use of sunscreen and avoiding UV radiation (*76*). Some of the cellular pathways that trigger melasma have been identified. Estrogen, which is elevated by pregnancy, can stimulate the G-protein coupled estrogen receptor (GPER) on melanocyte cell membranes to stimulate melanogenesis independently from the classical MC1R-UV damage response signaling pathway (*77*). While melasma is relatively common, no mouse models for the disease currently exist.

While too much pigmentation can lead to stigma, the loss of pigmentation can have a similar effect. Localized loss of melanocytes through targeted destruction by immune cells leads to the autoimmune disease known as vitiligo (*78*). Like melasma, vitiligo affects one percent of

the global population, however stigma associated with depigmentation disproportionately affects those with darker skin tones (*79*). Moreover, patients with vitiligo can often have skin itching/burning, an increased incidence of depression/anxiety, changes in vision, and even changes in hearing (*80*). During active disease, CD8 positive killer T-cells destroy melanocytes within the skin causing depigmentation (*1*). Current therapies include narrowband UVB therapy to trigger migration of melanocytes from hair follicles into the interfollicular epidermis (*81*). These methods show some efficacy in patients with stable disease, but don't always result in long-term repigmentation. This disease highlights the intimate communications that occur not only between melanocytes and keratinocytes, but melanocytes and the immune system. Mouse models that phenocopy certain features of vitiligo have been developed, but the $Mitf^{mi\text{-}vit}$ premature greying did not result from immune destruction of melanocytes and the other model relies on induced overactivation of T cells to induce the destruction of melanocytes (*82*, *83*).

The most common group of hypopigmentary diseases is albinism. Albinism occurs when melanocytes are present, but mutations in key proteins prevent the production of melanin. The most common types of oculocutaneous albinism are caused by mutations in *TYR* (50%) or mutations in *OCA2* (*84*), a protein that regulates pH (*85*) and contributes to the trafficking of TYR to the melanosome (*86*). Oculocutaneous albinism type 3 is caused by mutations in *TYRP1* and *SLC45A2* mutations result in type 4 (*87*). Mouse models for the genes associated with oculocutaneous albinism were some of the first established strains for the corresponding loci generated from mouse fanciers (*88*, *89*). After *Tyr* was mapped to the murine albino locus (*90*), defects in TYR trafficking to the melanosome and altering TYR activity or protein levels have been made possible through the use of *Tyr* mutant mice (*89*, *91*). *OCA2* is mutated in the pink-eyed dilution mouse strain and can be used as a model for oculocutaneous albinism, type 2 (*92*).

The mouse brown locus encodes TYRP1, and mouse mutant alleles have led to discoveries that TYRP1 affects the stability of TYR (*93*). Finally, mutations in *Scl45a2* lead to the underwhite mouse because of osmotic regulation defects caused by the encoded MATP (membrane-associated transporter protein) (*94*).

Due to the reliance of melanosomes and other lysosome-related organelles on endosomal and lysosomal trafficking machinery, mutations causing hypopigmentation can also be one characteristic of larger syndromes (*95*). Hermansky-Pudlak syndrome (HPS) is characterized by oculocutaneous albinism, defects in blood clotting, and pulmonary fibrosis due to mutations in the AP3, BLOC-1, BLOC-2, and BLOC-3 subunits (*87*). The subtypes of HPS are defined by the causal mutation (*87*). Through the use of the pale ear and light ear mouse mutants, HPS1 and HPS4 were identified as the subunits of BLOC-3 (*96*). The pearl mouse has been used a model for HPS type 2 due to corresponding mutation in *Ap3b1*, the beta 1 subunit of AP-3 (*97*) while HPS10 is caused by mutations in the delta subunit of AP-3 with the mocha mouse as a model (*95*). HPS types 3, 5 and 6 are recapitulated in the cocoa, ruby-eye2, and ruby-eye mice, respectively, and are caused by mutations in BLOC-2 (*98*). Mutations in subunits of BLOC-1, *DTNBP1, BLOC1S3,* and *PLDN* are responsible for HPS types 7-9 (*87*). In addition to these proteins, mouse models have led to the identification of other components of BLOC1: sandy (*Dntbp1)*, reduced-pigmentation (*Bloc1s3*), pallidin *(Pldn*), snapin (*Snapn*), muted (*Muted*), and Cappuccino (*Cno*) (*33–36*). Chediak-Higashi syndrome is a rare disorder that causes hypopigmentation, immunodeficiency, and progressive neurologic dysfunction. A causative mutation for Chediak-Higashi syndrome is found in the *LYST* gene and understanding the cellular phenotype of enlarged, perinuclear lysosome-related organelles was facilitated by the beige mouse (*99*). Another human disease associated with hypopigmentation and immunodeficiency or neurological symptoms is

Griscelli syndrome caused by defects in the trafficking of lysosome-related organelles (*95*, *100*). The mutations in dilute (*Myo5a)*, ashen (*Rab27a*), and leaden (*Mlph*) mice have been used to model the three subtypes of Griscelli syndrome (*95*).

Another category of human diseases that have benefited from *in vivo* models of pigmentation, are those associated with defects in the neural crest. The neural crest gives rise to melanocytes, neurons, gilia, smooth muscle cells, cartilage cells, bone cells, and adrenal cells found throughout the body (*101*). Piebaldism is a pigmentation disorder that results in loss of pigmentation on the ventral area and the head that can manifest with auditory disorders and anemia caused by mutations in *KIT* which are phenocopied by murine *Kit* mutants (*12*). Waardenburg syndrome (WS) is a large class of disorders that result in depigmentation of areas of the skin and hair, loss of pigment or heterochromia in the eyes, and sensorineural hearing loss with additional symptoms dependent on subtype (*102*). Mutations in *PAX3* lead to WS types 1 and 3 in humans and are located in the splotch locus of mice (*102*). WS type 2 can arise from a number of genetic mutations including *MITF*, *SNAI2*, and *SOX10* (*103*). WS type 4 or Waardenburg-Shah syndrome is associated with mutations in *EDN3, EDNRB,* and *SOX10* (*103*). Additionally, some of the same *MITF* mutations are found in patients with Tietz syndrome and some of the corresponding mutations for both Waardenburg and Tietz syndromes are found in murine *Mitf* alleles (*102*). EDN3 is a ligand for EDNRB and corresponds to the lethal spotting and piebald spotting mutant mice, respectively (*104*), and mutations in *EDNRB* can also lead to Hirschsprung's due to symptoms in the intestine (*102*).

MOUSE MODELS AS A TOOL FOR STUDYING PIGMENTATION

With the advance of technology, identifying key regulators of mouse coat pigmentation have incorporated alleles generated from spontaneous mutations to unbiased mutagenesis screens and targeted mutations (*11*, *105*). These tools have been instrumental in understanding the role of key regulators of melanocyte development, melanin synthesis, and melanosome maturation (*12*, *27*). Phosphoinositides (PIs) that contribute to endosomal and lysosomal trafficking were linked to melanosome maturation with the identification of pigment phenotypes associated with *Fig4* and *Vac14* mutants (*106*, *107*). FIG4, a phosphoinositide 5-phosphatase, and VAC14, a scaffold protein, are two components of the PIKFYVE complex that includes PIKFYVE, a phosphoinositide 5-kinase (*108*). While constitutive loss of *Pikfyve* is embryonically lethal (*108*), we utilized a combination of a *Pikfyve* conditional knockout mouse (*109*) with a *Tyr* inducible CRE line (*72*) to generate melanocyte specific *Pikfyve* knockout mice. Using this strain, we were able to identify PIKFYVE as a novel regulator of melanogenesis and describe the role of PIKFYVE in melanosome biogenesis *in vivo* (Chapter 2, (*110*)). In yeast an additional component of the homologous compound corresponds to mammalian WIPI1 (WD phosphoinositide interacting 1), an autophagy related protein that binds to PI containing membranes (*107*, *111*). WIPI1 is a known regulator of pigmentation *in vitro* (*112*, *113*), however its role *in vivo* is still unknown. In Chapter 3, we describe the phenotype associated with constitutive loss of *Wipi1* in black (non-agouti) and white-bellied agouti mice, as well as isolated melanocytes.

Another large component of pigmentation biology is focused on MITF. Mutant *Mitf* alleles have been curated since the initial discovery of the microphthalmia locus in 1942 with approximately 40 annotated murine alleles (*114*, *115*). *In vivo* studies utilizing *Mitf* have advanced the field of melanocyte development and understanding of human diseases (*105*, *116*), but one area

that is still not fully understood are the regulation and function of the unique isoforms of *Mitf* (*117*). Previous studies have also identified a role for retinoids in the stimulation of *MITF* expression (*118*). We identified a functional Retinoic Acid Response Element in the *MITF-A* promoter, generated *Mitf-A* and *Mitf-M* isoform specific knockout mice, and characterized the phenotypes of the skin, eye and kidney (Chapter 4, (*119*)). The identification of sporadic spotting in the *Mitf-M* knockout line has led to new insight into the requirement of the M isoform in melanocyte development (Chapter 5). Altogether, this work presents four novel mouse models to address both the role of phosphoinositide binding proteins in melanosome biogenesis and to better understand the role of *Mitf* isoforms in melanocytes.

REFERENCES

1. T. S. Kupper, R. C. Fuhlbrigge, Immune surveillance in the skin: Mechanisms and clinical consequences. *Nat. Rev. Immunol.* **4**, 211–222 (2004).
2. R. Wong, S. Geyer, W. Weninger, J. C. Guimberteau, J. K. Wong, The dynamic anatomy and patterning of skin. *Exp. Dermatol.* **25**, 92–98 (2016).
3. E. Fuchs, in *Current Topics in Developmental Biology* (2016; https://linkinghub.elsevier.com/retrieve/pii/S0070215315001994), vol. 116, pp. 357–374.
4. M. Cichorek, M. Wachulska, A. Stasiewicz, A. Tymińska, Skin melanocytes: Biology and development. *Postep. Dermatologii i Alergol.* **30**, 30–41 (2013).
5. W. C. Chou, M. Takeo, P. Rabbani, H. Hu, W. Lee, Y. R. Chung, J. Carucci, P. Overbeek, M. Ito, Direct migration of follicular melanocyte stem cells to the epidermis after wounding or UVB irradiation is dependent on Mc1r signaling. *Nat. Med.* **19**, 924–929 (2013).
6. M. Nakamura, M. Fukunaga-Kalabis, Y. Yamaguchi, T. Furuhashi, E. Nishida, H. Kato, T. Mizuno, M. Sugiura, A. Morita, Site-specific migration of human fetal melanocytes in volar skin. *J. Dermatol. Sci.* **78**, 143–148 (2015).
7. J. Hasegawa, Y. Goto, H. Murata, M. Takata, T. Saida, G. Imokawa, Downregulated melanogenic paracrine cytokine linkages in hypopigmented palmoplantar skin. *Pigment Cell Melanoma Res.* (2008), doi:10.1111/j.1755-148X.2008.00492.x.
8. T. Hirobe, H. Enami, Histochemical study of the distribution of epidermal melanoblasts and melanocytes in Asian human skin. *Ski. Res. Technol.* (2019), doi:10.1111/srt.12649.
9. T. Masaki, Y. Wang, J. J. Digiovanna, S. G. Khan, M. Raffeld, S. Beltaifa, T. J. Hornyak, T. N. Darling, C. C. R. Lee, K. H. Kraemer, High frequency of PTEN mutations in nevi and melanomas from xeroderma pigmentosum patients. *Pigment Cell Melanoma Res.* (2014), doi:10.1111/pcmr.12226.
10. K. Wakamatsu, R. Kavanagh, A. L. Kadekaro, S. Terzieva, R. A. Sturm, S. Leachman, Z. Abdel-Malek, S. Ito, Diversity of pigmentation in cultured human melanocytes is due to differences in the type as well as quantity of melanin. *Pigment Cell Res.* (2006), doi:10.1111/j.1600-0749.2006.00293.x.
11. M. L. Lamoreux, V. Delmas, L. Larue, D. C. Bennett, *The Colors of Mice: A Model Genetic Network* (2010).
12. N. Vandamme, G. Berx, From neural crest cells to melanocytes: cellular plasticity during development and beyond. *Cell. Mol. Life Sci.* **76**, 1919–1934 (2019).
13. L. L. Baxter, W. J. Pavan, Pmel17 expression is Mitf-dependent and reveals cranial melanoblast migration during murine development. *Gene Expr. Patterns*. **3**, 703–707 (2003).
14. Y. M. Wilson, K. L. Richards, M. L. Ford-Perriss, J. J. Panthier, M. Murphy, Neural crest cell lineage segregation in the mouse neural tube. *Development*. **131**, 6153–6162 (2004).
15. C. Grimm, M. P. Cuajungco, A. F. J. Van Aken, M. Schnee, S. Jörs, C. J. Kros, A. J. Ricci, S. Heller, A helix-breaking mutation in TRPML3 leads to constitutive activity

underlying deafness in the varitint-waddler mouse. *Proc. Natl. Acad. Sci. U. S. A.* **104**, 19583–19588 (2007).

16. J. Vachtenheim, L. Ondrusov, in *Recent Advances in the Biology, Therapy and Management of Melanoma* (InTech, 2013; http://www.intechopen.com/books/recent-advances-in-the-biology-therapy-and-management-of-melanoma/mitf-a-critical-transcription-factor-in-melanoma-transcriptional-regulatory-network).

17. K. Bharti, M. T. T. Nguyen, S. Skuntz, S. Bertuzzi, H. Arnheiter, The other pigment cell: Specification and development of the pigmented epithelium of the vertebrate eye. *Pigment Cell Res.* **19**, 380–394 (2006).

18. M. H. Goldgeier, L. E. Klein, S. Klein-Angerer, The distribution of melanocytes in the leptomeninges of the human brain. *J. Invest. Dermatol.* **82**, 235–238 (1984).

19. S. Colombo, I. Berlin, V. Delmas, L. Larue, in *Melanins and Melanosomes: Biosynthesis, Biogenesis, Physiological, and Pathological Functions* (Wiley-VCH Verlag GmbH & Co. KGaA, Weinheim, Germany, 2011; http://doi.wiley.com/10.1002/9783527636150.ch2), pp. 21–61.

20. E. M. Wolf Horrell, M. C. Boulanger, J. A. D'Orazio, Melanocortin 1 receptor: Structure, function, and regulation. *Front. Genet.* **7**, 95 (2016).

21. R. Cui, H. R. Widlund, E. Feige, J. Y. Lin, D. L. Wilensky, V. E. Igras, J. D'Orazio, C. Y. Fung, C. F. Schanbacher, S. R. Granter, D. E. Fisher, Central Role of p53 in the Suntan Response and Pathologic Hyperpigmentation. *Cell*. **128**, 853–864 (2007).

22. S. Benjannet, N. Rondeau, R. Day, M. Chrétien, N. G. Seidah, PC1 and PC2 are proprotein convertases capable of cleaving proopiomelanocortin at distinct pairs of basic residues. *Proc. Natl. Acad. Sci. U. S. A.* **88**, 3564–3568 (1991).

23. S. A. N. D'Mello, G. J. Finlay, B. C. Baguley, M. E. Askarian-Amiri, Signaling pathways in melanogenesis. *Int. J. Mol. Sci.* **17** (2016), doi:10.3390/ijms17071144.

24. C. Serre, V. Busuttil, J. M. Botto, Intrinsic and extrinsic regulation of human skin melanogenesis and pigmentation. *Int. J. Cosmet. Sci.* **40**, 328–347 (2018).

25. H. Murakami, H. Arnheiter, Sumoylation modulates transcriptional activity of MITF in a promoter-specific manner. *Pigment Cell Res.* (2005), doi:10.1111/j.1600-0749.2005.00234.x.

26. H. E. Seberg, E. Van Otterloo, R. A. Cornell, Beyond MITF: Multiple transcription factors directly regulate the cellular phenotype in melanocytes and melanoma. *Pigment Cell Melanoma Res.* (2017), doi:10.1111/pcmr.12611.

27. A. Sitaram, M. S. Marks, Mechanisms of protein delivery to melanosomes in pigment cells. *Physiology*. **27**, 85–99 (2012).

28. A. M. De Mazière, K. Muehlethaler, E. Van Donselaar, S. Salvi, J. Davoust, J. C. Cerottini, F. Lévy, J. W. Slot, D. Rimoldi, The melanocytic protein Melan-A/MART-1 has a subcellular localization distinct from typical melanosomal proteins. *Traffic* (2002), doi:10.1034/j.1600-0854.2002.30909.x.

29. C. Bissig, P. Croisé, X. Heiligenstein, I. Hurbain, G. M. Lenk, E. Kaufman, R. Sannerud,

W. Annaert, M. H. Meisler, L. S. Weisman, G. Raposo, G. Van Niel, The PIKfyve complex regulates the early melanosome homeostasis required for physiological amyloid formation. *J. Cell Sci.* **132**, jcs229500 (2019).

30. C. Wasmeier, M. Romao, L. Plowright, D. C. Bennett, G. Raposo, M. C. Seabra, Rab38 and Rab32 control post-Golgi trafficking of melanogenic enzymes. *J. Cell Biol.* **175**, 271–81 (2006).

31. A. Gerondopoulos, L. Langemeyer, J. R. Liang, A. Linford, F. A. Barr, BLOC-3 mutated in Hermansky-Pudlak syndrome is a Rab32/38 guanine nucleotide exchange factor. *Curr. Biol.* **22**, 2135–2139 (2012).

32. S. R. G. Setty, D. Tenza, S. T. Truschel, E. Chou, E. V. Sviderskaya, A. C. Theos, M. L. Lamoreux, S. M. Di Pietro, M. M. Starcevic, D. C. Bennett, E. C. Dell'Angelica, G. Raposo, M. S. Marks, BLOC-1 is required for cargo-specific sorting from vacuolar early endosomes toward lysosome-related organelles. *Mol. Biol. Cell*. **18**, 768–780 (2007).

33. M. Starcevic, E. C. Dell'Angelica, Identification of Snapin and three novel proteins (BLOS1, BLOS2, and BLOS3/reduced pigmentation) as subunits of biogenesis of lysosome-related organelles complex-1 (BLOC-1). *J. Biol. Chem.* **279**, 28393–28401 (2004).

34. J. M. Falcón-Pérez, M. Starcevic, R. Gautam, E. C. Dell'Angelica, BLOC-1, a novel complex containing the pallidin and muted proteins involved in the biogenesis of melanosomes and platelet-dense granules. *J. Biol. Chem.* **277**, 28191–28199 (2002).

35. S. L. Ciciotte, B. Gwynn, K. Moriyama, M. Huizing, W. A. Gahl, J. S. Bonifacino, L. L. Peters, Cappuccino, a mouse model of Hermansky-Pudlak syndrome, encodes a novel protein that is part of the pallidin-muted complex (BLOC-1). *Blood*. **101**, 4402–4407 (2003).

36. W. Li, Q. Zhang, N. Oiso, E. K. Novak, R. Gautam, E. P. O'Brien, C. L. Tinsley, D. J. Blake, R. A. Spritz, N. G. Copeland, N. A. Jenkins, D. Amato, B. A. Roe, M. Starcevic, E. C. Dell'Angelica, R. W. Elliott, V. Mishra, S. F. Kingsmore, R. E. Paylor, R. T. Swank, Hermansky-Pudlak syndrome type 7 (HPS-7) results from mutant dysbindin, a member of the biogenesis of lysosome-related organelles complex 1 (BLOC-1). *Nat. Genet.* **35**, 84–89 (2003).

37. C. Delevoye, I. Hurbain, D. Tenza, J.-B. B. Sibarita, S. Uzan-Gafsou, H. Ohno, W. J. C. Geerts, A. J. Verkleij, J. Salamero, M. S. Marks, G. Raposo, AP-1 and KIF13A coordinate endosomal sorting and positioning during melanosome biogenesis. *J. Cell Biol.* **187**, 247–264 (2009).

38. M. K. Dennis, A. R. Mantegazza, O. L. Snir, D. Tenza, A. Acosta-Ruiz, C. Delevoye, R. Zorger, A. Sitaram, W. de Jesus-Rojas, K. Ravichandran, J. Rux, E. V. Sviderskaya, D. C. Bennett, G. Raposo, M. S. Marks, S. R. G. Setty, BLOC-2 targets recycling endosomal tubules to melanosomes for cargo delivery. *J. Cell Biol.* **209**, 563–577 (2015).

39. S. M. Di Pietro, J. M. Falcón-Pérez, E. C. Dell'Angelica, Characterization of BLOC-2, a complex containing the Hermansky-Pudlak syndrome proteins HPS3, HPS5 and HPS6. *Traffic*. **5**, 276–283 (2004).

40. A. C. Theos, A. Martina, I. Hurbain, A. A. Peden, E. V Sviderskaya, A. Stewart, M. S.

Robinson, D. C. Bennett, D. F. Cutler, J. S. Bonifacino, M. S. Marks, D. Tenza, J. A. Martina, I. Hurbain, A. A. Peden, E. V Sviderskaya, A. Stewart, M. S. Robinson, D. C. Bennett, D. F. Cutler, J. S. Bonifacino, M. S. Marks, G. Raposo, Functions of adaptor protein (AP)-3 and AP-1 in tyrosinase sorting from endosomes to melanosomes. *Mol. Biol. Cell*. **16**, 5356–72 (2005).

41. M. J. Petris, The Menkes copper transporter is required for the activation of tyrosinase. *Hum. Mol. Genet.* **9**, 2845–2851 (2000).

42. S. R. G. Setty, D. Tenza, E. V. Sviderskaya, D. C. Bennett, G. Raposo, M. S. Marks, Cell-specific ATP7A transport sustains copper-dependent tyrosinase activity in melanosomes. *Nature*. **454**, 1142–1146 (2008).

43. A. Ramkumar, D. Murthy, D. A. Raja, A. Singh, A. Krishnan, S. Khanna, A. Vats, L. Thukral, P. Sharma, S. Sivasubbu, R. Rani, V. T. Natarajan, R. S. Gokhale, Classical autophagy proteins LC3B and ATG4B facilitate melanosome movement on cytoskeletal tracks. *Autophagy*. **13**, 1331–1347 (2017).

44. J. D'Orazio, S. Jarrett, A. Amaro-Ortiz, T. Scott, UV Radiation and the Skin. *Int. J. Mol. Sci.* **14**, 12222–48 (2013).

45. R. E. Boissy, in *Experimental Dermatology, Supplement* (Munksgaard International Publishers, 2003; http://doi.wiley.com/10.1034/j.1600-0625.12.s2.1.x), vol. 12, pp. 5–12.

46. W. J. Yun, E.-Y. Kim, J.-E. Park, S. Y. Jo, S. H. Bang, E.-J. Chang, S. E. Chang, Microtubule-associated protein light chain 3 is involved in melanogenesis via regulation of MITF expression in melanocytes. *Sci. Rep.* **6**, 19914 (2016).

47. R. Micillo, L. Panzella, K. Koike, G. Monfrecola, A. Napolitano, M. D'Ischia, "Fifty shades" of black and red or how carboxyl groups fine tune eumelanin and pheomelanin properties. *Int. J. Mol. Sci.* **17** (2016), doi:10.3390/ijms17050746.

48. T. H. Nasti, L. Timares, MC1R, eumelanin and pheomelanin: Their role in determining the susceptibility to skin cancer. *Photochem. Photobiol.* **91**, 188–200 (2015).

49. F. Van Nieuwpoort, N. P. M. Smit, R. Kolb, H. Van Der Meulen, H. Koerten, S. Pavel, Tyrosine-induced melanogenesis shows differences in morphologic and melanogenic preferences of melanosomes from light and dark skin types. *J. Invest. Dermatol.* **122**, 1251–1255 (2004).

50. S. Schmitz, P. D. Thomas, T. M. Allen, M. J. Poznansky, K. Jimbow, DUAL ROLE OF MELANINS AND MELANIN PRECURSORS AS PHOTOPROTECTIVE AND PHOTOTOXIC AGENTS: INHIBITION OF ULTRAVIOLET RADIATION-INDUCED LIPID PEROXIDATION. *Photochem. Photobiol.* (1995), doi:10.1111/j.1751-1097.1995.tb09883.x.

51. E. Wenczl, N. P. M. Smit, S. S. Pavel, A. A. Schothorst, G. P. Van Der Schans, A. J. Timmerman, L. Roza, R. M. Kolb, A. J. Timmerman, N. P. M. Smit, S. S. Pavel, A. A. Schothorst, (Pheo)melanin photosensitizes UVA-induced DNA damage in cultured human melanocytes. *J. Invest. Dermatol.* **111**, 678–682 (1998).

52. M. R. Chedekel, S. K. Smith, P. W. Post, A. Pokora, D. L. Vessell, Photodestruction of pheomelanin: role of oxygen. *Proc. Natl. Acad. Sci. U. S. A.* **75**, 5395–5399 (1978).

53. M. D. Morgan, E. Pairo-Castineira, K. Rawlik, O. Canela-Xandri, J. Rees, D. Sims, A. Tenesa, I. J. Jackson, Genome-wide study of hair colour in UK Biobank explains most of the SNP heritability. *Nat. Commun.* **9** (2018), doi:10.1038/s41467-018-07691-z.

54. C. Bonilla, L.-A. Boxill, S. A. M. Donald, T. Williams, N. Sylvester, E. J. Parra, S. Dios, H. L. Norton, M. D. Shriver, R. A. Kittles, The 8818G allele of the agouti signaling protein (ASIP) gene is ancestral and is associated with darker skin color in African Americans. *Hum. Genet.* **116**, 402–406 (2005).

55. M. Reissmann, A. Ludwig, Pleiotropic effects of coat colour-associated mutations in humans, mice and other mammals. *Semin. Cell Dev. Biol.* (2013), doi:10.1016/j.semcdb.2013.03.014.

56. R. L. Lamason, M.-A. A. P. K. Mohideen, J. R. Mest, A. C. Wong, H. L. Norton, M. C. Aros, M. J. Jurynec, X. Mao, V. R. Humphreville, J. E. Humbert, S. Sinha, J. L. Moore, P. Jagadeeswaran, W. Zhao, G. Ning, I. Makalowska, P. M. McKeigue, D. O'Donnell, R. Kittles, E. J. Parra, N. J. Mangini, D. J. Grunwald, M. D. Shriver, V. A. Canfield, K. C. Cheng, Genetics: SLC24A5, a putative cation exchanger, affects pigmentation in zebrafish and humans. *Science (80-.).* **310**, 1782–1786 (2005).

57. N. G. Crawford, D. E. Kelly, M. E. B. Hansen, M. H. Beltrame, S. Fan, S. L. Bowman, E. Jewett, A. Ranciaro, S. Thompson, Y. Lo, S. P. Pfeifer, J. D. Jensen, M. C. Campbell, W. Beggs, F. Hormozdiari, S. W. Mpoloka, G. G. Mokone, T. Nyambo, D. W. Meskel, G. Belay, J. Haut, H. Rothschild, L. Zon, Y. Zhou, M. A. Kovacs, M. Xu, T. Zhang, K. Bishop, J. Sinclair, C. Rivas, E. Elliot, J. Choi, S. A. Li, B. Hicks, S. Burgess, C. Abnet, D. E. Watkins-Chow, E. Oceana, Y. S. Song, E. Eskin, K. M. Brown, M. S. Marks, S. K. Loftus, W. J. Pavan, M. Yeager, S. Chanock, S. A. Tishkoff, Loci associated with skin pigmentation identified in African populations. *Science (80-.).* (2017), doi:10.1126/science.aan8433.

58. D. C. Whiteman, W. J. Pavan, B. C. Bastian, The melanomas: A synthesis of epidemiological, clinical, histopathological, genetic, and biological aspects, supporting distinct subtypes, causal pathways, and cells of origin. *Pigment Cell Melanoma Res.* (2011), , doi:10.1111/j.1755-148X.2011.00880.x.

59. N. G. Jablonski, G. Chaplin, The evolution of human skin coloration. *J. Hum. Evol.* **39**, 57–106 (2000).

60. A. Piotrowska, J. Wierzbicka, M. A. Zmijewski, Vitamin D in the skin physiology and pathology. *Acta Biochim. Pol.* **63**, 17–29 (2016).

61. G. Chaplin, N. G. Jablonski, Vitamin D and the evolution of human depigmentation. *Am. J. Phys. Anthropol.* **139**, 451–461 (2009).

62. G. S. Barsh, What controls variation in human skin color? *PLoS Biol.* (2003), doi:10.1371/journal.pbio.0000027.

63. G. B. Parker, H. Brotchie, R. K. Graham, Vitamin D and depression. *J. Affect. Disord.* **208**, 56–61 (2017).

64. R. Vieth, S. Kimball, A. Hu, P. G. Walfish, Randomized comparison of the effects of the vitamin D3 adequate intake versus 100 mcg (4000 IU) per day on biochemical responses and the wellbeing of patients. *Nutr. J.* **3**, 8 (2004).

65. A. M. Morgan, J. Lo, D. E. Fisher, How does pheomelanin synthesis contribute to melanomagenesis?: Two distinct mechanisms could explain the carcinogenicity of pheomelanin synthesis. *BioEssays*. **35**, 672–676 (2013).

66. B. Anna, Z. Blazej, G. Jacqueline, C. J. Andrew, R. Jeffrey, S. Andrzej, Mechanism of UV-related carcinogenesis and its contribution to nevi/melanoma. *Expert Rev. Dermatol.* **2**, 451–469 (2007).

67. L. B. Alexandrov, S. Nik-Zainal, D. C. Wedge, S. A. J. R. J. R. Aparicio, S. Behjati, A. V. Biankin, G. R. Bignell, N. Bolli, A. Borg, A.-L. L. Børresen-Dale, S. Boyault, B. Burkhardt, A. P. Butler, C. Caldas, H. R. Davies, C. Desmedt, R. Eils, J. E. Eyfjörd, J. A. Foekens, M. Greaves, F. Hosoda, B. Hutter, T. Ilicic, S. Imbeaud, M. Imielinsk, N. Jäger, D. T. W. W. Jones, D. T. W. W. Jones, S. Knappskog, M. Kool, S. R. Lakhani, C. López-Otín, S. Martin, N. C. Munshi, H. Nakamura, P. A. Northcott, M. Pajic, E. Papaemmanuil, A. Paradiso, J. V. Pearson, X. S. Puente, K. Raine, M. Ramakrishna, A. L. Richardson, J. Richter, P. Rosenstiel, M. Schlesner, T. N. Schumacher, P. N. Span, J. W. Teague, Y. Totoki, A. N. J. J. Tutt, R. Valdés-Mas, M. M. van Buuren, L. van 't Veer, A. Vincent-Salomon, N. Waddell, L. R. Yates, J. Zucman-Rossi, P. Andrew Futreal, U. McDermott, P. Lichter, M. Meyerson, S. M. Grimmond, R. Siebert, E. Campo, T. Shibata, S. M. Pfister, P. J. Campbell, M. R. Stratton, T. Shibata, S. M. Pfister, P. J. Campbell, M. R. Stratton, D. Jonas, S. Knappskog, M. Koo, S. R. Lakhani, C. López-Otín, S. Martin, N. C. Munshi, H. Nakamura, P. A. Northcott, M. Pajic, E. Papaemmanuil, A. Paradiso, J. V. Pearson, X. S. Puente, K. Raine, M. Ramakrishna, A. L. Richardson, J. Richter, P. Rosenstiel, M. Schlesner, T. N. Schumacher, P. N. Span, J. W. Teague, Y. Totoki, A. N. J. J. Tutt, R. Valdés-Mas, M. M. van Buuren, L. Van 'T Veer, A. Vincent-Salomon, N. Waddell, L. R. Yates, J. Zucman-Rossi, P. Andrew Futreal, U. McDermott, P. Lichter, M. Meyerson, S. M. Grimmond, R. Siebert, E. Campo, T. Shibata, S. M. Pfister, P. J. Campbell, M. R. Stratton, Signatures of mutational processes in human cancer. *Nature*. **500**, 415–421 (2013).

68. H. L. Kaufman, J. M. Kirkwood, F. S. Hodi, S. Agarwala, T. Amatruda, S. D. Bines, J. I. Clark, B. Curti, M. S. Ernstoff, T. Gajewski, R. Gonzalez, L. J. Hyde, D. Lawson, M. Lotze, J. Lutzky, K. Margolin, D. F. McDermott, D. Morton, A. Pavlick, J. M. Richards, W. Sharfman, V. K. Sondak, J. Sosman, S. Steel, A. Tarhini, J. A. Thompson, J. Titze, W. Urba, R. White, M. B. Atkins, The society for immunotherapy of cancer consensus statement on tumour immunotherapy for the treatment of cutaneous melanoma. *Nat. Rev. Clin. Oncol.* **10**, 588–598 (2013).

69. A. H. Shain, I. Yeh, I. Kovalyshyn, A. Sriharan, E. Talevich, A. Gagnon, R. Dummer, J. North, L. Pincus, B. Ruben, W. Rickaby, C. D'Arrigo, A. Robson, B. C. Bastian, The genetic evolution of melanoma from precursor lesions. *N. Engl. J. Med.* **373**, 1926–1936 (2015).

70. N. Dhomen, J. S. Reis-Filho, S. da Rocha Dias, R. Hayward, K. Savage, V. Delmas, L. Larue, C. Pritchard, R. Marais, Oncogenic Braf Induces Melanocyte Senescence and Melanoma in Mice. *Cancer Cell*. **15**, 294–303 (2009).

71. D. Dankort, D. P. Curley, R. A. Cartlidge, B. Nelson, A. N. Karnezis, W. E. Damsky, M. J. You, R. A. DePinho, M. McMahon, M. Bosenberg, BrafV600E cooperates with Pten loss to induce metastatic melanoma. *Nat. Genet.* **41**, 544–552 (2009).

72. M. Bosenberg, V. Muthusamy, D. P. Curley, Z. Wang, C. Hobbs, B. Nelson, C. Nogueira, J. W. Horner, R. DePinho, L. Chin, Characterization of melanocyte-specific inducible Cre recombinase transgenic mice. *Genesis*. **44**, 262–7 (2006).

73. L. N. Kwong, J. C. Costello, H. Liu, S. Jiang, T. L. Helms, A. E. Langsdorf, D. Jakubosky, G. Genovese, F. L. Muller, J. H. Jeong, R. P. Bender, G. C. Chu, K. T. Flaherty, J. A. Wargo, J. J. Collins, L. Chin, Oncogenic NRAS signaling differentially regulates survival and proliferation in melanoma. *Nat. Med.* **18**, 1503–1510 (2012).

74. O. A. Ogbechie-Godec, N. Elbuluk, Melasma: an Up-to-Date Comprehensive Review. *Dermatol. Ther. (Heidelb).* (2017), doi:10.1007/s13555-017-0194-1.

75. E. Nicolaidou, A. D. Katsambas, Pigmentation disorders: Hyperpigmentation and hypopigmentation. *Clin. Dermatol.* **32**, 66–72 (2014).

76. F. Boukari, E. Jourdan, E. Fontas, H. Montaudié, E. Castela, J. P. Lacour, T. Passeron, Prevention of melasma relapses with sunscreen combining protection against UV and short wavelengths of visible light: A prospective randomized comparative trial. *J. Am. Acad. Dermatol.* **72**, 189-190.e1 (2015).

77. C. A. Natale, E. K. Duperret, J. Zhang, R. Sadeghi, A. Dahal, K. T. O'Brien, R. Cookson, J. D. Winkler, T. W. Ridky, Sex steroids regulate skin pigmentation through nonclassical membrane-bound receptors. *Elife* (2016), doi:10.7554/eLife.15104.

78. M. Rashighi, J. E. Harris, Vitiligo Pathogenesis and Emerging Treatments. *Dermatol. Clin.* **35**, 257–265 (2017).

79. K. Ezzedine, V. Eleftheriadou, M. Whitton, N. van Geel, Vitiligo. *Lancet (London, England)*. **386**, 74–84 (2015).

80. K. Ezzedine, V. Sheth, M. Rodrigues, V. Eleftheriadou, J. E. Harris, I. H. Hamzavi, A. G. Pandya, Vitiligo is not a cosmetic disease. *J. Am. Acad. Dermatol.* **73**, 883–885 (2015).

81. S. A. Birlea, N. B. Goldstein, D. A. Norris, Repigmentation through Melanocyte Regeneration in Vitiligo. *Dermatol. Clin.* **35**, 205–218 (2017).

82. R. L. Sidman, B. Kosaras, M. Tang, Pigment epithelial and retinal phenotypes in the vitiligo, mivit, mutant mouse. *Investig. Ophthalmol. Vis. Sci.* (1996).

83. J. E. Harris, T. H. Harris, W. Weninger, E. J. Wherry, C. A. Hunter, L. A. Turka, A mouse model of vitiligo with focused epidermal depigmentation requires IFN-γ for autoreactive CD8+ T-cell accumulation in the skin. *J. Invest. Dermatol.* **132**, 1869–1876 (2012).

84. B. Kamaraj, R. Purohit, Mutational analysis of oculocutaneous albinism: A compact review. *Biomed Res. Int.* **2014**, 905472 (2014).

85. N. Puri, J. M. Gardner, M. H. Brilliant, Aberrant pH of melanosomes in pink-eyed dilution (p) mutant melanocytes. *J. Invest. Dermatol.* **115**, 607–613 (2000).

86. P. Manga, S. Pifko-Hirst, B. K. Zhou, S. J. Orlow, R. E. Boissy, Mislocalization of melanosomal proteins in melanocytes from mice with oculocutaneous albinism type 2. *Exp. Eye Res.* **72**, 695–710 (2001).

87. Y. Yamaguchi, V. J. Hearing, Melanocytes and their diseases. *Cold Spring Harb. Perspect. Med.* **4**, a017046- (2014).

88. E. S. Russell, A History of Mouse Genetics. *Annu. Rev. Genet.* **19**, 1–29 (1985).

89. F. Beermann, S. J. Orlow, M. L. Lamoreux, The Tyr (albino) locus of the laboratory mouse. *Mamm. Genome*. **15**, 749–758 (2004).

90. B. S. Kwon, A. K. Haq, M. Wakulchik, D. Kestler, D. E. Barton, U. Francke, M. L. Lamoreux, J. B. Whitney, R. Halaban, Isolation, chromosomal mapping, and expression of the mouse tyrosinase gene. *J. Invest. Dermatol.* **93**, 589–594 (1989).

91. E. K. Paterson, T. J. Fielder, G. R. MacGregor, S. Ito, K. Wakamatsu, D. L. Gillen, V. Eby, R. E. Boissy, A. K. Ganesan, Tyrosinase depletion prevents the maturation of melanosomes in the mouse hair follicle. *PLoS One*. **10** (2015), doi:10.1371/journal.pone.0143702.

92. H. Shoji, Y. Kiniwa, R. Okuyama, M. Yang, K. Higuchi, M. Mori, A nonsense nucleotide substitution in the oculocutaneous albinism II gene underlies the original pink-eyed dilution allele (Oca2p) in mice. *Exp. Anim.* **64**, 171 (2015).

93. P. Manga, K. Sato, L. Ye, F. Beermann, M. Lynn Lamoreux, S. J. Orlow, Mutational analysis of the modulation of tyrosinase by tyrosinase-related proteins 1 and 2 in vitro. *Pigment Cell Res.* **13**, 364–374 (2000).

94. J. M. Newton, O. Cohen-Barak, N. Hagiwara, J. M. Gardner, M. T. Davisson, R. A. King, M. H. Brilliant, Mutations in the human orthologue of the mouse underwhite gene (uw) underlie a new form of oculocutaneous albinism, OCA4. *Am. J. Hum. Genet.* **69**, 981–988 (2001).

95. S. L. Bowman, J. Bi-Karchin, L. Le, M. S. Marks, The road to lysosome-related organelles: Insights from Hermansky-Pudlak syndrome and other rare diseases. *Traffic*. **20**, 404–435 (2019).

96. P. W. Chiang, N. Oiso, R. Gautam, T. Suzuki, R. T. Swank, R. A. Spritz, The Hermansky-Pudlak syndrome 1 (HPS1) and HPS4 proteins are components of two complexes, BLOC-3 and BLOC-4, involved in the biogenesis of lysosome-related organelles. *J. Biol. Chem.* **278**, 20332–20337 (2003).

97. L. Feng, A. B. Seymour, S. Jiang, A. To, A. A. Peden, E. K. Novak, L. Zhen, M. E. Rusiniak, E. M. Eicher, M. S. Robinson, M. B. Gorin, R. T. Swank, The β3A subunit gene (Ap3b1) of the AP-3 adaptor complex is altered in the mouse hypopigmentation mutant pearl, a model for Hermansky-Pudlak syndrome and night blindness. *Hum. Mol. Genet.* **8**, 323–330 (1999).

98. R. Gautam, S. Chintala, W. Li, Q. Zhang, J. Tan, E. K. Novak, S. M. Di Pietro, E. C. Dell'Angelica, R. T. Swank, The Hermansky-Pudlak Syndrome 3 (Cocoa) Protein Is a Component of the Biogenesis of Lysosome-related Organelles Complex-2 (BLOC-2). *J. Biol. Chem.* **279**, 12935–12942 (2004).

99. J. Kaplan, I. De Domenico, D. M. V. Ward, Chediak-Higashi syndrome. *Curr. Opin. Hematol.* **15**, 22–29 (2008).

100. S. K. Fistarol, P. H. Itin, Disorders of pigmentation. *J. Ger. Soc. Dermatology*. **8**, 187–202 (2010).

101. R. Mayor, E. Theveneau, The neural crest. *Dev.* **140**, 2247–2251 (2012).

102. V. Pingault, D. Ente, F. Dastot-Le Moal, M. Goossens, S. Marlin, N. Bondurand, Review and update of mutations causing Waardenburg syndrome. *Hum. Mutat.* **31**, 391–406 (2010).

103. M. D. Saleem, Biology of human melanocyte development, Piebaldism, and Waardenburg syndrome. *Pediatr. Dermatol.* **36**, 72–84 (2019).

104. L. Montoliu, W. S. Oetting, D. C. Bennett, International Federation of Pigmented Cell Societies, Color Genes. *Eur. Soc. Pigment Cell Res.* (2017), (available at http://www.espcr.org/micemut.html).

105. E. Steingrímsson, N. G. Copeland, N. A. Jenkins, Melanocytes and the Microphthalmia Transcription Factor Network. *Annu. Rev. Genet.* **38**, 365–411 (2004).

106. C. Y. Chow, Y. Zhang, J. J. Dowling, N. Jin, M. Adamska, K. Shiga, K. Szigeti, M. E. Shy, J. Li, X. Zhang, J. R. Lupski, L. S. Weisman, M. H. Meisler, Mutation of FIG4 causes neurodegeneration in the pale tremor mouse and patients with CMT4J. *Nature*. **448**, 68–72 (2007).

107. N. Jin, C. Y. Chow, L. Liu, S. N. Zolov, R. Bronson, M. Davisson, J. L. Petersen, Y. Zhang, S. Park, J. E. Duex, D. Goldowitz, M. H. Meisler, L. S. Weisman, VAC14 nucleates a protein complex essential for the acute interconversion of PI3P and PI(3,5)P2 in yeast and mouse. *EMBO J.* **27**, 3221–34 (2008).

108. O. C. Ikonomov, D. Sbrissa, K. Delvecchio, Y. Xie, J. P. Jin, D. Rappolee, A. Shisheva, The phosphoinositide kinase PIKfyve is vital in early embryonic development: Preimplantation lethality of PIKfyve-/- embryos but normality of PIKfyve+/- mice. *J. Biol. Chem.* (2011), doi:10.1074/jbc.M111.222364.

109. S. Takasuga, Y. Horie, J. Sasaki, G.-H. H. Sun-Wada, N. Kawamura, R. Iizuka, K. Mizuno, S. Eguchi, S. Kofuji, H. Kimura, M. Yamazaki, C. Horie, E. Odanaga, Y. Sato, S. Chida, K. Kontani, A. Harada, T. Katada, A. Suzuki, Y. Wada, H. Ohnishi, T. Sasaki, Critical roles of type III phosphatidylinositol phosphate kinase in murine embryonic visceral endoderm and adult intestine. *Proc. Natl. Acad. Sci. U. S. A.* **110**, 1726–31 (2013).

110. M. C. Liggins, J. L. Flesher, S. Jahid, P. Vasudeva, V. Eby, S. Takasuga, J. Sasaki, T. Sasaki, R. E. Boissy, A. K. Ganesan, PIKfyve regulates melanosome biogenesis. *PLoS Genet.* **14** (2018), doi:10.1371/journal.pgen.1007290.

111. T. Proikas-Cezanne, S. Waddell, A. Gaugel, T. Frickey, A. Lupas, A. Nordheim, WIPI-1alpha (WIPI49), a member of the novel 7-bladed WIPI protein family, is aberrantly expressed in human cancer and is linked to starvation-induced autophagy. *Oncogene*. **23**, 9314–9325 (2004).

112. H. Ho, R. Kapadia, S. Al-Tahan, S. Ahmad, A. K. Ganesan, WIPI1 coordinates melanogenic gene transcription and melanosome formation via TORC1 inhibition. *J. Biol. Chem.* **286**, 12509–12523 (2011).

113. A. K. Ganesan, H. Ho, B. Bodemann, S. Petersen, J. Aruri, S. Koshy, Z. Richardson, L. Q. Le, T. Krasieva, M. G. Roth, P. Farmer, M. A. White, Genome-wide siRNA-based functional genomics of pigmentation identifies novel genes and pathways that impact melanogenesis in human cells. *PLoS Genet.* **4** (2008), doi:10.1371/journal.pgen.1000298.

114. P. Hertwig, Neue Mutationen und Kopplungsgruppen bei der Hausmaus. *Z. Indukt. Abstammungs- u. Vererbungsl.* **80**, 220–246 (1942).

115. C. J. Bult, J. A. Blake, C. L. Smith, J. A. Kadin, J. E. Richardson, A. Anagnostopoulos, R. Asabor, R. M. Baldarelli, J. S. Beal, S. M. Bello, O. Blodgett, N. E. Butler, K. R. Christie, L. E. Corbani, J. Creelman, M. E. Dolan, H. J. Drabkin, S. L. Giannatto, P. Hale, D. P. Hill, M. Law, A. Mendoza, M. McAndrews, D. Miers, H. Motenko, L. Ni, H. Onda, M. Perry, J. M. Recla, B. Richards-Smith, D. Sitnikov, M. Tomczuk, G. Tonorio, L. Wilming, Y. Zhu, Mouse Genome Database (MGD) 2019. *Nucleic Acids Res.* (2019), doi:10.1093/nar/gky1056.

116. H. Arnheiter, The discovery of the microphthalmia locus and its gene, Mitf. *Pigment Cell Melanoma Res.* **23**, 729–735 (2010).

117. E. Steingrímsson, All for one, one for all: alternative promoters and Mitf. *Pigment Cell Melanoma Res.* **21**, 412–414 (2008).

118. E. K. Paterson, H. Ho, R. Kapadia, A. K. Ganesan, 9-cis retinoic acid is the ALDH1A1 product that stimulates melanogenesis. *Exp. Dermatol.* **22**, 202–209 (2013).

119. J. L. Flesher, E. K. Paterson-Coleman, P. Vasudeva, R. Ruiz-Vega, M. Marshall, E. Pearlman, G. R. MacGregor, J. Neumann, A. K. Ganesan, Delineating the role of MITF isoforms in pigmentation and tissue homeostasis. *Pigment Cell Melanoma Res.* **33**, 279–292 (2020).

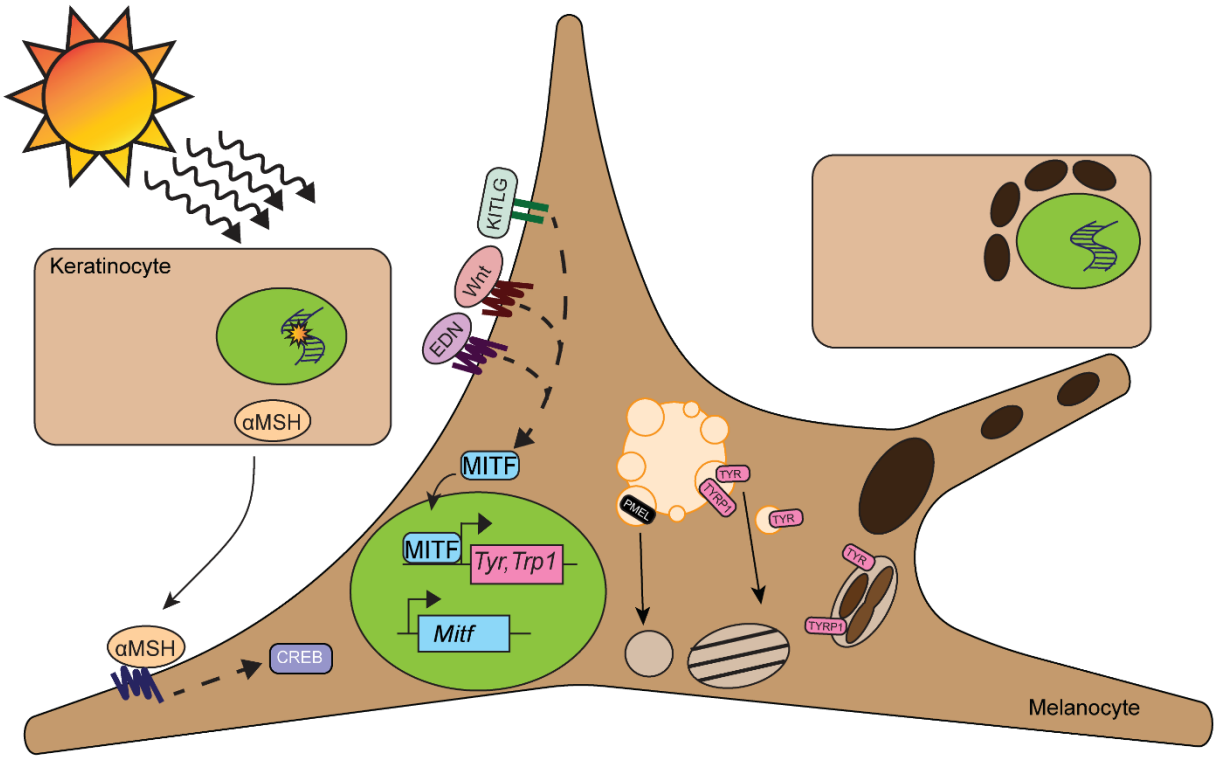
Keratinocyte
αMSH
KITLG
Wnt
EDN
MITF
MITF
Tyr, Trp1
Mitf
αMSH
CREB
PMEL
TYR
TYRP1
TYR
TYR
TYRP1
Melanocyte

Figure 1.1. Overview of Melanogenesis. Melanocytes in the skin are responsive to multiple signals following UV-induced DNA damage of keratinocytes leading to signaling cascades (dashed lines) that lead to upregulation and activation of MITF and subsequent melanocyte-specific gene transcription. Proteins required for melanogenesis are trafficked to maturing melanosomes for melanin synthesis. Melanosomes are pigmented and trafficked to neighboring keratinocytes where they form an apical cap over the nucleus of keratinocytes.

CHAPTER 2

PIKfyve Regulates Melanosome Biogenesis

Jessica L. Flesher, Marc C. Liggins, Sohail Jahid, Priya Vasudeva, Victoria Eby, Shunsuke Takasuga, Junko Sasaki, Takehiko Sasaki, Raymond E. Boissy, and Anand K. Ganesan

Modified from: Liggins MC, Flesher JL, Jahid S, Vasudeva P, Eby V, Takasuga S, et al. (2018) PIKfyve regulates melanosome biogenesis. PLoS Genet 14(3): e1007290. https://doi.org/10.1371/journal.pgen.1007290

ABSTRACT

PIKfyve, VAC14, and FIG4 form a complex that catalyzes the production of $PI(3,5)P_2$, a signaling lipid implicated in process ranging from lysosome maturation to neurodegeneration. While previous studies have identified VAC14 and FIG4 mutations that lead to both neurodegeneration and coat color defects, how PIKfyve regulates melanogenesis is unknown. In this study, we sought to better understand the role of PIKfyve in melanosome biogenesis. Melanocyte-specific PIKfyve knockout mice exhibit greying of the mouse coat and the accumulation of single membrane vesicle structures in melanocytes resembling multivesicular endosomes. PIKfyve inhibition blocks melanosome maturation, the processing of the melanosome protein PMEL, and the trafficking of the melanosome protein TYRP1. Taken together, these studies identify a novel role for PIKfyve in controlling the delivery of proteins from the endosomal compartment to the melanosome, a role that is distinct from the role of PIKfyve in the reformation of lysosomes from endolysosomes.

AUTHOR SUMMARY

In order for a cell to develop and maintain functional organelles, proteins must be delivered to developing organelles in a precise, sequential fashion. In this study, we used a well-established model for organelle biogenesis (the melanosome) to understand how phosphoinositides regulate vesicle trafficking and melanogenesis. Blocking $PI(3,5)P_2$ synthesis inhibits melanosome maturation and induces the accumulation of multivesicular endosomes. Intriguingly, this role is different from the role of $PI(3,5)P_2$ in lysosomal reformation. Taken together, these studies identify distinct roles for $PI(3,5)P_2$ in melanosome biogenesis.

INTRODUCTION

Melanin, a pigment produced within uveal and epidermal melanocytes, absorbs UV radiation, protecting the eyes and skin from UV-induced DNA damage (*120*). Melanin is synthesized in a lysosome-related organelle called the melanosome, which develops through four distinct stages that are readily distinguishable by electron microscopy (*27*, *121*). Several human monoallelic disorders that present with hypopigmentation also have deficits in the biogenesis of lysosomes and lysosome-related organelles (*122*), highlighting the utility of melanosome biogenesis as a model system to define pathways that regulate organelle biogenesis (*121*, *123*).

The complex process of melanosome biogenesis initiates when specialized early endosomes bud off into spherical vacuoles known as stage I melanosomes, marked by the presence of melanoma antigen recognized by T cells 1 (MART-1) and the premelanosome protein (PMEL) (*124–126*). Cleavage and fibrillation of PMEL marks the transition to stage II melanosomes (*125*) where PMEL fibrils serve as scaffold for melanin polymerization and deposition (*127*). Tyrosinase (TYR), and tyrosinase-related proteins 1 and 2 (TYRP1 & TYRP2) are three key enzymes involved in producing melanin (*128*). These proteins are glycosylated within the Golgi and packaged into adaptor protein-3 (AP-3) or -1 (AP-1) clathrin coated transport vesicles, which are transported to and fuse with stage II melanosomes (*40*). The initiation of tyrosinase enzymatic activity allows for the production of melanin (*128*), which is then deposited onto PMEL fibrils in stage III melanosomes (*127*). Mature, stage IV melanosomes are highly pigmented vesicles, which are opaque structures on electron microscopy filled with electron dense melanin (*121*, *123*). Finally, mature melanosomes are transferred to neighboring keratinocytes (*45*, *129*) through a process that is poorly understood.

Numerous studies have determined that proteins are delivered to the developing melanosome through multivesicular endosomes (MVEs). The stage I melanosome protein MART-1 is modified by K63 ubiquitin chains and delivered to a MVE (*130*). This protein is ultimately transported to the stage I melanosome by a mechanism requiring the ESCRT (endosomal sorting complex required for transport) machinery (*130*). In contrast, PMEL is sorted to intraluminal vesicles of MVEs by a process that is independent of ESCRT (*131*), and are then cleaved into PMEL fibrils in the developing melanosome (*127*). TYRP1 is trafficked to the melanosome limiting membrane through a process that requires both ESCRT I (*132*) and AP-1 (*37*). TYR enters the MVE and then is rapidly re-recruited by a complex containing AP-3 into vesicles that ultimately transports this cargo to Stage II melanosomes (*133*). While it is clear that many proteins are trafficked through multivesicular endosomes en route to melanosomes, it is still not known what signals are required for these proteins to exit the MVEs or what signals regulate the fusion of MVE-derived transport vesicles with the melanosome.

Phosphoinositides (PI) have been implicated in controlling the fusion of transport vesicles with its desired target membrane (*134*, *135*). The low abundance lipid PI(3,5)P_2 has undefined roles in organelle biogenesis but has been implicated in physiologic processes including autophagy (*136–138*), lysosome biogenesis (*139–144*), cytokine production (*145*), and vesicular trafficking (*143*, *146*). PI(3,5)P_2 is synthesized by the mammalian PI5-kinase core complex, composed of the kinase PIKfyve, FIG4, and a VAC14 dimer (*147–149*). Intriguingly, FIG4 and VAC14 mutant mice exhibit coat color defects and vesicle trafficking defects in the central nervous system (CNS), and the CNS effects are related to an accumulation of autophagosomes (*150*). PIKfyve inhibition *in vitro* has been recently shown to inhibit the reformation of lysosomes from endolysosomes

(*151*). In summary, these studies implicate functional roles for the PIKfyve protein and the lipid it produces ($PI(3,5)P_2$) in autophagy and lysosomal biogenesis/turnover.

In this study, we sought to better understand how PIKfyve regulates melanosome biogenesis. We determine that loss or inhibition of PIKfyve in melanocytes blocks melanosome maturation, resulting in the accumulation of single membrane vesicle structures that contain intraluminal vesicles. Taken together, these studies define a specific role for phosphoinositides in regulating the delivery of proteins from multivesicular endosomes to melanosomes, phenotypes that are distinct from the role of PIKfyve in lysosome biogenesis and turnover.

MATERIALS AND METHODS

Mouse Strains and Genotyping

All experiments involving mice conform to the NIH guidelines and were approved by the Institutional Animal Care and Use Committee (IACUC) of the University of California, Irvine, approval number 2011–3020. C57BL/6 *PIKfyve*$^{Flox/Flox}$ mice on a pure C57BL/6 background were obtained from Dr. Takehiko Sasaki (Akita University, Akita, Japan). *PIKfyve* genotyping primers and PCR parameters are described in (*109*). *PIKfyve*$^{Flox/Flox}$ were crossed to *Tyrosinase::CreER*^{T2} (JAX stock no: 012328) on a pure C57BL/6 background. The resulting *Tyrosinase::CreER*^{T2,} *PIKfyve*$^{Flox/+}$ progeny were backcrossed to *PIKfyve*$^{Flox/Flox}$ to generate *Tyrosinase::CreER*^{T2,} *PIKfyve*$^{Flox/Flox}$ mice. Upon weaning, mice were placed on tamoxifen feed (Harlan Laboratories, 250 mg/kg) for 29 days. Genomic DNA was isolated from mouse tail biopsies using the Quick Genotyping DNA Preparation Kit (Bioland Scientific, LLC) according to the manufacturer's instructions. *Tyrosinase::CreER*^{T2,} *PIKfyve*$^{Flox/Flox}$ mice were crossed with *ROSA*$^{mTmG/mTmG}$ mice obtained from Jackson laboratories. Genotypes of progeny was determined using specific

genotyping primers using guidelines provided by Jackson laboratories. Resulting *TyrCreER^{T2} PIKfyve$^{Flox/Flox}$ ROSA$^{mTmG/+}$* progeny were similarly placed on tamoxifen feed for 29 days as has been described above. A complete list of genotyping primers are found in Table 2.1.

Primary Melanocyte Isolation and Culture

Primary mouse melanocytes were collected based on methods described by Godwin et al.(*152*). In brief, newborn mice less than 3 days old were sacrificed and sterilized. The skin was removed and cleaned of muscle. To dissociate the epidermis, the skin was incubated for 1 hour in 5mg/ml trypsin (Sigma-Aldrich) at 37°C. The skin was washed and the epidermis was split off. The epidermis was chopped in 0.25% trypsin-EDTA solution (Gibco) and resuspended in growth media. The resuspended cells were filtered using an 100µm cell strainer (Falcon) and plated on 10 cm dishes. Once melanocytes were established, TPA concentration was increased to 400nM to treat fibroblast contamination and increase pigmentation. To increase purity of melanocytes for later experiments, cells isolated from epidermis were incubated on CD117 MicroBeads (Miltenyi Biotec) and sorted on MACS LS columns (Miltenyi Biotec). CD117+ melanocytes were then plated in 24-well dishes.

Harvested primary melanocytes were grown in RPMI-1640 (Thermo Fisher Scientific) supplemented with 10% FBS, antibiotic-antimycotic, 200nM 12-O-tetradecanoylphorbol 13-acetate (TPA) (Abcam), and 200pM cholera toxin (Sigma-Aldrich) or RPMI-1640 supplemented with 5% FBS, 50ng/ml Stem cell Factor (SCF) (Protech International), 20nM Endothelin-3 (EDN3) (Sigma-Aldrich) , 2.5ng/ml Fibroblast growth Factor (FGF) (Sigma-Aldrich), 100nM α-Melanocyte stimulating hormone (α-MSH) (Sigma-Aldrich), 1µM Phosphoethanolamine (Sigma-Aldrich), 10µM Ethanolamine (Sigma-Aldrich), and 1mg/ml Insulin (Sigma-Aldrich).

Electron Microscopy

Cultured melanocytes or whole mouse skin (*n*=2 per genotype) harvested from either anesthetized or euthanized mice using a 4-mm round punch biopsy were fixed in half-strength Karnovsky's fixative (*153*) for 24 hours before being transferred to sodium cacodylate buffer, 0.2M, pH 7.4 (Electron Microscopy Sciences). Tissue was then postfixed with 1% osmium tetroxide containing 1.5% potassium ferrocyanide. After being dehydrated, tissues were embedded in EPON and sections were obtained using a RMC-MT6000XL ultramicrotome and stained with uranyl acetate and lead citrate. Sections were viewed and selected images were digitally photographed using a JEOL JEM-1230 transmission electron microscope. For DOPA histochemistry and prior to postfixation, cells or tissues were incubated in a 0.1%solution of l-DOPA twice for 2.5 hours. The cells and tissues were washed and processed as described above.

Darkly pigmented melanocytes were treated with various dosages of YM-201636 (0 – 1000 nM) for 72 hours. Cells were then fixed for 4 hours in Karnovsky's fixative, pH 7.2, before being washed with sodium cacododylate buffer (0.2 M). Primary melanocytes were fixed for 30 minutes in Karnosky's fixative, pH 7.2, before being washed with sodium cacododylate buffer (0.2M). Samples were then processed for routine DOPA histochemistry electron microscopy. Melanosome stages (I – IV) were quantified visually in the electron micrographs and melanosome stage percentage was assessed versus vehicle treated controls. Electron microscopy on whole mouse skin was obtained and processed as previously described by (*91*).

Immunofluorescence Microscopy

For imaging mouse skin from *TyrCreER^{T2} PIKfyve$^{Flox/Flox}$ ROSA$^{mTmG/+}$*, mice was harvested, skin was frozen in OCT blocks and cryosectioned. 4µm sections were imaged using a Nikon Eclispse Ti fluorescent microscope.

Primary Melanocyte Treatment and Microscopy

Primary melanocytes were plated on 4-chambered coverglass (Thermo Fisher Scientific) and treated with 1µg/ml 4-hydroxytamoxifen (4-HTA) for 48hrs. Cells were fixed in 2% PFA for 1 hour at room temperature and imaged. Phase contrast images were acquired using a Nikon Eclipse Ti fluorescent microscope.

Mouse hair

Dorsal hairs of mice at P50, P100, or P365 were shaved and 1 mg was dissolved overnight in 1 mL of 9:1 Soluene-350 (PerkinElmer) and water. Quadruplicate 150 µL aliquots for each mouse hair sample were then analyzed for absorbance values at 405 nm as previously described (*91*).

RESULTS

Loss of PIKfyve leads to pigment loss *in vivo*

PIKfyve forms a complex with VAC14 and FIG4 (*107*, *147*) which then phosphorylates PI(3)P to PI(3,5)P_2 (*154*) and PIP to PI(5)P (*155*, *156*). VAC14 and FIG4 mutants are characterized by early lethality and accumulation of vacuoles in the CNS with accompanying coat color defects (*106*, *107*, *157*). PIKfyve knockout mice die during embryonic development (*108*),

making it difficult to assess the effects of PIKfyve on melanogenesis. To better elucidate the role of PIKfyve in melanosome biogenesis, we generated melanocyte-specific, inducible PIKfyve knockout mice by crossing an established *PIKfyve*$^{Flox/Flox}$ strain (*109*) with an established melanocyte-specific, inducible Cre strain under a tyrosinase promoter (*72*) on a pure C57B6 background. Induction of Cre recombination with tamoxifen results in the excision of the kinase domain of PIKfyve producing a slightly smaller protein than the full length PIKfyve (Figure 2.1A). Previously published studies suggested that truncated PIKfyve is unstable- infecting *PIKfyve*$^{Flox/Flox}$ mouse embryonic fibroblasts with adenovirus expressing Cre recombinase resulted in the loss PIKfyve protein (*109*). Initial experiments verified that treating *TyrCreER*^{T2} *PIKfyve*$^{Flox/Flox}$ melanocytes with tamoxifen also inhibited the accumulation of PIKfyve protein (Figure 2.1B). Notably, tamoxifen treatment did not result in the complete deletion of PIKfyve as was described previously (*109*), indicating that Cre recombination in this model system is less efficient. In addition, PIKfyve deletion inhibited the accumulation of pigmented melanosomes (Figure 2.1C, 2.1D), while also resulting in the accumulation of full length PMEL protein (Figure 2.1B).

To examine the effect of PIKfyve knockout on melanogenesis, *TyrCreER*^{T2} *PIKfyve*$^{Flox/Flox}$ mice were administered tamoxifen-containing chow for 29 days beginning at P21 (Figure 2.2A) to induce Cre-mediated excision of the kinase domain of PIKfyve. Mice were photographed initially (Figure 2.3A), shaved and depilated on a region of their back at P50, and hairs were allowed to regrow. *TyrCreER*^{T2} *PIKfyve*$^{Flox/Flox}$ mice fed tamoxifen for 29 days accumulated numerous white hairs that initially presented in the shaved and depilated area and were visually apparent at P85 (Figure 2.2B, 2.3B). The same hair phenotype was not observed in Cre negative *PIKfyve*$^{Flox/Flox}$ mice fed tamoxifen for 29 days or *TyrCreER*^{T2} *PIKfyve*$^{Flox/Flox}$ mice that were

administered a normal diet (Figure 2.2B, 2.3B-C). Additional experiments revealed that the weights of *PIKfyve*$^{Flox/Flox}$ mice that were fed tamoxifen were similar regardless of whether they expressed *TyrCreER*^{T2} (Figure 2.3D), indicating that the smaller relative size of the *TyrCreER*^{T2} *PIKfyve*$^{Flox/Flox}$ mice fed tamoxifen chow as compared to mice fed normal chow was a consequence of diet and not PIKfyve loss. Hair from the backs of experimental mice was solubilized and the relative accumulation of melanin was quantified using standard spectrophotometric methods (*91*, *158*). Hairs from the *TyrCreER*^{T2} *PIKfyve*$^{Flox/Flox}$ mice that were fed tamoxifen accumulated 50% less melanin as compared to mice that were not fed tamoxifen or Cre negative controls (Figure 2.2C).

To better assess whether this phenotype was exclusively related to an effect on melanogenesis, we allowed the hairs to regrow after shave depilation and observed whether there was an increased accumulation of white hair after the mice were switched off tamoxifen feed. More white hairs were visually apparent after the mice were fed a normal diet for an additional 20 days (p105, Figure 2.2B, 2.3B-C). This phenotype appeared to be progressive initially as even less melanin accumulated in the hair of *PIKfyve*$^{Flox/Flox}$ mice after they were taken off tamoxifen chow (Figure 2.2B). Over the course of a year, *PIKfyve*$^{Flox/Flox}$ mice continued to accumulate numerous white hairs on the head and upper back, areas that had never been shave depilated (Figure 2.3B-C), indicating that the phenotype was accelerated but not induced by shave depilation. The observed phenotype did not progress completely, as the mice continued to maintain the same relative level of depigmentation over the course of a year (Figure 2.3C). Taken together, these results indicate that PIKfyve loss inhibits melanin accumulation in the mouse hair and this phenotype is not progressive as would be expected if the phenotype were related to stem cell depletion (*159*).

To better understand how PIKfyve loss influences melanin accumulation, we next sought to characterize the PIKfyve knockout mice at the cellular level. Initial studies sought to better understand why *TyrCreER^{T2} PIKfyve$^{Flox/Flox}$* mice fed tamoxifen were not completely white but instead accumulated sporadic white hairs. *TyrCreER^{T2} PIKfyve$^{Flox/Flox}$* littermates fed either a control diet or tamoxifen diet were shave depilated at P50. In both groups, mice had entered the 3rd anagen by P60 with visible hair regrowth (Figure 2.4A). Histology on skin collected at P60 revealed that mice fed tamoxifen had both pigmented and unpigmented hair growing in follicles while mice fed the control diet had fully pigmented hair growth (Figure 2.4B). Since pigmented and unpigmented hairs are present in neighboring follicles, this suggests that loss of PIKfyve does not affect the growth of the hair. Further studies examined the structure of the hairs histologically and verified that the hairs from PIKfyve knockout mice had the same morphology as wild-type mice with the exception that a number of the hairs in the knockout mouse lacked pigment (Figure 2.5A). High magnification images of these hair follicles revealed that some of them exhibited the accumulation of cells with intracellular vesicles with some residual pigment (Figure 2.5B, I=intermediate), while other hairs exhibited the accumulation of cells with intracellular vesicles with little to no pigment (Figure 2.5B, Ab= abnormal). Still other hair follicles appeared normal (Figure 2.5B, N). The observation that not all hair follicles in the mice exhibit a vacuolated phenotype is consistent with *in vitro* results indicating that deletion of PIKfyve was not 100% efficient (Figure 2.1B). To further verify that the observed phenotypes were not a consequence of stem cell loss, *TyrCreER^{T2} PIKfyve$^{Flox/Flox}$* mice were crossed with *ROSA$^{mTmG/mTmG}$* mice, a Cre reporter strain in which Cre expressing cells would express GFP (*160*). Resulting animals (*TyrCreER^{T2} PIKfyve$^{Flox/Flox}$ ROSA$^{mTmG/+}$)* or controls (*TyrCreER^{T2} ROSA$^{mTmG/+}$)* were fed tamoxifen from p21 to p50, animals were sacrificed at p100 and frozen sections were examined

by fluorescence microscopy. Both control and PIKfyve knockout mouse skin had GFP positive cells associated with hair follicles (Figure 2.5C) while the PIKfyve knockouts accumulated white hairs (Figure 2.5D), suggesting that PIKfyve deletion does not significantly affect the survival of melanocytes *in vivo*.

Published studies have demonstrated that PIKfyve is essential for vesicular trafficking as loss or inhibition results in severe trafficking defects and vacuolization (*136*, *143*, *148*, *154*). Other studies have also demonstrated that PIKfyve is essential for lysosomal trafficking (*139*, *161*, *162*) and in lysosomal reformation from endolysosomes (*151*). To further characterize PIKfyve's role in melanosome biogenesis, skin biopsies were taken at p60 and assessed at the ultrastructural level by electron microscopy and DOPA histochemistry electron microscopy (EM). Intriguingly, melanocytes from knockout mice exhibit three morphological phenotypes when compared to controls (Figure 2.6A, subpanel a). Some of the melanocytes were phenotypically normal (N) (Figure 2.6A, subpanel b) while some exhibited profound vacuolization exhibiting vesicles within vacuoles resembling multivesicular endosomes (Figure 2.6A, subpanel d inset) plus very few melanosomes (Ab) (Figure 2.6A, subpanel d). Still others had an intermediate phenotype containing fewer melanosomes (I) (Figures 2.6A, subpanel c). Similarly, after DOPA incubation, morphologically normal cells contain minimal melanin reaction product in the Golgi area (Figure 2.6B, subpanel a), while uncharacteristic deposition was observed in intermediate cells (Figure 2.6B, subpanel b). The abnormal cells had less TYR reaction product (Figure 2.6B, subpanel c). Closer examination of the grossly abnormal melanocytes revealed the accumulation of single membrane vesicles that had multiple vesicles within them and some TYR reaction product, reminiscent of multivesicular endosomes (Figure 2.6B subpanel d). To understand whether the variable phenotypes observed *in vivo* were a consequence of partial/incomplete loss of PIKfyve,

we cultured melanocytes from *TyrCreER^{T2} PIKfyve$^{Flox/Flox}$* mice, treated them with tamoxifen or vehicle, and examined the structure of melanosomes in the cultured cells by electron microscopy. Electron microscopy analysis indicated that some tamoxifen treated *TyrCreER^{T2} PIKfyve$^{Flox/Flox}$* melanocytes accumulated single membrane structures resembling multivesicular endosomes with few stage IV melanosomes (Figure 2.6C, subanel a,b inset). Other treated melanocytes accumulated early and late stage melanosomes with a few single membrane structures (Figure 2.6C, subpanel c,d).

DISCUSSION

Published studies revealed that *VAC14 ingls* and *FIG4* pale tremor mice had lightening of the coat and severe neurologic disease, resulting in early lethality and the accumulation of autophagosomes within the CNS (*150*). These phenotypes made it difficult to determine how exactly these mutations resulted in the coat color defects observed. Similarly, the *PIKfyve* gene-trap mouse also had severe neurologic disease, which ultimately resulted in early lethality (*108*), making it difficult to assess whether PIKfyve regulates melanogenesis. To circumvent these limitations and study the effects on adult melanocytes, we generated a melanocyte lineage specific PIKfyve-knockout mouse model that utilized a tyrosinase driven Cre recombinase (*72*). Melanocytes were cultured from *TyrCreER^{T2} PIKfyve$^{Flox/Flox}$* mice and incubated in the presence and absence of tamoxifen (Figure 2.1). Tamoxifen treated melanocytes accumulated less melanosomes and less PIKfyve protein as compared to untreated cells (Figure 2.1B). While these cells accumulated less PIKfyve, PIKfyve was not completely absent as was observed in experiments where *PIKfyve$^{Flox/Flox}$* MEFs were infected with adenovirus expressing Cre recombinase (*109*).

Melanocyte-specific PIKfyve knockout mice accumulated grey hairs that were initially more obvious in shave depilated areas but that eventually were observed in hairs that were not shave depilated (Figure 2.3). This phenotype did not progress as the mice aged in contrast to other models of stem cell depletion (*159*). *TyrCreER^{T2} PIKfyve$^{Flox/Flox}$* mice were crossed with a Cre reporter strain (*ROSA^{mTmG}*) and treated with tamoxifen to determine whether PIKfyve deletion affected melanocyte viability *in vivo* (Figure 2.5C). Both PIKfyve knockout skin and control skin had GFP expressing melanocytes (Figure 2.5C), indicating that the observed phenotypes were not secondary to complete melanocyte loss. High magnification light microscopy images of mouse hair follicles revealed that not all of the hair follicles from PIKfyve knockout mice contained vacuolated cells (Figure 2.6C). Similarly, EM studies revealed that not all melanocytes from the animal accumulated abnormal endosomal vesicles (Figures 2.6A-B). Taken together, these results indicate that the mouse phenotype observed was not the result of complete deletion of PIKfyve but instead a partial loss of function phenotype. This allowed us to study the effects of PIKfyve depletion on melanosome biogenesis as melanocytes remained in the PIKfyve knockout animal.

As PIKfyve deficient melanocytes were still detectable in the adult animal (Figure 2.5C), we were able to then examine the consequences of PIKfyve depletion on melanosome biogenesis *in vivo*. Epidermal melanocytes from tamoxifen fed *TyrCreER^{T2} PIKfyve$^{Flox/Flox}$* mice accumulated abnormal single membrane vesicles with smaller vesicles within them reminiscent of MVEs that also contained tyrosinase reaction product (Figures 2.6A-B). A similar phenotype was observed when melanocytes from *TyrCreER^{T2} PIKfyve$^{Flox/Flox}$* were cultured and treated with tamoxifen (Figure 2.6C), and MVEs containing DOPA reaction product were also shown to accumulate in PIKfyve inhibitor treated primary melanocytes (*110*). Similarly, some of the MVE-like structures in the animal had DOPA reaction product within them, suggesting that they contain TYR, which

may be trapped within this compartment (Figure 2.6B). Consistent with these observations, immunofluorescence studies in MNT-1 cells demonstrated that PIKfyve inhibition blocked PMEL processing and the trafficking of TYRP1 to the melanosome (*110*). Other studies have shown that $PI(3,5)P_2$ plays an essential role in MVE protein sorting and retrograde trafficking (*146*, *163*, *164*). Specifically, $PI(3,5)P_2$ has been shown to regulate ESCRT-III function and MVE trafficking (*164*, *165*) downstream of ESCRT-I (*166*), which has been shown to be required for TYRP1 transport (*132*). Interestingly, PIKfyve inhibition also affected the trafficking of MART-1 (*110*), whose proper trafficking requires ESCRT-I. Taken together, these results are consistent with a model where PIKfyve regulates the delivery of TYRP1 and TYR from the endosome/MVE to the terminal melanosome (Figure 2.7).

Recently published studies revealed that $PI(3,5)P_2$ depletion inhibits the process of lysosome reformation from endolysosomes (*151*). While we observed that PIKfyve inhibition affected lysosomal enzyme processing (*110*), we observed a distinct phenotype in melanocytes-MVE accumulation. These results indicate that $PI(3,5)P_2$ or PI(5)P that is generated from $PI(3,5)P_2$ modulates the biogenesis of melanosomes in a way that is distinct from its effect on lysosomes. $PI(3,5)P_2$ or PI(5)P could control the biogenesis of melanosomes in several different ways. These lipids could control the budding of vesicle cargo from the MVE en route to the melanosome or the fusion of vesicle cargo with the developing melanosomes. Alternatively, $PI(3,5)P_2$ could be specifically required for ESCRT-I and ESCRT-III based trafficking of melanosome proteins. Finally, $PI(3,5)P_2$ may regulate melanosome biogenesis by influencing conductance regulators required for pigmentation. Two families of cation channels, the TPCs and the TRPMLs, act as $PI(3,5)P_2$ effectors and function in vesicular fusion (*141*, *167*, *168*). In particular, TPC2 was found to be activated by $PI(3,5)P_2$ and regulate pigmentation *in vitro* in an expression dependent context

(*140*, *169*, *170*). Furthermore, single-nucleotide polymorphisms in TPC2 have also been identified in humans that are correlated with skin, eye, and hair pigment variation (*171*). Finally, mice mutant for TRPML3, another putative $PI(3,5)P_2$ regulated channel, exhibit hypopigmentary phenotypes (*172*). Future studies will define the specific phosphoinositide that regulates melanogenesis, determine how and when these phosphoinositides regulate melanosome maturation, and identify phosphoinositide effectors protein present on the melanosome that participate in this process.

ACKNOWLEDGEMENTS

We thank Elyse Paterson, Rolando Ruiz, Chi-fen Chen, and Smanpreet Sandhu for their technical assistance. We thank Thomas Hornyak and Sandeep Joshi for their suggestions and providing protocols to optimally culture primary melanocytes.

REFERENCES

27. A. Sitaram, M. S. Marks, Mechanisms of protein delivery to melanosomes in pigment cells. *Physiology*. **27**, 85–99 (2012).

37. C. Delevoye, I. Hurbain, D. Tenza, J.-B. B. Sibarita, S. Uzan-Gafsou, H. Ohno, W. J. C. Geerts, A. J. Verkleij, J. Salamero, M. S. Marks, G. Raposo, AP-1 and KIF13A coordinate endosomal sorting and positioning during melanosome biogenesis. *J. Cell Biol.* **187**, 247–264 (2009).

40. A. C. Theos, A. Martina, I. Hurbain, A. A. Peden, E. V Sviderskaya, A. Stewart, M. S. Robinson, D. C. Bennett, D. F. Cutler, J. S. Bonifacino, M. S. Marks, D. Tenza, J. A. Martina, I. Hurbain, A. A. Peden, E. V Sviderskaya, A. Stewart, M. S. Robinson, D. C. Bennett, D. F. Cutler, J. S. Bonifacino, M. S. Marks, G. Raposo, Functions of adaptor protein (AP)-3 and AP-1 in tyrosinase sorting from endosomes to melanosomes. *Mol. Biol. Cell*. **16**, 5356–72 (2005).

45. R. E. Boissy, in *Experimental Dermatology, Supplement* (Munksgaard International Publishers, 2003; http://doi.wiley.com/10.1034/j.1600-0625.12.s2.1.x), vol. 12, pp. 5–12.

72. M. Bosenberg, V. Muthusamy, D. P. Curley, Z. Wang, C. Hobbs, B. Nelson, C. Nogueira, J. W. Horner, R. DePinho, L. Chin, Characterization of melanocyte-specific inducible Cre recombinase transgenic mice. *Genesis*. **44**, 262–7 (2006).

91. E. K. Paterson, T. J. Fielder, G. R. MacGregor, S. Ito, K. Wakamatsu, D. L. Gillen, V. Eby, R. E. Boissy, A. K. Ganesan, Tyrosinase depletion prevents the maturation of melanosomes in the mouse hair follicle. *PLoS One*. **10** (2015), doi:10.1371/journal.pone.0143702.

106. C. Y. Chow, Y. Zhang, J. J. Dowling, N. Jin, M. Adamska, K. Shiga, K. Szigeti, M. E. Shy, J. Li, X. Zhang, J. R. Lupski, L. S. Weisman, M. H. Meisler, Mutation of FIG4 causes neurodegeneration in the pale tremor mouse and patients with CMT4J. *Nature*. **448**, 68–72 (2007).

107. N. Jin, C. Y. Chow, L. Liu, S. N. Zolov, R. Bronson, M. Davisson, J. L. Petersen, Y. Zhang, S. Park, J. E. Duex, D. Goldowitz, M. H. Meisler, L. S. Weisman, VAC14 nucleates a protein complex essential for the acute interconversion of PI3P and PI(3,5)P2 in yeast and mouse. *EMBO J.* **27**, 3221–34 (2008).

108. O. C. Ikonomov, D. Sbrissa, K. Delvecchio, Y. Xie, J. P. Jin, D. Rappolee, A. Shisheva, The phosphoinositide kinase PIKfyve is vital in early embryonic development: Preimplantation lethality of PIKfyve-/- embryos but normality of PIKfyve+/- mice. *J. Biol. Chem.* (2011), doi:10.1074/jbc.M111.222364.

109. S. Takasuga, Y. Horie, J. Sasaki, G.-H. H. Sun-Wada, N. Kawamura, R. Iizuka, K. Mizuno, S. Eguchi, S. Kofuji, H. Kimura, M. Yamazaki, C. Horie, E. Odanaga, Y. Sato, S. Chida, K. Kontani, A. Harada, T. Katada, A. Suzuki, Y. Wada, H. Ohnishi, T. Sasaki, Critical roles of type III phosphatidylinositol phosphate kinase in murine embryonic visceral endoderm and adult intestine. *Proc. Natl. Acad. Sci. U. S. A.* **110**, 1726–31 (2013).

110. M. C. Liggins, J. L. Flesher, S. Jahid, P. Vasudeva, V. Eby, S. Takasuga, J. Sasaki, T.

Sasaki, R. E. Boissy, A. K. Ganesan, PIKfyve regulates melanosome biogenesis. *PLoS Genet.* **14** (2018), doi:10.1371/journal.pgen.1007290.

120. G.-E. Costin, V. J. Hearing, Human skin pigmentation: melanocytes modulate skin color in response to stress. *FASEB J.* (2007), doi:10.1096/fj.06-6649rev.

121. G. Raposo, M. S. Marks, Melanosomes - Dark organelles enlighten endosomal membrane transport. *Nat. Rev. Mol. Cell Biol.* (2007), doi:10.1038/nrm2258.

122. A. H. Wei, W. Li, Hermansky-Pudlak syndrome: Pigmentary and non-pigmentary defects and their pathogenesis. *Pigment Cell Melanoma Res.* (2013), doi:10.1111/pcmr.12051.

123. C. Wasmeier, A. N. Hume, G. Bolasco, M. C. Seabra, Melanosomes at a glance. *J. Cell Sci.* **121**, 3995–3999 (2008).

124. F. Giordano, C. Bonetti, E. M. Surace, V. Marigo, G. Raposo, The ocular albinism type 1 (OA1) G-protein-coupled receptor functions with MART-1 at early stages of melanogenesis to control melanosome identity and composition. *Hum. Mol. Genet.* (2009), doi:10.1093/hmg/ddp415.

125. B. Watt, G. van Niel, G. Raposo, M. S. Marks, PMEL: a pigment cell-specific model for functional amyloid formation. *Pigment Cell Melanoma Res.* **26**, 300–15 (2013).

126. Y. Yamaguchi, V. J. Hearing, Physiological factors that regulate skin pigmentation. *BioFactors* (2009), doi:10.1002/biof.29.

127. C. Bissig, L. Rochin, G. van Niel, PMEL amyloid fibril formation: The bright steps of pigmentation. *Int. J. Mol. Sci.* **17**, 1438 (2016).

128. A. Slominski, D. J. Tobin, S. Shibahara, J. Wortsman, Melanin pigmentation in mammalian skin and its hormonal regulation. *Physiol. Rev.* **84**, 1155–1228 (2004).

129. H. Y. Park, M. Kosmadaki, M. Yaar, B. A. Gilchrest, Cellular mechanisms regulating human melanogenesis. *Cell. Mol. Life Sci.* **66**, 1493–506 (2009).

130. Z. Erpapazoglou, M. Dhaoui, M. Pantazopoulou, F. Giordano, M. Mari, S. Léon, G. Raposo, F. Reggiori, R. Haguenauer-Tsapis, A dual role for K63-linked ubiquitin chains in multivesicular body biogenesis and cargo sorting. *Mol. Biol. Cell* (2012), doi:10.1091/mbc.E11-10-0891.

131. G. van Niel, S. Charrin, S. Simoes, M. Romao, L. Rochin, P. Saftig, M. S. Marks, E. Rubinstein, G. Raposo, The Tetraspanin CD63 Regulates ESCRT-Independent and -Dependent Endosomal Sorting during Melanogenesis. *Dev. Cell* (2011), doi:10.1016/j.devcel.2011.08.019.

132. S. T. Truschel, S. Simoes, S. R. G. Setty, D. C. Harper, D. Tenza, P. C. Thomas, K. E. Herman, S. D. Sackett, D. C. Cowan, A. C. Theos, G. Raposo, M. S. Marks, ESCRT-I function is required for Tyrp1 transport from early endosomes to the melanosome limiting membrane. *Traffic* (2009), doi:10.1111/j.1600-0854.2009.00955.x.

133. M. S. Marks, Organelle biogenesis: En BLOC exchange for RAB32 and RAB38. *Curr. Biol.* (2012), doi:10.1016/j.cub.2012.10.005.

134. G. Di Paolo, P. De Camilli, Phosphoinositides in cell regulation and membrane dynamics. *Nature*. **443**, 651–657 (2006).

135. D. Poccia, B. Larijani, Phosphatidylinositol metabolism and membrane fusion. *Biochem. J.* (2009), doi:10.1042/BJ20082105.

136. S. Martin, C. B. Harper, L. M. May, E. J. Coulson, F. A. Meunier, S. L. Osborne, Inhibition of PIKfyve by YM-201636 Dysregulates Autophagy and Leads to Apoptosis-Independent Neuronal Cell Death. *PLoS One* (2013), doi:10.1371/journal.pone.0060152.

137. M. Vicinanza, V. I. Korolchuk, A. Ashkenazi, C. Puri, F. M. Menzies, J. H. Clarke, D. C. Rubinsztein, PI(5)P regulates autophagosome biogenesis. *Mol. Cell*. **57**, 219–234 (2015).

138. C. J. Ferguson, G. M. Lenk, M. H. Meisler, Defective autophagy in neurons and astrocytes from mice deficient in PI(3,5)P2. *Hum. Mol. Genet.* (2009), doi:10.1093/hmg/ddp460.

139. S. H. Min, A. Suzuki, T. J. Stalker, L. Zhao, Y. Wang, C. McKennan, M. J. Riese, J. F. Guzman, S. Zhang, L. Lian, R. Joshi, R. Meng, S. H. Seeholzer, J. K. Choi, G. Koretzky, M. S. Marks, C. S. Abrams, Loss of PIKfyve in platelets causes a lysosomal disease leading to inflammation and thrombosis in mice. *Nat. Commun.* (2014), doi:10.1038/ncomms5691.

140. Y. Lin-Moshier, M. V. Keebler, R. Hooper, M. J. Boulware, X. Liu, D. Churamani, M. E. Abood, T. F. Walseth, E. Brailoiu, S. Patel, J. S. Marchant, The Two-pore channel (TPC) interactome unmasks isoform-specific roles for TPCs in endolysosomal morphology and cell pigmentation. *Proc. Natl. Acad. Sci. U. S. A.* (2014), doi:10.1073/pnas.1407004111.

141. X. P. Dong, D. Shen, X. Wang, T. Dawson, X. Li, Q. Zhang, X. Cheng, Y. Zhang, L. S. Weisman, M. Delling, H. Xu, PI(3,5)P2 controls membrane trafficking by direct activation of mucolipin Ca2+ release channels in the endolysosome. *Nat. Commun.* (2010), doi:10.1038/ncomms1037.

142. X. Li, S. ichiroh Saitoh, T. Shibata, N. Tanimura, R. Fukui, K. Miyake, Mucolipin 1 positively regulates TLR7 responses in dendritic cells by facilitating RNA transportation to lysosomes. *Int. Immunol.* (2015), doi:10.1093/intimm/dxu086.

143. J. de Lartigue, H. Polson, M. Feldman, K. Shokat, S. A. Tooze, S. Urbé, M. J. Clague, PIKfyve regulation of endosome-linked pathways. *Traffic* (2009), doi:10.1111/j.1600-0854.2009.00915.x.

144. A. S. Nicot, H. Fares, B. Payrastre, A. D. Chisholm, M. Labouesse, J. Laporte, The phosphoinositide kinase PIKfyve/Fab1p regulates terminal lysosome maturation in Caenorhabditis elegans. *Mol. Biol. Cell* (2006), doi:10.1091/mbc.e05-12-1120.

145. X. Cai, Y. Xu, A. K. Cheung, R. C. Tomlinson, A. Alcázar-Román, L. Murphy, A. Billich, B. Zhang, Y. Feng, M. Klumpp, J. M. Rondeau, A. N. Fazal, C. J. Wilson, V. Myer, G. Joberty, T. Bouwmeester, M. A. Labow, P. M. Finan, J. A. Porter, H. L. Ploegh, D. Baird, P. De Camilli, J. A. Tallarico, Q. Huang, PIKfyve, a class III PI Kinase, is the target of the small molecular IL-12/IL-23 inhibitor apilimod and a player in toll-like receptor signaling. *Chem. Biol.* (2013), doi:10.1016/j.chembiol.2013.05.010.

146. A. C. Rutherford, C. Traer, T. Wassmer, K. Pattni, M. V. Bujny, J. G. Carlton, H. Stenmark, P. J. Cullen, The mammalian phosphatidylinositol 3-phosphate 5-kinase (PIKfyve) regulates endosome-to-TGN retrograde transport. *J. Cell Sci.* (2006), doi:10.1242/jcs.03153.

147. D. Sbrissa, O. C. Ikonomov, H. Fenner, A. Shisheva, ArPIKfyve Homomeric and Heteromeric Interactions Scaffold PIKfyve and Sac3 in a Complex to Promote PIKfyve Activity and Functionality. *J. Mol. Biol.* (2008), doi:10.1016/j.jmb.2008.10.009.

148. O. C. Ikonomov, D. Sbrissa, H. Fenner, A. Shisheva, PIKfyve-ArPIKfyve-Sac3 core complex: Contact sites and their consequence for Sac3 phosphatase activity and endocytic membrane homeostasis. *J. Biol. Chem.* (2009), doi:10.1074/jbc.M109.037515.

149. D. Sbrissa, O. C. Ikonomov, Z. Fu, T. Ijuin, J. Gruenberg, T. Takenawa, A. Shisheva, Core protein machinery for mammalian phosphatidylinositol 3,5-bisphosphate synthesis and turnover that regulates the progression of endosomal transport: Novel Sac phosphatase joins the ArPIKfyve-PIKfyve complex. *J. Biol. Chem.* (2007), doi:10.1074/jbc.M611678200.

150. C. J. Ferguson, G. M. Lenk, M. H. Meisler, PtdIns(3,5)P2 and autophagy in mouse models of neurodegeneration. *Autophagy*. **6**, 170–1 (2010).

151. C. Bissig, I. Hurbain, G. Raposo, G. van Niel, PIKfyve activity regulates reformation of terminal storage lysosomes from endolysosomes. *Traffic* (2017), doi:10.1111/tra.12525.

152. L. S. Godwin, J. T. Castle, J. S. Kohli, P. S. Goff, C. J. Cairney, W. N. Keith, E. V. Sviderskaya, D. C. Bennett, *Curr. Protoc. Cell Biol.*, in press, doi:10.1002/0471143030.cb0108s63.

153. M. J. Karnovsky, A formaldehyde-glutaraldehyde fixative of high osmolality for use in electron microscopy. *J. Cell Biol.* **27**, 1965 (1965).

154. S. N. Zolov, D. Bridges, Y. Zhang, W.-W. W. Lee, E. Riehle, R. Verma, G. M. Lenk, K. Converso-Baran, T. Weide, R. L. Albin, A. R. Saltiel, M. H. Meisler, M. W. Russell, L. S. Weisman, In vivo, Pikfyve generates PI(3,5)P2, which serves as both a signaling lipid and the major precursor for PI5P. *Proc. Natl. Acad. Sci. U. S. A.* **109**, 17472–7 (2012).

155. A. Shisheva, D. Sbrissa, O. Ikonomov, Plentiful PtdIns5P from scanty PtdIns(3,5)P2 or from ample PtdIns? PIKfyve-dependent models: Evidence and speculation (response to: DOI 10.1002/bies.201300012). *BioEssays*. **37**, 267–77 (2015).

156. A. Shisheva, PtdIns5P: News and views of its appearance, disappearance and deeds. *Arch. Biochem. Biophys.* (2013), doi:10.1016/j.abb.2013.07.023.

157. G. M. Lenk, C. J. Ferguson, C. Y. Chow, N. Jin, J. M. Jones, A. E. Grant, S. N. Zolov, J. J. Winters, R. J. Giger, J. J. Dowling, L. S. Weisman, M. H. Meisler, Pathogenic mechanism of the FIG4 mutation responsible for charcot-marie-tooth disease CMT4J. *PLoS Genet.* (2011), doi:10.1371/journal.pgen.1002104.

158. H. Ozeki, S. Ito, K. Wakamatsu, A. J. Thody, Spectrophotometric characterization of eumelanin and pheomelanin in hair. *Pigment Cell Res.* (1996), doi:10.1111/j.1600-0749.1996.tb00116.x.

159. E. K. Nishimura, S. R. Granter, D. E. Fisher, Mechanisms of hair graying: Incomplete melanocyte stem cell maintenance in the niche. *Science (80-.).* (2005), doi:10.1126/science.1099593.

160. M. D. Muzumdar, B. Tasic, K. Miyamichi, N. Li, L. Luo, L. Li, L. Luo, A global double-fluorescent cre reporter mouse. *Genesis*. **45**, 593–605 (2007).

161. G. H. E. Kim, R. M. Dayam, A. Prashar, M. Terebiznik, R. J. Botelho, PIKfyve inhibition interferes with phagosome and endosome maturation in macrophages. *Traffic* (2014), doi:10.1111/tra.12199.

162. M. C. Kerr, J. T. H. Wang, N. A. Castro, N. A. Hamilton, L. Town, D. L. Brown, F. A. Meunier, N. F. Brown, J. L. Stow, R. D. Teasdale, Inhibition of the PtdIns(5) kinase PIKfyve disrupts intracellular replication of Salmonella. *EMBO J.* (2010), doi:10.1038/emboj.2010.28.

163. G. Odorizzi, M. Babst, S. D. Emr, Fab1p Ptdlns(3)P 5-kinase function essential for protein sorting in the multivesicular body. *Cell* (1998), doi:10.1016/S0092-8674(00)81707-9.

164. N. Jin, M. J. Lang, L. S. Weisman, Phosphatidylinositol 3,5-bisphosphate: Regulation of cellular events in space and time. *Biochem. Soc. Trans.* (2016), doi:10.1042/BST20150174.

165. P. Whitley, B. J. Reaves, M. Hashimoto, A. M. Riley, B. V. L. Potter, G. D. Holman, Identification of mammalian Vps24p as an effector of phosphatidylinositol 3,5-bisphosphate-dependent endosome compartmentalization. *J. Biol. Chem.* (2003), doi:10.1074/jbc.M306864200.

166. A. Shisheva, PIKfyve: Partners, significance, debates and paradoxes. *Cell Biol. Int.* (2008), doi:10.1016/j.cellbi.2008.01.006.

167. N. W. Bellono, E. V. Oancea, Ion transport in pigmentation. *Arch. Biochem. Biophys.* (2014), doi:10.1016/j.abb.2014.06.020.

168. X. Feng, Y. Huang, Y. Lu, J. Xiong, C. -On Wong, P. Yang, J. Xia, D. Chen, G. Du, K. Venkatachalam, X. Xia, M. X. Zhu, Drosophila TRPML forms PI(3,5)P2-activated cation channels in both endolysosomes and plasma Membrane. *J. Biol. Chem.* (2014), doi:10.1074/jbc.M113.506501.

169. N. W. Bellono, I. E. Escobar, E. V. Oancea, N. W. Bellono, E. V. Oancea, R. H. Michell, V. L. Heath, M. A. Lemmon, S. K. Dove, C. Y. Chow, X. P. Dong, X. Wang, X. P. Dong, D. Shen, M. Samie, C. Cang, X. Cheng, C. Cang, B. Bekele, D. Ren, P. Sulem, Y. Lin-Moshier, P. J. Calcraft, S. J. Pitt, A. Kosiniak-Kamysz, J. M. Kocarnik, I. Palmisano, K. Cortese, N. W. Bellono, I. E. Escobar, A. J. Lefkovith, M. S. F. I. G. 4. Marks, E. V. Oancea, M. Ruas, A. Sitaram, F. A. Ran, J. Ancans, A. J. Thody, R. Halaban, J. Ancans, E. V. Sviderskaya, M. S. F. I. G. 4. Marks, B. E. Steinberg, E. V. Sviderskaya, S. R. G. Setty, N. W. Bellono, L. G. Kammel, A. L. Zimmerman, E. V. Oancea, A melanosomal two-pore sodium channel regulates pigmentation. *Sci. Rep.* **6**, 26570 (2016).

170. A. L. Ambrosio, J. A. Boyle, A. E. Aradi, K. A. Christian, S. M. Di Pietro, TPC2 controls pigmentation by regulating melanosome pH and size. *Proc. Natl. Acad. Sci. U. S. A.* **113**, 5622–5627 (2016).

171. P. Sulem, D. F. Gudbjartsson, S. N. Stacey, A. Helgason, T. Rafnar, M. Jakobsdottir, S. Steinberg, S. A. Gudjonsson, A. Palsson, G. Thorleifsson, S. Pálsson, B. Sigurgeirsson, K. Thorisdottir, R. Ragnarsson, K. R. Benediktsdottir, K. K. Aben, S. H. Vermeulen, A. M. Goldstein, M. A. Tucker, L. A. Kiemeney, J. H. Olafsson, J. Gulcher, A. Kong, U. Thorsteinsdottir, K. Stefansson, Two newly identified genetic determinants of pigmentation in Europeans. *Nat. Genet.* (2008), doi:10.1038/ng.160.

172. H. Xu, M. Delling, L. Li, X. Dong, D. E. Clapham, Activating mutation in a mucolipin transient receptor potential channel leads to melanocyte loss in varitint-waddler mice. *Proc. Natl. Acad. Sci. U. S. A.* (2007), doi:10.1073/pnas.0709096104.

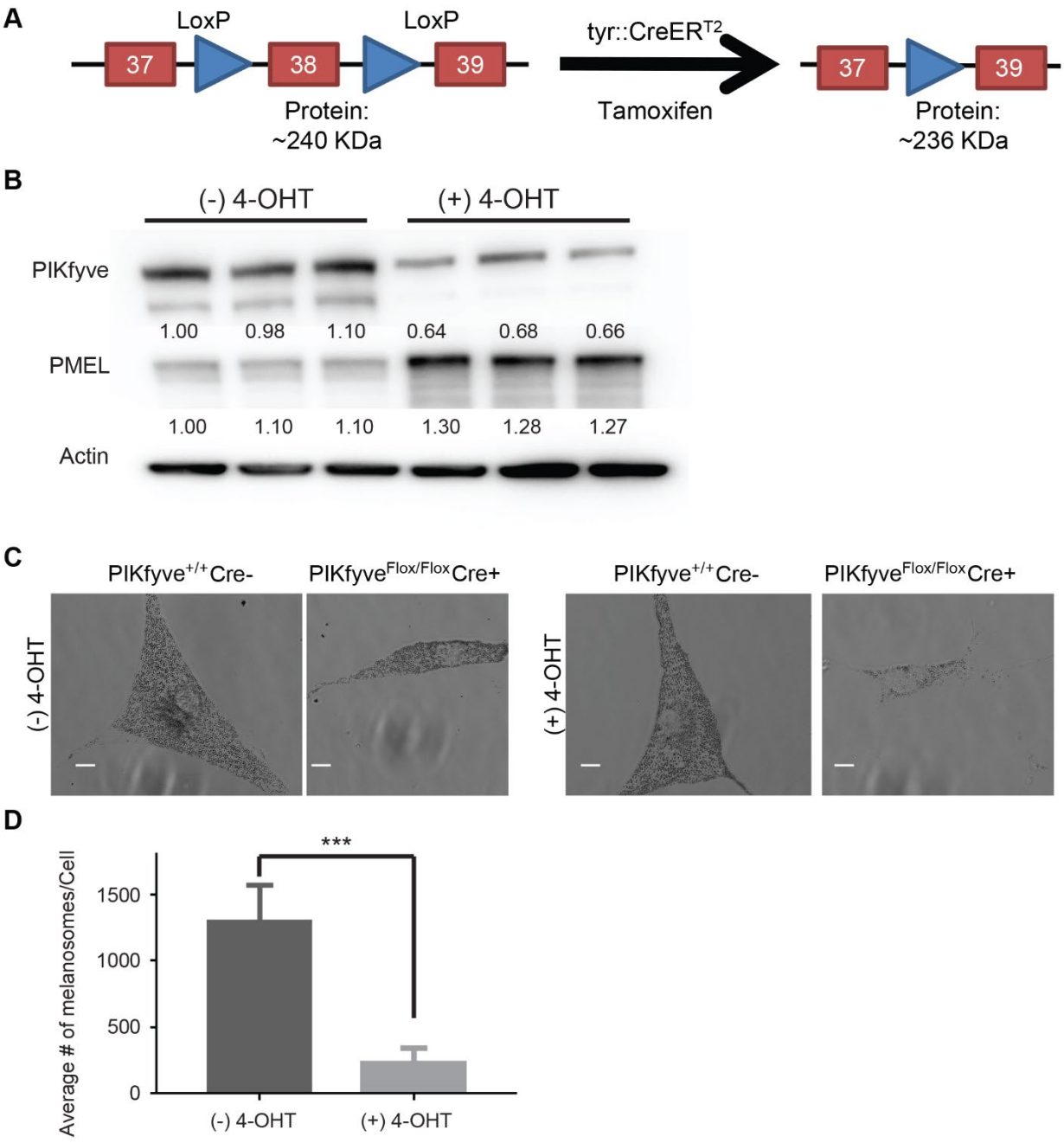
A
LoxP
LoxP
37
38
39
Protein:
~240 KDa
tyr::CreER^{T2}
Tamoxifen
37
39
Protein:
~236 KDa
B
(-) 4-OHT
(+) 4-OHT
PIKfyve
1.00
0.98
1.10
0.64
0.68
0.66
PMEL
1.00
1.10
1.10
1.30
1.28
1.27
Actin
C
PIKfyve$^{+/+}$Cre-
PIKfyve$^{Flox/Flox}$Cre+
PIKfyve$^{+/+}$Cre-
PIKfyve$^{Flox/Flox}$Cre+
(-) 4-OHT
(+) 4-OHT
D
***
Average # of melanosomes/Cell
1500
1000
500
0
(-) 4-OHT
(+) 4-OHT

Figure 2.1. Loss of PIKfyve alters melanosome number. A) Schematic of *Tyrosinase::Cre*^{ERT2} *PIKfyve*$^{Flox/Flox}$ knockout mice. In this model, the *PIKfyve* exon 38 (kinase domain) is flanked by intronic LoxP sites. Cells were treated with 4-hydroxytamoxifen (4-OHT) and mice were administered feed containing tamoxifen (TAM) to remove exon 38 resulting in the inactivation of the PIKfyve kinase. B) Six different batches of primary melanocytes isolated from neonatal *Tyrosinase::Cre*^{ERT2}; *PIKfyve*$^{Flox/Flox}$ were treated with 4-OHT or vehicle control for 48hrs. Protein lysates were collected immunoblotted with the indicated Abs to measure PIKfyve and Pmel levels. C) Cells from *Tyrosinase::Cre*^{ERT2}; *PIKfyve*$^{Flox/Flox}$ or wild type mice treated with 4-OHT or vehicle were then fixed and imaged using phase contrast microscopy, scale bar = 10μm. D) The number of melanosomes per cell in *Tyrosinase::Cre*^{ERT2}; *PIKfyve*$^{Flox/Flox}$ melanocytes treated with 4-OHT or vehicle was counted and quantified using ImageJ. ***, $p < 0.001$ using a two-tailed Student's paired T test.

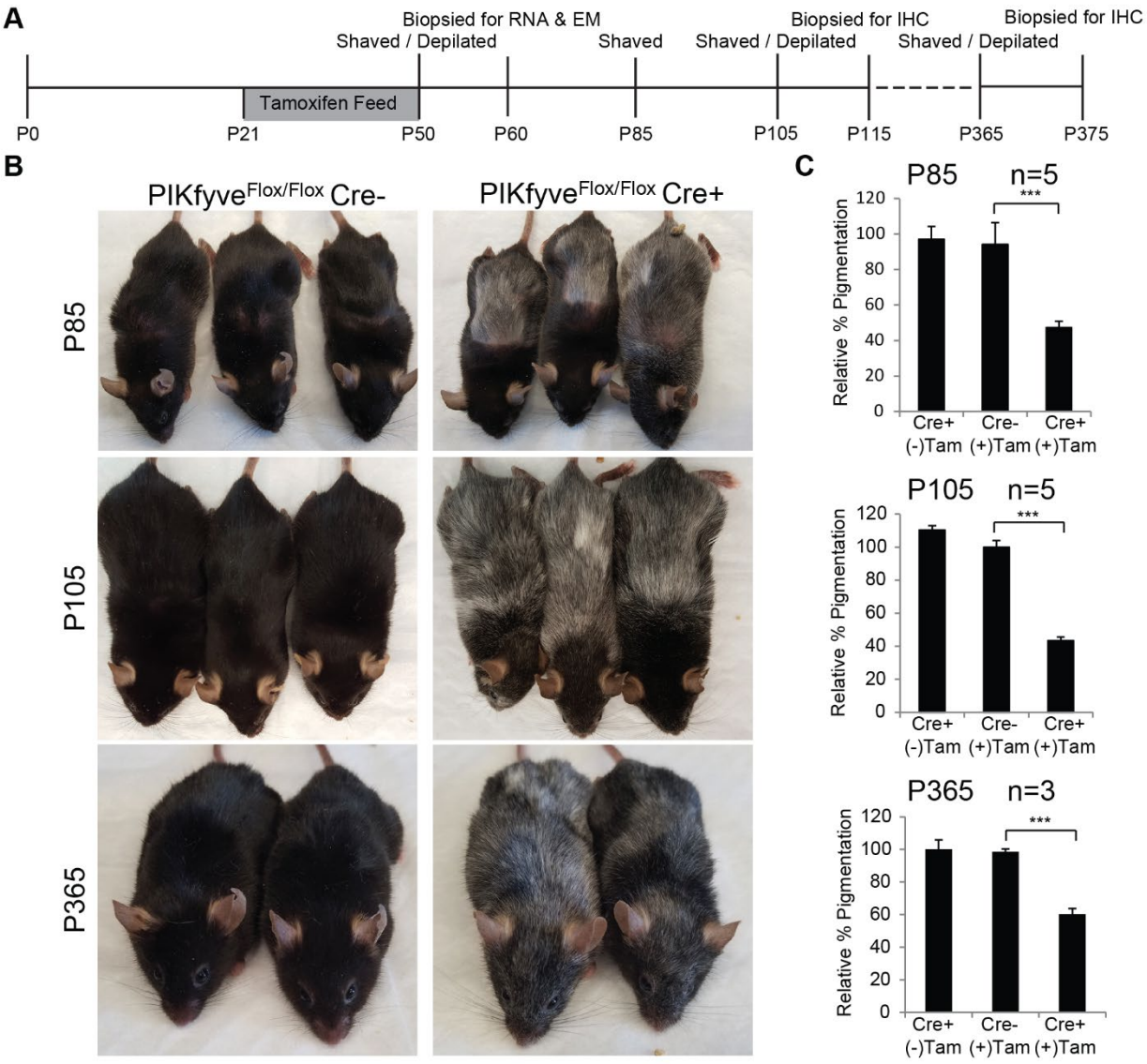
A
Biopsied for RNA & EM
Shaved / Depilated
Shaved
Biopsied for IHC
Shaved / Depilated
Biopsied for IHC
Shaved / Depilated
Tamoxifen Feed
P0
P21
P50
P60
P85
P105
P115
P365
P375
B
PIKfyve Flox/Flox Cre-
PIKfyve Flox/Flox Cre+
P85
P105
P365
C
P85 n=5
P105 n=5
P365 n=3
***
Relative % Pigmentation
0
20
40
60
80
100
120
Cre+ (-)Tam
Cre- (+)Tam
Cre+ (+)Tam

Figure 2.2. Melanocyte specific PIKfyve knockout mice exhibit hair greying. A) Timeline of *in vivo* experiments. Five *Tyrosinase::Cre*^{ERT2}; *PIKfyve*$^{Flox/Flox}$ and 5 *PIKfyve*$^{Flox/Flox}$ mice were administered tamoxifen chow for 29 days. A control group of 5 *Tyrosinase::Cre*^{ERT2}; *PIKfyve*$^{Flox/Flox}$ mice were fed a control diet throughout the course of the experiment. All mice were shave depilated at p50 and subsequently fed normal chow beginning at p50 for the subsequent days. Gray bar denotes the duration that mice, with the exception of the control group, were on tamoxifen feed. B) Littermates were photographed at P85, P105, and P365. C) Mouse hair from the genotypes indicated was dissolved in solune-350 and melanin quantitation was performed as described. The relative amount of melanin in the hair was calculated relative to *Cre*- controls at P85, P105, and P365. Data shown are mean ± S.D. (n = 5 or 3 as indicated by error bars. ***, $p < 0.001$ using a two-tailed Student's paired T test.

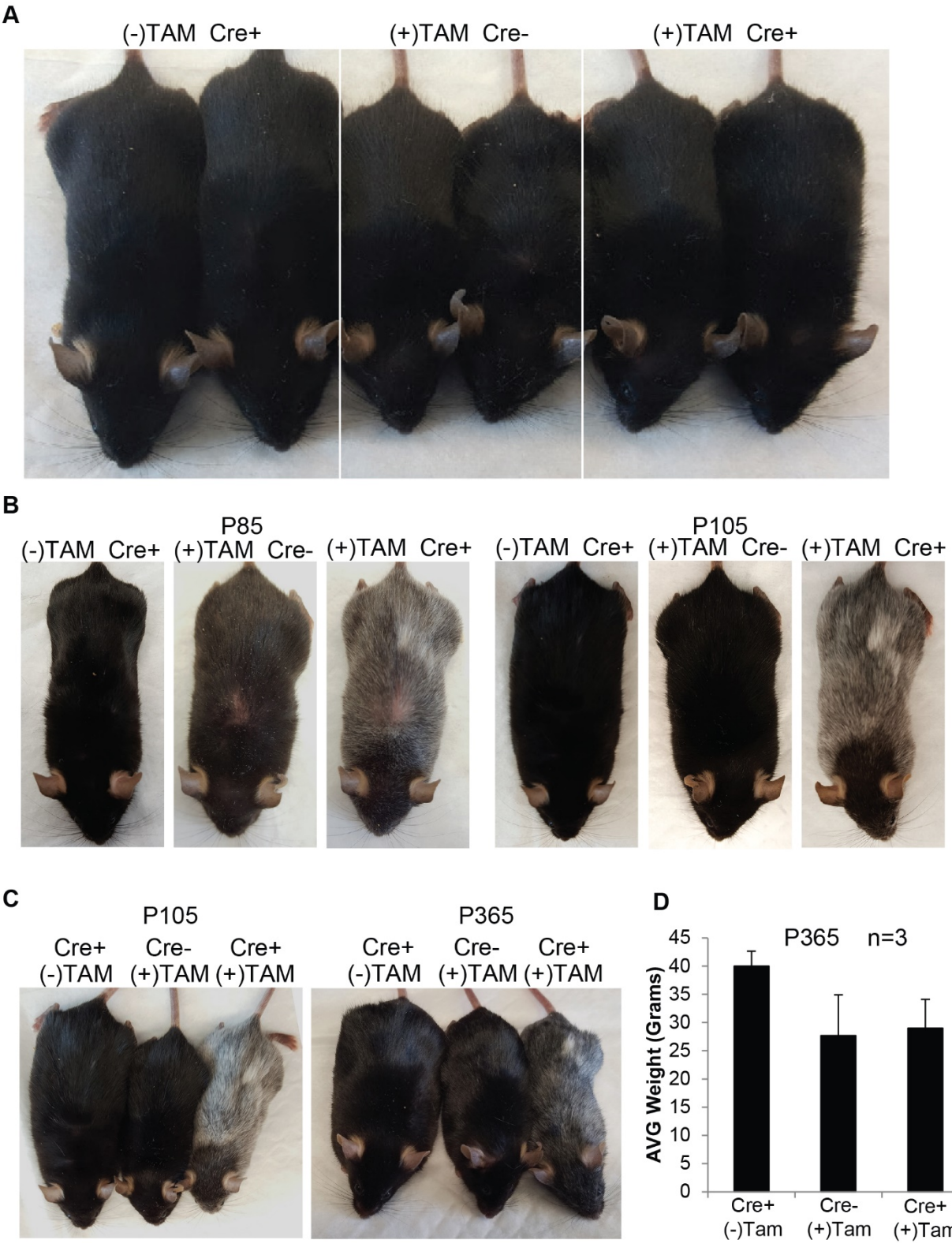
A
(-)TAM Cre+
(+)TAM Cre-
(+)TAM Cre+
B
P85
(-)TAM Cre+
(+)TAM Cre-
(+)TAM Cre+
P105
(-)TAM Cre+
(+)TAM Cre-
(+)TAM Cre+
C
P105
Cre+ (-)TAM
Cre- (+)TAM
Cre+ (+)TAM
P365
Cre+ (-)TAM
Cre- (+)TAM
Cre+ (+)TAM
D
P365 n=3
AVG Weight (Grams)
45
40
35
30
25
20
15
10
5
0
Cre+ (-)Tam
Cre- (+)Tam
Cre+ (+)Tam

Figure 2.3. Melanocyte specific PIKfyve knockout mice exhibit hair greying, continued. (A) Representative photographs of female littermates of p35 *Tyrosinase::Cre*^{ERT2}; *PIKFYVE*$^{Flox/Flox}$ littermates. Cre- and Cre+ mice were administered tamoxifen (or normal) feed from day 21 to 35. (B) Representative photographs of individual littermates from each group taken at P85 or P105. (C) Side-by-side comparison of representative female littermates photographed at P105 or P365. (D) Mice were administered normal or tamoxifen containing feed for 29 days (P21-P50) after which all mice were administered normal feed. Mice were weighed at P365 and average weight of mice was calculated. For all experiments, all data are mean ± S.D. (n = 3 as indicated by error bars

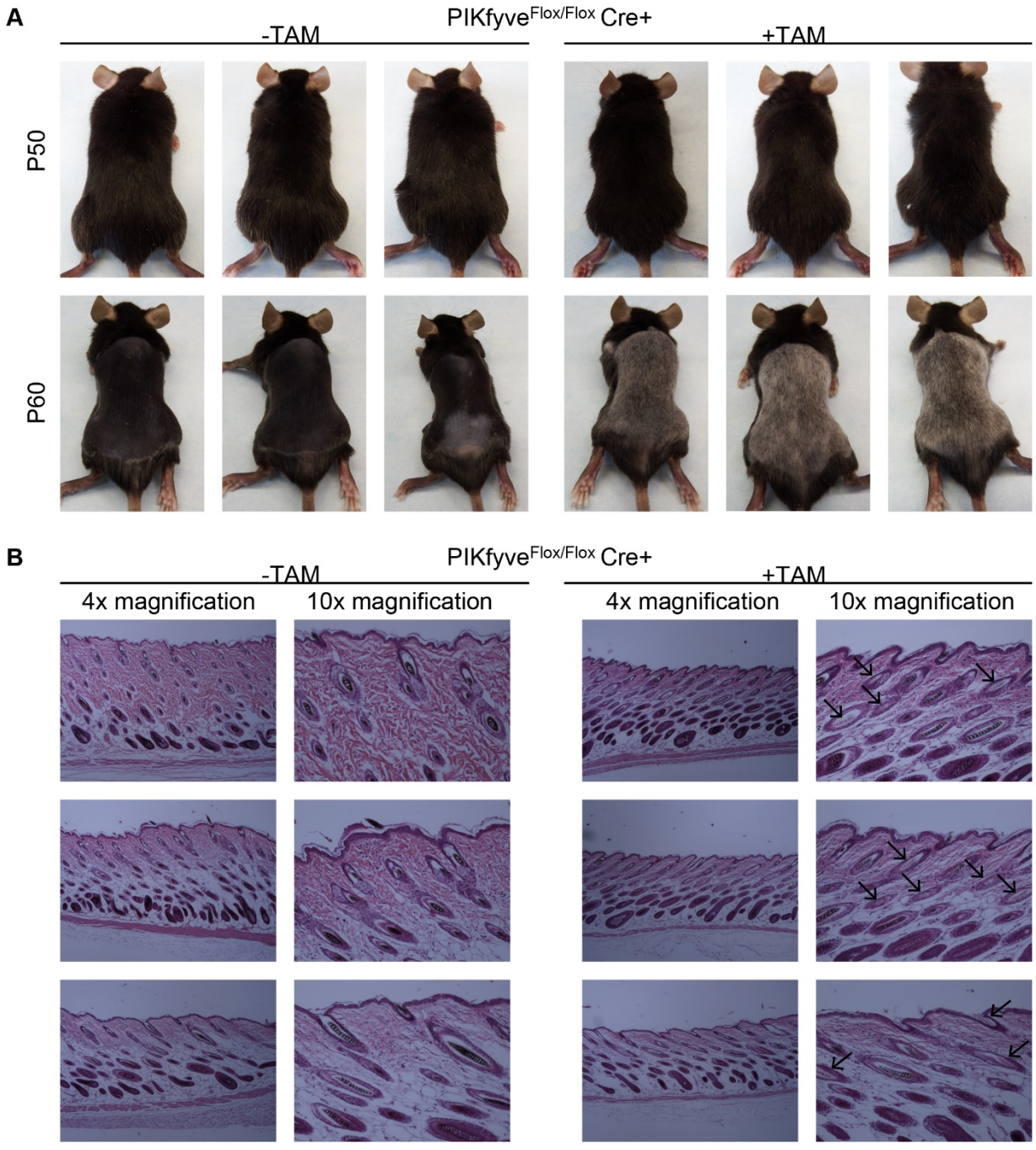
A
PIKfyve Flox/Flox Cre+
-TAM
+TAM
P50
P60
B
PIKfyve Flox/Flox Cre+
-TAM
+TAM
4x magnification
10x magnification
4x magnification
10x magnification

Figure 2.4. PIKfyve inhibition does not alter hair cycle of mice. (A) *Tyrosinase::Cre*^{ERT2}; *PIKFYVE*$^{Flox/Flox}$ littermates were administered normal or tamoxifen (TAM) containing feed for 21 days (P28-P50). At P50, mice were photographed, and then shaved and depilated at to stimulate the 3rd hair cycle. By P60 mice were again photographed showing the regrowth of white hairs. (B) H&E staining of skin collected from mice at P60 imaged at 4x and 10x magnification. All visible hairs from mice fed a normal diet are pigmented. In contrast, mice fed TAM have both pigmented and unpigmented hairs in the skin. Black arrows denote unpigmented hairs.

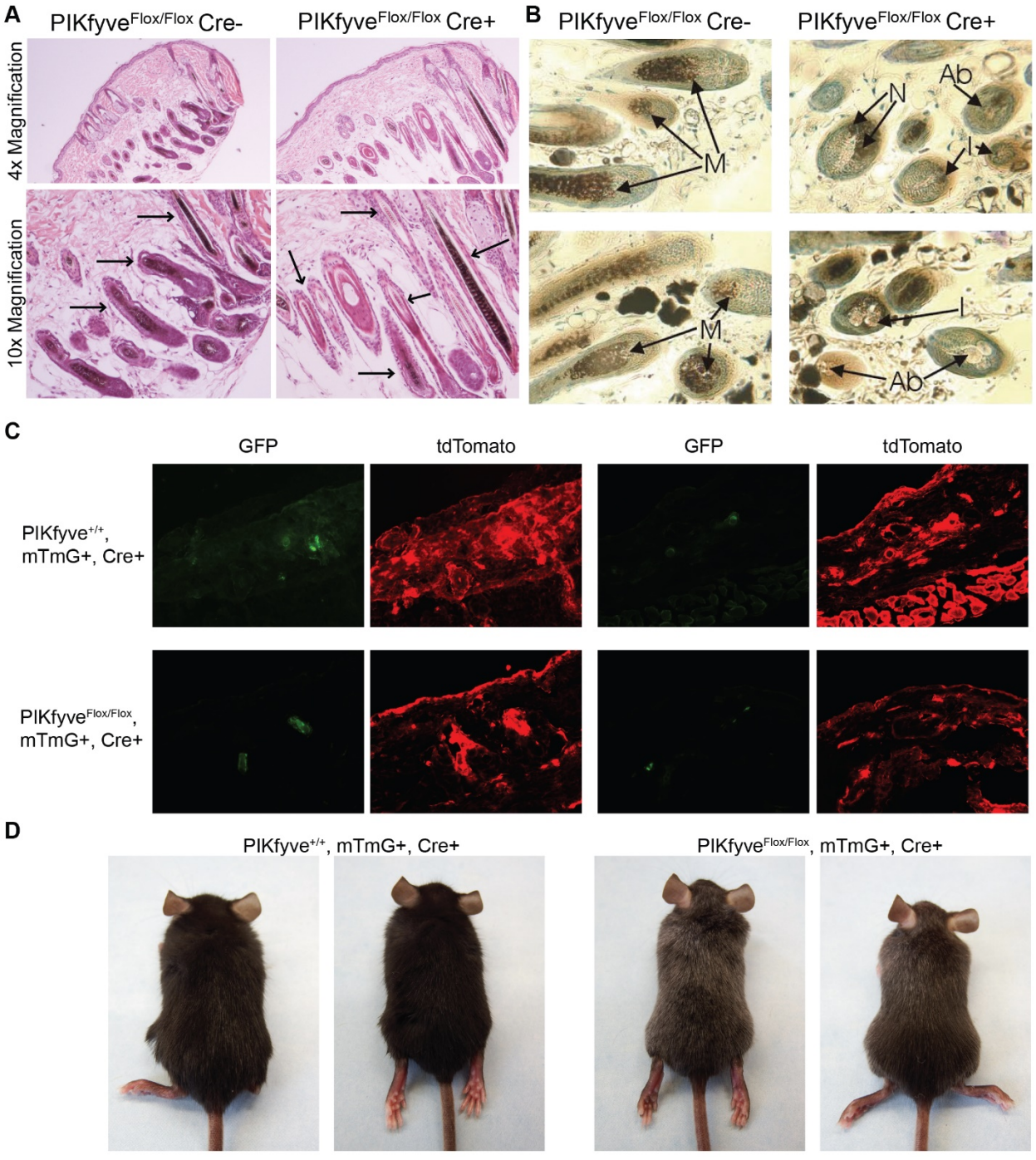
A
PIKfyve Flox/Flox Cre-
PIKfyve Flox/Flox Cre+
4x Magnification
10x Magnification
B
PIKfyve Flox/Flox Cre-
PIKfyve Flox/Flox Cre+
M
N
Ab
I
C
GFP
tdTomato
GFP
tdTomato
PIKfyve+/+, mTmG+, Cre+
PIKfyve Flox/Flox, mTmG+, Cre+
D
PIKfyve+/+, mTmG+, Cre+
PIKfyve Flox/Flox, mTmG+, Cre+

Figure 2.5. Melanocyte specific PIKfyve knockout mice exhibit vacuolar accumulation in select mouse hairs. A) Haematoxylin and eosin stained sections from mice of the indicated genotypes at p60 was examined by light microscopy at 4x and 10x magnification. B) Toluene Blue stained semi-thin sections from mice of the indicated genotypes examined by light microscopy at 100x magnification. Anagen hair follicles from control PIKfyve$^{Flox/Flox}$Cre- mice (left panel) demonstrating normal melanocytes (M) at the epidermal/dermal papilla interface and from PIKfyve$^{Flox/Flox}$Cre+ mice (right panel) demonstrating melanocytes that appear morphologically normal (N), abnormal without containing melanin (Ab) and intermediate with minimal amount of melanin (I). C) Skin from *TyrCreER^{T2} PIKfyve$^{Flox/Flox}$ ROSA$^{mTmG/+}$* at P100 was embedded in OCT and examined by fluorescent microscopy at 4x magnification. D) Representative images of TyrCreERT^{2} *PIKfyve$^{Flox/Flox}$ ROSA$^{mTmG/+}$* mice and *TyrCreER^{T2} PIKfyve^{++} ROSA$^{mTmG/+}$* mice at P50. Note the early greying phenotype shown here is similar to what is observed in *TyrCreER^{T2} PIKfyve$^{Flox/Flox}$* mice at p50.

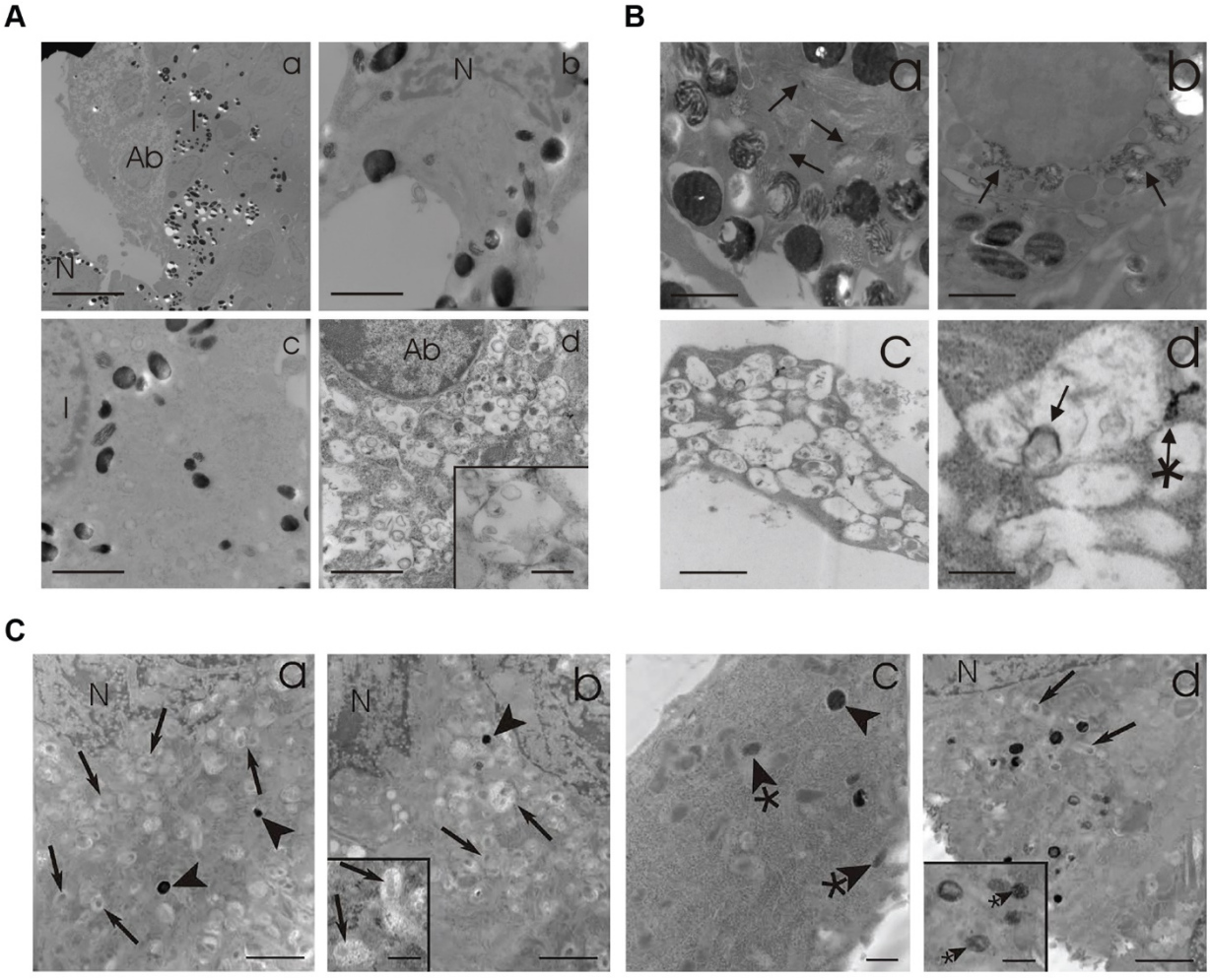
A
a
Ab
I
N
b
N
c
I
Ab
d
B
a
b
c
d
C
N
a
N
b
c
N
d

Figure 2.6. Melanocyte specific PIKfyve knockout mice exhibit abnormal melanocyte morphology and trafficking. A) 4mm biopsies were obtained from PIKfyve knockout mice and processed for electron microscopy. (a) Anagen hair bulbs contained melanocytes in various conditions, i.e. normal (N), abnormal (Ab), and intermediate (I). (b) Approximately 40% appeared morphologically normal resembling follicular melanocytes in C57Bl mice (N). (d) Another 40% exhibited profound vacuolization exhibiting vesicles within vacuoles resembling multivesicular bodies (inset to d) with very few if any melanosomes. (c) Occasionally, approximately 20% melanocytes relatively fewer melanosomes generally of earlier stages than the morphologically normal melanocytes. BARS: a = 10 microns, b, c & d = 3.0 microns, inset to d = 0.75 microns. **B)** 4mm biopsies were obtained from PIKfyve knockout mice and processed for DOPA histochemistry and electron microscopy. (a) morphologically normal melanocytes exhibited minimal DOPA reaction product in the trans Golgi network and associated 50 nm vesicles (arrows). (b) Intermediate melanocyte exhibited uncharacteristic DOPA reaction product that was clustered in large vacuoles some of which contained filamentous material (arrows). (c) The vacuoles of abnormal melanocytes exhibited very little DOPA reaction product with an occasional deposition around vesicles within the vacuoles (arrow) and attached to the limiting membrane of the vacuole (arrow with asterisk). BARS: a, b & c = 1.0 microns, d = 0.3 microns. **C)** Ultrastructure of melanocytes cultured from PIKfyve knockout mice recapitulate the aberrant morphology observed in hair bulb melanocytes from PIKfyve knockout mice. a & b) A prominent number of cultured melanocytes exhibited vacuoles with a central core of amorphorus material (arrows) with occasional stage IV melansomes (arrowheads). c & d) A significant number of melanocytes exhibited many stage IV melanosomes (arrowheads) and earlier stage melanosomes with normally arraigned melanofilaments (arrowheads with asterisks) as well as few vacuoles with

a central core of amorphorus material (arrows). N = nucleus. Bars: a-d = 5 microns, insets = 2 microns.

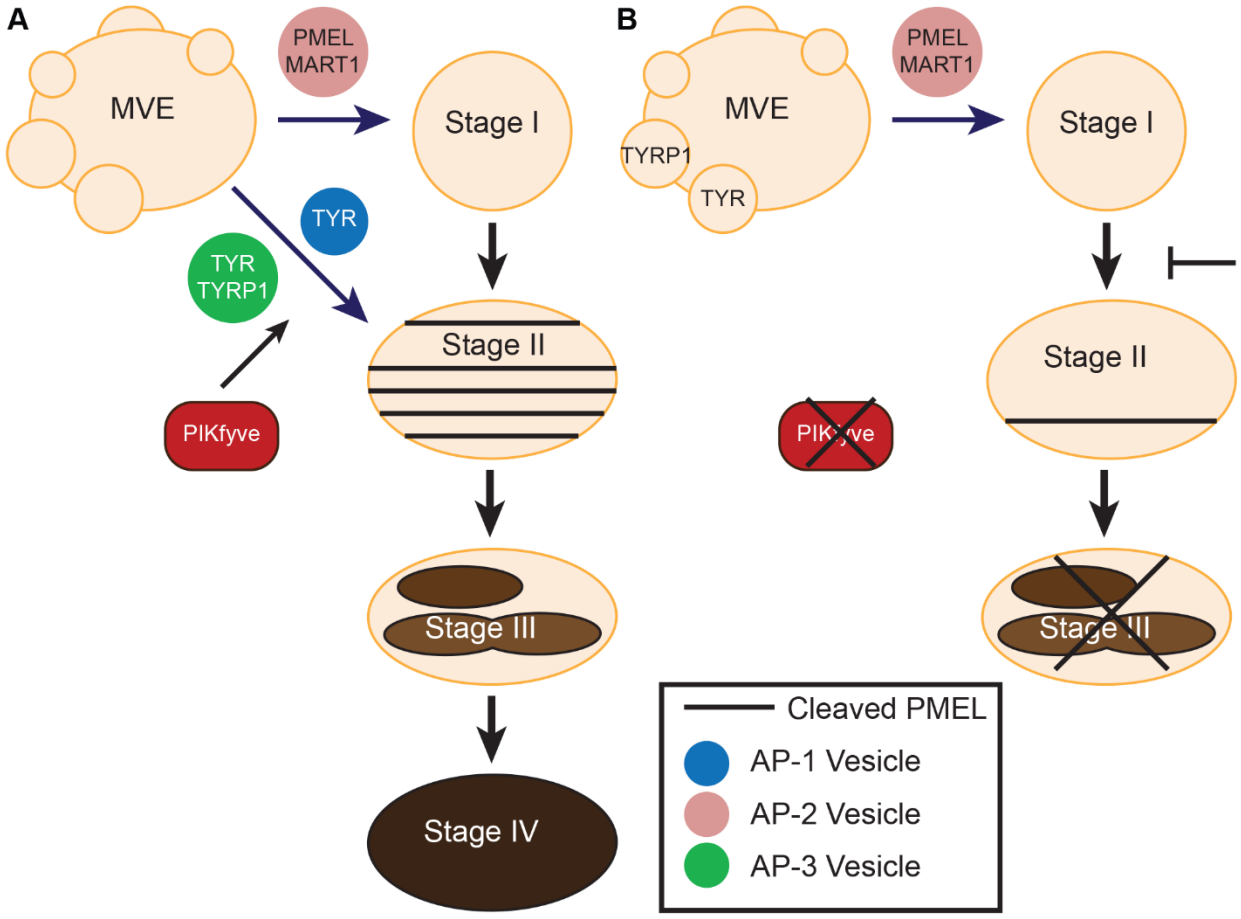
A
MVE
PMEL
MART1
Stage I
TYR
TYR
TYRP1
Stage II
PIKfyve
Stage III
Stage IV
B
MVE
TYRP1
TYR
PMEL
MART1
Stage I
Stage II
PIKfyve
Stage III
Cleaved PMEL
AP-1 Vesicle
AP-2 Vesicle
AP-3 Vesicle

Figure 2.7. PIKfyve regulates melanosome maturation. A) In normal melanocytes, PIKfyve regulates melanosome biogenesis by controlling the delivery of TYR and TYRP1 to the melanosome and inducing PMEL processing. B) Inhibition or loss of PIKfyve blocks PMEL processing and prevents TYR and TYRP1 from being trafficked to stage II melanosomes.

Table 2.1. List of primers used in experiments and their sequences, 5' to 3'.

Primer	Sequence 5' to 3'	Animal	Application
Cre For	GCGGTCTGGCAGTAAAAACTATC	Mouse	Genotyping
Cre Rev	GTGAAACAGCATTGCTGTCACTT	Mouse	Genotyping
PIKfyve^{Flox} For	GAGAAAGGGGACAGTGTTTGGC	Mouse	Genotyping
PIKfyve^{Flox} Rev	CCAGATCTTGCACTGTAACCACAAACCAC	Mouse	Genotyping
ROSA^{mTmG} For	CTCTGCTGCCTCCTGGCTTCT	Mouse	Genotyping
ROSA WT Rev	CGAGGCGGATCACAAGCAATA	Mouse	Genotyping
ROSA^{mTmG} Rev	TCAATGGGCGGGGGTCGTT	Mouse	Genotyping

CHAPTER 3

Wipi1 and its role in pigmentation *in vivo*

Jessica L. Flesher, Ilse Sears-Kraxberger, Oswald Steward, and Anand K. Ganesan

ABSTRACT

Melanosomes are lysosome-related organelles dedicated to melanin synthesis. To generate this specialized compartment, melanocytes must develop specific methods to transport proteins to the melanosome and not to other organelles. Recent work from our group and others have indicated that several proteins involved in other endosomal and lysosomal biogenesis processes can play non-overlapping roles in melanosome biogenesis. WIPI1, an autophagy related protein, binds phosphoinositides that regulate autophagy and contributes to melanosome formation and maturation. *In vivo*, *Wipi1* loss causes subtle changes in mouse coat color. In culture, *Wipi1* null melanocytes have increased accumulation of early stage melanosomes, indicating that WIPI1 plays a role in generating early stage melanosomes.

MAIN TEXT

Introduction

The production of the pigment melanin is confined within a lysosome-related organelle called the melanosome (*173*). Melanosomes contain specific markers, including proteins for melanin synthesis and deposition including Tyrosinase (TYR), Tyrosinase-related proteins 1 and 2 (TYRP1 and DCT), and a premelanosome protein (PMEL) (*27*). To sequester the essential membranes and generate an acidic environment for melanin synthesis, melanosomes rely on the function of additional proteins from multiple ubiquitous organelles (*174*). The ER chaperone protein, calreticulin, is required for processing TYR, the enzyme that catalyzes the rate-limiting step of melanin synthesis (*175*). Calreticulin and another chaperone protein found on melanosomes, BiP/GRP78 (*174*), also ensure the ER-associated degradation of soluble TYR in oculocutaneous albinism patients with mutations in the transmembrane domain of TYR (*176*).

Multiple lysosomal proteins have been found on melanosomes including LAMP1 (*174*, *177*) and TPC2, a cation release channel (*170*). Vesicle trafficking proteins are also required for the proper delivery of catalytic enzymes to the melanosome. Mutations in *HPS1* and *HPS4*, subunits of BLOC-3 (biogenesis of lysosome-related organelles complex 3) (*96*), are responsible for the pale ear and light ear mice (*178*) and, in humans, cause a distinct form of albinism (*96*).

Autophagy, the intracellular removal of unwanted protein aggregates and organelles, is another process that delivers proteins to the melanosome (*179*). RNAi knockdown of *ATG5*, an autophagy protein that colocalizes to melanosomes, causes hypopigmentation in pigmented cell lines (*112*, *113*); ATG4B and LC3B are required for normal trafficking of melanosomes (*43*); heterozygous deletion of *Beclin1* results in decreased pigment accumulation in mice (*113*); and loss of *Atg7* causes a subtle loss of coat color in mice (*180*). Another autophagy protein that alters pigmentation in cell lines is WIPI1 (WD repeat domain, phosphoinositide-interacting 1). Depletion of WIPI1 decreases melanin production and alters melanosome maturation (*112*, *113*). During autophagy, WIPI1 and its homologue WIPI2 bind ER membranes containing phosphoinositide 3-phosphate (PI(3)P) and transport these membranes to the growing phagophore (*181*, *182*). WIPI1 is retained on the autophagosome through its fusion with the lysosome and can be used as a marker of mammalian autophagy (*183*). The functional role of WIPI1 during melanosome biosynthesis is not fully understood.

To further elucidate the role of WIPI1 in melanogenesis we sought to identify the phosphoinositides bound by WIPI1 and generate *Wipi1* null mice to characterize the role of *Wipi1 in vivo*. We have generated WIPI1 constructs with altered phosphoinositide binding. *In vivo* studies have revealed a subtle coat color phenotype associated with the loss of *Wipi1*, not visibly apparent on black (non-agouti) or agouti coat backgrounds. Isolation and culture of primary

melanocytes from *Wipi1* knockout mice indicate defects in melanosome maturation marked by more early stage melanosomes.

WIPI1 binds to multiple phosphoinositides

WIPI1 is a member of the PROPPIN family that consists of four 7-bladed β-propeller proteins that bind to specific phosphoinositides through a conserved FRRG motif (*111*). To characterize the binding function of WIPI1 in vitro, WIPI1 mutant constructs were designed where the arginines within the FRRD domain, R226 and R227, were removed. Protein lysate was collected from HEK 293T cells overexpressing wildtype WIPI1, WIPI1^{R226A}, or WIPI1^{R227A} for lipid binding assays. Lysates containing wildtype and mutant WIPI1 were assayed against a panel of phosphoinositide coated beads (Figure 3.1A). Wildtype WIPI1 binds PI(3)P and PI(3,5)P2 consistent with previous findings (*111*, *181*), but also binds PI(5)P (Figure 3.1B). Loss of R226, results in loss of WIPI1 binding to PI(3,5)P2, but not PI(3)P or PI(5)P. While the R227A construct binds none of the phosphoinositide targets (Figure 3.1B).

Previous studies have identified that the kinase PIKFYVE generates critical PIs required for melanosome formation (*110*). PIKFYVE forms a complex with the phosphatase FIG4 (*106*) and the scaffold protein VAC14 (*29*) and knockout of any of the three components of this complex results in a dilute coat color phenotype in mice. In yeast, the homologous Fab1 protein complex can also include an additional PI binding protein, Atg18 (Autophagy related protein 18) (*107*), the yeast homolog to mammalian WIPI1 (*111*). Preliminary studies have shown WIPI1 as not part of the stable mammalian complex (data not shown). Further studies are needed to determine if WIPI1 interacts with the PIKFYVE complex and the identity of PIs that regulate melanosome formation.

Loss of *Wipi1 in vivo* results in a subtle pigment phenotype

To elucidate the mechanism through which WIPI1 regulates melanogenesis *in vivo*, *Wipi1* was constitutively knocked out in C57BL/6NTac mice. Hair from control and *Wipi1* knockout mice was collected at P50 and hair regrowth was stimulated through depilation. Loss of only one copy of *Wipi1* resulted in a 16% decrease in pigment accumulation in hair, p-value 0.007 (Figure 3.2A), and loss of both copies of *Wipi1* lead to a 20% reduction in melanin accumulation, p-value 0.028 (Figure 3.2A). However, mice lacking Wipi1 did not have a visible decrease in a black coat color (Figure 3.2B). After inducing hair growth and melanogenesis for 10 days, RNA from whole mouse skin was subjected to Nanostring analysis. *Wipi1* knockout mice had loss of *Wipi1* with 0.42% of wildtype mice *Wipi1* expression levels, p-value 0.049 (Figure 3.2C). In the same panel of mice, there was no significant loss of melanocyte-specific gene expression (Figure 3.2C).

In vitro studies in melanocyte and melanoma cell lines have shown that WIPI1 regulates melanogenesis (*112*, *113*), but the *in vivo* phenotype in black mice is subtle. One possible explanation is the prevalence of dark eumelanin in the hair is masking the phenotype as seen with the *Pmel* knockout mouse (*184*). On a C57BL/6J background, the loss of *Pmel* resulted in an approximately 40% reduction in melanin accumulation in the hair and a visible phenotype was only detected after the allele was crossed to a lighter coat color background (*184*). Likewise, loss of *Mlana* (MART1 gene) alters melanosome morphology, with a visibly slight dilution of coat color (*185*). Agouti mice have a distinct band of pheomelanin present in the hair compared to non-agouti black mice (*186*). To generate a *Wipi1* knockout mouse on an agouti coat color background, *Wipi1* null black mice were crossed to wildtype white-bellied agouti mice. Progeny were then backcrossed for five generations to create an agouti strain of *Wipi1* knockout mice. As was observed on the black coat color background, *Wipi1* null mice on an agouti coat color background

have no visible decrease in pigmentation (Figure 3.2D). Additional crosses with an *Mitf-M* null heterozygote (data not shown) and a melanocyte-specific *Pikfyve* heterozygote (data not shown) did not show any visible coat color phenotype. To observe a pigment phenotype with *Wipi1* loss, crosses with diluted pigment phenotypes found in *Tyr* alleles (*186*) could provide a coat color background with enough contrast to reveal a visible change in coat color indicative of the 15-20% decrease seen with loss of *Wipi1* on a black (non-agouti) coat.

As a regulator of autophagy, mammalian WIPI1 plays a semi-redundant role with WIPI2, both orthologues of yeast Atg18 (*182*). During autophagy, both WIPI1 and WIPI2 bind and recruit ER membranes containing PI(3)P to generate the phagophore where both proteins are retained during autophagy (*181*, *187*). WIPI2 has an additional role in autophagy to recruit ATG16L1, a component of the LC3-conjugation complex that is necessary for the conjugation of cleaved LC3 to phosphotidylethanolamine on the autophagosome membrane (*188*). With the constitutive loss of *Wipi1*, it is possible that *Wipi2* could be compensating. In an attempt to shift WIPI2 into autophagy, preliminary studies utilizing calorie restriction in *Wipi1* knockout mice were completed between P50 and P100. There was no sign of alterations in coat color, though calorie restriction caused weight-loss and delayed hair growth (data not shown). Since mouse models for *Wipi2* loss are not available, future studies on primary melanocytes will address whether cells with loss of *Wipi1* are more sensitive to knockdown of *Wipi2*.

Alterations in primary melanocytes from *Wipi1* knockout mice

The loss of *Wipi1 in vivo* resulted in a significant decrease in pigment accumulation of the hair without a visible phenotype. To delve into the cell autonomous phenotype of *Wipi1* null melanocytes, we generated primary cultures from neonatal skin. Primary melanocytes were

prepared for electron microscopy to determine how loss of *Wipi1* alters melanosome maturation by staging melanosomes. Representative images of *Wipi1* wildtype and null melanocytes are in Figure 3.3A, with representative melanosomes depicted for stages I-IV. For each cell melanosomes were staged and counted. There was no significant difference in melanosome counts in *Wipi1* knockout melanocytes compared to wildtype ($p = 0.340$), though *Wipi1* knockouts had 39% more melanosomes on average (Figure 3.3B). This might have been a result of variability in the few cells used per group. Preliminary results suggest that *Wipi1* knockout melanocytes have 21-fold increased accumulation of stage I ($p = 0.066$) and 3-fold increase in stage II ($p = 0.061$) melanosomes compared to wildtype melanocytes (Figure 3.3C). Increased accumulation of stage III melanosomes by 95% and stage IV melanosomes by 22% were not approaching significance, $p = 0.149$ and 0.680, respectively (Figure 3.3C). Murine phenotypes with mutations in regulators of melanosome biogenesis including *Pmel, Mlana*, and *Pikfyve* inhibit maturation and alter the structure of melanosomes (*110*, *184*, *185*). Unlike these models, knockdown or knockout of autophagy related proteins including ATG7, ATG4B, and LC3B still contain late stage melanosomes, though early stages were not quantified (*43*, *180*). Our results indicate that loss of *Wipi1* induces accumulation of early stage and some late stage melanosomes yet these melanocytes produce less pigment in the hair. This argues that WIPI1 plays a role in regulating the trafficking of specific constituents or vesicles to fuse with the melanosomes, as the process of melanosome maturation itself is not disrupted.

Localization of melanosome proteins is another indicator of defects in melanosome maturation (*110*, *112*). Loss of *Wipi1* results in a perinuclear localization of TYRP1 melanosomes, and loss of colocalization with LC3 (Figure 3.3D). Perinuclear localization of melanosomes was also seen with knockdown of *LC3B* (*43*) suggesting a defect in trafficking of melanosomes across

microtubules. Preliminary results indicate that LAMP1, a lysosomal marker that colocalizes to melanosomes (*177*), has some loss of colocalization and accumulation around the nucleus (Figure 3.3D). EEA1, an endosomal marker (*189*), has no mislocalization with loss of *Wipi1*(Figure 3.3D).

In this study, we present the initial findings of a subtle pigment phenotype with loss of *Wipi1, in vivo*. While the loss of *Wipi1* does not result in a visible pigment phenotype, the significant loss of melanin accumulation in the hair is due to defects in the maturation of early stage melanosomes. As a component of PI signaling and autophagy, understanding how WIPI1 contributes to melanosome formation will aid our understanding of melanosome maturation and recruitment from other distinct organelle compartments.

MATERIALS AND METHODS

Mutagenesis of Wipi1 Constructs

The original plasmid containing human WIPI1 was purchased from GeneCopoeia (EX-Z1566-Lv102). The lipid binding pocked of WIPI1 were mutated using site-directed mutagenesis kit (Agilent Technologies, catalog number 200521). Desired mutations were confirmed with Sanger sequencing (GeneWiz).

Cell Lines, Culture, and Lipid Binding Assays

HEK293T cells were purchased from the ATCC and cultured in DMEM supplemented with 10% fetal bovine serum and antibiotic-antimycotic. HEK cells plated in 6-well plates were transfected with WIPI1 constructs using Lipofectamine 3000 (Invitrogen) following manufacturer's instructions. After 48 hours, cells were lysed in Lipid Binding Buffer (20mM Tris-

HCl, 150mM NaCl, and 1mM EDTA (pH 7.5)) with 0.1% Halt Protease and Phosphatase Inhibitor (Thermo Fisher Scientific) and passed through a 25-gauge needle 10 times. Cells were sonicated on ice for 5 mins and spun at 13,000xg for 1 hour at 4°C. Protein concentration was determined using a BCA assay (Thermo Fisher Kit), and aliquots of 200ug were made to reduce free-thaw cycles. Lipid binding assays were performed in non-stick tubes (ThermoFisher Scientific), where 40µg was diluted in Lipid Binding Buffer to 50µL. Phospholipid conjugated beads (Echelon Biosciences) were mixed and 100µL were added to protein lysate. Proteins were incubated on the beads for 4 hours at 4°C. Following incubation, the beads were washed 5 times in Lipid Wash Buffer (10mM HEPES (pH 7.5), 150mM NaCl, 0.25% NP 40 substitute). The final pellet was resuspended in 2X Laemmli's Buffer for western blot analysis.

Western Blot Analysis

Lipid-bound proteins were subjected to SDS-PAGE on 4-12% Tris-Glycine gels and transferred onto Immobilon-P membranes (EMD Millipore). Membranes were blocked in 10% non-fat milk in 1X TBS with 0.1% Tween-20, and probed with WIPI1 and GFP antibodies. Protein levels were assessed using densitometry analysis (ImageJ, NIH).

Mouse Strains and Genotyping

All animal experiments were approved by the UC Irvine Institutional Animal Care and Use Committee (IACUC) (AUP-17-230). *Wipi1*$^{tm1(KOMP)Vlcg}$ (*Wipi1* knockout) allele used for this research project was generated by the trans-NIH Knock-Out Mouse Project (KOMP) and obtained from the KOMP Repository (www.komp.org) generated on a C57BL/6NTac background. Genomic DNA was isolated from distal toe clips of altricial animals using the Quick Genotyping

DNA preparation Kit (Bioland Scientific, LLC) according to the manufacturer's instructions. White-bellied agouti mice (129S1/SvImJ) were purchased from The Jackson Laboratory (Stock Number 008875) and crossed to B6 *Wipi1* knockout mice to generate F1 mixed background mice. *Wipi1* F1 heterozygous mice were then backcrossed for five generations on to the wildtype agouti mice to produce *Wipi1* knockout mice on a white-bellied agouti background. Genotyping primers follow guidelines provided by the KOMP repository for the *Wipi1* wildtype allele (Forward Primer 5'-CCTCGGACAAACAGTCAGTCTATCC-3', Reverse Primer 5'-AGAGAAAGGGCTCCTGAGCTTCC-3') and the neo cassette in the *Wipi1* knockout allele (Forward Primer 5'-GCAGCCTCTGTTCCACATACACTTCA-3', Reverse Primer 5'-TGTGGTTTGAAGGTCTTTTAGACTGC-3').

Melanin Quantification of Hair

Dorsal hair from mice was collected at post-natal day 50 (P50) during the second telogen phase. To measure melanin absorbance at 405nm, 1mg of hair was dissolved overnight at 65°C in 1mL of 90% Soluene-350 (PerkinElmer) and 10% water. An average of four 150µL aliqouts was used for each mouse hair sample. Statistics were calculated in R (version 3.3.2) using a one-way ANOVA.

RNA Isolation and Nanostring nCounter Analysis

Mice were shaved and depilated at P50 to stimulate the 3rd Anagen. At P60, whole skin was collected from mice for RNA isolation and immediately stabilized overnight in RNAlater (Invitrogen) at 4°C. Skin samples placed in hard tissue homogenizing reinforced tubes with 2.8mm ceramic beads (Bertin Corporation) for homogenization using the Precellys24 high-

throughput tissue homogenizer (Precellys). RNA was extracted from the homogenized skin following the RNeasy Fibrous Tissue Mini Kit (Qiagen) following manufacturer's instructions. RNA was normalized to a concentration of 20ng/µL and 5µL of normalized sample was then added to a 20µL aliquot of reporter codeset master mice. The samples were then hybridized at 65°C for 16-18 hours, and then transferred to the prep station. The prep station was run on the high sensitivity setting. Upon completion of the prep station step, the cartridge was loaded onto the nCounter and scanned using the "max" setting which attempts to capture 1155 fields of view (FOV). Resultant data was analyzed using the nSolver analysis software (Nanostring Technologies).

Isolation and Culture of Primary Melanocytes

Neonatal mouse melanocytes were collected as previously described (*110*, *152*). C57BL/6N mice less than 3 days old were euthanized and sterilized. Skin was removed and cleaned of muscle. The epidermis was separated from the dermis following a 1-hour incubation in 5mg/ml trypsin (Sigma-Aldrich) at 37°C. The epidermis was chopped in 0.25% trypsin-EDTA solution (Gibco) and resuspended in RPMI with 5% FBS. The resuspended cells were filtered using a 100µm cell strainer followed by a 40µm cell strainer. Cells were sedimented and washed in PBS (pH 7.2) with 0.5% BSA (Fisher Scientific). The cell pellet was resuspended and incubated with CD117 MicroBeads (Miltenyi Biotec) following the manufacturers protocol. Cells were cultured using previously described methods (*190*) in RPMI (Corning) with 5% FBS, antibiotic-antimycotic, and additional growth factors (alpha-MSH, FGF, SCF, insulin, EDN3, ethanolamine, phosphoenthanolamine).

Electron Microscopy

Primary melanocytes were seeded at $5x10^4$ into 8-well chamber slides (Thermo Fisher Scientific, Catalog Number 1256518). Forty-eight hours after seeding media was replaced with Karnovsky's Fixative (*153*) for four hours at room temperature. Cells were washed in 0.2M sodium cacodylate buffer for 15 minutes three times. Samples were then processed for electron microscopy as previously described (*91*, *110*). Melanosome stages (I – IV) were quantified visually in the electron micrographs and melanosome stage percentage was assessed versus vehicle treated controls. Images were edited for figures in Photoshop (21.0.1 release). Statistical analysis of melanosome counts was completed in R (version 3.5.3) using pairwise t-tests with Benjamin & Hochberg test for false discovery rate.

Immunofluorescence

Primary melanocytes were seeded at $5x10^4$ into 8-well chamber slides and grown for an additional 48 hours. Melanocytes were fixed in 2% PFA for an hour at room temperature and washed in PBS. Cells were permeabilized for 1 hour in 1X PBS with 1% BSA, 0.4% saponin, and 0.1% Tween20 prior to staining. Primary antibodies were used to detect TYRP1 (Abcam, catalog number ab3312), LC3 (Abcam, catalog number ab51520), LAMP1 (Abcam catalog number ab24170), and EEA1 (abcam, catalog number ab2900) with fluorophore-tagged secondary antibodies (AlexaFluor594 anti-rabbit, catalog number A11037 and AlexaFluor488 anti-mouse, catalog number A11059). Coverslips were mounted with Vectashield containing DAPI (Vector Laboratories, catalog number H-1200). Images were acquired using a Nikon Eclipse Ti fluorescent microscope. Overlaid images were generated by merging individual channels using the stitching

plugin (*191*) in ImageJ (version 1.52). Images were cropped for presentation in Photoshop (21.0.1 release).

ACKNOWLEDGEMENTS

We would like to thank Sohail Jahid for generating the WIPI1 constructs and Francisco Espitia for establishing the colony of *Wipi1* knockout mice. This work was supported by grants from the National Institutes of Health (R01AR063116) to AKG. The research reported in this publication was supported by the National Cancer Institute of the National Institutes of Health Award Number T32CA009054-37 to JLF. This work was made possible, in part, through access to the Genomics High Throughput Facility Shared Resource of the Cancer Center Support Grant (P30CA-062203) at the University of California, Irvine and NIH shared instrumentation grants 1S10RR025496-01, 1S10OD010794-01, and 1S10OD021718-01. NIH grants to Velocigene at Regeneron Inc (U01HG004085) and the CSD Cosortium (U01HG004080) funded the generation of gene-targeted ES cells for 8500 genes in the KOMP Program and archived and distributed by the KOMP Repository at UC Davis and CHORI (U42RR024244). The content is solely the responsibility of the authors and does not necessarily represent the official views of the National Institutes of Health.

REFERENCES

27. A. Sitaram, M. S. Marks, Mechanisms of protein delivery to melanosomes in pigment cells. *Physiology*. **27**, 85–99 (2012).

43. A. Ramkumar, D. Murthy, D. A. Raja, A. Singh, A. Krishnan, S. Khanna, A. Vats, L. Thukral, P. Sharma, S. Sivasubbu, R. Rani, V. T. Natarajan, R. S. Gokhale, Classical autophagy proteins LC3B and ATG4B facilitate melanosome movement on cytoskeletal tracks. *Autophagy*. **13**, 1331–1347 (2017).

91. E. K. Paterson, T. J. Fielder, G. R. MacGregor, S. Ito, K. Wakamatsu, D. L. Gillen, V. Eby, R. E. Boissy, A. K. Ganesan, Tyrosinase depletion prevents the maturation of melanosomes in the mouse hair follicle. *PLoS One*. **10** (2015), doi:10.1371/journal.pone.0143702.

96. P. W. Chiang, N. Oiso, R. Gautam, T. Suzuki, R. T. Swank, R. A. Spritz, The Hermansky-Pudlak syndrome 1 (HPS1) and HPS4 proteins are components of two complexes, BLOC-3 and BLOC-4, involved in the biogenesis of lysosome-related organelles. *J. Biol. Chem.* **278**, 20332–20337 (2003).

106. C. Y. Chow, Y. Zhang, J. J. Dowling, N. Jin, M. Adamska, K. Shiga, K. Szigeti, M. E. Shy, J. Li, X. Zhang, J. R. Lupski, L. S. Weisman, M. H. Meisler, Mutation of FIG4 causes neurodegeneration in the pale tremor mouse and patients with CMT4J. *Nature*. **448**, 68–72 (2007).

107. N. Jin, C. Y. Chow, L. Liu, S. N. Zolov, R. Bronson, M. Davisson, J. L. Petersen, Y. Zhang, S. Park, J. E. Duex, D. Goldowitz, M. H. Meisler, L. S. Weisman, VAC14 nucleates a protein complex essential for the acute interconversion of PI3P and PI(3,5)P2 in yeast and mouse. *EMBO J.* **27**, 3221–34 (2008).

110. M. C. Liggins, J. L. Flesher, S. Jahid, P. Vasudeva, V. Eby, S. Takasuga, J. Sasaki, T. Sasaki, R. E. Boissy, A. K. Ganesan, PIKfyve regulates melanosome biogenesis. *PLoS Genet.* **14** (2018), doi:10.1371/journal.pgen.1007290.

111. T. Proikas-Cezanne, S. Waddell, A. Gaugel, T. Frickey, A. Lupas, A. Nordheim, WIPI-1alpha (WIPI49), a member of the novel 7-bladed WIPI protein family, is aberrantly expressed in human cancer and is linked to starvation-induced autophagy. *Oncogene*. **23**, 9314–9325 (2004).

112. H. Ho, R. Kapadia, S. Al-Tahan, S. Ahmad, A. K. Ganesan, WIPI1 coordinates melanogenic gene transcription and melanosome formation via TORC1 inhibition. *J. Biol. Chem.* **286**, 12509–12523 (2011).

113. A. K. Ganesan, H. Ho, B. Bodemann, S. Petersen, J. Aruri, S. Koshy, Z. Richardson, L. Q. Le, T. Krasieva, M. G. Roth, P. Farmer, M. A. White, Genome-wide siRNA-based functional genomics of pigmentation identifies novel genes and pathways that impact melanogenesis in human cells. *PLoS Genet.* **4** (2008), doi:10.1371/journal.pgen.1000298.

127. C. Bissig, P. Croisé, X. Heiligenstein, I. Hurbain, G. M. Lenk, E. Kaufman, R. Sannerud, W. Annaert, M. H. Meisler, L. S. Weisman, G. Raposo, G. Van Niel, The PIKfyve complex regulates the early melanosome homeostasis required for physiological amyloid formation. *J. Cell Sci.* **132**, jcs229500 (2019).

152. L. S. Godwin, J. T. Castle, J. S. Kohli, P. S. Goff, C. J. Cairney, W. N. Keith, E. V. Sviderskaya, D. C. Bennett, *Curr. Protoc. Cell Biol.*, in press, doi:10.1002/0471143030.cb0108s63.

153. M. J. Karnovsky, A formaldehyde-glutaraldehyde fixative of high osmolality for use in electron microscopy. *J. Cell Biol.* **27**, 1965 (1965).

170. A. L. Ambrosio, J. A. Boyle, A. E. Aradi, K. A. Christian, S. M. Di Pietro, TPC2 controls pigmentation by regulating melanosome pH and size. *Proc. Natl. Acad. Sci. U. S. A.* **113**, 5622–5627 (2016).

173. G. Raposo, M. S. Marks, D. F. Cutler, Lysosome-related organelles: driving post-Golgi compartments into specialisation. *Curr. Opin. Cell Biol.* **19**, 394–401 (2007).

174. V. Basrur, F. Yang, T. Kushimoto, Y. Higashimoto, K.-I. Yasumoto, J. Valencia, J. Muller, W. D. Vieira, H. Watabe, J. Shabanowitz, V. J. Hearing, D. F. Hunt, E. Appella, Proteomic Analysis of Early Melanosomes: Identification of Novel Melanosomal Proteins. *J. Proteome Res.* **2**, 69–79 (2003).

175. A. Kawase, T. Kushimoto, Y. Kawa, K. Ohsumi, H. Nishikawa, T. Kawakami, M. Mizoguchi, Y. Soma, Proteomic analysis of immature murine melanocytes at different stages of maturation: A crucial role for calreticulin. *J. Dermatol. Sci.* **49**, 43–52 (2008).

176. C. I. Popescu, C. Paduraru, R. A. Dwek, S. M. Petrescu, Soluble tyrosinase is an endoplasmic reticulum (ER)-associated degradation substrate retained in the ER by calreticulin and BiP/GRP78 and not calnexin. *J. Biol. Chem.* **280**, 13833–13840 (2005).

177. B. K. Zhou, R. E. Boissy, S. Pifko-Hirst, D. J. Moran, S. J. Orlow, Lysosome-associated membrane protein-1 (LAMP-1) is the melanocyte vesicular membrane glycoprotein band II. *J. Invest. Dermatol.* **100**, 110–114 (1993).

178. P. W. Lane, E. L. Green, Pale ear and light ear in the house mouse: Mimic mutations in linkage groups XII and xvii. *J. Hered.* **58**, 17–20 (1967).

179. H. Ho, A. K. Ganesan, The pleiotropic roles of autophagy regulators in melanogenesis. *Pigment Cell Melanoma Res.* **24**, 595–604 (2011).

180. C. F. Zhang, F. Gruber, C. Ni, M. Mildner, U. Koenig, S. Karner, C. Barresi, H. Rossiter, M. S. Narzt, I. M. Nagelreiter, L. Larue, D. J. Tobin, L. Eckhart, E. Tschachler, Suppression of autophagy dysregulates the antioxidant response and causes premature senescence of melanocytes. *J. Invest. Dermatol.* **135**, 1348–1357 (2015).

181. T. Proikas-Cezanne, Z. Takacs, P. Dönnes, O. Kohlbacher, WIPI proteins: essential PtdIns3P effectors at the nascent autophagosome. *J. Cell Sci.* **128**, 207–17 (2015).

182. H. E. J. Polson, J. de Lartigue, D. J. Rigden, M. Reedijk, S. Urbé, M. J. Clague, S. A. Tooze, Mammalian Atg18 (WIPI2) localizes to omegasome-anchored phagophores and positively regulates LC3 lipidation. *Autophagy*. **6**, 506–22 (2010).

183. T. Proikas-Cezanne, S. Ruckerbauer, Y. D. Stierhof, C. Berg, A. Nordheim, Human WIPI-1 puncta-formation: A novel assay to assess mammalian autophagy. *FEBS Lett.* **581**, 3396–3404 (2007).

184. A. R. Hellström, B. Watt, S. S. Fard, D. Tenza, P. Mannström, K. Narfström, B. Ekesten,

S. Ito, K. Wakamatsu, J. Larsson, M. Ulfendahl, K. Kullander, G. Raposo, S. Kerje, F. Hallböök, M. S. Marks, L. Andersson, Inactivation of Pmel alters melanosome shape but has only a subtle effect on visible pigmentation. *PLoS Genet.* **7**, e1002285 (2011).

185. I. T. Aydin, E. Hummler, N. P. M. Smit, F. Beermann, Coat color dilution in mice because of inactivation of the melanoma antigen MART-1. *Pigment Cell Melanoma Res.* **25**, 37–46 (2012).

186. W. K. Silvers, *The Coat Colors of Mice* (1979).

187. M. Grimmel, C. Backhaus, T. Proikas-Cezanne, WIPI-Mediated Autophagy and Longevity. *Cells* (2015), doi:10.3390/cells4020202.

188. M. I. Wilson, H. C. Dooley, S. A. Tooze, WIPI2b and Atg16L1: setting the stage for autophagosome formation. *Biochem. Soc. Trans.* **42**, 1327–1334 (2014).

189. K. Hirosaki, T. Yamashita, I. Wada, H. Y. Jin, K. Jimbow, Tyrosinase and tyrosinase-related protein 1 require Rab7 for their intracellular transport. *J. Invest. Dermatol.* **119**, 475–480 (2002).

190. S. S. Joshi, B. Tandukar, L. Pan, J. M. Huang, F. Livak, B. J. Smith, T. Hodges, A. A. Mahurkar, T. J. Hornyak, CD34 defines melanocyte stem cell subpopulations with distinct regenerative properties. *PLoS Genet.* **15**, e1008034 (2019).

191. S. Preibisch, S. Saalfeld, P. Tomancak, Globally optimal stitching of tiled 3D microscopic image acquisitions. *Bioinformatics* (2009), doi:10.1093/bioinformatics/btp184.

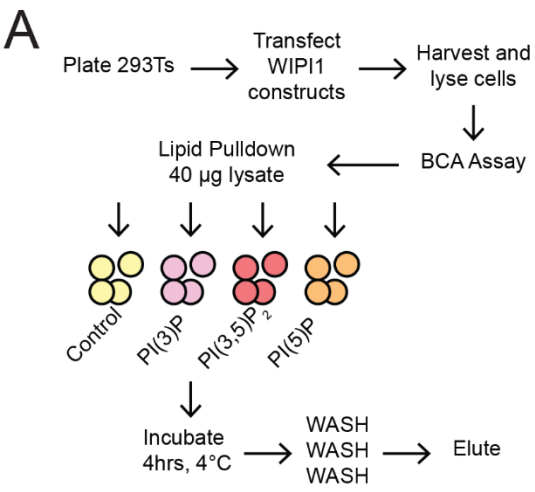
A
Plate 293Ts
Transfect WIPI1 constructs
Harvest and lyse cells
BCA Assay
Lipid Pulldown 40 µg lysate
Control
PI(3)P
PI(3,5)P2
PI(5)P
Incubate 4hrs, 4°C
WASH
WASH
WASH
Elute

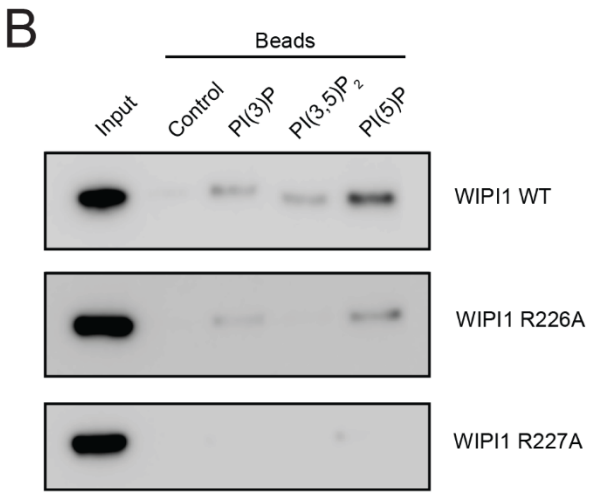
B
Beads
Input
Control
PI(3)P
PI(3,5)P2
PI(5)P
WIPI1 WT
WIPI1 R226A
WIPI1 R227A

Figure 3.1. WIPI1 binds to multiple phosphoinositides. A) Schematic of phosphoinositide binding assay. **B)** Wildtype human WIPI1 binds PI(3)P, PI(3,5)P_2, and PI(5)P. Mutations of arginines conserved amongst the PROPPIN family abolish phosphoinositide binding.

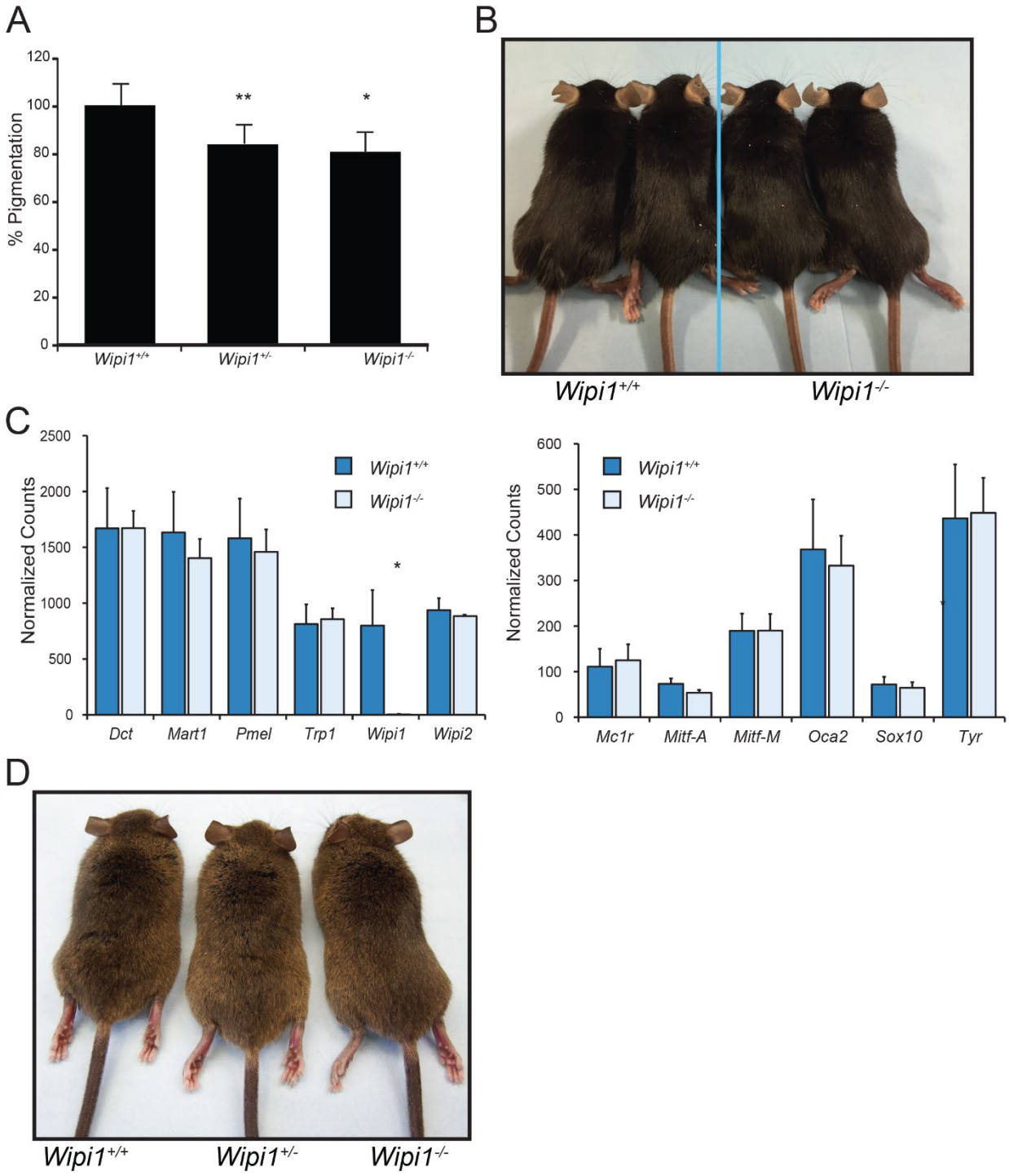
A
% Pigmentation
120
100
80
60
40
20
0
**
*
Wipi1+/+
Wipi1+/-
Wipi1-/-
B
Wipi1+/+
Wipi1-/-
C
Normalized Counts
2500
2000
1500
1000
500
0
Wipi1+/+
Wipi1-/-
*
Dct
Mart1
Pmel
Trp1
Wipi1
Wipi2
Normalized Counts
600
500
400
300
200
100
0
Wipi1+/+
Wipi1-/-
Mc1r
Mitf-A
Mitf-M
Oca2
Sox10
Tyr
D
Wipi1+/+
Wipi1+/-
Wipi1-/-

Figure 3.2. Loss of *Wipi1* results in a subtle pigment phenotype. A) Total melanin quantification of hair collected at P50 normalized to wildtype C57BL/6N mice. Both *Wipi1* heterozygotes and *Wipi1* knockouts have a significant reduction in melanin accumulation in hair at P50, $p = 0.007$ and 0.028, respectively. Data shown is mean ± sd, $n = 10$. **B)** Representative images of wildtype and *Wipi1* knockout mice on a C57BL/6N background imaged at P50. **C)** There is significant loss of *Wipi1* expression, $p = 0.049$, but no change in expression for melanocyte specific genes. Data shown is mean normalized counts of mRNA for gene, $n = 3$. **D)** Representative images of wildtype, *Wipi1* heterozygotes, and *Wipi1* null on a white-bellied agouti coat color background imaged at P50.

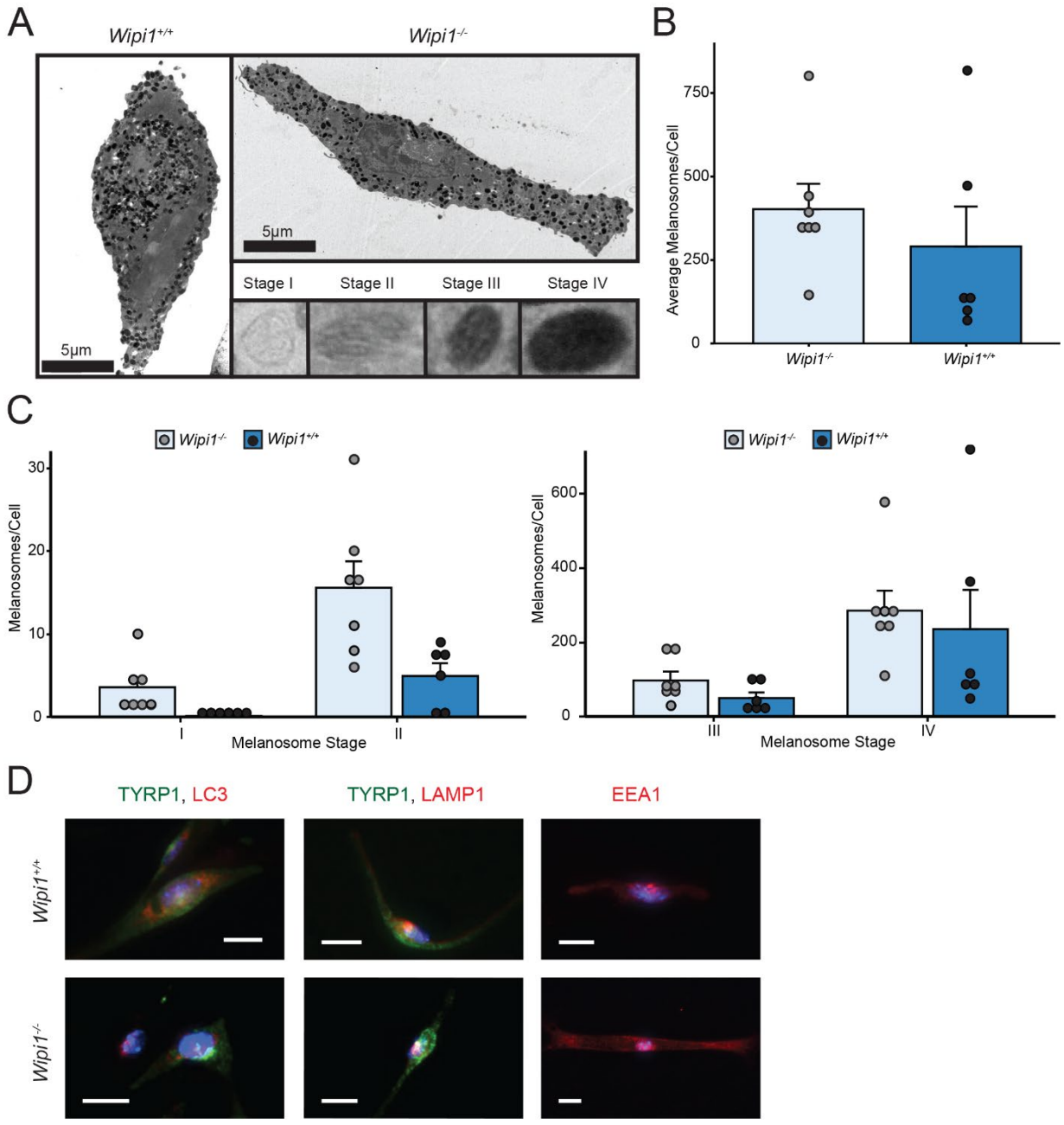
A
Wipi1+/+
Wipi1-/-
5μm
5μm
Stage I
Stage II
Stage III
Stage IV
B
Average Melanosomes/Cell
750
500
250
0
Wipi1-/-
Wipi1+/+
C
Wipi1-/-
Wipi1+/+
Melanosomes/Cell
30
20
10
0
I
II
Melanosome Stage
Wipi1-/-
Wipi1+/+
Melanosomes/Cell
600
400
200
0
III
IV
Melanosome Stage
D
TYRP1, LC3
TYRP1, LAMP1
EEA1
Wipi1+/+
Wipi1-/-

Figure 3.3. Characteristics of primary melanocytes from *Wipi1* knockout mice. A) Representative electron microscopy images of primary melanocytes taken from *Wipi1* wildtype and *Wipi1* knockout mice, scale bar is 5µm. Insets are representative images of melanosomes in distinct stages. **B)** Average number of melanosomes per melanocyte for wildtype and *Wipi1* null primary melanocytes. **C)** Melanosome stage counts from wildtype and *Wipi1* knockout primary melanocytes, n = 6 wildtype melanocytes and 7 *Wipi1* knockout melanocytes, error bars indicate mean ± standard error. **D)** Representative immunofluorescence staining of indicated markers in wildtype and *Wipi1* knockout primary melanocytes, scale bar is 10µm.

CHAPTER 4

Delineating the Roles of *MITF* Isoforms in Pigmentation and Tissue Homeostasis

Jessica L. Flesher, Elyse K. Paterson-Colman, Priya Vasudeva, Rolando Ruiz-Vega, Michaela Marshall, Eric Pearlman, Grant R. MacGregor, Jonathan Neumann, and Anand K. Ganesan

Citation: Flesher, JL, Paterson-Coleman, EK, Vasudeva, P, et al. Delineating the role of *MITF* isoforms in pigmentation and tissue homeostasis. *Pigment Cell Melanoma Res*. 2020; 33: 279– 292. https://doi.org/10.1111/pcmr.12828

ABSTRACT

MITF, a gene that is mutated in familial melanoma and Waardenburg syndrome, encodes multiple isoforms expressed from alternative promoters that share common coding exons but have unique amino termini. It is not completely understood how these isoforms influence pigmentation in different tissues and how expression of these independent isoforms of *MITF* are regulated. Here, we show that melanocytes express two isoforms of *MITF*, *MITF-A* and *MITF-M*. Expression of *MITF-A* is partially regulated by a newly identified retinoid enhancer element located upstream of the *MITF-A* promoter. *Mitf-A* knockout mice have only subtle changes in melanin accumulation in the hair and reduced *Tyr* expression in the eye. In contrast, *Mitf-M* null mice have enlarged kidneys, lack neural crest derived melanocytes in the skin, choroid, and iris stroma; yet maintain pigmentation within the retinal pigment epithelium and iris pigment epithelium of the eye. Taken together, these studies identify a critical role for *MITF-M* in melanocytes, a minor role for *MITF-A* in regulating pigmentation in the hair and *Tyr* expression in the eye, and a novel role for *MITF-M* in size control of the kidney.

SIGNIFICANCE

Mutations in *MITF* cause hypopigmentation and increase the risk for familial melanoma in humans. There are multiple different isoforms of *MITF*, and it is currently unclear how these different isoforms contribute to pigment cell development in the eye, hair, and skin. In this study, we identified two isoforms of *MITF* that are present in melanocytes of the skin and use genome editing technology to block the expression of one or the other of these isoforms in mice. Taken together, our work illustrates how protein isoforms can differentially contribute to biological phenotypes, findings that have relevance to human disease.

INTRODUCTION

In the human genome, alternative promoters are present in 30-50% of coding genes where they contribute to the diversity of the proteome and allow more sophisticated control of gene expression (*192*). Alternative promoters contain unique sequences to regulate expression of distinct isoforms in response to environmental or developmental cues. Genes including *EIF1AX* and *HBG1* utilize alternative promoters where one promoter lacks a TATA box for the expression of isoforms at the correct time during development (*192*, *193*). In differentiation, alternative promoters allow for the expression of isoforms in tissue and cell-specific manners (*194*). Aberrant use of alternative promoters is associated with cancer. Transcripts generated through the *TP53* P1 promoter produce p53 protein isoforms containing transactivation domains that allow p53 to regulate its tumor suppressor functions (*195*), while transcription from the P2 promoter produces p53 protein that lack the transactivation domains (*195*), and promote breast cancer stem cell maintenance (*196*).

MITF (microphthalmia-associated transcription factor) is the master regulator of melanocyte cell identity, controlling the production of melanin that gives skin, hair, and eyes color (*16*). Mutations in the human *MITF* locus are associated with increased risk for familial melanoma, Waardenburg syndrome, and Tietz syndrome (*102*, *197*). The *MITF* gene has nine distinct isoforms that are produced using alternative first coding exons (*198*). Some isoforms have ubiquitous expression, while others are more restricted to specific cell types and tissues (*199*). While the amino-terminus of MITF isoforms differ, all isoforms contain the basic helix-loop-helix leucine-zipper that is required for DNA binding and dimer formation with other bHLH family transcription factors (*200*). *Mitf* mutations in mice cause varied phenotypes with distinct features including premature greying, microphthalmia, and depigmentation (*201*). Although mice with

mutations in the promoter regions of *Mitf* have been identified (*105*), the mutant alleles involve loss of multiple isoforms, so it is still unclear how specific isoforms of MITF regulate pigmentation. Established methods for studying the role of *Mitf* isoforms rely on: 1) mutant alleles that affect multiple isoforms (*105*); 2) examination of the expression pattern of isoforms in target tissues of wildtype and *Mitf* mutant animals to infer their function during development (*198*); 3) isoform specific overexpression studies to determine the function of individual isoforms (*202*); or 4) isoform-specific knockouts as previously performed (*203*, *204*). More precise knockout models are needed to deconvolute the role of individual isoforms in tissue development and disease.

While published studies suggest that *MITF-M* is the main isoform expressed in melanocytes, the role of other *MITF* isoforms in melanocyte biology has not been studied. Here, we demonstrate that the human *MITF-A* isoform is expressed in melanocytes and its expression is regulated by retinoids. To distinguish the roles of *Mitf-A* and *Mitf-M* in pigment cell development and melanogenesis, we use CRISPR/Cas9 to generate *Mitf-A* and *Mitf-M* isoform-specific knockout mice. We observe that *Mitf-A* knockout mice have a subtle loss of pigmentation in the hair, while *Mitf-M* knockout mice lack melanocytes in the epidermis, hair follicle, iris, and choroid. Our study illustrates the utility of a CRISPR/Cas9 based approach to define specific roles for MITF isoforms in tissue development and pigmentation.

MATERIALS AND METHODS

Mouse strains and genotyping

All animal experiments were approved by the UC Irvine Institutional Animal Care and Use Committee (IACUC) (AUP-17-230). *ROSA*$^{mTmG/mTmG}$ mice (Stock No: 007576), C57BL/6J (Stock No: 000664) and B6(Cg)-Tyr^{c-2J}/J mice (Stock No: 000058) were obtained from The Jackson

Laboratory. C57BL/6NTac zygotes for genome editing were obtained from Taconic Biosciences. C57BL/6N mice used for *crb1* genotyping were obtained from the KOMP repository. Genotyping primers for *Mitf* mice were designed following characterization of deletions. All other genotyping primers follow guidelines provided by The Jackson Laboratory.

Genomic DNA was isolated from distal toe clips of altricial animals using the Quick Genotyping DNA Preparation Kit (Bioland Scientific, LLC) according to the manufacturer's instructions. Genomic DNA was sequenced to characterize the deletions of mice containing CRISPR/Cas9 generated deletions in *Mitf* at the Roy J. Carver Biotechnology Center (*https://biotech.illinois.edu/htdna*). Following the identification of 7bp deletion in exon 1A of *Mitf*, the effect on protein sequence was visualized in SnapGene Viewer (version 4.1.2) (from GSL Biotech; available at snapgene.com). After characterization of deletions, genotypes of progeny were determined using designed genotyping primers for *Mitf* mice. For the *Mitf-A* line, wildtype and homozygous knockouts are indistinguishable, so genotyping PCR reaction product was purified using the QIAquick PCR Purification Kit (Qiagen) and submitted for Sanger Sequencing (GENEWIZ) to determine whether the 7bp deletion was present. To identify the presence of *Crb1 rd8* mutation present in mutant mice generated from the C57BL/6NTac line, we used established genotyping primers (Table 4.S5). C57BL/6J albino mice purchased from The Jackson Laboratories and C57BL/6N mice obtained from the KOMP repository (www.komp.org) were used as wildtype and *rd8* mutant controls, respectively, to verify the mixed C57BL/6NTac and C57BL/6J background. Allele frequencies for wildtype and *rd8* alleles were calculated based on genotyping of approximately 50 mice of each *Mitf* line.

CRISPR/Cas9 genome-editing

Mitf mutant mice were generated by pronuclear injection of CRISPR/Cas9 reagents into C57BL/6NTac zygotes. Guide-RNAs (gRNAs) were designed using sgRNA Designer (Broad Institute, MIT) and GTScan (EMBL, Australia) algorithms. Guide-RNA templates were synthesized by PCR using oligos and GBLOCK oligos (IDT, Coralville, IA). *In-Vitro* Transcribed (IVT) gRNA were made using mMessage mMachine (Thermo-Fisher) and purified by MEGAclear kit (Thermo-Fisher). Cas9 mRNA was made by IVT using the same reagents with px330 plasmid (Addgene plasmid #42230) (*205*). RNAs were injected at 20 ng/ul each. Resulting mice were screened by PCR and T7 endonuclease. T7 endo-positive alleles were amplified by nested PCR and Sanger sequenced. CRISPR alleles were separated from hemizygous founders by outcrossing the mice to C57BL/6J mice (The Jackson Laboratories, Stock No: 000664). Lines were established from the F2 generation that were predicted to knock out expression of each specific *Mitf* transcript. All primers and gRNA used are listed in Table S6.

The *Mitf*^{em1Gane} allele (MGI:6273202) contains a 7bp deletion in chromosome 6, spanning 97,807,194 – 97,807,200 in Ensembl assembly GRCm38.p6. The deletion in this allele results in a loss of the *Mitf-A* isoform, designated as *Mitf* variant 202 in Ensembl and NM_001113198 in NCBI. Homozygotes for the *Mitf*^{em1Gane} are referred to as *Mitf-A* knockouts or nulls. The *Mitf*^{em2Gane} allele (MGI:6273203) contains an 18bp deletion in chromosome 6, spanning 97,991,944 – 97,991,961 in Ensembl assembly GRCm38.p6. The deletion in the *Mitf*^{em2Gane} allele results in loss of the *Mitf-M* isoform through loss of a splice site, and this is designated as *Mitf* variant 201 in Ensembl and NM_008601 in NCBI. Homozygotes for the *Mitf*^{em2Gane} deletion are referred to as *Mitf-M* knockouts or nulls.

Single cell isolation, sorting, and RNA-seq

Fat was scrapped off isolated back skin of *ROSA*^{mTmG} mice using a scalpel, and then the skin was cut into approximately 2mm by 2mm pieces. All pieces of each skin were placed into a Gentlemacs C Tube (Miltenyi) digested for 1 hour in an enzyme cocktail containing 232U DNAse I (Sigma-Aldrich), 0.25mg/ml liberase (Sigma-Aldrich), 23.2mM HEPES, 2.32mM sodium pyruvate (Corning), 0.0025g hyaluronidase (Fisher Scientific), and 1mg/mL dispase:collagenase (Sigma-Aldrich) in 5mL RPMI 1640 (Corning). Dissociation was stopped with 10µL of 0.5M EDTA and 400µL FBS. The skin was fully dissociated using gentlemacs m_imptumor_01 protocol (Miltenyi Biotec). Each sample was filtered twice in fresh RPMI containing FBS.

Whole back skin of P54 *ROSA*^{mTmG} mice was dissociated into a single cell suspension and incubated with Ghost Dye Red 780 (Tonbo biosiences) to identify viable cells. Live GFP+ and tdTomato+ cells were sorted using a BD FACSAria Fusion Sorter.

Total RNA from GFP+ and tdTomato+ cells from mice 1-4 was monitored for quality control using the Agilent Bioanalyzer Nano RNA chip. Library construction was performed according to the Illumina TruSeq RNA v2 protocol. The input quantity for total RNA was 1µg, and mRNA was enriched using oligo dT magnetic beads. The enriched mRNA was chemically fragmented for four minutes. First strand cDNA synthesis was performed using random primers, dNTPs, and reverse transcriptase to make cDNA. After second strand synthesis the cDNA was cleaned using AMPure XP beads, the cDNA was end repaired, and then the 3' ends were adenylated. Illumina barcoded adapters were ligated on the ends, and the adapter ligated fragments were enriched through nine cycles of PCR. The resulting libraries were validated by qPCR and sized by Agilent Bioanalyzer DNA high sensitivity chip. The concentrations for the libraries were normalized and then multiplexed together. The concentration for clustering on the flowcell was

12.5pM. The multiplexed libraries were sequenced on three lanes using paired-end 100 cycles chemistry for the HiSeq 2500. The version of HiSeq control software used was HCS 2.2.38 with real time analysis software, RTA 1.18.61. Paired-end sequencing reads were trimmed of adapter sequences, analyzed for quality using the Fastqc program (http://www.bioinformatics.babraham.ac.uk/projects/fastqc/), and aligned to the mouse reference genome version mm10 using the Tophat alignment software (version 2.0.12) (*206*). Fragments and exons were quantified using the Cufflinks program (version 2.2.1) (*207*). DEseq2 (version 1.14.1) (*208*) was utilized to distinguish differentially expressed genes from GFP+ and tdTomato+ populations in R (3.3.2). The data discussed in this publication have been deposited in NCBI's Gene Expression Omnibus (*209*) and are accessible through GEO Series accession number GSE138538 (https://www.ncbi.nlm.nih.gov/geo/query/acc.cgi?acc=GSE138538).

Analysis of read junctions

BAM files generated in Tophat were visualized against the annotated mm10 transcriptome in IGV (version 2.4.8) (*210*, *211*). After identifying read junctions present between exons 1A to 1B, 1B to 2A, and 1M to 2A, read junctions were counted between exons 1B and 2A as proxy for *Mitf-A* as no other isoforms containing exon 1B were found. Read junctions between exons 1M and 2A was counted as proxy for *Mitf-M*. The percentage of *Mitf-A* and *Mitf-M* transcripts was determined for GFP+ and tdTomato+ cells. To account for differential expression of *Mitf* between melanocytes and other skin cells, the percentage of each isoform was multiplied by the relative abundance of *Mitf* in the respective cell population. A Pearson's Chi-squared test performed in R (version 3.3.2) was used to determine if the expression of individual isoforms was significantly different between samples.

Human RNAseq raw data files (SRP039354) were retrieved from the SRA database (*212*) and aligned to the NCBI human reference genome GRCh38 using Tophat alignment software (version 2.0.12) (*206*). BAM files were visualized as described above. To delineate isoforms containing exon 1B, the proportion of read junctions from upstream exons (1A, 1J, 1C, 1E, and 1H) to 1B was multiplied by the proportion of read junctions to 2A containing 1B. Read junctions between 1M and 2A were still used as proxy for *MITF-M*.

Melanocyte isolation using CD117 microbeads

Neonatal mouse melanocytes were collected as previously described (*110*, *152*). Mice less than 3 days old were euthanized and sterilized. Skin was removed and cleaned of muscle. The epidermis was separated from the dermis following a 1-hour incubation in 5mg/ml trypsin (Sigma-Aldrich) at 37°C. The epidermis was chopped in 0.25% trypsin-EDTA solution (Gibco) and resuspended in RPMI with 5% FBS. The resuspended cells were filtered using a 100µm cell strainer followed by a 40µm cell strainer. Cells were sedimented and washed in PBS (pH 7.2) with 0.5% BSA (Fisher Scientific). The cell pellet was resuspended and incubated with CD117 MicroBeads (Miltenyi Biotec) following the manufacturers protocol. CD117 positive and CD117 negative cells were then lysed for RNA extraction using RNAeasy Mini Kit (Qiagen) and cDNA was generated using a high-capacity RNA to cDNA kit (Life Technologies).

Cell lines and cell culture

Human MNT-1 melanoma cells, a gift from M. Marks (University of Pennsylvania), were cultured in high-glucose DMEM (containing sodium pyruvate and L-glutamine) (Caisson) supplemented with 15% fetal bovine serum (CellGro), MEM vitamin solution (Invitrogen),

antibiotic-antimycotic (Invitrogen), and 10% AIM-V medium (Invitrogen). Human deeply-pigmented neonatal epidermal melanocytes (Invitrogen) were cultured in Medium 254 (Invitrogen) supplemented with phorbol 12-myristate 13-acetate-free Human Melanocyte growth supplement-2 (Invitrogen). As these melanocyte strains were purchased from commercial entities, no IRB approval was required prior to their use.

RNA isolation, reverse-transcriptase quantitative PCR (RT-qPCR)

Human cell lines were harvested using Tri-Reagent solution (Ambion) and RNA was extracted using a Direct-zol RNA miniprep kit (Zymo Research). Complementary DNA (cDNA) was synthesized from total RNA using a high-capacity RNA to cDNA kit (Life Technologies). Enucleated eyes from adult mice were dissected to isolate the posterior chamber under a Leica DMC2900 stereo-microscope. The retina was carefully removed, and the cells of the choroid and RPE were scraped from the sclera and placed into RNAlater (Invitrogen). RNA was extracted using the RNAeasy kit (Qiagen) with cDNA was synthesized utilizing SuperScript II RT (Invitrogen) and random primers.

Primers were designed to target the unique amino-terminus of human *MITF-A* and *MITF-M* using Primer3 (*213*, *214*). Primers for the unique first exons of *Mitf* isoforms were previously described (*198*) with additional primers designed utilizing Primer3. All primers used are listed in Table 4.S4. Power SYBR Green PCR master mix (Life Technologies) was used to amplify pure cDNA. All reactions were completed in technical and biological triplicate (n=3). A 7900HT Fast Real-Time PCR system (Applied Biosystems) and SDS 2.4 (Applied Biosystems) were used to determine Ct values for each sample. Values for human genes were normalized to either *β-actin* or *GAPDH* and values from mouse tissue were normalized to *Hprt* using the relative quantification

mathematical model (Pfaffl) as previously described (*118*). A two-tailed Student's t-test and two-way ANOVA were employed to determine statistical significance with R statistical Software (version 3.3.2).

To confirm the mutation present in *Mitf-A* transcripts from *Mitf-A* mutant mice, cDNA from wild-type and *Mitf-A* knockout mice was amplified using a sequencing forward primer that was upstream of the deletion and the common Exon 1 Reverse qPCR primer. PCR reaction product was purified using the QIAquick PCR Purification Kit (Qiagen) and submitted for Sanger Sequencing (GENEWIZ) to determine whether the 7bp deletion was present. The sequences were aligned to the mouse *Mitf-A* transcript (NM_001113198.1) in SnapGene (version 4.2.6) with primers and amino acid sequence labeled.

Nanostring nCounter analysis on whole-mouse skin

RNA was isolated from mice at P60 following stimulation of 3rd Anagen as described (*91*). Mice were shaved and depilated at P50 to stimulate the 3rd Anagen. Whole mouse skin was harvested from euthanized mice at P60 and immediately stabilized overnight in RNAlater (Invitrogen) at 4°C. Skin samples were homogenized using the Precellys24 high-throughput tissue homogenizer (Precellys) in hard tissue homogenizing reinforced tubes that contain 2.8mm ceramic beads (Bertin Corporation). After homogenization, RNA was extracted from each sample using the RNeasy Fibrous Tissue Mini Kit according to the manufacturer's instructions (Qiagen). RNA was normalized to a concentration of 20ng/μL and 5μL of normalized sample was then added to a 20μL aliquot of reporter codeset master mice. The samples were then hybridized at 65°C for 16-18 hours, and then transferred to the prep station. The prep station was run on the high sensitivity setting. Upon completion of the prep station step, the cartridge was loaded onto the nCounter and

scanned using the "max" setting which attempts to capture 1155 fields of view (FOV). Resultant data was analyzed using the nSolver analysis software (Nanostring Technologies). For RT-qPCR analysis on skin, cDNA was synthesized as described above for cells sorted with CD117 beads.

Identification of binding motifs and chromatin immunoprecipitation (ChIP)

Putative RXR/RAR binding sites in the *MITF-A* promoter was identified using MotifMap and the hg18 reference genome (*215*, *216*). Human NCBI accession numbers used were NM_00198159 (*MITF-A*) and NM_00248 (*MITF-M*) and corresponding mouse NCBI accession numbers are NM_002223198 (*Mitf-A*) and NM_008601 (*Mitf-M*). Conservation of the RXR/RAR binding site between human and mouse (mm10 reference genome) was determined by aligning 1000bp upstream of the transcription start site of *MITF-A* for the human and murine sequences in MegAlign (version 14.0.0) (DNASTAR). Two-kilobases of DNA upstream of the transcription start site for each human promoter was designated as the "promoter region" and tiled using four 500bp "tiles". Primers for quantitative PCR targeted each of these four tiled regions are listed in Table S4 and described in Supplemental Materials and Methods.

Drug treatment and dual-luciferase reporter assay

HEK293T cells were transfected with 1µg of a firefly luciferase reporter driven by human *MITF-A* full-length promoter (MITF-A EcoRI) or a truncated *MITF-A* promoter (MITF-A SmaI). Both plasmids were a kind gift of Dr. Shigeki Shibahara as previously described (*217*). An additional construct with a mutagenized promoter (MITF-A Mut) was generated by site-specific mutagenesis (Agilent Technologies) as described in Supplemental Materials and Methods

Melanin quantification

After shaving the dorsal hairs of mice at post-natal day 50 (P50), 1mg of hair was dissolved overnight in 1mL of 90% Soluene-350 (PerkinElmer) and 10% water at 65°C. Quadruplicate 150µL aliquots for each mouse hair sample were analyzed for absorbance at 405nm as previously described (*110*). Melanin quantification of tail skin was performed on 1cm sections of whole skin dissolved in 90% Soluene-350 as described above. To measure melanin in eyes of mice, the eyes were enucleated and dissected. The iris and the posterior chamber of the eye, following retina removal, were separated and dissolved overnight in Soluene-350 as described above.

Histology

Eyes were collected from adult mice, and connective tissue around the eye was removed. The eyes were than fixed in 10% formalin, dehydrated in ethanol, and embedded in paraffin. Seven-micron thick sections were de-waxed and rehydrated in ethanol and stained with hematoxylin and eosin to view general structure. Images at 20X were taken using a Nikon Eclipse E200. High magnification images of iris were taken with a 63X oil lens on a Zeica ApoTome2.

Western blots and immunoprecipitation

Both eyes from adult mice were incubated in LysisT buffer (250mM NaCl; 50mM Tris, pH 7.5; 0.125% Na deoxycholate; 0.375% Triton X-100; 0.15% NP-40; 4mM EDTA; 10µM Aprotinin; 50µM Leupeptin; 1mM PMSF) with Halt Protease and Phosphatase Inhibitor (Thermo Scientific) for 10 minutes. The samples were homogenized using the Precellys24 high-throughput tissue homogenizer as described above. Next, the samples were incubated on ice for 30 minutes prior to centrifugation to collect protein lysate. Lysates were subjected to SDS-PAGE on 8% Tris-

Glycine gels and transferred onto Immobilon-P membranes (EMD Millipore). Membranes were blocked in 5% non-fat milk with 1X TBS and 1% Tween-20, and probed with rabbit polyclonal GAPDH, 5174, lot# 6; rabbit monoclonal MITF, 12950, lot# 2 (Cell Signaling Technology). Protein levels were assessed using densitometry analysis (ImageJ, NIH). Total MITF levels was measured by generating protein lysates from both eyes of adult mice and subjecting them to immunoblotting with an MITF antibody as described in Supplemental Materials and Methods.

Immunofluorescence Staining

Skin from mice were collected at P56 and processed following established protocols (*218*). Dissected skin was cut into 1cm x 1cm square and fixed in 2% formaldehyde in 1X PBS for 30 minutes on ice. Fixed tissue was washed overnight in PBS at 4°C, followed by an overnight wash in 10% sucrose in PBS at 4°C. Skin was embedded in OCT (Fisher Scientific) and stored at -80°C. Ten-micron sections of skin were cut and dried overnight at room temp. Slides were blocked in 1% BSA (Fisher Scientific) in 1X PBS with 0.1% Tween-20 (Fisher Scientific) and probed with rat monoclonal CD117, CL8936AP, lot# 103628G (Cedarlane) and chicken anti-rat, Alexa488 (Life Technologies). Slides were imaged using Nikon Eclipse Ti fluorescent microscope. The number of CD117 positive hair follicles was counted in two distinct (non-sequential) slides and averaged for each mouse. A one-way ANOVA was used to calculate statistical significance with R statistical software (version 3.5.1). Images were post processed using Adobe Photoshop.

Eyes collected at P56 were fixed and cut in half prior to embedding, each half of the eye was embedded separately. Sectioning and staining were completed as described above.

Kidney characterization

Kidneys were collected from 4-month-old mice of both genders (3 males, 3 females for each genotype). The ratio of kidney to body mass was calculated from the combined weight of both kidneys divided by the weight of the individual mouse. For each mouse, one kidney was fixed and embedded in paraffin for histological analysis and imaged using methods described above. The other kidney was de-capsulated and macerated for 30 minutes in 5N HCl at 37°C. Tissue was rinsed in deionized water and stored at 4°C overnight. Tubules and glomeruli were dissociated through shaking and suspended in 25 ml of deionized water. Glomeruli were counted on five different 100µl aliquots. This procedure was modified from a published protocol (*204*). Statistical significance was determined using a two-way ANOVA with R statistical software (version 3.5.1).

Kidneys from 4-month-old mice were collected for RNA isolation and stabilized in RNAlater overnight. Following the same homogenization procedure described above for the skin, kidney RNA was isolated using the RNAeasy Mini Extraction Kit (Qiagen) with on-column DNase digestion. cDNA synthesis was performed using methods described for CD117+ and CD117- cells.

RESULTS

Multiple *Mitf* isoforms are expressed in melanocytes

To identify which *Mitf* isoforms are expressed in melanocytes, we first crossed *Tyr::Cre-^{ERT2}* mice (*72*) with *ROSA^{mTmG}* mice (*160*). In *Tyr::Cre^{ERT2}, ROSA^{mTmG}* double heterozygous mice, injection of tamoxifen induces melanocytes to express EGFP whereas all other cells in the epidermis express tdTomato (Figure 4.1A) (*110*). Single cell suspensions were generated from

mouse skin of the indicated genotypes and sorted into tdTomato+ and EGFP+ populations for bulk RNA-seq. A PCA plot demonstrates that our sorting procedure could separate melanocytes from other skin cell types (Figure 4.1B). We next examined the expression of a panel of melanocyte, keratinocyte, fibroblast, and endothelial cell-specific transcripts in EGFP+ and tdTomato+ cells (Figure 4.2A, Table 4.1). Almost all (97%) of the transcripts encoding known melanogenesis regulators were expressed in the GFP+ sorted cells (Figure 4.2B). The remaining 3% of transcripts encoding melanocyte specific markers were expressed in tdTomato+ cells, indicating that the induction of the *Tyr::Cre*^{ERT2} transgene was incomplete. In contrast, over 99% of *Trp63* transcripts (a transcription factor that regulates keratinocyte development (*219*, *220*)) were found in the tdTomato+ populations (Fig 4.1C), indicating that our method could efficiently sort melanocytes from other skin cells.

To determine the isoforms of *Mitf* expressed in mouse skin, BAM files for MITF transcripts were visualized and unique read junctions were counted using IGV 2.3.77 (*210*, *211*). Read junctions between exon 1A and 1B would correspond to *Mitf*-A. Notably, no other read junctions between exon 1B and other exons were observed in our dataset when aligned to the annotated mouse transcriptome. For simplicity, read junctions between exons 1B and 2A were counted as a proxy for *Mitf-A*, while read junctions between exons 1M and 2A were considered a proxy for *Mitf-M* (Figure 4.2C). In EGFP+ melanocytes, *Mitf-A* accounts for 9% of total *Mitf*, while *Mitf-M* accounts for the other 91% (Figure 4.2D). Of the *Mitf* expression in tdTomato+ skin cells, 66% was identified as *Mitf-M* (Figure 4.2D). To account for the differential expression of *Mitf* isoforms in EGFP+ and tdTomato+ cell populations, we calculated the relative abundance of these transcripts in melanocytes as compared to all other skin cells (Figure 4.2E). To validate RNAseq findings, cKit+ cells (an established marker of melanocytes (*221*)) were isolated from wildtype

neonatal epidermis. RNA was isolated from cKit+ and cKit- cells and reverse transcribed to quantify *Mitf* isoform expression. *Mitf* transcripts were abundant in cKit-expressing cells and largely absent in cKit negative cells (Figure 4.2F), suggesting that the low levels of *Mitf* transcripts detected in tdTomato+ cells are a result of the presence of uninduced melanocytes in that sample.

To verify that both *MITF-M* and *MITF-A* are expressed in human melanocytes, we measured the relative abundance of *MITF-M* and *MITF-A* transcripts using isoform-specific RT-qPCR primers. In MNT-1 pigmented melanoma cells and deeply-pigmented human melanocytes, both *MITF-M* and *MITF-A* are expressed at similar proportions as observed in the adult mouse (Figure 4.1D-E). Additionally, utilizing a published human epidermal melanocyte RNAseq dataset (*212*), we determined the relative isoform abundance of *MITF* isoforms by counting read junctions as proxy for individual isoforms. Multiple isoforms containing exon 1B were identified, so read junctions between exons 1B and 2 were taken as proxy for all exon 1B containing isoforms (Figure 4.1F). Relative abundance for each individual isoform containing exon 1B was proportioned by counting read junctions from exons 1A, 1J, 1C, 1E, and 1H to exon 1B (Figure 4.1F). Read junctions between exons 1M and 2 were counted as proxy for *MITF-M* (Figure 4.1F). In human melanocytes, 73% of *MITF* was *MITF-M* and the next most abundant isoform was *MITF-A,* which accounted for 21% (Figure 4.2G). The other isoforms present accounted for less than 6% of total *MITF* expression (Figure 4.2G). These results confirm that *MITF-M* is the primary isoform expressed in both mouse and human melanocytes, and *MITF-A* is the second most abundant isoform expressed in melanocytes.

The *MITF-A* promoter contains a RXR/RAR binding site

To determine how *MITF-A* is differentially regulated in melanocytes, we searched for unique binding motifs in the alternative promoters for human *MITF-A* and *MITF-M*. Utilizing MotifMap (*215*, *216*), we verified the presence of known sites that mediate *MITF-M* transcription including CREB and PAX (Table 4.2). We also identified a putative RXR/RAR DR5 binding site 714 base pairs (bp) upstream of the transcription start for *MITF-A* (Table 4.3). While the promoter regions, including the RXR/RAR binding site, for the A isoform are conserved in the mouse 740bp upstream of the transcription start site (Figure 4.3), expression of *MITF-A* is more robust in human melanocytes (Figure 4.1-2). We previously showed that 9-*cis* retinoic acid upregulates *MITF* and *TYR* expression in cultured melanocytes, stimulating pigment production in melanocyte and melanoma cell lines (*118*). Both the retinoic acid receptors (RAR) and retinoid x receptors (RXR) form dimers that are activated in response to retinoids (*222*). Additionally, RXRα is expressed in melanocytes (*223*) and a RXRα hypomorphic (I273N) mouse mutant exhibits premature greying (*224*).

Having established that *MITF-A* expression levels were higher in human melanocytes compared to mouse, we next sought to validate the binding of RXR and RAR to the *MITF-A* human promoter. For ChIP analysis, we designed tiled primers for 2kb upstream of transcription start sites for both *MITF-A* and *MITF-M* (Figure 4.4A). The putative RXR/RAR DR5 binding site is located in tile A3. In the human MNT-1 melanoma cell line, we found that pulldown with RARα significantly enriched for tiles A3 and A4 (Figure 4.4B) and RXRα enriched for tile A4 (Figure 4.4C). Using deeply pigmented (DP) human melanocytes, tile A4 was significantly enriched with RARα while tiles A2 and A3 were approaching significance (Figure 4.4D). For RXRα in DP

melanocytes, only tile A3 was approaching significance (Figure 4.4E). Consistent with our MotifMap findings, RARα and RXRα did not bind to the *MITF-M* tiles (Figure 4.4B-E).

Retinoids stimulate *MITF-A* promoter

Having demonstrated binding of RXR/RAR to a region within the *MITF-A* promoter, we next investigated whether RXR and RAR ligands could induce *MITF-A* promoter activity. To test the activity of the human *MITF-A* promoter, we used *MITF-A* promoter luciferase plasmid constructs containing either full length or truncated *MITF-A* promoter (Figure 4.3A). Luciferase experiments were conducted in HEK293T cells. The full length *MITF-A* promoter construct had activity similar to the truncated construct in serum-starved, vehicle (ethanol) treated cells (Figure 4.5B). By contrast, 9-*cis* retinoic acid induced luciferase activity of the full length *MITF-A* promoter construct, but failed to induce luciferase activity of the truncated *MITF-A* construct (Figure 4.5B). In the presence of DMSO, the vehicle for some retinoid receptor ligands, the full-length construct had a higher baseline activation compared to the truncated promoter (Figure 4.5C-E). Stimulation of the RXR subunit alone using the pan-RXR agonist LG100268 increased the activation of the luciferase reporter above baseline (Figure 4.5C), verifying that RXR can induce the luciferase activity of this reporter. Likewise, increasing concentrations of BMS753, a potent RARα agonist, stimulated the activity of the full length *MITF-A* promoter construct (Figure 4.5D). Taken together, these results suggest that RXR/RAR heterodimers can regulate the expression of *MITF-A.* This is consistent with previous findings that 9-*cis* retinoic acid can regulate *MITF* expression (*118*).

Having verified that the *MITF-A* promoter responds to retinoids, RXR-, and RAR-agonists, we next tested whether RXR/RAR regulates *MITF-A* expression via the newly identified

RXR/RAR binding site. Using site-directed mutagenesis, we deleted 28bp encompassing the 17bp motif identified through MotifMap to generate a mutant promoter construct (Figure 4.5A). Baseline luciferase activity from the mutant construct was significantly reduced compared to the full-length promoter construct, although the mutant retained higher levels of lucifierase expression when compared to the truncated promoter (Figure 4.5E). These results can be explained by the presence of other enhancer elements in the promoter that are known to activate *MITF-A* expression. Taken together, these studies indicate that RXR/RAR activation can induce the expression of *MITF-A.*

Mitf isoform-specific mutant mice

While expression studies have defined *Mitf-M* as the melanocyte specific isoform and *Mitf-A* as a regulator of eye development (*225*), the specific function of each isoform during development is unclear. Established mouse *Mitf* mutant alleles have loss of expression or function of multiple isoforms (Steingrímsson et al., 2003, 2004; Steingrímsson, 2008), making it difficult to determine the distinct roles of *Mitf* isoforms in tissue development. Because each isoform has its own unique first exon, we sought to generate mutant mice specifically lacking a single isoform. We designed guide RNAs for CRISPR/Cas9 gene-editing for exons 1A and 1M of *Mitf*. Utilizing this technique, we generated a 7bp deletion at the beginning of the coding region of exon 1A that produces a frameshift mutation that causes multiple premature stop codons (Figure 4.6A, 4.7A-B). This allele was designated $Mitf^{em1Gane}$, but for clarity, homozygous mice will hereafter be referred to as *Mitf-A* knockout or null mice. Similarly, we also generated an 18bp deletion spanning the splice site for exon 1M of *Mitf* (Figure 4.6A, 4.7C) designated $Mitf^{em2Gane}$. Mice

homozygous for the *Mitf*^{em2Gane} allele, with targeted deletion of the *Mitf-M* isoform, will hereafter be referred to as *Mitf-M* knockout or null.

Loss of specific isoforms of *Mitf* produced distinct pigment phenotypes. While mice lacking *Mitf-A* have no visible defect on a black (non-agouti) coat-color background (Figure 4.6B, 4.8A-B, 4.9A-B), quantitative analysis of the hair detected a 7% reduction in melanin accumulation of *Mitf-A* knockout mice compared to wildtype black mice (Figure 4.6C). In contrast, mutation of *Mitf-M* results in a loss of melanin in the hair and the skin of the ears and tail similar to the phenotype seen in albino mice (Figure 4.6D-F, 4.8C-D, 4.9C-D). Despite this dramatic loss of coat color, *Mitf-M* knockout mice are distinct from albino mice since their eyes contain some pigment and appear dark (Figure 4.6D, Figure 4.8C). Other studies have shown that mice heterozygous for mutations in the *Mitf* promoter region do not have appreciable differences in coat color (*226*). Similarly, loss of one copy of *Mitf-M* does not result in an appreciable change in pigmentation as mice appear black (Figure 4.6D). Moreover, there was no quantifiable differences in pigmentation in these animals, as they accumulate similar amounts of melanin in their hair as wildtype mice (Fig 4.6E).

Previous studies have shown that overexpression of *Mitf-A* in kidneys can increase the ratio of kidney to body mass and increase the number of glomeruli, while deletion of *Mitf-A* and elements upstream of the *Mitf-A* promoter results in experimental mice with kidneys that have less glomeruli (*204*). Histological analysis of kidneys from our *Mitf-A* null, 4-month-old mice showed no gross morphological changes as determined by two separate pathologists (Figure 4.10A-D). Additionally, in our mice, loss of *Mitf-A* did not significantly alter the ratio of kidney to body mass (Figure 4.6F, 4.10E) or the number of glomeruli in the kidney (Figure 4.6G, 4.10E). The melanocyte-specific isoform *Mitf-M* was also detected in the kidneys (Figure 4.10F-G) and loss

did significantly increase the ratio of kidney to body mass in both males and females (Figure 4.6F). However, while there was a trend towards increased glomeruli in *Mitf-M* knockout mice, the difference was not significant (Figure 4.6G, 4.10E). In *Mitf-M* knockout mice, there was no significant change in relative isoform abundance with the exception of *Mitf-A* and total *Mitf* (Figure 4.10F), however there is a trend toward enrichment of the *Mitf-C* isoform with loss of *Mitf-M* in the kidney (Figure 4.10G).

To more closely examine the expression of melanocyte isoforms of *Mitf* in the skin, we examined melanocyte-specific gene expression in whole back skin from wildtype and isoform-specific knockout mice using Nanostring. *Mitf-A* knockout mice had a similar gene expression profile compared to wildtype mice (Figure 4.11A). While the 7bp deletion causes a frameshift (Figure 4.7B), it did not alter the stability of the mRNA transcript, and *Mitf-A* expression levels were unchanged in knockout mice. To verify that the *Mitf-A* knockout mice lack functional MITF-A protein, we collected protein lysate from whole eyes of wildtype and *Mitf-A* knockout mice, as *Mitf-A* is the predominant isoform in the eye. *Mitf-A* knockout mice had ~50% reduced levels of total MITF in the eye (p-value = 0.003) (Figure 4.11B). Consistent with the visual loss of pigmentation, *Mitf-M* knockout mice had decreased expression of all melanocyte-specific genes in the skin without notable changes in expression of *Mitf-A* (Figure 4.11C). Mice heterozygous for the *Mitf-M* mutation showed no significant change in *Mitf-M* expression using RT-qPCR (Figure 4.11D), suggesting that the wildtype allele is upregulated in *Mitf-M* heterozygotes. RT-qPCR was not sensitive enough to detect the different isoforms of *Mitf* expressed in the skin. This type of the analysis would likely require isolation of melanocytes from the skin to generate enough *Mitf* transcripts that could be reproducibly measured. We did note that the downregulation of melanogenesis markers in *Mitf-M* knockout mice coincides with the loss of cKit positive

melanocytes in the hair follicle (Figure 4.11E-F). This loss of cKit positive cells was observed in *Mitf-M* knockout mice, but not in *Mitf-A* null or albino mice, suggesting that the pigment phenotype observed in these mice is secondary to the loss of melanocytes.

During normal development, MITF controls the migration of melanoblasts to target tissues including the epidermal basal membrane, the hair follicle, the iris stroma, and the choroid of the eye (*16*). Choroidal and iris stromal melanocytes and the pigmented epithelia of the iris (IPE) and retina (RPE) are thought to rely on MITF to induce melanin production. Unlike the neural crest-derived melanocytes, the cells of the pigmented epithelium are derived from the optic cup and express multiple isoforms of *Mitf* (*17*). Because these distinct pigment layers in the eye rely on different isoforms of *Mitf*, we investigated whether *Mitf* isoform-specific knockout mice had any eye phenotype. Live animal images taken of mice suggest a subtle loss of pigment in the iris of *Mitf-M* knockout mice (Figure 4.12A (top), 4.13A-D). There was a significant reduction (~35%) of pigmentation in the iris of *Mitf-M* knockout mice (Figure 4.12B) when melanin absorbance of the isolated iris was quantified. In contrast, *Mitf-A* knockout mice had no significant change in iris pigmentation (Figure 4.12B). Moreover, the difference in iris pigmentation was somewhat apparent when hematoxylin and eosin (H&E) stained sections were visualized at 20X magnification (Figure 4.14A-D), and even more apparent when these sections were visualized at 63X magnification (Figure 4.14E-H). Upon enucleation of the eyes, it became apparent that loss of *Mitf-M*, but not *Mitf-A* affected pigment accumulation in the posterior of the eye (Figure 4.12A, 4.13E-H), a result that was even more evident after removal of the retina from the posterior segment. Overall, the posterior segment of the eye of *Mitf-M* knockout mice had 30% of the pigment present in wild type eyes as measured by relative melanin absorbance (Figure 4.12C). *Mitf-M* knockout mice did have significantly more pigment in their eyes when compared to B6

albino mice (Figure 4.12B-C), which are known to lack pigment in both melanocytes and the retinal pigment epithelium. H&E staining of wildtype and *Mitf-A* knockout mice revealed pigmentation in both the choroid and RPE, however, loss of *MITF-M* results in the loss of choroidal pigmentation while the RPE appears normally pigmented (Figure 4.12D, 4.14I-L). Choroidal cKit positive melanocytes are also absent in *Mitf-M* knockout mice (Figure 4.12E). While histology reveals no gross morphological defects in the retina, we next sought to ensure any phenotypes observed in the *Mitf* knockout mice are not due to changes in retina degeneration caused by the presence of the *Crb1 rd8* mutation from the C57BL/6N line. Since the *Mitf-A* and *Mitf-M* lines are on a mixed 6N and 6J background, 50 mice of each line were genotyped for the *Crb1* wildtype and *rd8* alleles. Primers were validated with C57BL/6J mice, which lack the *rd8* mutation, and C57BL/6N, which are homozygous for the *rd8* mutation. The *Mitf-M* mice tested in these studies were all either heterozygous or lack the *rd8* allele altogether. Their eye phenotypes were compared against the eyes of wildtype mice, including those from the C57BL/6N line, which are known to be homozygous for *rd8*. Given these results, it is highly unlikely that the phenotypes observed are related to *rd8*, as none of the *Mitf-M* mice examined were *rd8* homozygotes while, in contrast, the control mice examined were *rd8* homozygotes (Figure 4.13I-J). Using RT-qPCR, we compared expression of isoforms in the combined choroid and RPE of the mice. The mutation in *Mitf-M* resulted in the expected downregulation of the *Mitf-M* transcript as well as total *Mitf*, *Tyr*, and *Mart1* (Figure 4.12F). In *Mitf-A* knockout mice there was an increase in the mutated *Mitf-A* transcript that results in premature stop codons. The mutation was verified using Sanger sequencing of wildtype and knockout *Mitf-A* transcripts (Figure 4.15). Interestingly, more *Mitf-J* transcripts also accumulated in *Mitf-A* knockout eyes when compared to the choroid and RPE of wildtype mice. These changes in specific transcripts is highlighted by the change in relative

abundance of *Mitf* isoforms in the eye (Figure 4.12G). Finally, we also observed decreased accumulation of *Tyr* transcript in *Mitf-A* knockout eyes (Figure 4.12F), consistent with other studies that indicate that MITF-A regulates *TYR* expression in the eye (*199*). Together, these studies show that deletion of *Mitf-A* or *Mitf-M* has distinct effects on the development of the skin, eyes, and kidneys.

DISCUSSION

Use of alternative promoters by a gene enables more sophisticated control of the gene's expression. Such elaboration helps facilitate development and tissue specification, and is also associated with unique disease states (*192*). In the eye, mouse *Mitf* isoforms are known to be differentially regulated during the formation of the RPE (*198*). We show here that expression of *MITF-A*, the second most abundant isoform in human melanocytes (Figure 4.2), is regulated by retinoids, transcriptional activators that have a prominent role in eye development (*227*). Retinoids can regulate alternative promoters. The *Stra6* gene contains two alternative promoters, with the intronic promoter containing a retinoic acid response element (RARE). Under excessive vitamin A levels, there is increased expression of *Stra6$_S$* from the intronic promoter (*228*). Similarly, it is conceivable that levels of retinoids may dictate *MITF* isoform expression within the RPE, as retinoids are known regulators of eye development.

Our group has shown that 9-*cis* retinoic acid and retinal stimulate melanogenesis in pigmented cell lines (*118*), while others have shown that retinal increases the sensitivity of melanocytes to UVA-induced pigment production (*229*). Based on the finding that 9-*cis* retinoic acid led to an upregulation in *MITF* expression (*118*), we identified a RARE binding motif in the human *MITF* promoter upstream of the 1A exon. Apart from the *MITF-M* promoter, the regulators

of other isoform-specific promoters are poorly understood (*117*). While it is possible that the RARE facilitates chromatin looping to regulate distant genes or additional *MITF* isoforms, we have shown this binding motif contributes to human *MITF-A* promoter activity (Figure 4.5). Consistent with this notion, retinoid receptors have also been linked to pigmentation. A germline mutation of RXRα in the $RXRa^{Pke}$ mouse results in premature greying starting when mice reach 5 weeks (*224*). $RXRa^{Pke}$ mice also experience alopecia and are hairless at 4 months (*224*), so the isolated effect of RXRα on melanocytes and pigmentation is still unknown. Conditional deletion of RXRα in keratinocytes causes a dilute coat color (*230*), suggesting that RXRα may regulate pigmentation in a melanocyte cell autonomous and non-autonomous manner. Taken together, these results indicate that deletion of MITF-A in melanocytes, like the RXRα knockout, only partially affects hair follicle pigmentation.

In humans, mutations in *MITF* have been linked to Waardenburg Syndrome, type 2A and Tietz Syndrome, disorders characterized by pigmentary defects including a white forelock and hearing loss (*102*, *231*). These mutations occur throughout the *MITF* gene, but are most common in the DNA binding domains (*232*) with some of the mutations recapitulated in mice (*102*). Similarly, mutations in humans associated with familial melanoma and predisposition to renal cell carcinoma (*197*, *232*) are also within the DNA binding domains. The characterized mouse mutations in *Mitf* only partially recapitulate pigmentary disorders, but cause a wide range of phenotypes including pigmentation defects, microphthalmia, hearing loss, changes in bone density, and deficiency in immune cells (*105*). The majority of mouse mutations occur in the DNA binding and dimerization domains that can alter all isoforms of MITF, which explains the wide range of tissues affected (*105*). Even mutations in the promoter regions have variable phenotypes. Both the $Mitf^{mi\text{-}vga9}$, a MITF null, and $Mitf^{mi\text{-}rw}$ mice, which has a deletion of multiple unique first

exons and promoter regions, have pigmentation and eye defects found only in homozygous mice (*233*, *234*). To distinguish the role of different isoforms, we generated *Mitf-A* and *Mitf-M* isoform-specific knockout mice. These unique specific isoform knockout reagents can be used to better delineate the function of individual isoforms, as described in this manuscript.

While *Mitf-A* was first thought to play an important role in the development of the RPE (*199*), similar to loss of *Mitf-D* and *-H* in the $Mitf^{mi\text{-}rw}$ mouse (*198*), we found that *Mitf-A* is not required for the development of the RPE (Figure 4.12). These results suggest that though *Mitf-A* plays a role in pigmentation of the hair and eye (Figures 4.6, 4.11-12), it is redundant in melanocytes and both the IPE and RPE cells. Lack of a phenotype in the RPE may be a result of compensation by additional *Mitf* isoforms, as was shown with loss of *Mitf-D* (*203*). Since *Mitf-A* is expressed in multiple tissues (*199*), the A isoform may have more specific roles in other organs like the kidney, where overexpression of *Mitf-A* caused an increase in size and nephron number while the deletion of the promoter and *Mitf-A* decreases the glomeruli number (*204*). In our study, we found no significant change in kidney mass in our *Mitf-A* knockout mice (Figure 4.6, 4.9). This difference in phenotype may be secondary to the deletion of almost 6,000bp that include exon 1A and the *Mitf-A* promoter in (*204*) as compared to the more specific deletion within the 1A exon presented in this study. Since the *Mitf* isoforms can be regulated by distant regulatory elements, large changes in the promoter regions may modulate the expression of multiple isoforms, as observed in mice with the $Mitf^{vga9}$ allele. In contrast, exon specific deletions could affect promoter regulation in cases where *Mitf* isoforms themselves differentially activate *Mitf* promoters. Future studies will address the broad impacts of loss of individual *Mitf* isoforms on the expression of other *Mitf* isoforms and *Mitf* target genes at different times during development.

The loss of *Mitf-M* results in the loss of melanocytes in the hair, skin, iris stroma, and choroid, but not the cells of the IPE and RPE (Figures 4.6, 4.11-12). This phenotype is similar to the phenotype of $Mitf^{mi\text{-}bw}$ mice, where a LINE1 element is inserted between the common exons 3 and 4 (*235*, *236*). While the $Mitf^{mi\text{-}bw}$ mice have loss of *Mitf-M* expression in the skin and eye, the LINE insertion also results in reduced expression and alternatively spliced transcripts of *Mitf-A* and *-H* (*235*). During embryonic development aberrant *Mitf-M* transcripts were also detected (*237*), indicating the $Mitf^{mi\text{-}bw}$ allele is not a clean knockout of the M isoform. *Mitf-M* heterozygotes have no pigment defects (Figure 4.6D-E), which suggests that one copy of *Mitf-M* is sufficient to maintain *Mitf-M* expression levels (Figure 4.11D). In this study, we have generated a specific *Mitf-M* knockout mouse and demonstrated that loss of *MITF-M* results in the loss of iris stromal and choroidal melanocytes. Our findings also demonstrate that while *Mitf-M* may be expressed in the adult RPE (*238*) and can rescue loss of pigmentation in $Mitf^{vga9}$ mice (*202*), it is not required for pigmentation of the RPE. Additionally, the loss of *Mitf-M* increased the size of the kidneys (Figure 4.6), indicating that loss of a single isoform affects distinct tissues differently, further highlighting the utility of the isoform specific knockout reagents generated in this study.

Recent studies in the eye have identified the *Crb1* mutant *rd8* allele present in the C57BL/6N mice as a cause of retinal degeneration (*239*, *240*). While the *rd8* allele is present in both of the knockout lines from the original C57BL/6NTac embryos, both lines were outcrossed to C57BL/6J to isolate individual CRISPR alleles. In the 50 mice from the *Mitf-M* line studied here, all were either wild type or heterozygous for the *rd8* allele at the *Crb1* locus (Figure 4.13J). Published studies have shown that *rd8* heterozygous mice show no signs of retinal degeneration as compared to *rd8* homozygous mice (*241*). In this study, eye phenotype comparisons were made between *Mitf-M* knockout mice and C57BL/6N mice, which are homozygous for the *rd8* allele.

While we cannot exclude that the *rd8* allele can influence the RPE phenotypes observed here, it is unlikely that our observed results are caused by an *rd8* mutation. Moreover, *Mitf-M* knockout mice not only have a pigment phenotype in the choroid but also in the iris stroma, further evidence that the phenotype observed here is independent of *rd8* mutation.

In summary, this study demonstrates that differential regulation of *MITF* isoforms plays a critical role in tissue development. *MITF-A* is regulated by retinoids, signaling molecules that are crucial in eye development, yet *Mitf-A* knockout mice have no eye phenotype although they have reduced MITF protein levels. These findings suggest that low levels of MITF are likely required for RPE pigmentation and *Mitf* isoforms play redundant roles in this process. In contrast, *Mitf-M* deletion results in the loss of melanocytes in both the skin and choroid, indicating that this isoform is necessary for melanocyte development in these tissues. This work provides a first glimpse at how two distinct *Mitf* isoforms regulate three distinct tissues and is another example of how protein isoforms can be differentially regulated in tissues, resulting in distinct developmental phenotypes that influence human disease.

ACKNOWLEDGEMENTS

We thank Kai-Xuan Shi and Shuling Wang of the UCI Transgenic Mouse Facility (TMF) for pronuclear injection and molecular analysis, respectively, for production of *Mitf-A* and *Mitf-M* CRISPR knockout mice. We thank Dr. Shigeki Shibahara for his kind gift of the *MITF-A* luciferase plasmid constructs and Feng Zhang for his kind gift of the pX330-U6-Chimeric_BB-CBh-hSpCas9 plasmid. We thank Sahil Telang and Madeline McCanne for assistance with luciferase assays and Yumay Chen for examining kidney histology. We thank Amber Habowski, Chi-Fen Chen, Jessica Shiu, and Klemens Hertel for advice on experimental design and editing

the manuscript. We thank the UCI Genomics High Throughput Facility (GHTF) for their help with Nanostring nCounter and RNA-sequencing. We thank the Institute for Immunology Flow Cytometry Core Facility (FCCF) for assistance with sorting cells using FACS. This work was supported by grants from the National Institutes of Health (R01AR063116, R01CA151513, U54-CA217378) to AKG. Research reported in this publication was supported by the National Cancer Institute of the National Institutes of Health Award Number T32CA009054-37 and an Anti-Cancer Challenge research grant from the University of California, Irvine Chao Family Comprehensive Cancer Center to JLF. The TMF, GHTF, and FCCF are Shared Resources funded in part by the Chao Family Comprehensive Cancer Center Support Grant (P30CA062203) from the National Cancer Institute and NIH shared instrumentation grants (1S10RR025496-01, 1S10OD010794-01, and 1S10OD021718-01). The content is solely the responsibility of the authors and does not necessarily represent the official views of the National Institutes of Health.

REFERENCES

16. J. Vachtenheim, L. Ondrusov, in *Recent Advances in the Biology, Therapy and Management of Melanoma* (InTech, 2013; http://www.intechopen.com/books/recent-advances-in-the-biology-therapy-and-management-of-melanoma/mitf-a-critical-transcription-factor-in-melanoma-transcriptional-regulatory-network).

17. K. Bharti, M. T. T. Nguyen, S. Skuntz, S. Bertuzzi, H. Arnheiter, The other pigment cell: Specification and development of the pigmented epithelium of the vertebrate eye. *Pigment Cell Res.* **19**, 380–394 (2006).

72. M. Bosenberg, V. Muthusamy, D. P. Curley, Z. Wang, C. Hobbs, B. Nelson, C. Nogueira, J. W. Horner, R. DePinho, L. Chin, Characterization of melanocyte-specific inducible Cre recombinase transgenic mice. *Genesis*. **44**, 262–7 (2006).

91. E. K. Paterson, T. J. Fielder, G. R. MacGregor, S. Ito, K. Wakamatsu, D. L. Gillen, V. Eby, R. E. Boissy, A. K. Ganesan, Tyrosinase depletion prevents the maturation of melanosomes in the mouse hair follicle. *PLoS One*. **10** (2015), doi:10.1371/journal.pone.0143702.

102. V. Pingault, D. Ente, F. Dastot-Le Moal, M. Goossens, S. Marlin, N. Bondurand, Review and update of mutations causing Waardenburg syndrome. *Hum. Mutat.* **31**, 391–406 (2010).

105. E. Steingrímsson, N. G. Copeland, N. A. Jenkins, Melanocytes and the Microphthalmia Transcription Factor Network. *Annu. Rev. Genet.* **38**, 365–411 (2004).

110. M. C. Liggins, J. L. Flesher, S. Jahid, P. Vasudeva, V. Eby, S. Takasuga, J. Sasaki, T. Sasaki, R. E. Boissy, A. K. Ganesan, PIKfyve regulates melanosome biogenesis. *PLoS Genet.* **14** (2018), doi:10.1371/journal.pgen.1007290.

117. E. Steingrímsson, All for one, one for all: alternative promoters and Mitf. *Pigment Cell Melanoma Res.* **21**, 412–414 (2008).

118. E. K. Paterson, H. Ho, R. Kapadia, A. K. Ganesan, 9-cis retinoic acid is the ALDH1A1 product that stimulates melanogenesis. *Exp. Dermatol.* **22**, 202–209 (2013).

152. L. S. Godwin, J. T. Castle, J. S. Kohli, P. S. Goff, C. J. Cairney, W. N. Keith, E. V. Sviderskaya, D. C. Bennett, *Curr. Protoc. Cell Biol.*, in press, doi:10.1002/0471143030.cb0108s63.

160. M. D. Muzumdar, B. Tasic, K. Miyamichi, N. Li, L. Luo, L. Li, L. Luo, A global double-fluorescent cre reporter mouse. *Genesis*. **45**, 593–605 (2007).

192. R. V. Davuluri, Y. Suzuki, S. Sugano, C. Plass, T. H.-M. Huang, The functional consequences of alternative promoter use in mammalian genomes. *Trends Genet.* **24**, 167–177 (2008).

193. W. Davis, R. M. Schultz, Developmental change in TATA-box utilization during preimplantation mouse development. *Dev. Biol.* **218**, 275–283 (2000).

194. J. R. Landry, D. L. Mager, B. T. Wilhelm, Complex controls: The role of alternative promoters in mammalian genomes. *Trends Genet.* **19**, 640–648 (2003).

195. S. Kim, S. S. A. An, Role of p53 isoforms and aggregations in cancer. *Med. (United States)*. **95**, e3993 (2016).

196. N. Arsic, G. Gadea, E. L. Lagerqvist, M. Bußon, N. Cahuzac, C. Brock, F. Hollande, V. Gire, J. Pannequin, P. Roux, The p53 isoform Δ133p53β promotes cancer stem cell potential. *Stem Cell Reports*. **4**, 531–540 (2015).

197. C. Bertolotto, F. Lesueur, S. Giuliano, T. Strub, M. De Lichy, K. Bille, P. Dessen, B. D'Hayer, H. Mohamdi, A. Remenieras, E. Maubec, A. De La Fouchardière, V. Molinié, P. Vabres, S. Dalle, N. Poulalhon, T. Martin-Denavit, L. Thomas, P. Andry-Benzaquen, N. Dupin, F. Boitier, A. Rossi, J. L. Perrot, B. Labeille, C. Robert, B. Escudier, O. Caron, L. Brugières, S. Saule, B. Gardie, S. Gad, S. Richard, J. Couturier, B. T. Teh, P. Ghiorzo, L. Pastorino, S. Puig, C. Badenas, H. Olsson, C. Ingvar, E. Rouleau, R. Lidereau, P. Bahadoran, P. Vielh, E. Corda, H. Blanché, D. Zelenika, P. Galan, F. Aubin, B. Bachollet, C. Becuwe, P. Berthet, Y. Jean Bignon, V. Bonadona, J. L. Bonafe, M. N. Bonnet-Dupeyron, F. Cambazard, J. Chevrant-Breton, I. Coupier, S. Dalac, L. Demange, M. D'Incan, C. Dugast, L. Faivre, L. Vincent-Fétita, M. Gauthier-Villars, B. Gilbert, F. Grange, J. J. Grob, P. Humbert, N. Janin, P. Joly, D. Kerob, C. Lasset, D. Leroux, J. Levang, J. M. Limacher, C. Livideanu, M. Longy, A. Lortholary, D. Stoppa-Lyonnet, S. Mansard, L. Mansuy, K. Marrou, C. Matéus, C. Maugard, N. Meyer, C. Nogues, P. Souteyrand, L. Venat-Bouvet, H. Zattara, V. Chaudru, G. M. Lenoir, M. Lathrop, I. Davidson, M. F. Avril, F. Demenais, R. Ballotti, B. Bressac-De Paillerets, A SUMOylation-defective MITF germline mutation predisposes to melanoma and renal carcinoma. *Nature*. **480**, 94–98 (2011).

198. K. Bharti, W. Liu, T. Csermely, S. Bertuzzi, H. Arnheiter, Alternative promoter use in eye development: The complex role and regulation of the transcription factor MITF. *Development*. **135**, 1169–1178 (2008).

199. S. Amae, N. Fuse, K. Yasumoto, S. Sato, I. Yajima, H. Yamamoto, T. Udono, Y. K. Durlu, M. Tamai, K. Takahashi, S. Shibahara, Identification of a novel isoform of microphthalmia-associated transcription factor that is enriched in retinal pigment epithelium. *Biochem. Biophys. Res. Commun.* **247**, 710–5 (1998).

200. V. Pogenberg, M. H. Ögmundsdóttir, K. Bergsteinsdóttir, A. Schepsky, B. Phung, V. Deineko, M. Milewski, E. Steingrímsson, M. Wilmanns, Restricted leucine zipper dimerization and specificity of DNA recognition of the melanocyte master regulator MITF. *Genes Dev.* **26**, 2647–2658 (2012).

201. C. Levy, M. Khaled, D. E. Fisher, MITF: master regulator of melanocyte development and melanoma oncogene. *Trends Mol. Med.* **12**, 406–414 (2006).

202. H. T. Michael, C. Graff-Cherry, S. Chin, C. Rauck, A. D. Habtemichael, P. Bunda, T. Smith, M. M. Campos, K. Bharti, H. Arnheiter, G. Merlino, C. P. Day, Partial rescue of ocular pigment cells and structure by inducible ectopic expression of Mitf-M in MITF-deficient mice. *Investig. Ophthalmol. Vis. Sci.* **59**, 6067–6073 (2018).

203. K. Bharti, M. Gasper, J. Ou, M. Brucato, K. Clore-Gronenborn, J. Pickel, H. Arnheiter, A regulatory loop involving PAX6, MITF, and WNT signaling controls retinal pigment epithelium development. *PLoS Genet.* **8**, e1002757 (2012).

204. A. Phelep, D. Laouari, K. Bharti, M. Burtin, S. Tammaccaro, S. Garbay, C. Nguyen, F.

Vasseur, T. Blanc, S. Berissi, F. Langa-Vives, E. Fischer, A. Druilhe, H. Arnheiter, G. Friedlander, M. Pontoglio, F. Terzi, MITF – A controls branching morphogenesis and nephron endowment. *PLoS Genet.* **13**, e1007093 (2017).

205. L. Cong, F. A. Ran, D. Cox, S. Lin, R. Barretto, Multiplex genome engineering using CRISPR/Cas systems. *Mult. genome Eng. using Cris. Syst.* **339**, 819–823 (2013).

206. C. Trapnell, L. Pachter, S. L. Salzberg, TopHat: Discovering splice junctions with RNA-Seq. *Bioinformatics*. **25**, 1105–1111 (2009).

207. C. Trapnell, D. G. Hendrickson, M. Sauvageau, L. Goff, J. L. Rinn, L. Pachter, Differential analysis of gene regulation at transcript resolution with RNA-seq. *Nat. Biotechnol.* **31**, 46–53 (2013).

208. M. I. Love, W. Huber, S. Anders, Moderated estimation of fold change and dispersion for RNA-seq data with DESeq2. *Genome Biol.* **15**, 550 (2014).

209. R. Edgar, M. Domrachev, A. E. Lash, Gene Expression Omnibus: NCBI gene expression and hybridization array data repository. *Nucleic Acids Res.* **30**, 207–210 (2002).

210. J. T. Robinson, H. Thorvaldsdóttir, W. Winckler, M. Guttman, E. S. Lander, G. Getz, J. P. Mesirov, Integrative genomics viewer. *Nat. Biotechnol.* **29**, 24–26 (2011).

211. H. Thorvaldsdóttir, J. T. Robinson, J. P. Mesirov, Integrative Genomics Viewer (IGV): High-performance genomics data visualization and exploration. *Brief. Bioinform.* **14**, 178–192 (2013).

212. K. D. Haltaufderhyde, E. Oancea, Genome-wide transcriptome analysis of human epidermal melanocytes. *Genomics*. **104**, 482–489 (2014).

213. T. Koressaar, M. Remm, Enhancements and modifications of primer design program Primer3. *Bioinformatics*. **23**, 1289–1291 (2007).

214. A. Untergasser, I. Cutcutache, T. Koressaar, J. Ye, B. C. Faircloth, M. Remm, S. G. Rozen, Primer3-new capabilities and interfaces. *Nucleic Acids Res.* **40**, e115 (2012).

215. K. Daily, V. R. Patel, P. Rigor, X. Xie, P. Baldi, MotifMap: Integrative genome-wide maps of regulatory motif sites for model species. *BMC Bioinformatics*. **12**, 495 (2011).

216. X. Xie, P. Rigor, P. Baldi, MotifMap: A human genome-wide map of candidate regulatory motif sites. *Bioinformatics*. **25**, 167–174 (2009).

217. T. Udono, K. I. Yasumoto, K. Takeda, S. Amae, K. I. Watanabe, H. Saito, N. Fuse, M. Tachibana, K. Takahashi, M. Tamai, S. Shibahara, Structural organization of the human microphthalmia-associated transcription factor gene containing four alternative promoters. *Biochim. Biophys. Acta - Gene Struct. Expr.* **1491**, 205–219 (2000).

218. M. L. Harris, T. D. Fufa, J. W. Palmer, S. S. Joshi, D. M. Larson, A. Incao, D. E. Gildea, N. S. Trivedi, A. N. Lee, C. P. Day, H. T. Michael, T. J. Hornyak, G. Merlino, W. J. Pavan, A direct link between MITF, innate immunity, and hair graying. *PLoS Biol.* **16**, e2003648 (2018).

219. A. A. Mills, B. Zheng, X. J. Wang, H. Vogel, D. R. Roop, A. Bradley, p63 is a p53 homologue required for limb and epidermal morphogenesis. *Nature*. **398**, 708–713 (1999).

220. A. Yang, R. Schweitzer, D. Sun, M. Kaghad, N. Walker, R. T. Bronson, C. Tabin, A.

Sharpe, D. Caput, C. Crum, F. McKeon, p63 is essential for regenerative proliferation in limb, craniofacial and epithelial development. *Nature*. **398**, 714–718 (1999).

221. H. Aoki, Y. Yamada, A. Hara, T. Kunisada, W. J. Pavan, H. Arnheiter, Two distinct types of mouse melanocyte: differential signaling requirement for the maintenance of non-cutaneous and dermal versus epidermal melanocytes. *Development*. **136**, 2511–21 (2009).

222. G. Allenby, M. T. Bocquel, M. Saunders, S. Kazmer, J. Speck, M. Rosenberger, A. Lovey, P. Kastner, J. F. Grippo, P. Chambon, A. A. Levin, Retinoic acid receptors and retinoid X receptors: Interactions with endogenous retinoic acids. *Proc. Natl. Acad. Sci. U. S. A.* **90**, 30–34 (1993).

223. J. Reichrath, T. Munssinger, A. Kerber, C. Rochette-Egly, P. Chambon, F. A. Bahmer, H. P. Baum, In situ detection of retinoid-X receptor expression in normal and psoriatic human skin. *Br. J. Dermatol.* **133**, 168–175 (1995).

224. X. Du, K. Tabeta, N. Mann, K. Crozat, S. Mudd, B. Beutler, An essential role for Rxr alpha in the development of Th2 responses. *Eur. J. Immunol.* **35**, 3414–23 (2005).

225. M. Reinisalo, J. Putula, E. Mannermaa, A. Urtti, P. Honkakoski, Regulation of the human tyrosinase gene in retinal pigment epithelium cells: The significance of transcription factor orthodenticle homeobox 2 and its polymorphic binding site. *Mol. Vis.* **18**, 38–54 (2012).

226. H. Grüneberg, The relations of microphthalmia and white in the mouse. *J. Genet.* **51**, 359–362 (1953).

227. J. K. McBee, K. Palczewski, W. Baehr, D. R. Pepperberg, Confronting complexity: The interlink of phototransduction and retinoid metabolism in the vertebrate retina. *Prog. Retin. Eye Res.* **20**, 469–529 (2001).

228. K. B. Laursen, V. Kashyap, J. Scandura, L. J. Gudas, An alternative retinoic acid-responsive Stra6 promoter regulated in response to retinol deficiency. *J. Biol. Chem.* **290**, 4356–4366 (2015).

229. N. L. Wicks, J. W. Chan, J. A. Najera, J. M. Ciriello, E. Oancea, UVA phototransduction drives early melanin synthesis in human melanocytes. *Curr. Biol.* **21**, 1906–11 (2011).

230. M. Li, H. Chiba, X. Warot, N. Messaddeq, C. Gérard, P. Chambon, D. Metzger, RXRα ablation in skin keratinocytes results in alopecia and epidermal alterations. *Development*. **128**, 675–688 (2001).

231. G. Wildhardt, B. Zirn, L. M. Graul-Neumann, J. Wechtenbruch, M. Suckfüll, A. Buske, A. Bohring, C. Kubisch, S. Vogt, G. Strobl-Wildemann, M. Greally, O. Bartsch, D. Steinberger, Spectrum of novel mutations found in waardenburg syndrome types 1 and 2: Implications for molecular genetic diagnostics. *BMJ Open*. **3**, e001917 (2013).

232. C. Grill, K. Bergsteinsdó ttir, M. H. Ögmundsdó ttir, V. Pogenberg, A. Schepsky, M. Wilmanns, V. Pingault, E. Steingrímsson, MITF mutations associated with pigment deficiency syndromes and melanoma have different effects on protein function. *Hum. Mol. Genet.* **22**, 4357–4367 (2013).

233. C. A. Hodgkinson, K. J. Moore, A. Nakayama, E. Steingrímsson, N. G. Copeland, N. A. Jenkins, H. Arnheiter, Mutations at the mouse microphthalmia locus are associated with defects in a gene encoding a novel basic-helix-loop-helix-zipper protein. *Cell*. **74**, 395–

404 (1993).

234. K. I. Watanabe, K. Takeda, K. I. Yasumoto, T. Udono, H. Saito, K. Ikeda, T. Takasaka, K. Takahashi, T. Kobayashi, M. Tachibana, S. Shibahara, Identification of a distal enhancer for the melanocyte-specific promoter of the MITF gene. *Pigment Cell Res.* **15**, 201–211 (2002).

235. I. Yajima, S. Sato, T. Kimura, K. I. Yasumoto, S. Shibahara, C. R. Goding, H. Yamamoto, An L1 element intronic insertion in the black-eyed white (Mitf(mi-bw)) gene: The loss of a single Mitf isoform responsible for the pigmentary defect and inner ear deafness. *Hum. Mol. Genet.* **8**, 1431–1441 (1999).

236. H. Hozumi, K. Takeda, Y. Yoshida-Amano, Y. Takemoto, R. Kusumi, U. Fukuzaki-Dohi, A. Higashitani, H. Yamamoto, S. Shibahara, Impaired development of melanoblasts in the black-eyed white Mitf mi-bw mouse, a model for auditory-pigmentary disorders. *Genes to Cells*. **17**, 494–508 (2012).

237. K. Takeda, H. Hozumi, K. Nakai, M. Yoshizawa, H. Satoh, H. Yamamoto, S. Shibahara, Insertion of long interspersed element-1 in the Mitf gene is associated with altered neurobehavior of the black-eyed white Mitfmi-bwmouse. *Genes to Cells*. **19**, 126–140 (2014).

238. J. Maruotti, T. Thein, D. J. Zack, N. Esumi, MITF-M, a “melanocyte-specific” isoform, is expressed in the adult retinal pigment epithelium. *Pigment Cell Melanoma Res.* **25**, 641–644 (2012).

239. B. A. Moore, M. J. Roux, L. Sebbag, A. Cooper, S. G. Edwards, B. C. Leonard, D. M. Imai, S. Griffey, L. Bower, D. Clary, K. C. K. Lloyd, Y. Hérault, S. M. Thomasy, C. J. Murphy, A. Moshiri, A population study of common ocular abnormalities in C57BL/6N rd8 mice. *Investig. Ophthalmol. Vis. Sci.* **59**, 2252–2261 (2018).

240. M. J. Mattapallil, E. F. Wawrousek, C. C. Chan, H. Zhao, J. Roychoudhury, T. A. Ferguson, R. R. Caspi, The Rd8 mutation of the Crb1 gene is present in vendor lines of C57BL/6N mice and embryonic stem cells, and confounds ocular induced mutant phenotypes. *Invest. Ophthalmol. Vis. Sci.* **53**, 2921–2927 (2012).

241. U. F. O. Luhmann, L. S. Carvalho, S. M. kleine Holthaus, J. A. Cowing, S. Greenaway, C. J. Chu, P. Herrmann, A. J. Smith, P. M. G. Munro, P. Potter, J. W. B. Bainbridge, R. R. Ali, The severity of retinal pathology in homozygous Crb1rd8/rd8 mice is dependent on additional genetic factors. *Hum. Mol. Genet.* **24**, 128–141 (2015).

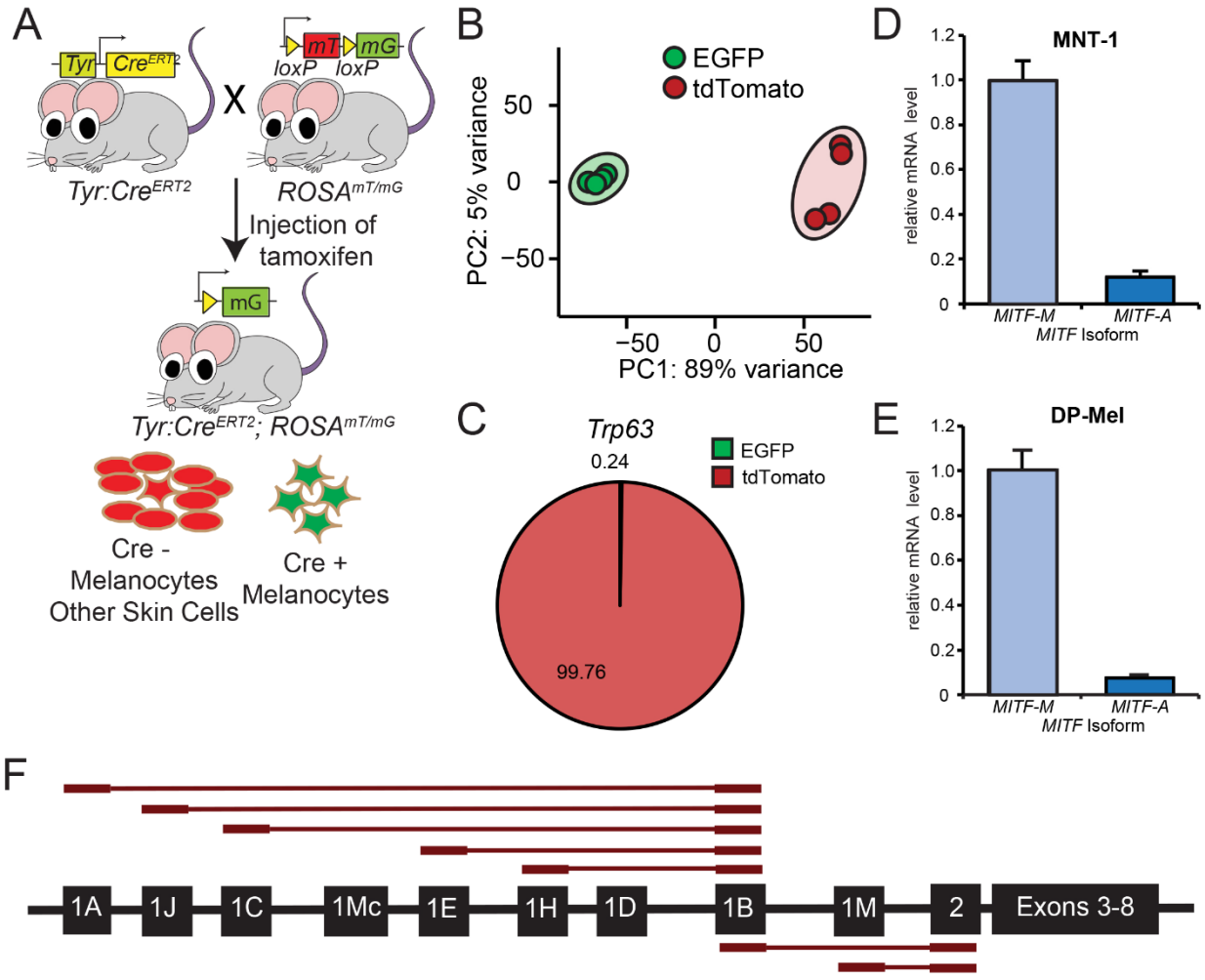
A
Tyr
Cre^ERT2
X
mT
mG
loxP
loxP
Tyr:Cre^ERT2
ROSA^mT/mG
Injection of
tamoxifen
mG
Tyr:Cre^ERT2; ROSA^mT/mG
Cre -
Melanocytes
Other Skin Cells
Cre +
Melanocytes
B
EGFP
tdTomato
PC2: 5% variance
50
0
−50
−50
0
50
PC1: 89% variance
C
Trp63
0.24
EGFP
tdTomato
99.76
D
MNT-1
relative mRNA level
1.2
1.0
0.8
0.6
0.4
0.2
0
MITF-M
MITF-A
MITF Isoform
E
DP-Mel
relative mRNA level
1.2
1.0
0.8
0.6
0.4
0.2
0
MITF-M
MITF-A
MITF Isoform
F
1A
1J
1C
1Mc
1E
1H
1D
1B
1M
2
Exons 3-8

Figure 4.1. Generation of *Tyr:Cre^{ERT2}, ROSA^{mTmG}* mice. (A) Cross to generate *Tyr:Cre^{ERT2}*, *ROSA^{mTmG}* double heterozygous mice. Mice were injected with tamoxifen once daily for 10 days to generate melanocyte specific EGFP expression. EGFP+ and tdTomato+ cells were sorted using FACS. (B) A Principal component analysis (PCA) plot of RNA-seq data that characterizes trends of the expression profiles of EGFP+ melanocytes (green) and all other skin cells that are tdTomato+ (red). (C) Expression of *Trp63* in EGFP+ and tdTomato+ cells of mouse skin. (D-E) RNA isolated from (D) MNT-1 human melanoma cells and (E) darkly-pigmented human epidermal melanocytes (DP-Mel) was analyzed using RT-qPCR with primers designed to target exon 1 of *MITF-A* and *MITF-M*, n=3. (F) Outline of read junctions used to determine *MITF* isoform abundance from human RNAseq data.

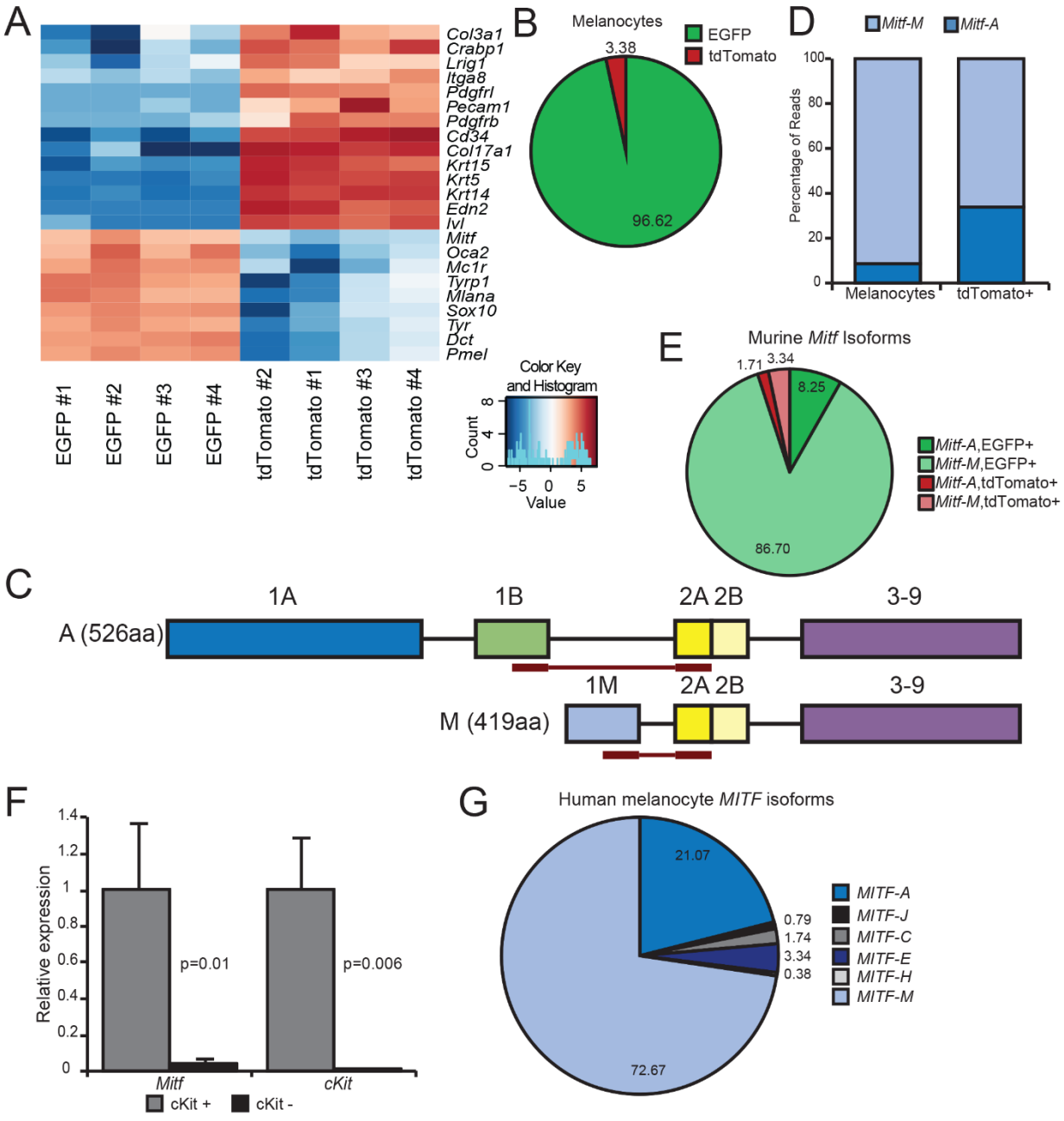
A
Col3a1
Crabp1
Lrig1
Itga8
Pdgfrl
Pecam1
Pdgfrb
Cd34
Col17a1
Krt15
Krt5
Krt14
Edn2
lvl
Mitf
Oca2
Mc1r
Tyrp1
Mlana
Sox10
Tyr
Dct
Pmel
EGFP #1
EGFP #2
EGFP #3
EGFP #4
tdTomato #2
tdTomato #1
tdTomato #3
tdTomato #4
Color Key and Histogram
Count
Value
B
Melanocytes
EGFP
tdTomato
3.38
96.62
D
Mitf-M
Mitf-A
Percentage of Reads
Melanocytes
tdTomato+
E
Murine Mitf Isoforms
1.71
3.34
8.25
86.70
Mitf-A,EGFP+
Mitf-M,EGFP+
Mitf-A,tdTomato+
Mitf-M,tdTomato+
C
1A
1B
2A 2B
3-9
A (526aa)
1M
M (419aa)
F
Relative expression
p=0.01
p=0.006
Mitf
cKit
cKit +
cKit -
G
Human melanocyte MITF isoforms
21.07
0.79
1.74
3.34
0.38
72.67
MITF-A
MITF-J
MITF-C
MITF-E
MITF-H
MITF-M

Figure 4.2. Melanocytes express multiple isoforms of *Mitf*. Cells were collected from *Tyr:Cre*^{ERT2}, *ROSA*^{mTmG} mice at P54 and sorted into EGFP+ and tdTomato+ populations using FACS. (A) Heatmap of RNA-seq gene expression for melanocyte-specific genes and other skin cell markers in EGFP+ and tdTomato+ cells. Transcripts range from those with high abundance (dark red) to those with low abundance (dark blue). (B) Melanocyte-specific gene expression in EGFP+ and tdTomato+ cells. (C) Schematic illustrating read junctions for *Mitf-A* and *Mitf-M*. (D) Relative distribution of *Mitf* isoforms in mouse EGFP+ melanocytes and tdTomato+ skin cell subpopulations. $n = 4$, $\chi^2 = 37663$, $p < 0.0001$. (E) Distribution of *Mitf* isoforms in melanocytes and other skin cell populations of the skin. (F) Relative *Mitf* expression of cKit positive and negative cells from neonatal epidermis sorted on microbeads. (G) *MITF* isoform relative abundance in human melanocytes.

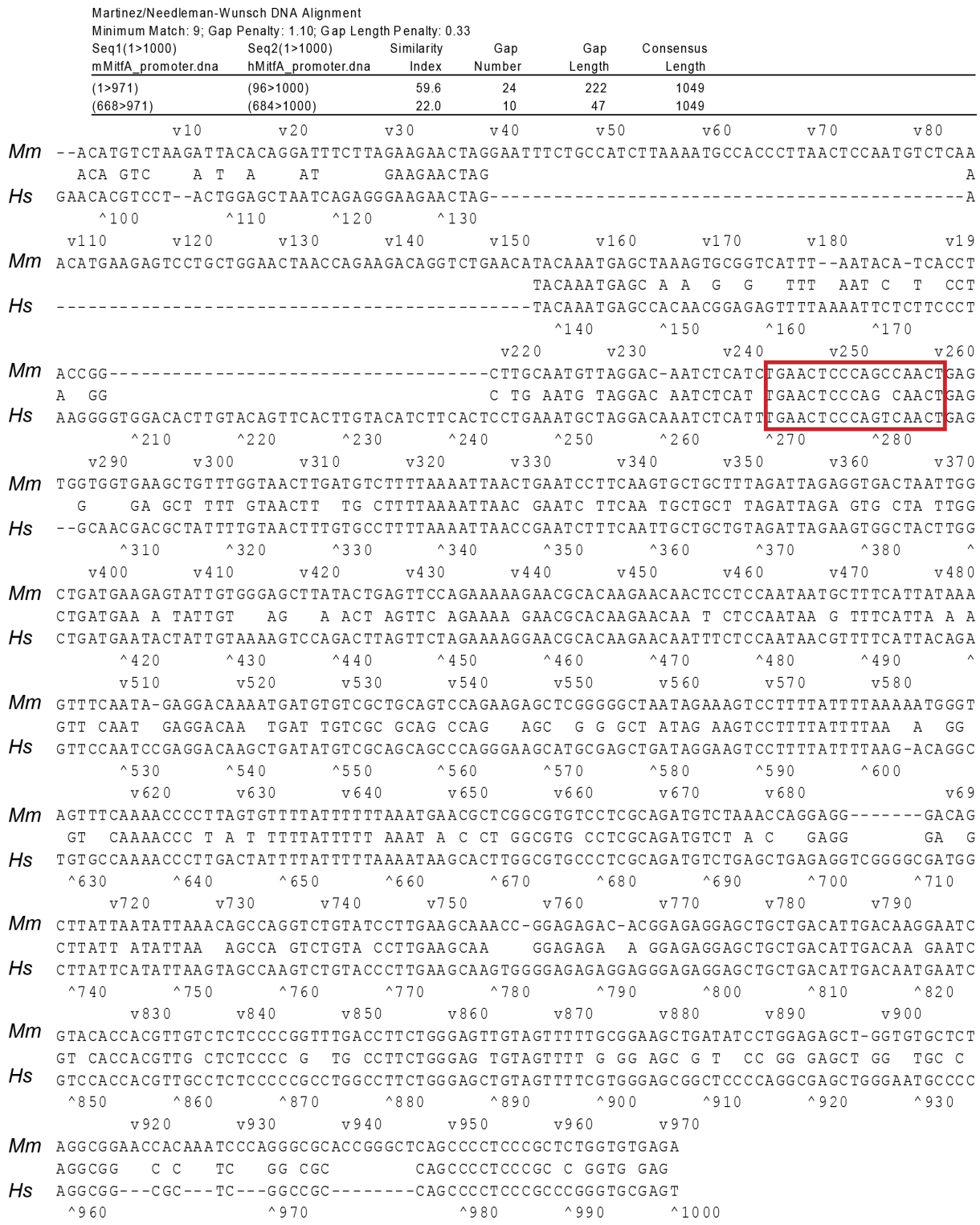
Martinez/Needleman-Wunsch DNA Alignment
Minimum Match: 9; Gap Penalty: 1.10; Gap Length Penalty: 0.33
Seq1(1>1000) mMitfA_promoter.dna
Seq2(1>1000) hMitfA_promoter.dna
Similarity Index
Gap Number
Gap Length
Consensus Length
(1>971) (96>1000) 59.6 24 222 1049
(668>971) (684>1000) 22.0 10 47 1049
Mm
Hs

Figure 4.3. RXR/RAR binding site is conserved between mouse and human. The human *MITF-A* promoter and the murine *Mitf-A* promoter were aligned using the first 1000bp upstream of the transcription start site for the A isoform. A red box indicates the conserved RXR/RAR putative binding site.

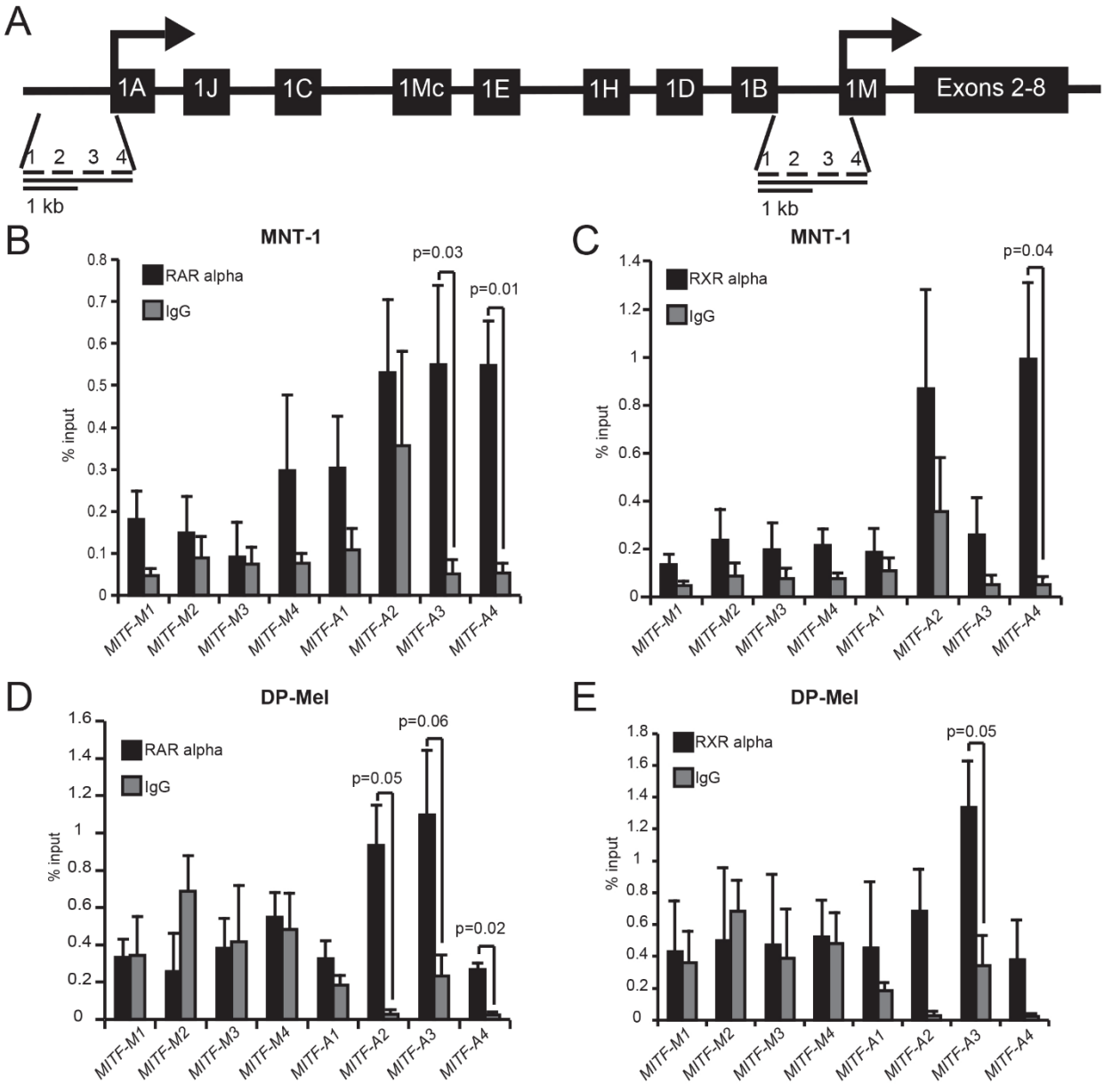
A
1A
1J
1C
1Mc
1E
1H
1D
1B
1M
Exons 2-8
1 2 3 4
1 kb
1 2 3 4
1 kb
B
MNT-1
RAR alpha
IgG
% input
p=0.03
p=0.01
MITF-M1
MITF-M2
MITF-M3
MITF-M4
MITF-A1
MITF-A2
MITF-A3
MITF-A4
C
MNT-1
RXR alpha
IgG
% input
p=0.04
D
DP-Mel
RAR alpha
IgG
% input
p=0.06
p=0.05
p=0.02
E
DP-Mel
RXR alpha
IgG
% input
p=0.05

Figure 4.4. RXR/RAR bind upstream of the human *MITF-A* promoter. (A) Tiled primers for ChIP analysis were designed to target the promoter region 2 kb upstream of the transcription start site for both *MITF-A* and *MITF-M* isoforms. (B-E) Enrichment of both (B,D) RARα and (C,E) RXRα in *MITF* promoter regions was investigated using ChIP RT-qPCR analysis in (B-C) MNT-1 cells and (D-E) darkly pigmented human melanocytes (DP-Mel), n=3.

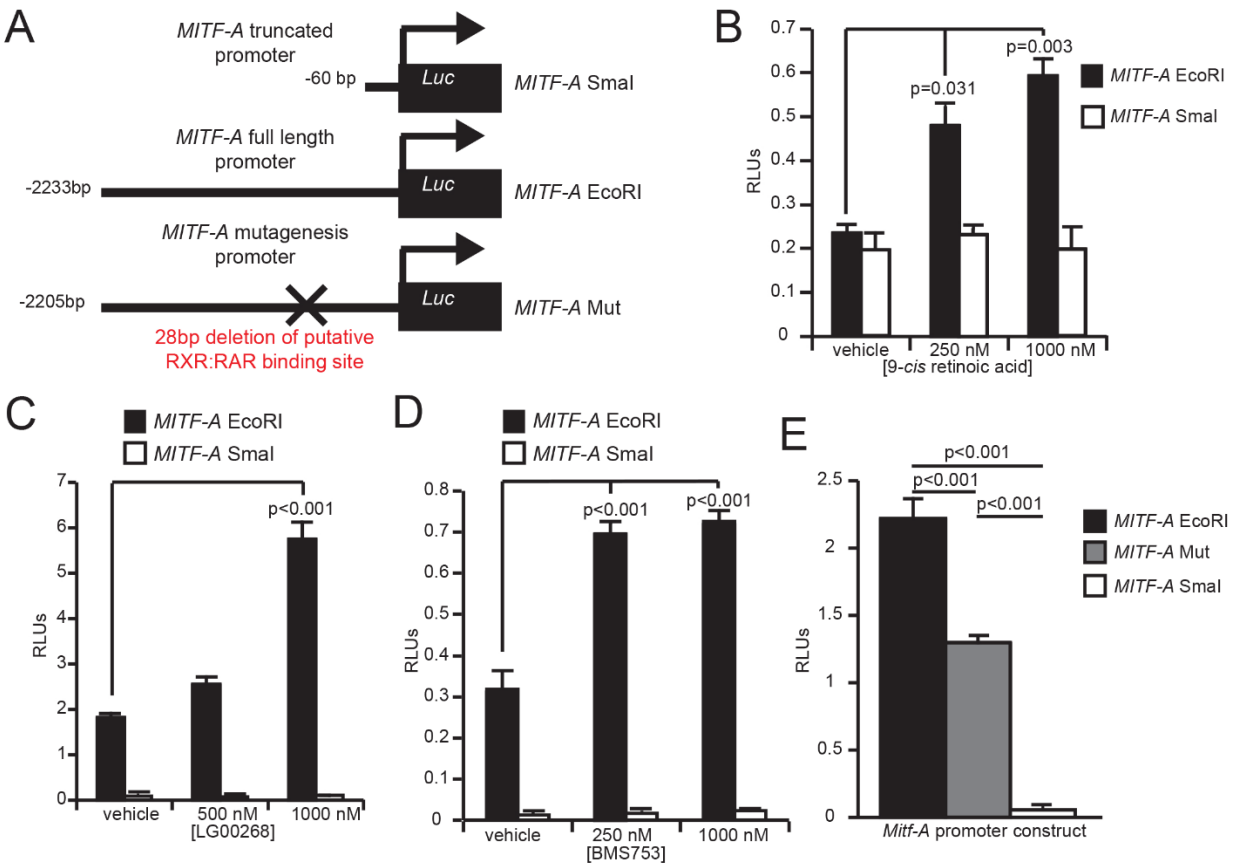
A
MITF-A truncated promoter
-60 bp
Luc
MITF-A SmaI
MITF-A full length promoter
-2233bp
Luc
MITF-A EcoRI
MITF-A mutagenesis promoter
-2205bp
Luc
MITF-A Mut
28bp deletion of putative RXR:RAR binding site
B
RLUs
p=0.031
p=0.003
MITF-A EcoRI
MITF-A SmaI
vehicle
250 nM
1000 nM
[9-cis retinoic acid]
C
MITF-A EcoRI
MITF-A SmaI
RLUs
p<0.001
vehicle
500 nM
1000 nM
[LG00268]
D
MITF-A EcoRI
MITF-A SmaI
RLUs
p<0.001
p<0.001
vehicle
250 nM
1000 nM
[BMS753]
E
p<0.001
p<0.001
p<0.001
RLUs
MITF-A EcoRI
MITF-A Mut
MITF-A SmaI
Mitf-A promoter construct

Figure 4.5. Retinoids stimulate the human *MITF-A* promoter through RXR/RAR binding site. (A) Schematic showing the size of *MITF-A* promoter upstream of the *luciferase* gene in the pGL3-*luciferase* plasmid constructs. (B-D) HEK293T cells were transfected with *MITF-A* promoter constructs and co-transfected with a Renilla luciferase reporter as an internal control. The cells were treated with the indicated dose of (B) 9-*cis* retinoic acid; (C) LG100268, a RXR agonist; and (D) BMS753, a RARα-specific agonist. (E) HEK293T cells were transfected with promoter constructs including a mutant *MITF-A* promoter lacking the putative RXR/RAR binding site. n=3.

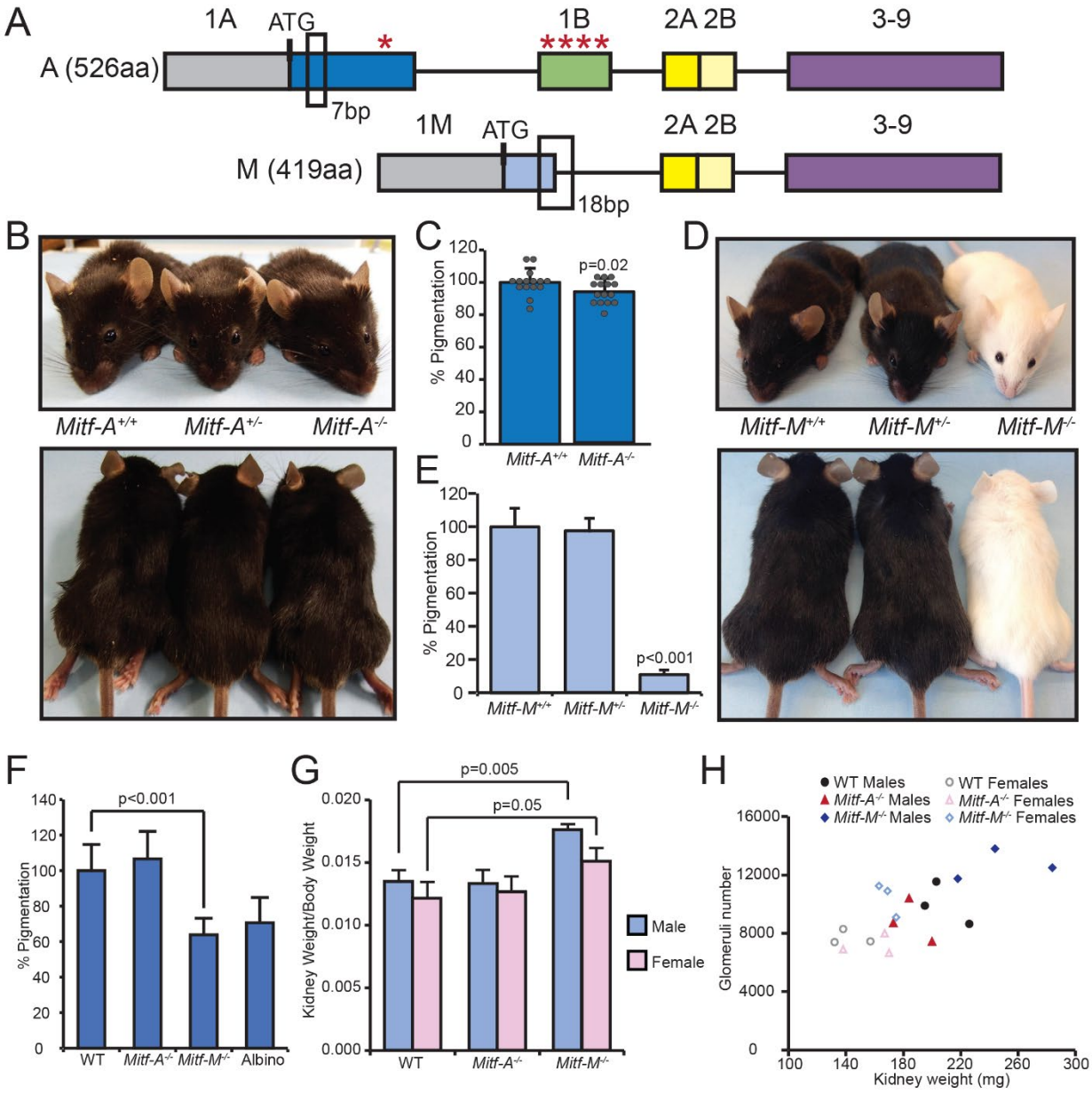
A
1A
ATG
1B
2A 2B
3-9
A (526aa)
7bp
1M
ATG
2A 2B
3-9
M (419aa)
18bp
B
Mitf-A+/+
Mitf-A+/-
Mitf-A-/-
C
% Pigmentation
p=0.02
Mitf-A+/+
Mitf-A-/-
D
Mitf-M+/+
Mitf-M+/-
Mitf-M-/-
E
% Pigmentation
p<0.001
Mitf-M+/+
Mitf-M+/-
Mitf-M-/-
F
% Pigmentation
p<0.001
WT
Mitf-A-/-
Mitf-M-/-
Albino
G
Kidney Weight/Body Weight
p=0.005
p=0.05
Male
Female
WT
Mitf-A-/-
Mitf-M-/-
H
WT Males
WT Females
Mitf-A-/- Males
Mitf-A-/- Females
Mitf-M-/- Males
Mitf-M-/- Females
Glomeruli number
Kidney weight (mg)

Figure 4.6. *Mitf-A* and *Mitf-M* isoform-specific mutant mice generated using CRISPR/Cas9 gene targeting platform. (A) Schematic of 7bp deletion in exon 1A for *Mitf-A* knockout mice and 18bp deletion in exon 1M and intron for *Mitf-M* knockout mice. Untranslated regions of exons 1A and 1M are grey, while coding regions are blue. Red asterisks denote premature stop codons in first 2 exons caused by 7bp deletion. (B) Wildtype and *Mitf-A* isoform specific knockout heterozygous and homozygous mice imaged at p50. (C) Melanin quantification of hair collected at p50 normalized to wildtype mice. n = 15. (D) Comparison of wildtype and *Mitf-M* isoform specific knockout heterozygous and homozygous mice imaged at p50. (E) Melanin quantification of hair collected at p50 normalized to wildtype mice. n = 10. (F) Melanin quantification on tail skin of wildtype, *Mitf-A*$^{-/-}$, *Mitf-M*$^{-/-}$, and B6 albino mice. (G) Quantification of total kidney mass to body mass for males and females of indicated genotypes, n = 3. (H) Scatterplot of glomeruli number and kidney weight for individual male (filled shapes) and female (open shapes) of wildtype (circles), *Mitf-A*$^{-/-}$ (triangles), and *Mitf-M*$^{-/-}$ (diamonds) mice.

A

Mitf-A CRISPR deletion

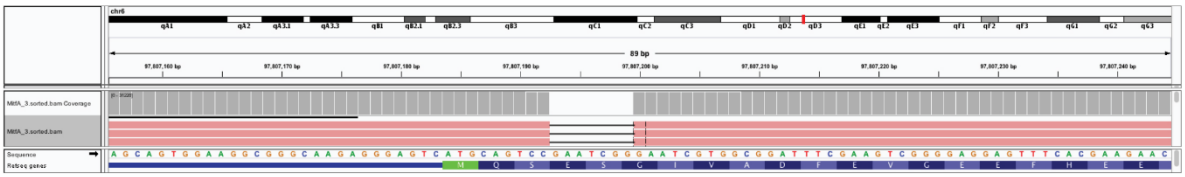

B

Mitf-A$^{+/+}$ 7bp deletion

Mitf-A$^{-/-}$ deletion

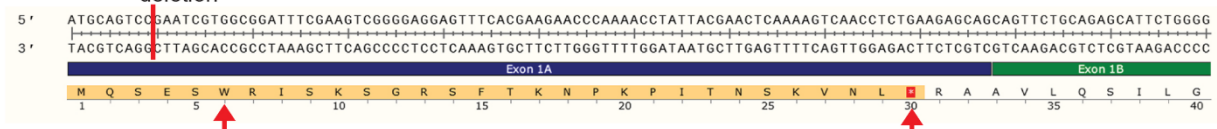

C

Mitf-M CRISPR deletion

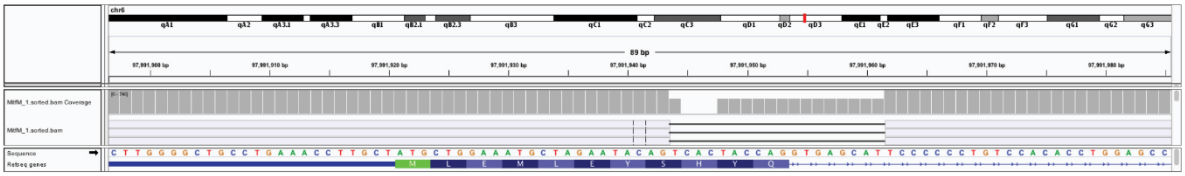

Figure 4.7. Validation of CRISPR/Cas9 knockout of *Mitf* isoforms. (A) IGV visualization of DNA sequencing results showing location of deletion in exon 1A of *Mitf* in *Mitf-A* knockout mice. (B) Comparison of wildtype and knockout *Mitf-A* DNA sequence and resulting amino acid sequence visualized in SnapGene Viewer. Seven-base pair deletion highlighted in wildtype sequence with red box and a red line marks the deletion in the knockout sequence. Red arrows indicate first change in amino acid sequence and the first premature stop codon resulting from CRISPR/Cas9 deletion. (C) Visualization of DNA sequencing results showing location of deletion spanning the splice site for exon 1M of *Mitf* in *Mitf-M* knockout mice.

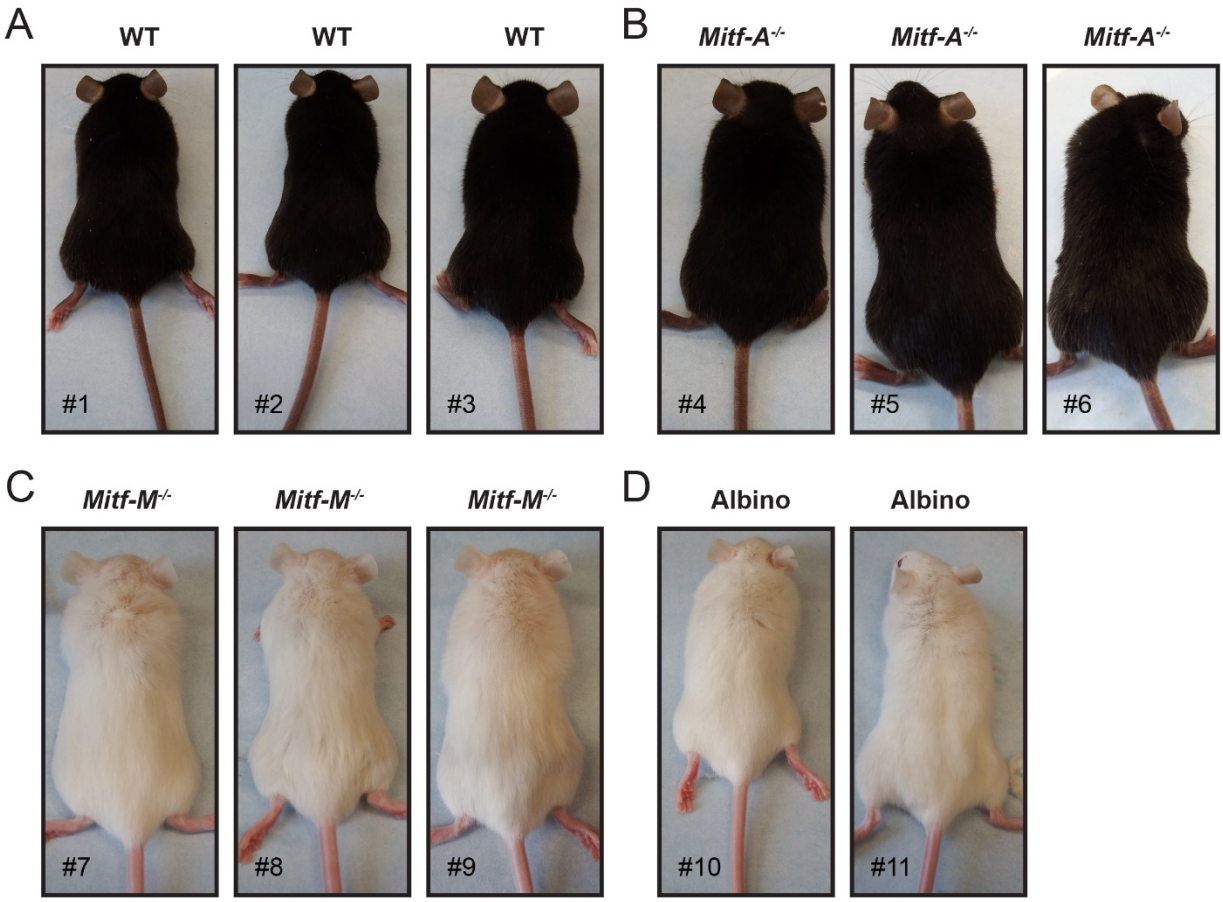
A
WT
WT
WT
#1
#2
#3
B
Mitf-A-/-
Mitf-A-/-
Mitf-A-/-
#4
#5
#6
C
Mitf-M-/-
Mitf-M-/-
Mitf-M-/-
#7
#8
#9
D
Albino
Albino
#10
#11

Figure 4.8. Consistent coat colors of *Mitf* isoform-specific knockout mice. (A-D) Images showing coat color of (A) *Mitf* wildtype mice, (B) *Mitf-A* knockout mice, (C) *Mitf-M* knockout mice, and (D) C57BL/6 albino mice. All mice were imaged on the same day for consistent lighting conditions and are within two weeks of age.

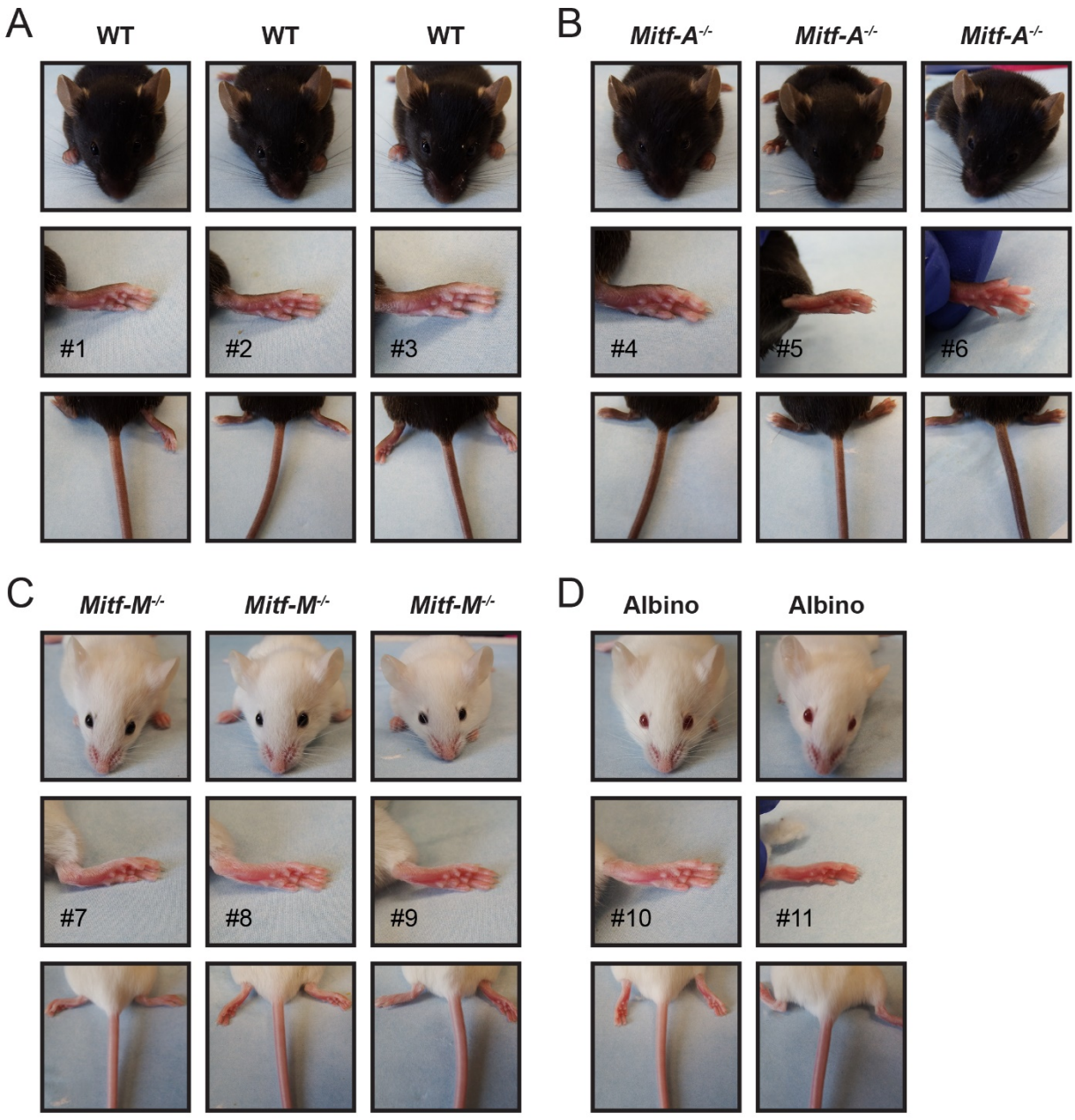
A
WT
WT
WT
#1
#2
#3
B
Mitf-A-/-
Mitf-A-/-
Mitf-A-/-
#4
#5
#6
C
Mitf-M-/-
Mitf-M-/-
Mitf-M-/-
#7
#8
#9
D
Albino
Albino
#10
#11

Figure 4.9. Loss of *Mitf-M* alters pigmentation of tails and paws. (A) Images of *Mitf* wildtype mice showing eyes, paws, and tail. (B) *Mitf-A* knockout mice illustrating eye, paw, and tail pigmentation. (C) Images of *Mitf-M* knockout mice showing loss of pigment in nose, paws, and tails, but retention in the eye. (D) C57BL/6 albino mice illustrating eye, paw, and tail pigmentation.

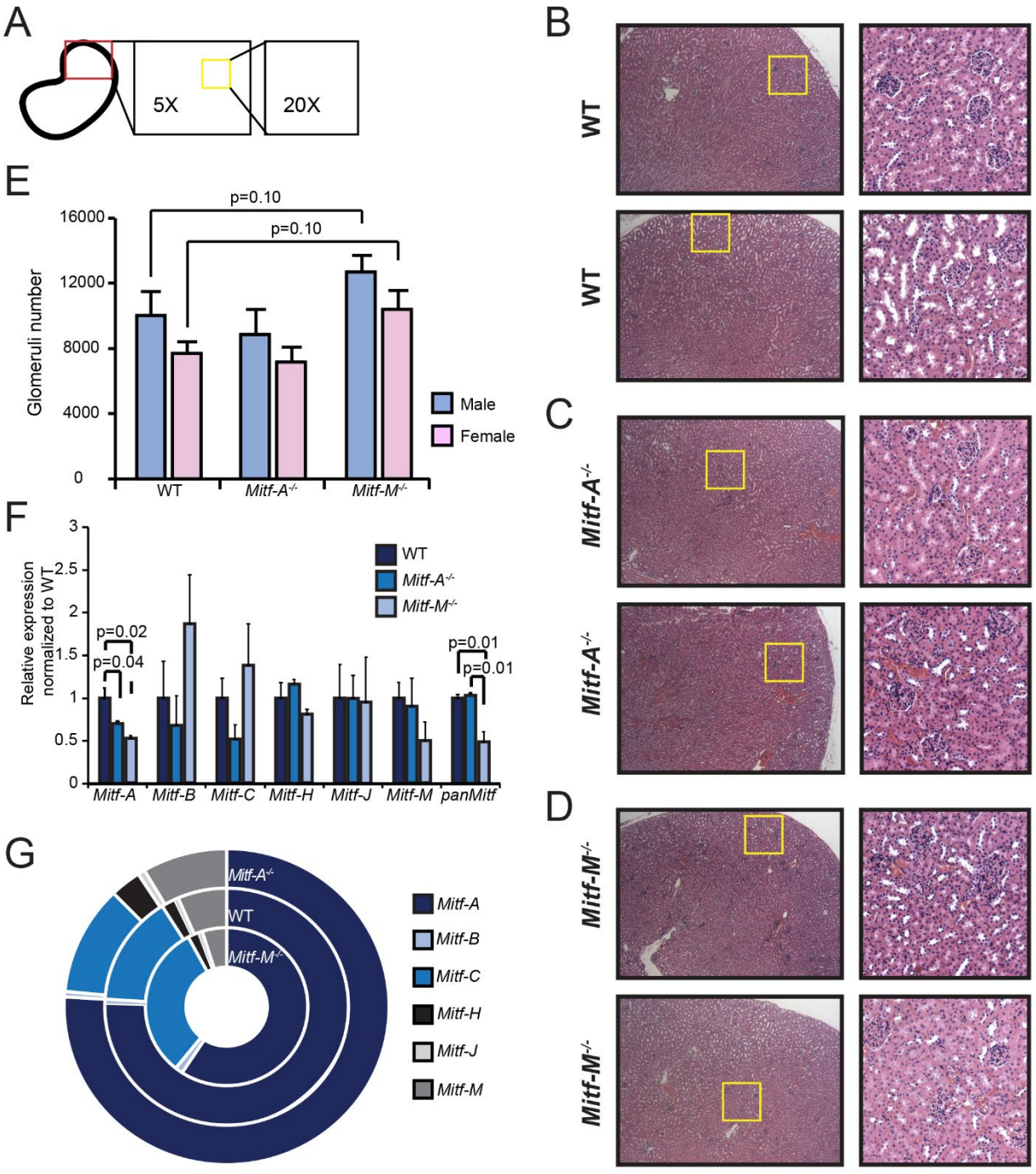
A
5X
20X
B
WT
WT
C
Mitf-A-/-
Mitf-A-/-
D
Mitf-M-/-
Mitf-M-/-
E
p=0.10
p=0.10
16000
12000
8000
4000
0
Glomeruli number
Male
Female
WT
Mitf-A-/-
Mitf-M-/-
F
3
2.5
2
1.5
1
0.5
0
Relative expression normalized to WT
WT
Mitf-A-/-
Mitf-M-/-
p=0.02
p=0.04
p=0.01
p=0.01
Mitf-A
Mitf-B
Mitf-C
Mitf-H
Mitf-J
Mitf-M
panMitf
G
Mitf-A-/-
WT
Mitf-M-/-
Mitf-A
Mitf-B
Mitf-C
Mitf-H
Mitf-J
Mitf-M

Figure 4.10. *Mitf* isoforms play overlapping roles in the kidney. (A) Diagram of kidney region depicted in H&E staining of kidneys at 5X and 20X magnification. (B) Representative images of kidney histology from wildtype mice at 5X magnification (left) and 20X magnification (right). (C) Kidney histology of *Mitf-A*$^{-/-}$ mice. (D) Representative kidney histology from *Mitf-M*$^{-/-}$ mice. (E) Quantification of glomeruli number for males and females of indicated genotypes, n = 3. (F) Relative expression of *Mitf* isoforms in kidneys of indicated mice normalized to wildtype mice. (G) Further comparison of *Mitf* isoform abundance in the kidneys of wildtype and *Mitf* knockout mice.

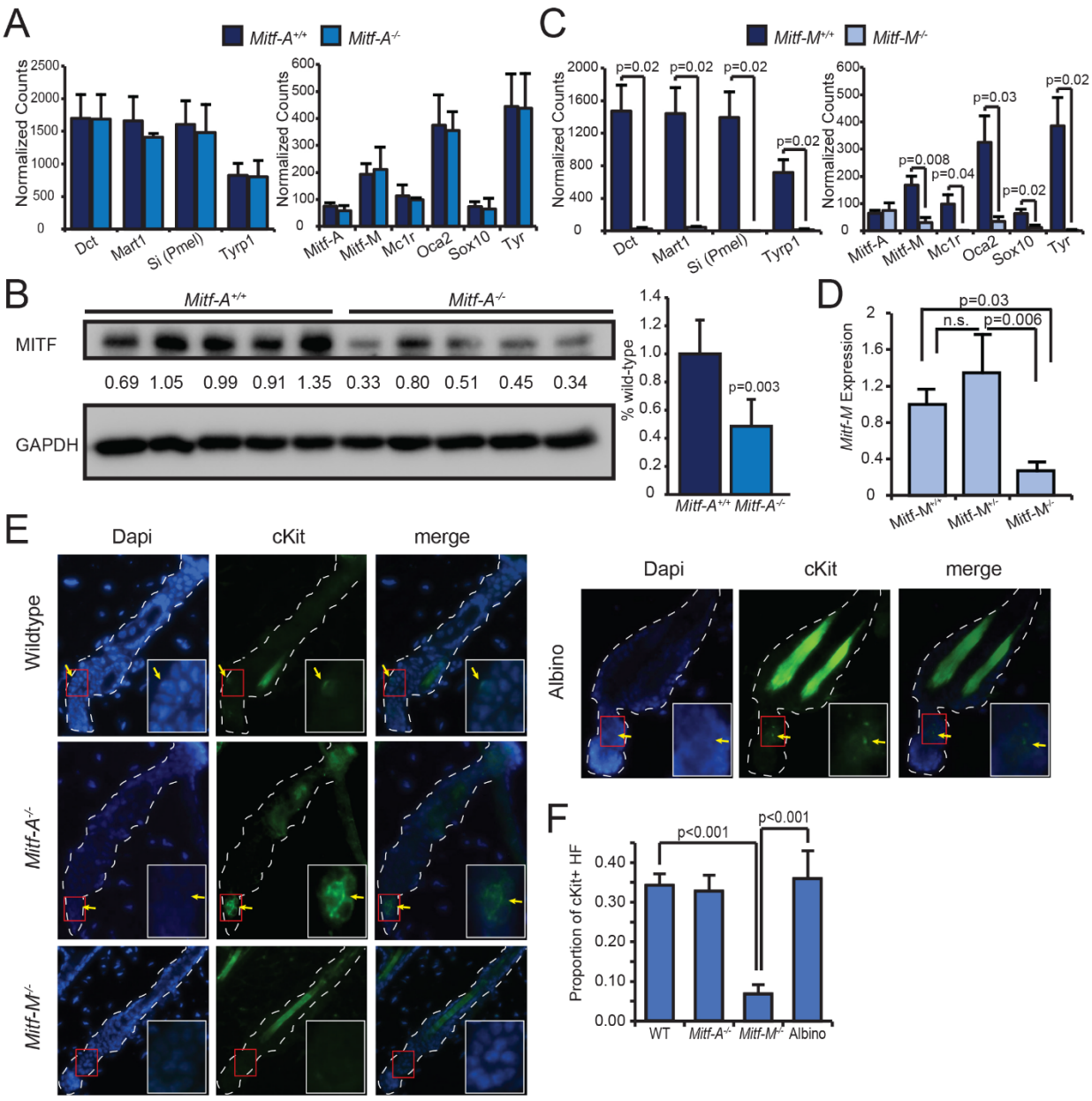
A
Mitf-A+/+
Mitf-A-/-
Normalized Counts
Dct
Mart1
Si (Pmel)
Tyrp1
Mitf-A
Mitf-M
Mc1r
Oca2
Sox10
Tyr
C
Mitf-M+/+
Mitf-M-/-
p=0.02
p=0.03
p=0.008
p=0.04
B
MITF
0.69 1.05 0.99 0.91 1.35 0.33 0.80 0.51 0.45 0.34
GAPDH
% wild-type
p=0.003
D
Mitf-M Expression
p=0.03
n.s.
p=0.006
E
Dapi
cKit
merge
Wildtype
Mitf-A-/-
Mitf-M-/-
Albino
F
Proportion of cKit+ HF
p<0.001
WT
Albino

Figure 4.11. *Mitf* isoform-specific knockout mice have distinct skin gene expression phenotypes. Skin was collected at P60 for RNA extraction after stimulating the hair cycle at P50. Purified RNA was subjected to Nanostring analysis on melanocyte specific genes. Data shown is mean normalized counts of mRNA for each gene in (A) *Mitf-A* knockout mice and (C) *Mitf-M* knockout mice compared to wildtype litter mates. Wildtype, *Mitf-M*$^{-/-}$ n = 3; *Mitf-A*$^{-/-}$ n=2. (B) Western blot for pan-Mitf on whole eye protein lysates from *Mitf-A*$^{+/+}$ and *Mitf-A*$^{-/-}$ mice. (D) Relative expression of *Mitf-M* in *Mitf-M* wildtype, heterozygous, and knockout mice. (E) cKit staining on indicated mouse skin collected at P56 with cKit positive melanocytes indicated by arrows and bounded by the red box, inset. (F) Quantification of cKit positive hair follicles (HF), n = 3.

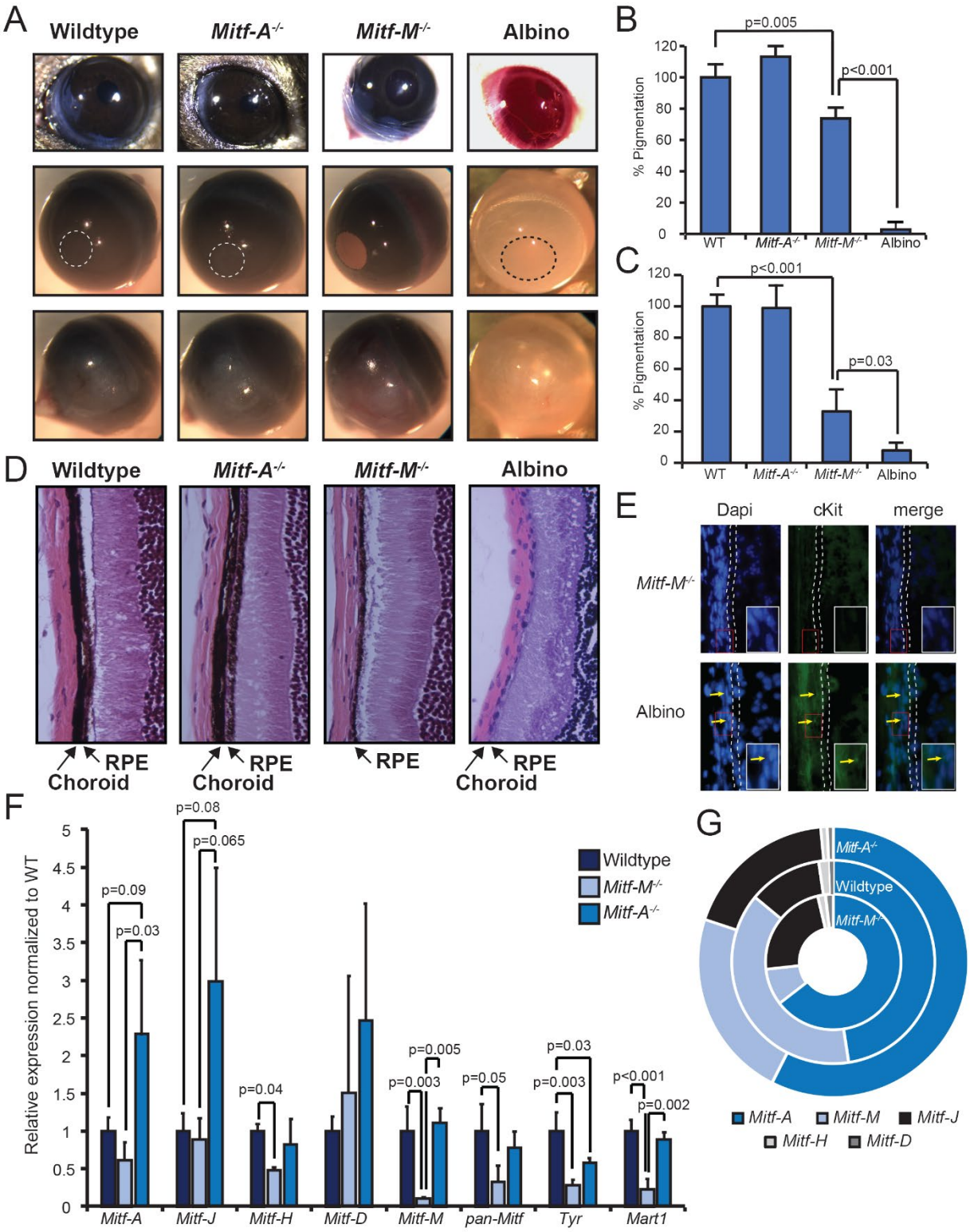
A
Wildtype
Mitf-A-/-
Mitf-M-/-
Albino
B
% Pigmentation
p=0.005
p<0.001
WT
Mitf-A-/-
Mitf-M-/-
Albino
C
% Pigmentation
p<0.001
p=0.03
WT
Mitf-A-/-
Mitf-M-/-
Albino
D
Wildtype
Mitf-A-/-
Mitf-M-/-
Albino
RPE
Choroid
E
Dapi
cKit
merge
Mitf-M-/-
Albino
F
Relative expression normalized to WT
Wildtype
Mitf-M-/-
Mitf-A-/-
p=0.09
p=0.03
p=0.08
p=0.065
p=0.04
p=0.005
p=0.003
p=0.05
p=0.03
p=0.003
p<0.001
p=0.002
Mitf-A
Mitf-J
Mitf-H
Mitf-D
Mitf-M
pan-Mitf
Tyr
Mart1
G
Mitf-A-/-
Wildtype
Mitf-M-/-
Mitf-A
Mitf-M
Mitf-J
Mitf-H
Mitf-D

Figure 4.12. *Mitf* isoform-specific knockout mice have distinct eye phenotypes. (A) Representative images of whole eyes of indicated mice before (top) and following enucleation of iris with pupil indicated (middle) and posterior surface of the eye (bottom). (B) Melanin quantification on dissected iris of indicated mice, n=3. (C) Pigment assay on combined RPE, choroid, and sclera of wildtype, *Mitf-A*$^{-/-}$, *Mitf-M*$^{-/-}$, and Albino mice, n = 4. (D) H&E sections from paraffin embedded eyes with choroid and RPE indicated by arrows. (E) cKit staining of choroid, with RPE highlighted and cKit positive melanocytes indicated with arrows. The inset area is highlighted by the red box. (F) Relative expression of *Mitf* isoforms in the isolated RPE and choroid of wildtype and Mitf isoform-specific mutant mice, n = 3. (G) Further comparison of *Mitf* isoform abundance in the RPE and choroid of wildtype and *Mitf* knockout mice.

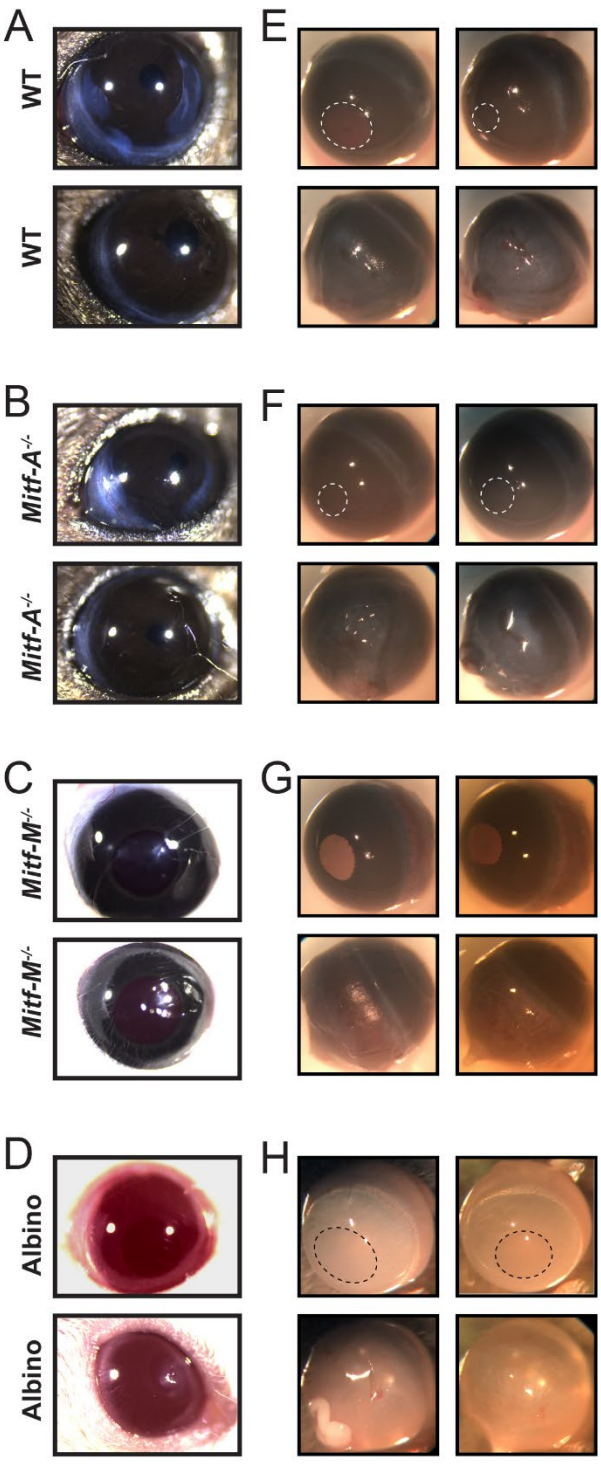

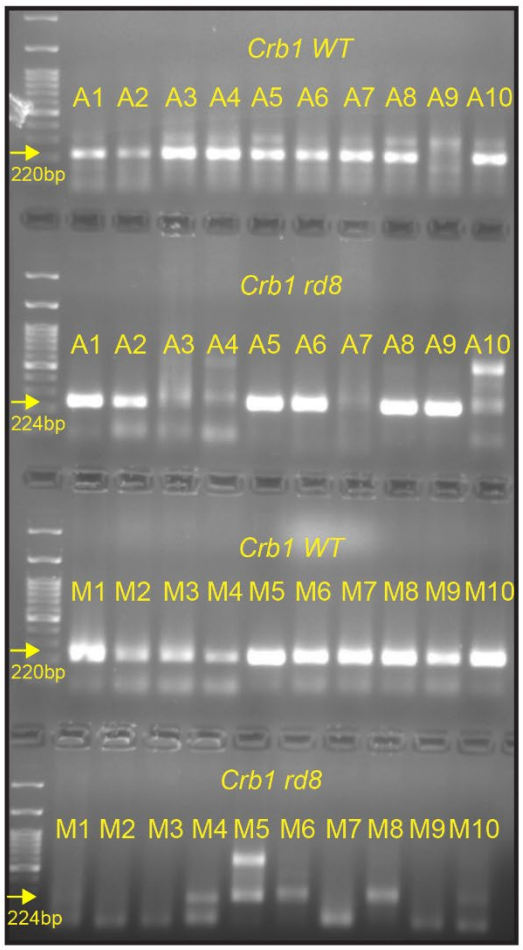

J

	Crb1$^{+/+}$	*Crb1*$^{+/rd8}$	*Crb1*$^{rd8/rd8}$
C57BL/6J	17	0	0
C57BL/6N	0	0	17
Mitf-A line	23	14	14
Mitf-M line	30	20	0

	Crb1 WT allele	*Crb1 rd8* allele
Mitf-A line	0.59	0.41
Mitf-M line	0.80	0.20

Figure 4.13. Loss of *Mitf-M* alters pigmentation of the eye. (A-D) Live animal images of eyes from (A) wildtype, (B) *Mitf-A*$^{-/-}$ mice, (C) *Mitf-M*$^{-/-}$ mice, and (D) albino mice. (E-H) Whole-eye images of iris with pupil indicated (upper) and posterior surface (lower) of (E) wild-type mice, (F) *Mitf-A* knockout mice, (G) *Mitf-M* knockout mice, and (H) albino mice that lack all pigmentation, with reduced pigmentation of the eye in (G). (I) Representative gel showing genotyping at *Crb1* gene for *rd8* allele for 10 mice in both the *Mitf-A* line and the *Mitf-M* line. Arrows denote expected size for wildtype (220bp) and *rd8* (224bp) alleles. (J) Genotyping results from 17 C57BL/6J, 17 C57BL/6N, 51 *Mitf-A* mice, and 50 *Mitf-M* mice. Allele frequencies of wildtype and *rd8 Crb1* alleles were calculated from genotyped mice.

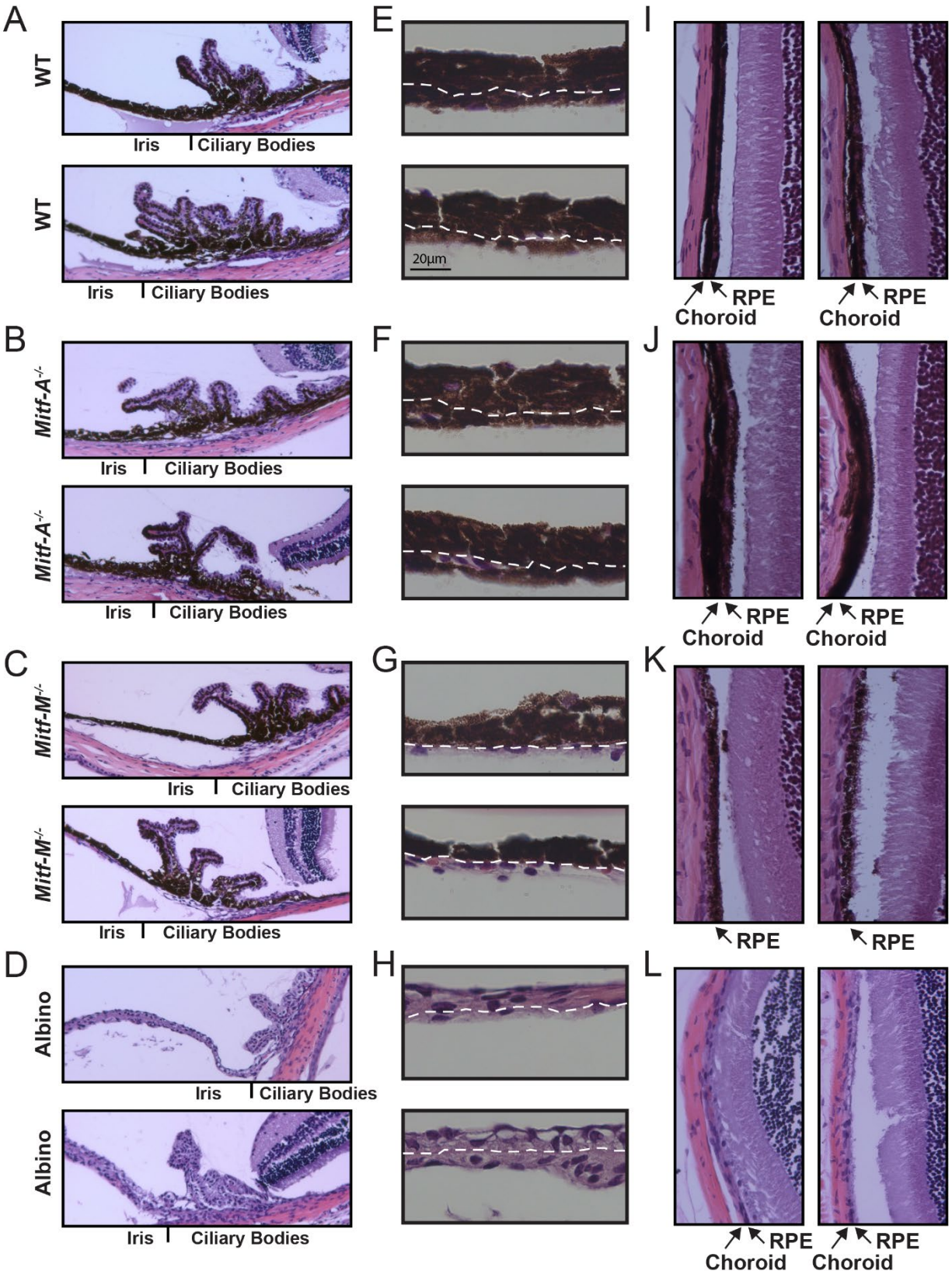
A
WT
Iris
Ciliary Bodies
WT
Iris
Ciliary Bodies
E
20μm
I
RPE
Choroid
RPE
Choroid
B
Mitf-A-/-
Iris
Ciliary Bodies
Mitf-A-/-
Iris
Ciliary Bodies
F
J
RPE
Choroid
RPE
Choroid
C
Mitf-M-/-
Iris
Ciliary Bodies
Mitf-M-/-
Iris
Ciliary Bodies
G
K
RPE
RPE
D
Albino
Iris
Ciliary Bodies
Albino
Iris
Ciliary Bodies
H
L
RPE
Choroid
RPE
Choroid

Figure 4.14. Depigmentation of iris stroma and choroid in *Mitf-M* knockout mice. (A-D) H&E staining focused on the iris and ciliary bodies collected at 20X of (A) wild-type, (B) *Mitf-A* knockout, (C) *Mitf-M* knockout, and (D) albino mice. (E-H) Iris histology showing iris pigment epithelium (above dashed line) and iris stroma (below line) at 63X magnification of (E) wild-type, (F) *Mitf-A*$^{-/-}$ mice, (G) *Mitf-M*$^{-/-}$ mice, and (H) albino mice. (I-L) H&E staining of retinal histology focusing on the choroid and RPE collected at 40X of (I) wild-type mice, (J) *Mitf-A* knockout mice, (K) *Mitf-M* knockout mice, and (L) albino mice.

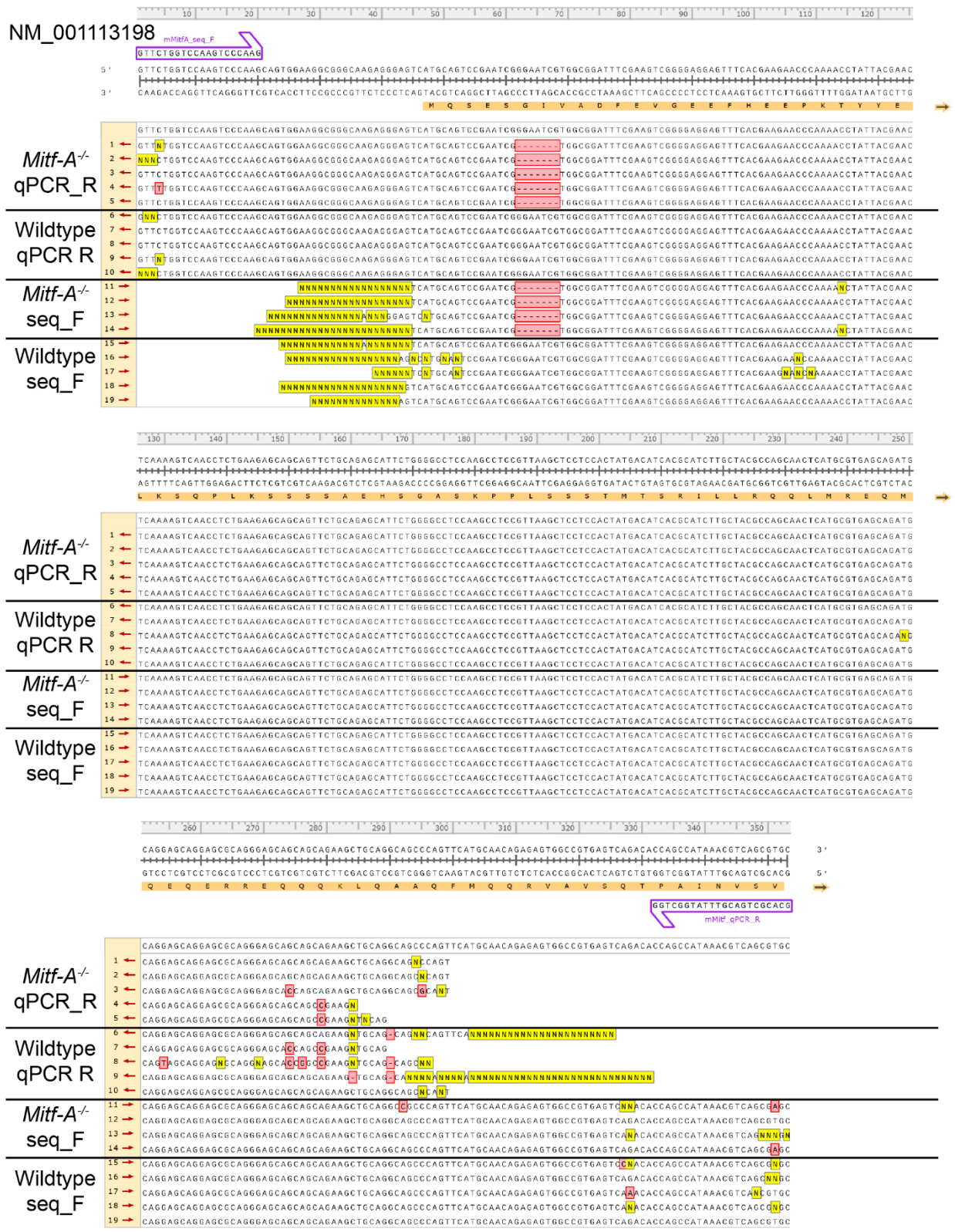
NM_001113198
mMitfA_seq_F
GTTCTGGTCCAAGTCCCAAG
Mitf-A-/- qPCR_R
Wildtype qPCR R
Mitf-A-/- seq_F
Wildtype seq_F
mMitf_qPCR_R
GGTCGGTATTTGCAGTCGCACG

Figure 4.15. *Mitf-A* transcripts from *Mitf-A* knockout mice retain deletion. Alignment of Sanger sequencing reads from wild-type and *Mitf-A* knockout mice following amplification. Protein sequence is highlighted in orange under NM_001113198 sequence, with the 7bp deletion highlighted in red.

Table 4.1. Panel of skin cell markers. RNAseq expression for melanocyte, keratinocyte, fibroblast, and endothelial cell markers.

Genomic Assembly: mm10

	gene	baseMean	log2FoldChange	lfcSE	stat	pvalue	padj	G_r1.counts	G_r2.counts	G_r3.counts	G_r4.counts	R_r1.counts	R_r2.counts	R_r3.counts	R_r4.counts
4288	Cd34	1286.485668	-9.512394703	0.56576172	-16.813429	1.95E-63	6.02E-61	0.8317165	5.7[illegible]5818	0.8389407	5.38889386	1763.51764	1651.389921	3060.4688	3803.7448
5051	Col17a1	3133.467374	-8.495453819	0.74918332	-11.33962	8.35E-30	6.01E-28	1.663433	1.9[illegible]5273	8.3894074	44.1889296	6558.17293	7843.031648	4691.49709	5918.894
5065	Col3a1	388.7605229	-4.515200866	1.28083832	-3.5251919	0.0004232	0.0019995	70.6959025	15.212218	1.6778815	0	1870.13074	592.3308706	313.377345	246.65922
5228	Crabp1	561.6892944	-6.679708315	0.70594219	-9.462118	3.02E-21	1.19E-19	23.288062	8.5568727	5.0336444	0	858.773428	1308.837129	502.136798	1786.8884
5841	Dct	143254.0727	5.026554372	0.63134168	7.96170213	1.70E-15	4.06E-14	282004.292	345156.67	238190.38	249432.497	2732.81658	1270.299939	10214.0856	17031.541
6570	Edn2	219.2208838	-10.8140398	1.32157517	-8.1826899	2.78E-16	7.23E-15	0	0	0	0	531.109307	663.6960358	248.319475	310.64225
10916	Itga8	14.93665687	-5.521543464	1.07867802	-5.118806	3.07E-07	2.75E-06	0.8317165	0	0.8389407	0	16.6277315	32.82797596	21.0750846	47.291806
10961	Ivl	179.8421232	-9.063974287	0.8771811	-10.333071	4.99E-25	2.55E-23	0	0	1.6778815	0	357.985279	436.7548106	256.566247	385.75277
11434	Krt14	62653.41167	-8.930936466	0.23984934	-37.23561	1.81E-303	2.80E-299	202.938826	232.93709	227.35294	340.578092	100890.228	136012.0136	136671.007	126650.24
11435	Krt15	22977.82548	-8.302540179	0.43613183	-19.036767	8.46E-81	4.36E-78	137.233223	161.62982	53.692207	189.689064	55518.0393	66438.11413	35613.2277	25710.978
11460	Krt5	22159.45669	-8.965211141	0.2660466	-33.697898	6.21E-249	4.80E-245	64.873887	112.19011	84.733014	82.9889654	42144.4527	57687.31759	35163.3205	41935.777
11909	Lrig1	404.2725857	-4.364412672	0.78094527	-5.5886281	2.29E-08	2.45E-07	30.7735105	79.864146	20.134578	2.15555754	1125.79523	1387.33881	291.385952	296.7329
12364	Mc1r	493.981941	4.866961642	0.73086886	6.65914494	2.75E-11	4.26E-10	886.609789	888.964	708.06598	1351.53458	0.97810185	34.25527926	12.8283124	68.619483
13823	Mitf	2362.920238	4.196811926	0.37258263	11.2641106	1.97E-29	1.38E-27	3595.51043	3355.2449	3591.5053	7406.49572	133.999954	278.324144	247.403167	294.87832
13839	Mlana	10175.6298	4.522436903	0.73877332	6.1215488	9.27E-10	1.21E-08	12178.8247	12447.398	30003.038	23732.6886	144.759074	97.05662458	1011.60406	1789.6703
15174	Oca2	111.448578	5.660369961	0.72463664	7.81132182	5.66E-15	1.29E-13	116.44031	281.42604	104.86759	373.989234	0	2.854606605	3.6652321	8.3456128
16813	Pdgfrb	34.84477569	-7.229576149	1.2047922	-6.0006831	1.96E-09	2.45E-08	0	0.9507636	0	0	119.328426	12.84572972	73.304642	72.328644
16814	Pdgfrl	39.61715608	-8.654362634	1.43566429	-6.0281242	1.66E-09	2.08E-08	0	0	0	0	85.0948613	108.475051	74.22095	49.146386
16869	Pecam1	63.41392102	-7.892296169	1.26223193	-6.2526514	4.04E-10	5.50E-09	0.8317165	0	0	0	46.948889	19.98224624	385.765679	53.782838
17325	Pmel	51573.32419	4.612708381	0.67754451	6.80797837	9.90E-12	1.61E-10	91684.2684	105065.09	83757.326	117311.908	1104.27699	488.1377295	4046.41624	9129.1731
20565	Sox10	1253.897218	4.819420235	0.68553578	7.03015125	2.06E-12	3.66E-11	2245.63455	2453.921	2182.0849	2839.94706	34.2335649	4.281909908	129.199432	141.87542
22701	Tyr	13644.04075	4.488311682	0.61114638	7.34408624	2.07E-13	4.07E-12	24199.6233	21330.382	24467.707	34824.1099	469.48889	195.5405525	1169.20904	2496.2655
22704	Tyrp1	70780.2138	4.529546799	0.81215624	5.57718647	2.44E-08	2.60E-07	103447.235	89462.105	177752.25	175032.35	893.985094	265.4784143	6145.67793	13242.633

Table 4.2. Binding sites in *MITF-M* promoter. Putative binding sites located in the *MITF-M* promoter identified in MotifMap.

Transcript Accession # NM_00248 Genome Assembly: hg18

Location	+/-	BBLS	BLS	NLOD	Z-Score	FDR	Motif ID	TF Name	Gene	Distance (bp)	Region
chr3:70067507..70067514	+	1.684	2.089	1	4.054	0.074	0	MAFA	MITF	-933	Upstream
chr3:70067506..70067512	-	1.41	2.089	1	3.817	0.055	0	MAFB	MITF	-928	Upstream
chr3:70067895..70067902	+	1.931	2.612	1	3.81	0.035	0	ETS2	MITF	-545	Upstream
chr3:70067982..70068000	-	0.192	1.031	0.823	4.686	0.201	0.067494	GCNF	MITF	-440	Upstream
chr3:70068047..70068055	-	1.143	1.467	1	4.192	0.163	0.103395	STAT1	MITF	-385	Upstream
chr3:70068177..70068188	+	1.355	2.376	0.916	4.485	0.288	0	Pax	MITF	-263	Upstream
chr3:70068202..70068211	+	2.029	2.705	0.977	4.459	0.012	0	SF1	MITF	-238	Upstream
chr3:70068202..70068210	+	1.938	2.607	0.973	4.362	0.022	0	SF1	MITF	-238	Upstream
chr3:70068202..70068209	+	2.677	2.737	1	3.933	0.488	0.164887	NURR1	MITF	-238	Upstream
chr3:70068277..70068288	+	1.573	2.515	0.919	4.403	0.028	0.017217	CREB	MITF	-163	Upstream
chr3:70068279..70068288	+	2.139	2.737	0.968	4.596	0.014	0.005239	CREB, ATF	MITF	-161	Upstream
chr3:70068280..70068288	+	2.515	2.515	1	4.856	0.013	0	ATF2:c-Jun	MITF	-160	Upstream
chr3:70068280..70068288	+	2.515	2.515	1	4.782	0.035	0.015874	CREB	MITF	-160	Upstream
chr3:70068280..70068288	-	2.515	2.515	1	4.856	0.013	0	ATF2:c-Jun	MITF	-152	Upstream
chr3:70068280..70068288	-	2.515	2.515	1	4.782	0.035	0.015874	CREB	MITF	-152	Upstream
chr3:70068280..70068289	-	2.135	2.737	0.927	4.296	0.019	0.00943	CREB, ATF	MITF	-151	Upstream
chr3:70068379..70068396	+	0.925	2.312	0.908	4.662	0.195	0.126351	Octamer	MITF	-61	Upstream
chr3:70068379..70068395	+	0.526	2.312	0.842	4.447	0.12	0.054055	HOXA1	MITF	-61	Upstream
chr3:70068379..70068395	+	0.002	2.312	0.858	4.279	0.296	0.215901	Barhl-1	MITF	-61	Upstream
chr3:70068380..70068397	+	1.233	2.312	0.918	4.936	0.1	0.065	K-2b	MITF	-60	Upstream
chr3:70068380..70068397	+	1.316	2.312	0.934	4.73	0.084	0.032656	ALX-3	MITF	-60	Upstream
chr3:70068380..70068397	+	1.729	2.312	0.894	4.689	0	0	Lhx4	MITF	-60	Upstream
chr3:70068380..70068397	+	1.145	2.312	0.9	4.447	0.171	0.07348	LH-2	MITF	-60	Upstream
chr3:70068380..70068397	+	0.559	2.312	0.881	4.42	0.173	0.106641	Evx-1	MITF	-60	Upstream
chr3:70068380..70068397	+	0.043	2.312	0.857	4.319	0.17	0.14261	Pax-4	MITF	-60	Upstream
chr3:70068381..70068397	+	0.35	2.312	0.902	4.284	0.165	0.064201	Barx-2	MITF	-59	Upstream
chr3:70068381..70068397	+	0.002	2.312	0.882	4.278	0.202	0.101899	ipf1	MITF	-59	Upstream
chr3:70068382..70068396	+	1.735	2.737	0.908	4.759	0.083	0.054038	CHX10	MITF	-58	Upstream
chr3:70068384..70068394	-	0.835	2.312	0.965	4.437	0.082	0.001928	ipf1	MITF	-46	Upstream
chr3:70068379..70068395	-	0.338	2.312	0.877	4.444	0.233	0.156188	HOXA5	MITF	-45	Upstream
chr3:70068379..70068395	-	0.368	2.312	0.915	4.394	0.183	0.075767	Barx-2	MITF	-45	Upstream
chr3:70068379..70068395	-	0.077	2.312	0.851	4.343	0.29	0.206274	HoxA2	MITF	-45	Upstream
chr3:70068379..70068396	-	1.738	2.312	0.954	5.255	0	0	Lhx4	MITF	-44	Upstream
chr3:70068379..70068396	-	1.318	2.312	0.941	4.79	0.094	0.030396	ALX-3	MITF	-44	Upstream
chr3:70068379..70068396	-	1.158	2.312	0.932	4.736	0.207	0.080117	LH-2	MITF	-44	Upstream
chr3:70068379..70068396	-	0.767	2.312	0.889	4.657	0.107	0.053699	Gbx2	MITF	-44	Upstream
chr3:70068379..70068396	-	0.568	2.312	0.892	4.523	0.194	0.120386	Evx-1	MITF	-44	Upstream
chr3:70068379..70068396	-	0.364	2.312	0.874	4.47	0.23	0.151346	EMX2	MITF	-44	Upstream
chr3:70068379..70068396	-	0.211	2.312	0.849	4.422	0.236	0.038607	lhx6.1	MITF	-44	Upstream

chr3:70068379..70068396	-	0.284	2.312	0.893	4.395	0.148	0.099891	Shox2	MITF	-44	Upstream
chr3:70068379..70068396	-	0.043	2.312	0.857	4.314	0.166	0.139458	Pax-4	MITF	-44	Upstream
chr3:70068379..70068396	-	1.214	2.312	0.852	4.309	0.068	0.04563	K-2b	MITF	-44	Upstream
chr3:70068381..70068397	-	0.536	2.312	0.857	4.596	0.131	0.054031	HOXA1	MITF	-43	Upstream
chr3:70068380..70068397	-	0.111	2.312	0.881	4.34	0.247	0.166681	Esx1	MITF	-43	Upstream
chr3:70068383..70068397	-	0.162	2.312	0.91	4.337	0.178	0.127473	HOXA3	MITF	-43	Upstream
chr3:70068383..70068397	-	0.024	2.312	0.898	4.293	0.191	0.141397	Dlx-1	MITF	-43	Upstream
chr3:70068426..70068435	-	1.504	2.376	0.929	4.531	0.113	0.047217	ELK4	MITF	-5	Upstream
chr3:70069036..70069046	-	0.464	1.935	0.982	4.519	0.49	0.078064	Nkx2-2	MITF	606	Downstream
chr3:70069118..70069135	-	0.077	1.184	0.859	4.417	0.491	0.34801	Otx2	MITF	695	Downstream
chr3:70069426..70069443	+	0.129	1.137	0.871	4.43	0.221	0.138776	PMX2B	MITF	986	Downstream
chr3:70069426..70069442	+	0.309	1.621	0.893	4.404	0.172	0.094936	PMX2A	MITF	986	Downstream
chr3:70069427..70069444	+	0.271	1.071	0.869	4.428	0.157	0.134465	Pax-4	MITF	987	Downstream
chr3:70069427..70069444	+	0.222	1.796	0.872	4.408	0.165	0.115194	POU6F1	MITF	987	Downstream
chr3:70069427..70069444	+	0.133	1.399	0.883	4.303	0.14	0.098622	Shox2	MITF	987	Downstream
chr3:70069429..70069443	+	1.155	2.098	0.89	4.604	0.142	0.086475	CHX10	MITF	989	Downstream
chr3:70069427..70069441	-	1.147	2.098	0.851	4.27	0.103	0.071226	CHX10	MITF	1001	Downstream
chr3:70069426..70069443	-	0.121	1.251	0.869	4.502	0.396	0.311282	HOXC4	MITF	1003	Downstream
chr3:70069426..70069443	-	0.107	1.031	0.883	4.453	0.48	0.331461	HOXC5	MITF	1003	Downstream
chr3:70069426..70069443	-	0.122	1.39	0.858	4.343	0.229	0.179117	Alx-4	MITF	1003	Downstream

Table 4.3. Binding sites in *MITF-A* promoter. Putative binding sites located in the *MITF-A* promoter identified in MotifMap.

Transcript Accession # NM_198159 Genome Assembly: hg18

Location	+/-	BBLS	BLS	NLOD	Z-Score	FDR	Motif ID	TF Name	Gene	Distance (bp)	Region
chr3:69870544..69870561	-	0.242	1.57	0.857	4.316	0.193	0.017745	RXR::RAR_DR5	MITF	-714	Upstream
chr3:69870735..69870762	-	0.554	1.898	0.817	4.578	0.276	0.17229	GR	MITF	-513	Upstream
chr3:69870735..69870762	-	0.341	1.665	0.793	4.538	0.404	0.239734	PR	MITF	-513	Upstream
chr3:69870944..69870955	+	1.024	1.805	0.935	4.552	0.474	0.368917	AhR	MITF	-331	Upstream
chr3:69870946..69870955	+	1.117	1.805	0.949	4.353	0.41	0.269831	AhR, Arnt, HIF-1	MITF	-329	Upstream
chr3:69871055..69871062	+	1.868	2.591	1	4.241	0.365	0.176799	MZF1	MITF	-220	Upstream
chr3:69871080..69871086	+	2.591	2.591	1	3.817	0.026	0	MAFB	MITF	-195	Upstream
chr3:69871078..69871085	-	2.516	2.591	1	4.054	0.058	0	MAFA	MITF	-190	Upstream
chr3:69871127..69871138	-	1.241	2.794	0.878	4.39	0.116	0.070463	MYC::MAX	MITF	-137	Upstream
chr3:69871149..69871156	+	2.459	2.794	1	3.933	0.484	0.182584	NURR1	MITF	-126	Upstream
chr3:69871150..69871172	+	2.34	2.794	0.952	6.758	0	0	LM4_M2	MITF	-125	Upstream
chr3:69871144..69871165	-	0.601	2.154	0.89	4.818	0.038	0.007155	Staf	MITF	-110	Upstream
chr3:69871184..69871191	-	1.986	2.794	1	4.241	0.358	0.172302	MZF1	MITF	-84	Upstream
chr3:69871199..69871209	+	0.551	1.028	0.924	4.319	0.059	0	NF-kappaB	MITF	-76	Upstream
chr3:69871199..69871210	+	0.477	1.159	0.896	4.37	0.216	0.031858	NFKB1	MITF	-76	Upstream
chr3:69871199..69871209	-	0.45	1.159	0.897	4.416	0.074	0	NF-kappaB (p50)	MITF	-66	Upstream
chr3:69871200..69871210	-	0.555	1.028	0.936	4.412	0.052	0	NF-kappaB	MITF	-65	Upstream
chr3:69871200..69871210	-	0.759	1.296	0.975	4.72	0.052	0	REL	MITF	-65	Upstream
chr3:69871199..69871210	-	0.477	1.159	0.888	4.303	0.23	0.018875	NFKB1	MITF	-65	Upstream
chr3:69871200..69871210	-	0.763	1.296	0.975	4.714	0.338	0.057601	c-Rel	MITF	-65	Upstream
chr3:69871198..69871214	-	0.362	1.028	0.884	4.454	0.165	0.07197	NF-kappaB	MITF	-61	Upstream
chr3:69871219..69871241	-	1.417	2.794	0.843	5.562	0	0	LM4_M2	MITF	-34	Upstream
chr3:69871553..69871559	+	2.612	2.695	1	3.989	0.007	0	Neuro D	MITF	278	Downstream
chr3:69871547..69871558	-	1.716	2.391	0.957	4.454	0.08	0.008152	TGIF	MITF	283	Downstream
chr3:69871553..69871559	-	2.612	2.695	1	3.989	0.007	0	Neuro D	MITF	284	Downstream
chr3:69871546..69871562	-	0.054	2.019	0.871	4.321	0.161	0.048591	PKNOX2	MITF	287	Downstream
chr3:69871546..69871562	-	0.439	2.182	0.84	4.405	0.257	0.174713	TGIF2	MITF	287	Downstream
chr3:69871640..69871658	-	1.024	2.337	0.836	4.387	0.071	0.032818	ESR2	MITF	383	Downstream
chr3:69871641..69871661	-	0.869	2.486	0.792	4.39	0.064	0.010943	ESR1	MITF	386	Downstream
chr3:69871646..69871664	-	0.341	1.456	0.818	4.353	0.434	0.275125	MIF-1	MITF	389	Downstream
chr3:69871668..69871686	-	1.026	2.337	0.842	4.439	0.067	0.026511	ESR2	MITF	411	Downstream
chr3:69871813..69871823	+	1.128	2.106	0.989	4.563	0.009	0	TAL1	MITF	538	Downstream
chr3:69871813..69871822	+	1.335	1.485	1	4.335	0.014	0	AP-4	MITF	538	Downstream
chr3:69871813..69871821	+	1.455	1.688	1	4.607	0.016	0	HEB	MITF	538	Downstream
chr3:69871815..69871821	+	1.912	2.103	1	3.989	0.013	0	Neuro D	MITF	540	Downstream
chr3:69871815..69871821	-	1.912	2.103	1	3.989	0.013	0	Neuro D	MITF	546	Downstream
chr3:69871818..69871825	-	1.771	2.103	1	4.054	0.07	0	MAFA	MITF	550	Downstream
chr3:69871839..69871846	+	1.509	1.632	1	4.241	0.423	0.208925	MZF1	MITF	564	Downstream
chr3:69872140..69872149	+	1.524	1.844	1	4.003	0.074	0.019945	PUR1	MITF	865	Downstream

Table 4.4. List of primers for RT-qPCR and ChIP analysis. Primers designed for chromatin immunoprecipitation (ChIP) and reverse transcriptase-quantitative PCR (qPCR) in human cell lines and mouse tissues.

Primer	Species	Application	Sequence 5' to 3'
MITF-A1 Forward	Human	ChIP	AAACTTCTGGTGAGCCCAAA
MITF-A1 Reverse	Human	ChIP	TGCTTGGAATATGGGAGGAG
MITF-A2 Forward	Human	ChIP	TGAAAGGCCAAACACCAAA
MITF-A2 Reverse	Human	ChIP	AGCCTCCATTTCTTCATCCA
MITF-A3 Forward	Human	ChIP	GGAACACGTCCTACTGGAGCTA
MITF-A3 Reverse	Human	ChIP	ATAGCGTCGTTGCTCTCTGC
MITF-A4 Forward	Human	ChIP	CATGCGAGCTGATAGGAAGTC
MITF-A4 Reverse	Human	ChIP	CCGCTAGTGCAACTCCTGTT
MITF-M1 Forward	Human	ChIP	ATTCCCACATGGCCACAATC
MITF-M1 Reverse	Human	ChIP	CACTACTGACCTCTGTGGCA
MITF-M2 Forward	Human	ChIP	TGGGTTAGAAACAGCTGGAGA
MITF-M2 Reverse	Human	ChIP	GCTTTCTATGTGGCACTGTCA
MITF-M3 Forward	Human	ChIP	TCCTGGGCATTAGACAACAT
MITF-M3 Reverse	Human	ChIP	ACTTATATTCTGGGGTGAGGCA
MITF-M4 Forward	Human	ChIP	AGGATGCAAGAAGAGGCTGT
MITF-M4 Reverse	Human	ChIP	CCGAATAACTGCCACTTCCG
GAPDH Forward	Human	qPCR	CCAACGTGTCAGTGGTGGA
GAPDH Reverse	Human	qPCR	CGTCAAAGGTGGAGGAGTGG
MITF Exon 1A Forward	Human	qPCR	CGGGCTCTGTTCTCACTTTC
MITF Exon 1A Reverse	Human	qPCR	TGAAACTCCTCCCCGACTTC
MITF Exon 1M Forward	Human	qPCR	ACCTTCTCTTTGCCAGTCCA
MITF Exon 1M Reverse	Human	qPCR	CCAATCCAGTGAGAGACGGT
β-actin Forward	Human	qPCR	GGGAAATCGTGCGTGACATT
β-actin Reverse	Human	qPCR	AAGGAAGGCTGGAAGAGTGC
Hprt Forward	Mouse	qPCR	GCGATGATGAACCAGGTTATGA
Hprt Reverse	Mouse	qPCR	TCCAAATCCTCGGCATAATGA
Mitf Exon 1 Reverse	Mouse	qPCR	GCACGCTGACGTTTATGGCTGG
Mitf Exon 1A Forward	Mouse	qPCR	GCGGATTTCGAAGTCGGGGAGG
Mitf Exon 1D Forward	Mouse	qPCR	GTTGGGACCTGACAGGCTCTGAATACAG
Mitf Exon 1H Forward	Mouse	qPCR	GGGCTTGCAGAACACCTTAAAGG
Mitf Exon 1J Forward	Mouse	qPCR	TCTCGCCGTGTCTCTGGGCATC
Mitf Exon 1M Forward	Mouse	qPCR	TATGGTGCCTTCTTTATGCC
Mitf Exon 1M Reverse	Mouse	qPCR	AGCATAGCAAGGTTTCAGG
panMitf Forward	Mouse	qPCR	CGTGTATTTTTCCCACAGAGTC
panMitf Reverse	Mouse	qPCR	GCTCCTTAATGCGGTCGTTTA
Mitf Exon 1A Seq Forward	Mouse	Sequencing validation	GTTCTGGTCCAAGTCCCAAG

qPCR conditions		
Denaturation	95°C	5 min
Amplification (40 cycles)	95°C	30 sec
	60°C	30 sec
	72°C	1 min
Extension	72°C	5 min

Table 4.5. List of mouse genotyping primers

Primer	Sequence 5' to 3'	Denaturation	Amplification
Mitf-A For	CGCTCTGGTGTGAGAGTAAAC	94°C for 2 min	(94°C for 30 sec, 60°C for 30 sec, 68°C for 1 min) 35x
Mitf-A Rev	TCACCACTCTCATGCTCTTCA		
Mitf-M1 For	GACTAAGTGGTCTGCGGTGTC	94°C for 2 min	(94°C for 30 sec, 55°C for 30 sec, 68°C for 1 min) 35x
Mitf-M2 For	GTCACTACCAGGTGAGCATT		
Mitf-M Rev	GATCTGTCCCCTTTTCGAATCGG		
ROSA mTmG For	CTCTGCTGCCTCCTGGCTTCT	94°C for 2 min	(95°C for 30 sec, 60°C for 1 min, 72°C for 1min) 35x
ROSA mTmG Rev	TCAATGGGCGGGGGTCGTT		
Cre For	GGTGTCCAATTTACTGACCGTACA		
Cre Rev	CGGATCCCGCCGCATAACCAGTG		
mCrb1 For1	GTGAAGACAGCTACAGTTCTGATC	94°C for 5 min	(94°C for 30 sec, 56°C for 30 sec, 72°C for 30 sec) 35x
mCrb1 Rev	GCCCCATTTGCACACTGATGAC		
mCrb1 For2	GCCCCTGTTTGCATGGAGGAAACTTGGAAGACAGCTACAGTTCTTCTG		Final extension: 72 °C for 7 min

Table 4.6. List of primers and gRNA used for generation of *Mitf* isoform-specific mutant mice

Name	Type	Sequence 5' to 3'
gRNA Reverse	primer	AAAAAAGCACCGACTCGGTGCC
gRNA Forward	primer	GTTAATACGACTCACTATAGGXXXXXX
Mitf-A geno Forward (TMF54)	primer	CTCCCGCTCTGGTGTGA
Mitf-A geno Reverse (TMF55)	primer	TCACCACTCACCTGCTCTT
Mitf-A geno nested Forward (TMF56)	primer	CTCTCCCCGGTTTGACCTTC
Mitf-A geno nested Reverse (TMF57)	primer	GAGCCATCCCAAGAGACTCG
Mitf-M geno Forward (TMF66)	primer	GCTGCTGCTGTGATAACGTC
Mitf-M geno Reverse (TMF67)	primer	AAAGAGGCCGATTAGCCCAG
Mitf-M geno nested Forward (TMF68)	primer	CTCTGAAGAGGGCATCCAGC
Mitf-M geno nested Reverse (TMF69)	primer	AAGAGCTGCTCGGGAGAAAG
Mitf-M1	gRNA	TGCCTGAAACCTTGCTATGC
Mitf-M2	gRNA	GCTAGAATACAGTCACTACC
Mitf-A1	gRNA	GGGAGTCATGCAGTCCGAAT
Mitf-A2	gRNA	GCAGTCCGAATCGGGAATCG

CHAPTER 5

Sporadic Spotting in *Mitf-M* Knockout Mice

Jessica L. Flesher and Anand K. Ganesan

ABSTRACT

Spotting in mammals is generally a result of defects in melanocyte differentiation, and existing *Mitf* mutant mice commonly have spotting phenotypes. Here we describe a novel phenotype observed in five percent of mice homozygous for a *Mitf-M* isoform-specific deletion. Observed spots vary in size and body region, but are visible on pups and maintain pigmentation as mice age. Gene expression of skin from wildtype, *Mitf-A* knockout mice and *Mitf-M* knockout mice reveal unique targets of *Mitf* isoforms. Skin from the *Mitf-M* knockout spot has rescue of gene expression required for pigmentation, but maintains some similarity to unpigmented skin from *Mitf-M* knockout mice. Initial findings suggest that the spots are not caused by alternative splicing that rescues *Mitf-M* expression, but rather compensation from alternative promoter driven isoforms of *Mitf*.

MAIN TEXT

Introduction

Spotting is a common phenotype found in mammals as varied as cows (*242*), horses (*243*), dogs (*244*), and mice with similar mutations causing human pigmentation disorders such as Waardenburg syndrome (*245*). The study of mouse white spotting mutants has revealed the key regulators of melanoblast migration from the neural crest and differentiation into mature melanocytes (*245*). In the classical model of melanocyte development, murine neural crest precursors expressing *Pax3* turn on *Sox10* to become bipotent progenitors. These progenitors can become melanoblast committed to melanocyte differentiation when they express *Mitf* and *Kit* (*12*). Melanoblasts from the cranial neural crest populate the eyes and ears (*13*), while cervical and trunk neural crest melanoblasts populate the skin (*14*).

Murine mutations in *Mitf* cause a wide range of phenotypes by altering bone density, hearing, and eye morphology in addition to coat pigmentation and patterning (*105*). Alleles containing mutations that alter the basic domain, required for DNA binding of *Mitf* (*200*), result in white spotting for heterozygotes and complete loss of pigmentation with microphthalmia for homozygotes, including $Mitf^{mi}$, $Mitf^{mi\text{-}Or}$, and $Mitf^{mi\text{-}H}$ (*105*, *114*, *246–248*). $Mitf^{mi\text{-}bws}$ and $Mitf^{mi\text{-}rw}$ alleles that alter splicing and promoter regulation of isoforms exhibit phenotypes only in homozygote or compound heterozygote mice (*105*, *226*, *234*, *249*, *250*). Complete loss of *Mitf* with the $Mitf^{vga9}$ allele or loss of the M isoform in $Mitf^{mi\text{-}bw}$ and $Mitf^{em2Gane}$ are characterized by a loss of coat color and neural crest derived melanocytes (*119*, *233*, *235*). A pigmented spot around the neck is a common feature of the $Mitf^{mi\text{-}rw}$ allele and black spotting arose out of the $Mitf^{mi\text{-}bw}$ line generating a stable line of spotted mice (*105*, *251*). *Mitf* is a key determinant in melanocyte development, but the precise requirements for *Mitf* and its isoforms in melanocyte differentiation and survival is not fully understood. Here we present the characterization of spotting in a *Mitf-M* isoform specific knockout mouse with the $Mitf^{em2Gane}$ allele. Additionally, we compare gene expression profiles of *Mitf-A* ($Mitf^{em1Gane}$) and *Mitf-M* knockout mice, including the *Mitf-M* knockout spot, to reveal new candidates for *Mitf* isoform specific gene regulation.

Mitf-M knockout mice have sporadic spotting

Isoform-specific loss of *Mitf-M* results in a loss of melanocytes and pigmentation of the hair, skin, choroid, and iris stroma (*119*). While breeding colonies of $Mitf^{em2Gane}$ mice, hereafter referred to as *Mitf-M* knockout mice, sporadic spotting was observed in individual homozygotes with loss of *Mitf-M* (Figure 5.1A) where *Mitf-M* null littermates were unspotted as previously described (*119*) (Figure 5.1A). The *Mitf-M* heterozygote breeding pairs produced pups with

genotype frequencies that are not significantly different than expected Mendelian inheritance patterns, $X^2 = 0.2231$ (Figure 5.1B). Spotting was observed in 4.95% of *Mitf-M* knockout mice from both *Mitf-M* heterozygote and homozygous knockout breeding pairs (Figure 5.1C), but is not inheritable. This is distinct from the stable spotting phenotype that arose out of the $Mitf^{mi\text{-}bw}$ strain with multiple spots per mouse (*251*) or the pigmented head spot found in the $Mitf^{mi\text{-}rw}$ mice (*105*). Histology of the skin from spotted mice reveal pigmented hair follicles from spots neighboring unpigmented hair follicles (Figure 5.1D). We do observe occasional minor belly spots in *Mitf-M* heterozygotes (Figure 5.1E), a phenomenon seen with other recessive *Mitf* mutant alleles (*105*). In *Mitf-M* knockout mice, spots were predominantly observed on the lower back of the mice ranging in size and color (Figure 5.2A), but were also observed in other body regions including the rump, leg, head, eye, and ear (Figure 5.2B-C). During development, melanoblasts must migrate from the neural crest to the skin before differentiating into melanocytes to pigment the hair (*245*). Melanoblast distribution in embryos varies with higher density in the head, cervical, and tail region compared to the trunk (*245*). The locations of the spots on the back, rump, head, eye, and ear may be due to high density of melanocyte precursors during these early stages of development. Two spotted mice were identified with multiple spots where one spot was located on the back and one was located in another region including the rump (Figure 5.2B (rump), 5.2D).

Murine melanocyte pigmentation of hair is first noticeable a few days after birth and generally remains pigmented through hair cycles through the life of the mouse (*252*). The pigmented spots in *Mitf-M* null mice were generally visible by P10 (Figure 5.2D). Spots were followed in individual mice and maintained pigmentation following depilation at P60 and remained pigmented at P732 (2 years) (Figure 5.2D). Another mouse where the spot was identified at P5 is pictured following depilation at P108 (Figure 5.2E). Since the spots do not prematurely

grey, this suggests that there are functional melanocyte stem cells within the spot to maintain the pigmentation over time.

Loss of melanocyte specific gene expression in *Mitf-M* knockout mouse skin is partially rescued in spots

Within the skin, melanocytes have a very distinct gene expression profile that relies heavily on *Mitf* expression. *Mitf-M* has long been thought to be the major isoform that contributes to melanoblast specification due to the high expression levels in melanocytes (*253*), the ability to rescue eye pigmentation of *Mitf* null mice (*202*), and the absence of melanocytes with loss of *Mitf-M* in adult skin (*119*). The Mitf-A isoform has been shown to regulate some of the same genes required for pigmentation of the retinal pigment epithelium (RPE) (*199*) with subtle roles in pigmentation of the skin (*119*). To better understand how pigmentation was rescued in *Mitf-M* knockout mice and the subtle phenotype of $Mitf^{em1Gane}$ mice, hereafter referred to as *Mitf-A* knockout mice (*119*), we collected skin samples for bulk RNA sequencing from wildtype, *Mitf-A* isoform specific knockouts, and *Mitf-M* isoform specific knockouts including one mouse with a spot where we collected pigmented and unpigmented skin (Figure 5.2D). To initiate the hair cycle and melanocyte growth, mice were shaved and depilated at P50, ten days prior to collection of biopsies. Using principal component analysis wildtype and *Mitf-A* knockout samples showed high similarity while the unpigmented *Mitf-M* knockouts clustered together (Figure 5.3A) with the exception of sample M2 which had low similarity as shown by the MA-plot (Figure 5.3B). The sample from the pigmented spot (Mspot) fell between the wildtype/*Mitf-A* knockout cluster and the *Mitf-M* knockout cluster. Numerous differential genes were identified when comparing all of the samples with at least a log2 fold change above 1-fold and adjusted p-value below 0.05 (Table

5.1). Utilizing pairwise comparisons, we identified genes differentially expressed in *Mitf-A* knockout mice compared to wildtype (Table 5.2) and *Mitf-M* knockout mice compared to wildtype (Table 5.3). Figure 5.3C represents the genes that passed this cut-off for *Mitf-A* knockout skin and the top 10 upregulated and top 20 downregulated genes in *Mitf-M* knockout skin. Our previous studies utilizing targeted nanostring probes identified no differences between gene expression of *Mitf-A* null and wildtype mice (*119*), but with sequencing data *Erdr1* is enriched 9-fold in the skin of mice with loss of *Mitf-A* (Figure 5.3C, Table 5.2). Similar to previous results, loss of *Mitf-M* results in downregulation of key components of melanogenesis including *Tyr, Tyrp1,* and *Dct*. With the rescue of pigmentation in the spot (Mspot), these same pigment genes have expression similar to those found in wildtype skin even compared to unpigmented skin from the same mouse (M4) (Figure 5.3C). Due to available mice, samples M1, M3, M4, and Mspot represent male mice resulting in enrichment of genes found on the Y chromosome (*Kdm5d, Uty, Eif2s3y, Dxd3y*) in the *Mitf-M* knockout mice. Comparisons between *Mitf-A* and *Mitf-M* knockout mice also highlighted differences in genes required for melanogenesis (Table 5.4).

MITF is a known regulator of many gene programs in melanocytes from differentiation to cell survival (*16*), with many identified gene targets (*254*). In *Mitf-M* knockout skin, a number of known neural crest lineage markers (*Pax3, Sox10,* and *Kit)* and MITF target genes are downregulated including *Tyr, Dct,* and *Mc1r* (Figure 5.3D). The unique amino termini of MITF isoforms is thought to give specificity to MITF isoforms (*117*). MITF-M gene targets like *Tyr*, can be activated by the MITF-A isoform (*199*) while the MITF-Mc isoform acts as a repressor. While the expression of genes required for melanogenesis within the spot resembles wildtype skin, the most downregulated genes by log2 fold change have patterns similar to the skin of *Mitf-M* knockout mice (Figure 5.3E). Further inquiry into these genes with MotifMap (*215*, *216*)

identified numerous genes containing an MITF binding motif (M02099) with the CAKGTGV consensus sequence (bolded genes in Figure 5.3D-E, Table 5.5). Further investigation is necessary to identify if these represent MITF-M specific target genes.

To better understand the changes in gene expression of *Mitf* knockout mice, we utilized Gene Set Enrichment Analysis (GSEA) and identified gene ontology sets that were differentially regulated between pairwise comparisons of genotypes. In *Mitf-A* knockout mouse skin compared to wildtype skin numerous mitochondrial and ribosomal gene sets are enriched (Figure 5.4A-B, Table 5.6). In general, depilation at P50 during second telogen (*252*) will stimulate the third anagen cycle (*255*), but small changes in signaling within the skin can alter the response to depilation (*256*). Alterations in mitochondrial and ribosomal genes can delay the hair cycle in mice (*257*), suggesting that most of the observed gene expression changes correspond to differences between hair cycle. One gene set enriched in wildtype skin is related to eye morphogenesis (Figure 5.4B-C, Table 5.7) which is consistent with research showing *Mitf-A* contributes to proper development of the pigmented regions of the eye (*119*, *198*, *199*). No striking pathways were enriched when comparing wildtype and *Mitf-A* knockout mice by Ingenuity Pathway Analysis (IPA) (data not shown). The top enriched gene sets when comparing wildtype and *Mitf-M* knockout skin included a number of gene sets associated with melanocytes, pigmentation, and melanin synthesis in wildtype skin (Figure 5.5A-B, Table 5.8). Enrichment of methylation related gene sets in *Mitf-M* knockout mice is reliant on Y chromosome genes and may be a byproduct since the mice included were predominantly male (Figure 5.5B-C, Table 5.9). Pathways identified by IPA comparing wildtype and *Mitf-M* null mice included melanocyte development and pigmentation signaling, which had decreased expression of multiple markers including *Mc1r, Sox10, Pax3, Tyr, Tyrp1,* and *Dct* (Figure 5.5D). Further analysis into diseases

and biological functions identified a number of annotated pathways regarding melanocytes including synthesis of melanin with the majority of related genes downregulated in *Mitf-M* knockout mice (Figure 5.5E). This also corresponded with the predicted inhibition of MITF based on expression changes in target genes (Figure 5.5F). Intriguingly, we also found that within our data set a number of genes related to toxicity or injury in the kidney had altered expression levels (Figure 5.5F), consistent with previous findings that *Mitf-M* alters the homeostatic control of the kidney (*119*). Comparisons between *Mitf-A* and *Mitf-M* knockout mice included similar gene sets associated with changes in pigmentation (Figure 5.6A-C, Table 5.10-11) which was also apparent by IPA (data not shown).

Due to the variability of spot size and pigmentation, our data set only includes one *Mitf-M* knockout mouse with matched unpigmented and pigmented spot skin. To get a preliminary glimpse of differentially expressed genes within the spot, we compared two normal *Mitf-M* knockout mice (M1, M3) with the matched set of biopsies from the spotted mouse (M4, Mspot). *Oca2* was the only gene identified that passed thresholds described above with 23-fold change and adjusted p-value of 0.0050. GSEA revealed that the spotted mouse had enrichment for gene sets associated with RNA processing and pigmentation (Figure 5.7A-B, Table 5.12) with gene ontology sets associated with channels were enriched in the unspotted mice (Figure 5.7B-C, Table 5.13). Based on activation of downstream targets in IPA, MITF activity was predicted to be activated in the spotted mouse (Figure 5.7D). Inclusion of additional matched unpigmented and pigmented spots from *Mitf-M* knockouts is necessary to better understand the specific gene expression changes occurring to generate and maintain the pigmented spots in these mice.

Mitf-A and *Mitf-J* may compensate for loss of *Mitf-M* in spots of *Mitf-M* knockout mice

Mitf-M knockout mice were characterized as lacking melanocytes in adult skin (*119*). The presence of pigmentation in these mice suggests three possibilities: 1) MiT/TFE family members (MITF, TFEB, TFE3, TFEC) are compensating for the loss of *Mitf-M* in a small portion of cells. Family members form homodimers and heterodimers to bind to CACGTG E-boxes as basic helix-loop-helix zipper transcription factors and TCATGTG M-boxes, a unique target of the MiT family (*258*). There was no significant change in expression for the three other family members (*Tfeb, Tfec,* and *Tfe3*) with loss of *Mitf-M* or in skin from the spotted mouse (Figure 5.3C). However, additional samples from spots are needed to validate this observation. 2) Alternative splicing rescues aberrant *Mitf-M* transcripts. The $Mitf^{mi\text{-}bw}$ allele is caused by a LINE1 insertion between exons 3 and 4 of *Mitf* that results in a black-eyed white phenotype (*235*) and is phenocopied by our *Mitf-M* knockout mice (*119*). A stable spotting phenotype arose out of the $Mitf^{mi\text{-}bw}$strain that was caused by alternative splicing that skipped exons 3 and/or 4, producing a functional, but truncated *Mitf-M* transcript (*251*). Additionally, the black spotting phenotype exhibited premature greying and was inheritable (*251*), which we do not observe in the *Mitf-M* knockout spotted mice (Figure 5.2). Splicing analysis identified rare skipped exons within *Mitf*, but there was no significant changes between the unspotted *Mitf-M* knockouts when compared to the skin samples from the $Mitf\text{-}M^{-/-}$ spotted mouse. Inclusion of exons 2, 3, 4, or 6 was found in approximately 99% of read junctions identified (Figure 5.8A), suggesting that alternative splicing of *Mitf* is not rescuing aberrant *Mitf-M* transcripts. 3) Alternative promoter driven isoforms of *Mitf* can compensate in a small portion of cells lacking *Mitf-M*. To investigate which *Mitf* isoforms could be compensating in the *Mitf-M* knockout mice, we analyzed read junctions present in our bulk sequencing data set after alignment. Read junctions were counted if they included known first

exons (Figure 5.8B). Since both the A and J isoforms include exon 1B, the proportion of read junctions between 1B and exon 2 was distributed based off the proportion of junctions from exons 1A and 1J to exon 1B. In whole skin wildtype mice have approximately equal proportions of *Mitf-A*, *Mitf-J*, and *Mitf-M* (Figure 5.8C). *Mitf-M* knockout mice including the skin from the spot have complete loss of *Mitf-M* (Figure 5.8C), however no significant difference in *Mitf-A* and *Mitf-J* expression were observed between the white *Mitf-M* knockout skin and the spotted *Mitf-M* knockout skin. When running validation with full-length PCR using isoform specific primers, all three isoforms were detected at full-length (Figure 5.8D). Of note, sample 3, corresponding to the *Mitf-M* knockout spot skin, had a similar sized product to full length *Mitf-M.* Utilizing the read fragments from bulk sequencing, we identified an intronic splice junction with exon 2 that could be generated from the *Mitf-M* promoter (Figure 5.9). This predicted transcript still retains the 18 base pair deletion of the *Mitf-M* knockout allele with multiple (14) stop codons present in the intronic sequence to ablate production of a functional protein (Figure 5.9), supporting the idea that the loss of *Mitf-M* expression is not rescued within the spot. Additionally, using PacBio long-read sequencing of select samples (WT1, A1, M1, and Mspot) we were able to verify the presence of both *Mitf-A* and *Mitf-J* promoter driven isoforms in *Mitf-M* knockout mice (Figure 5.8E). As a validation of the methods used, we also quantified the frequency of *Trp63* TA and ΔN isoforms driven by alternative promoters that plays an important role in keratinocyte differentiation (*220*). No significant differences in *Trp63* isoforms was observed across samples (Figure 5.10). Our findings suggest that in a handful of melanoblasts, expression of alternative *Mitf* promoter driven isoforms compensate for the loss of *Mitf-M*, allowing differentiation into functional melanocyte populations.

In summary, we have identified spotting in five percent of mice lacking *Mitf-M*, identified potential *Mitf* isoform specific gene targets, and presented preliminary results from efforts to identify the cause of spotting. Additional experiments are necessary to confirm our hypothesis on the presence of spotting in *Mitf-M* knockout mice, including analyzing skin from additional spots and sequencing of the *Mitf-M* transcript present in the spot. One drawback to these studies is the sporadic nature of spotting in the *Mitf-M* null line, making it difficult to isolate melanocytes or RNA from spotted skin. Future studies can utilize other established *Mitf* alleles to generate compound heterozygotes that may develop more frequent and robust spotting phenotypes that recapitulate key characteristics observed in spotted *Mitf-M* knockout mice. Understanding the origin of spotting in *Mitf-M* knockout mice may reveal unique roles of additional isoforms of *Mitf* or confirm the reliance of melanocytes on the *Mitf-M* isoform.

MATERIALS AND METHODS

Mouse strains and genotyping

All animal experiments were approved by the UC Irvine Institutional Animal Care and Use Committee (IACUC) (AUP-17-230). The $Mitf^{em1Gane}$ allele (MGI:6273202) and $Mitf^{em2Gane}$ allele (MGI:6273203) are previously described (*119*) and generated with the help of the Transgenic Mouse Facility at UC Irvine. Homozygotes for the $Mitf^{em1Gane}$ allele have a 7 bp deletion resulting in the loss of the *Mitf-A* isoform (Ensembl variant 202, NCBI variant NM_001113198) and are referred to as *Mitf-A* knockouts or nulls. Homozygotes for the $Mitf^{em2Gane}$ allele have an 18 bp deletion resulting in the loss of the *Mitf-M* isoform (Ensembl variant 201, NCBI variant NM_008601) are referred to as *Mitf-M* knockouts or nulls. Genotyping primers and PCR conditions are provided in Table 5.15. For the *Mitf-A* line, wildtype and homozygous knockouts

are indistinguishable, so genotyping PCR reaction product was purified using the QIAquick PCR Purification Kit (Qiagen) and submitted for Sanger Sequencing (GENEWIZ) to determine whether the 7bp deletion was present. Mice with spots were imaged when identified. Additional photographs were taken during procedures and on indicated days. Calculations of genotyping frequencies and spotting were calculated only from genotyped animals. The Pearson's Chi-squared test to validate Mendelian inheritance was determined in R (version 3.5.3).

RNA isolation from mouse skin

RNA was isolated from whole mouse skin at P60 following stimulation of 3rd Anagen as previously described (*91*, *119*). Mice were shaved and depilated at P50 to stimulate the 3rd Anagen. Four mm punch biopsies were collected from the skin of mice at P60 and immediately stabilized in RNAlater (Invitrogen) at 4°C. Skin samples were homogenized using the Precellys24 high-throughput tissue homogenizer (Precellys) in hard tissue homogenizing reinforced tubes that contain 2.8mm ceramic beads (Bertin Corporation). After homogenization, RNA was extracted from each sample using the RNeasy Fibrous Tissue Mini Kit according to the manufacturer's instructions (Qiagen).

Full-length mRNA was converted to cDNA using SuperScript IV First-Strand Kit (ThermoFisher) with oligodT primers. Forward primers for full-length PCR were previously published (*119*) or designed to include most of the unique exon 1 of individual *Mitf* isoforms using Primer3 (*213*, *214*) along with the reverse primer for exon 9. All primers and PCR conditions are listed in Table 5.15.

Bulk RNA sequencing and analysis

Total RNA from whole mouse skin was monitored for quality control using the Agilent Bioanalyzer Nano RNA chip and Nanodrop absorbance ratios for 260/280nm and 260/230nm. Library construction was performed according to the Illumina TruSeq mRNA stranded protocol. The input quantity for total RNA within the recommended range and mRNA was enriched using oligo dT magnetic beads. The enriched mRNA was chemically fragmented. First strand synthesis used random primers and reverse transcriptase to make cDNA. After second strand synthesis the ds cDNA was cleaned using AMPure XP beads and the cDNA was end repaired and then the 3' ends were adenylated. Illumina barcoded adapters were ligated on the ends and the adapter ligated fragments were enriched by nine cycles of PCR. The resulting libraries were validated by qPCR and sized by Agilent Bioanalyzer DNA high sensitivity chip. The concentrations for the libraries were normalized and then multiplexed together. The multiplexed libraries were sequenced using paired end 100 cycles chemistry on the NovaSeq 6000. Post-processing of the run to generate the FASTQ files was performed at the Institute for Genomics and Bioinformatics (UCI IGB).

Paired-end sequencing reads were trimmed of adapter sequences using Trimmomatic (version 0.35) (*259*), analyzed for quality using the Fastqc program (http://www.bioinformatics.babraham.ac.uk/projects/fastqc/), and aligned to the mouse reference genome version mm10 using the HISAT2 alignment software (version 2.1.0) (*260*). Fragments and exons were quantified using featureCounts pipeline from the subread module (version 1.5.0) (*261*). DEseq2 (version 1.22.2) (*208*) was utilized to distinguish differentially expressed genes between mouse genotypes and phenotypes. Genes identified in pairwise comparisons with adjusted p value below 0.05 and a log2 fold change greater than 1 or less than -1 were sorted by log2 fold change and input into Gene Set Enrichment Analysis (GSEA) software (version 4.0.3)

(*262*, *263*) using the GSEAPreranked pipeline with the C5-Gene Ontology database, classic enrichment statistic, and mouse gene symbols as reference. Enriched gene sets were filter with nominal p-value below 0.05, false discovery rate (FDR) below 0.25, and family wise error rate (FWER) below 0.25. Top enriched gene sets for each pairwise comparison was further processed using leading edge analysis to identify overlap between gene sets. The data sets were filtered to include genes with a log2 fold change greater than 1 or less than -1 and analyzed with Ingenuity Pathway Analysis (IPA, version 51963813) (Qiagen).

Analysis of read junctions

BAM files generated in Hisat2 were visualized against the annotated mm10 transcriptome in Integrative Genomics Viewer (IGV) (version 2.7.2) (*210*, *211*). After identifying read junctions present between *Mitf* exons 1A to 1B, 1J to 1B, and 1B to 2A, read junctions were counted between exons 1B and 2A and divided based on the proportion of junctions to exon 1B from either 1A (proxy for *Mitf-A*) or 1J (proxy for *Mitf-J*). Read junctions between exons 1M and 2A were used as proxy for *Mitf-M*. For *Trp63*, read junctions were identified spanning exons TA to 2, 2 to 3, 3 to 4, and ΔN to 4. Read junctions between exons 3 and 4 were used as proxy for the *Trp63* TA promoter driven isoform while junctions between ΔN and 4 were used as proxy for the *Trp63* ΔN promoter driven isoform. The read junctions used are illustrated in Figure 5.5. To determine if there were statistical differences between isoform abundance in the different mouse genotypes, we utilized ANOVA in R (version 3.5.3).

Predicted aberrant *Mitf-M* promoter driven transcripts were determined from visualizing reads in IGV. The predicted transcript was aligned against the *Mitf-M* transcript (Ensembl variant 201, NCBI variant NM_008601) and a modified *Mitf-M* transcript with the intron was retained

through the observed read junctions to exon 2M using the Clustal Omega algorithms in MegAlignPro (version 17.0.2). These three transcripts allowed the visualization of the entire deletion found in *Mitf-M* knockout mice.

Transcriptome-wide analysis of splicing events was completed using rMATS (replicate Multivariate Analysis of Transcript Splicing) (version 4.0.2) (*264–266*), including statistical analysis of pairwise comparisons. Skipped exons, retained introns, mutually exclusive exons, alternative 5' splice sites, and alternative 3' splice sites were identified by rMATS. *Mitf* splicing events, all skipped exons, were characterized using the UCSC Genome Browser (*267*). Individual read junction counts for each sample and splicing event were used to calculate the percent of events where the skipped exon was included.

PacBio full transcript RNA sequencing and analysis

RNA samples were prepped as described above. The IsoSeq libraries were constructed following the protocol from the Lexogen Telo Prime Full Length cDNA Amplification Kit v2 (P/N K01324, Vienna, Austria). One microgram of RNA was processed to full length cDNA which was then amplified by PCR. The cDNA products were quantified by Qubit and analyzed on the Agilent DNA High Sensitivity chip. The amplified cDNA products were used for SMRTbell template preparation with no size selection using the SMRTbell Express Template Prep Kit 1.0 (P/N: 100-259-100 Pacific BioSciences, Menlo Park, CA). The final SMRTbell templates were quantified by Qubit and analyzed on an Agilent DNA 1200 Agilent chip in order to verify the template length. The templates were prepared for sequencing by annealing the sequencing primer v3 (component of SMRTbell Express Template Prep Kit 1.0 (P/N: 100-259-100) and binding the polymerase to the primer-annealed template (component of Sequel Binding Kit 3.0 P/N: 101-626-600). Each

SMRTbell template was loaded by diffusion at 8pM and sequenced for 20 hours with a pre-extension time of 4 hours. The templates were loaded on a 1M v3 LR SMRTcell tray (P/N: 101-531-001). The templates were sequenced using sequencing kit 3.0 (4rxn) (P/N: 101-597-900) on the PacBo Sequel platform. Post-processing of the run to generate the subread bam files was performed at the Institute for Genomics and Bioinformatics (UCI IGB).

PacBio SMRT sequencing subreads were analyzed using smrtanalysis software (version 7.0.0) following steps of the isoseq3 analysis. Briefly, the circular consensus sequences were generated, the cDNA primers were removed, and transcripts were clustered by similarity of consensus sequences. While the 5' cDNA primer was unmodified (5'-TGGATTGATATGTAATACGACTCACTATAG-3'), to recognize full length transcripts with a polyA-tail, the 3' cDNA primer had to be modified (5'-TCTCAGGCGTTTT-3'). This modification also reduced the number of chimeric reads detected and analysis proceeded with full-length non-chimeric reads. Clustered reads were than aligned using Minimap2 (*268*) to the mm10 genome. TranscriptClean (version 1.0.7) (*269*) and TALON (version 4.0) (*270*) were used to clean-up splice junctions and classify transcripts as known, novel-in-catalog, or novel not in-catalog. Tracks containing transcripts of interest were uploaded to the UCSC Genome Browser (*267*) to visualize full-length reads.

ACKNOWLEDGEMENTS

We thank the UCI Genomics High Throughput Facility (GHTF) for their help with RNA sequencing. This work was supported by grants from the National Institutes of Health R01AR063116 to AKG. The research reported in this publication was supported by the National Cancer Institute of the National Institutes of Health Award Number T32CA009054-37 to JLF. The

TMF and GHTF are Shared Resources funded in part by the Chao Family Comprehensive Cancer Center Support Grant (P30CA062203) from the National Cancer Institute and NIH shared instrumentation grants (1S10RR025496-01, 1S10OD010794-01, and 1S10OD021718-01). The content is solely the responsibility of the authors and does not necessarily represent the official views of the National Institutes of Health.

REFERENCES

12. N. Vandamme, G. Berx, From neural crest cells to melanocytes: cellular plasticity during development and beyond. *Cell. Mol. Life Sci.* **76**, 1919–1934 (2019).

13. L. L. Baxter, W. J. Pavan, Pmel17 expression is Mitf-dependent and reveals cranial melanoblast migration during murine development. *Gene Expr. Patterns*. **3**, 703–707 (2003).

14. Y. M. Wilson, K. L. Richards, M. L. Ford-Perriss, J. J. Panthier, M. Murphy, Neural crest cell lineage segregation in the mouse neural tube. *Development*. **131**, 6153–6162 (2004).

16. J. Vachtenheim, L. Ondrusov, in *Recent Advances in the Biology, Therapy and Management of Melanoma* (InTech, 2013; http://www.intechopen.com/books/recent-advances-in-the-biology-therapy-and-management-of-melanoma/mitf-a-critical-transcription-factor-in-melanoma-transcriptional-regulatory-network).

91. E. K. Paterson, T. J. Fielder, G. R. MacGregor, S. Ito, K. Wakamatsu, D. L. Gillen, V. Eby, R. E. Boissy, A. K. Ganesan, Tyrosinase depletion prevents the maturation of melanosomes in the mouse hair follicle. *PLoS One*. **10** (2015), doi:10.1371/journal.pone.0143702.

114. P. Hertwig, Neue Mutationen und Kopplungsgruppen bei der Hausmaus. *Z. Indukt. Abstammungs- u. Vererbungsl.* **80**, 220–246 (1942).

117. E. Steingrímsson, All for one, one for all: alternative promoters and Mitf. *Pigment Cell Melanoma Res.* **21**, 412–414 (2008).

119. J. L. Flesher, E. K. Paterson-Coleman, P. Vasudeva, R. Ruiz-Vega, M. Marshall, E. Pearlman, G. R. MacGregor, J. Neumann, A. K. Ganesan, Delineating the role of MITF isoforms in pigmentation and tissue homeostasis. *Pigment Cell Melanoma Res.* **33**, 279–292 (2020).

150. E. Steingrímsson, N. G. Copeland, N. A. Jenkins, Melanocytes and the Microphthalmia Transcription Factor Network. *Annu. Rev. Genet.* **38**, 365–411 (2004).

198. K. Bharti, W. Liu, T. Csermely, S. Bertuzzi, H. Arnheiter, Alternative promoter use in eye development: The complex role and regulation of the transcription factor MITF. *Development*. **135**, 1169–1178 (2008).

199. S. Amae, N. Fuse, K. Yasumoto, S. Sato, I. Yajima, H. Yamamoto, T. Udono, Y. K. Durlu, M. Tamai, K. Takahashi, S. Shibahara, Identification of a novel isoform of microphthalmia-associated transcription factor that is enriched in retinal pigment epithelium. *Biochem. Biophys. Res. Commun.* **247**, 710–5 (1998).

200. V. Pogenberg, M. H. Ögmundsdóttir, K. Bergsteinsdóttir, A. Schepsky, B. Phung, V. Deineko, M. Milewski, E. Steingrímsson, M. Wilmanns, Restricted leucine zipper dimerization and specificity of DNA recognition of the melanocyte master regulator MITF. *Genes Dev.* **26**, 2647–2658 (2012).

202. H. T. Michael, C. Graff-Cherry, S. Chin, C. Rauck, A. D. Habtemichael, P. Bunda, T. Smith, M. M. Campos, K. Bharti, H. Arnheiter, G. Merlino, C. P. Day, Partial rescue of ocular pigment cells and structure by inducible ectopic expression of Mitf-M in MITF-

deficient mice. *Investig. Ophthalmol. Vis. Sci.* **59**, 6067–6073 (2018).

208. M. I. Love, W. Huber, S. Anders, Moderated estimation of fold change and dispersion for RNA-seq data with DESeq2. *Genome Biol.* **15**, 550 (2014).

210. J. T. Robinson, H. Thorvaldsdóttir, W. Winckler, M. Guttman, E. S. Lander, G. Getz, J. P. Mesirov, Integrative genomics viewer. *Nat. Biotechnol.* **29**, 24–26 (2011).

211. H. Thorvaldsdóttir, J. T. Robinson, J. P. Mesirov, Integrative Genomics Viewer (IGV): High-performance genomics data visualization and exploration. *Brief. Bioinform.* **14**, 178–192 (2013).

213. T. Koressaar, M. Remm, Enhancements and modifications of primer design program Primer3. *Bioinformatics*. **23**, 1289–1291 (2007).

214. A. Untergasser, I. Cutcutache, T. Koressaar, J. Ye, B. C. Faircloth, M. Remm, S. G. Rozen, Primer3-new capabilities and interfaces. *Nucleic Acids Res.* **40**, e115 (2012).

215. K. Daily, V. R. Patel, P. Rigor, X. Xie, P. Baldi, MotifMap: Integrative genome-wide maps of regulatory motif sites for model species. *BMC Bioinformatics*. **12**, 495 (2011).

216. X. Xie, P. Rigor, P. Baldi, MotifMap: A human genome-wide map of candidate regulatory motif sites. *Bioinformatics*. **25**, 167–174 (2009).

220. A. Yang, R. Schweitzer, D. Sun, M. Kaghad, N. Walker, R. T. Bronson, C. Tabin, A. Sharpe, D. Caput, C. Crum, F. McKeon, p63 is essential for regenerative proliferation in limb, craniofacial and epithelial development. *Nature*. **398**, 714–718 (1999).

226. H. Grüneberg, The relations of microphthalmia and white in the mouse. *J. Genet.* **51**, 359–362 (1953).

233. C. A. Hodgkinson, K. J. Moore, A. Nakayama, E. Steingrímsson, N. G. Copeland, N. A. Jenkins, H. Arnheiter, Mutations at the mouse microphthalmia locus are associated with defects in a gene encoding a novel basic-helix-loop-helix-zipper protein. *Cell*. **74**, 395–404 (1993).

234. K. I. Watanabe, K. Takeda, K. I. Yasumoto, T. Udono, H. Saito, K. Ikeda, T. Takasaka, K. Takahashi, T. Kobayashi, M. Tachibana, S. Shibahara, Identification of a distal enhancer for the melanocyte-specific promoter of the MITF gene. *Pigment Cell Res.* **15**, 201–211 (2002).

235. I. Yajima, S. Sato, T. Kimura, K. I. Yasumoto, S. Shibahara, C. R. Goding, H. Yamamoto, An L1 element intronic insertion in the black-eyed white (Mitf(mi-bw)) gene: The loss of a single Mitf isoform responsible for the pigmentary defect and inner ear deafness. *Hum. Mol. Genet.* **8**, 1431–1441 (1999).

242. S. Hofstetter, F. Seefried, I. M. Häfliger, V. Jagannathan, T. Leeb, C. Drögemüller, A non-coding regulatory variant in the 5′-region of the MITF gene is associated with white-spotted coat in Brown Swiss cattle. *Anim. Genet.* **50**, 27–32 (2019).

243. J. Henkel, C. Lafayette, S. A. Brooks, K. Martin, L. Patterson-Rosa, D. Cook, V. Jagannathan, T. Leeb, Whole-genome sequencing reveals a large deletion in the MITF gene in horses with white spotted coat colour and increased risk of deafness. *Anim. Genet.* **50**, 172–174 (2019).

244. L. Andersson, Genome-wide association analysis in domestic animals: A powerful approach for genetic dissection of trait loci. *Genetica*. **136**, 341–349 (2009).

245. L. L. Baxter, L. Hou, S. K. Loftus, W. J. Pavan, Spotlight on spotted mice: a review of white spotting mouse mutants and associated human pigmentation disorders. *Pigment cell Res.* **17**, 215–24 (2004).

246. C. Thaung, Novel ENU-induced eye mutations in the mouse: models for human eye disease. *Hum. Mol. Genet.* (2002), doi:10.1093/hmg/11.7.755.

247. K. Stelzner, No Title. *Mouse News Lett.* **31**, 40 (1964).

248. K. Stelzner, No Title. *Mouse News Lett.* **34**, 41 (1966).

249. H. Sweet, Recessive spotting mutation mapped to the Mitf<mi> locus on chromosome 6. *Mouse News Lett.* **94**, 145 (1996).

250. B. Wen, Y. Chen, H. Li, J. Wang, J. Shen, A. Ma, J. Qu, K. Bismuth, J. Debbache, H. Arnheiter, L. Hou, Allele-specific genetic interactions between Mitf and Kit affect melanocyte development. *Pigment Cell Melanoma Res.* **23**, 441–447 (2010).

251. K. Takeda, H. Hozumi, K. Ohba, H. Yamamoto, S. Shibahara, Regional Fluctuation in the Functional Consequence of LINE-1 Insertion in the Mitf Gene: The Black Spotting Phenotype Arisen from the Mitfmi-bw Mouse Lacking Melanocytes. *PLoS One*. **11**, e0150228 (2016).

252. S. Müller-Röver, B. Handjiski, C. van der Veen, S. Eichmüller, K. Foitzik, I. A. McKay, K. S. Stenn, R. Paus, A comprehensive guide for the accurate classification of murine hair follicles in distinct hair cycle stages. *J. Invest. Dermatol.* **117**, 3–15 (2001).

253. L. Hou, W. J. Pavan, Transcriptional and signaling regulation in neural crest stem cell-derived melanocyte development: do all roads lead to Mitf? *Cell Res.* **18**, 1163–1176 (2008).

254. K. S. Hoek, N. C. Schlegel, O. M. Eichhoff, D. S. Widmer, C. Praetorius, S. O. Einarsson, S. Valgeirsdottir, K. Bergsteinsdottir, A. Schepsky, R. Dummer, E. Steingrimsson, Novel MITF targets identified using a two-step DNA microarray strategy. *Pigment Cell Melanoma Res.* **21**, 665–676 (2008).

255. K. S. Stenn, R. Paus, Controls of hair follicle cycling. *Physiol. Rev.* **81**, 449–494 (2001).

256. M. V Plikus, C. M. Chuong, Macroenvironmental regulation of hair cycling and collective regenerative behavior. *Cold Spring Harb. Perspect. Med.* **4**, a015198 (2014).

257. J. M. Shin, J. W. Ko, C. W. Choi, Y. Lee, Y. J. Seo, J. H. Lee, C. D. Kim, Deficiency of Crif1 in hair follicle stem cells retards hair growth cycle in adult mice. *PLoS One*. **15**, e0232206 (2020).

258. M. Yang, E. Liu, L. Tang, Y. Lei, X. Sun, J. Hu, H. Dong, S. M. Yang, M. Gao, B. Tang, Emerging roles and regulation of MiT/TFE transcriptional factors. *Cell Commun. Signal.* **16** (2018), doi:10.1186/s12964-018-0242-1.

259. A. M. Bolger, M. Lohse, B. Usadel, Trimmomatic: A flexible trimmer for Illumina sequence data. *Bioinformatics*. **30**, 2114–2120 (2014).

260. D. Kim, J. M. Paggi, C. Park, C. Bennett, S. L. Salzberg, Graph-based genome alignment

and genotyping with HISAT2 and HISAT-genotype. *Nat. Biotechnol.* **37**, 907–915 (2019).

261. Y. Liao, G. K. Smyth, W. Shi, FeatureCounts: An efficient general purpose program for assigning sequence reads to genomic features. *Bioinformatics*. **30**, 923–930 (2014).

262. A. Subramanian, P. Tamayo, V. K. Mootha, S. Mukherjee, B. L. Ebert, M. A. Gillette, A. Paulovich, S. L. Pomeroy, T. R. Golub, E. S. Lander, J. P. Mesirov, Gene set enrichment analysis: A knowledge-based approach for interpreting genome-wide expression profiles. *Proc. Natl. Acad. Sci. U. S. A.* **102**, 15545–15550 (2005).

263. V. K. Mootha, C. M. Lindgren, K. F. Eriksson, A. Subramanian, S. Sihag, J. Lehar, P. Puigserver, E. Carlsson, M. Ridderstråle, E. Laurila, N. Houstis, M. J. Daly, N. Patterson, J. P. Mesirov, T. R. Golub, P. Tamayo, B. Spiegelman, E. S. Lander, J. N. Hirschhorn, D. Altshuler, L. C. Groop, PGC-1α-responsive genes involved in oxidative phosphorylation are coordinately downregulated in human diabetes. *Nat. Genet.* **34**, 267–273 (2003).

264. S. Shen, J. W. Park, Z. X. Lu, L. Lin, M. D. Henry, Y. N. Wu, Q. Zhou, Y. Xing, rMATS: Robust and flexible detection of differential alternative splicing from replicate RNA-Seq data. *Proc. Natl. Acad. Sci. U. S. A.* **111**, E5593–E5601 (2014).

265. S. Shen, J. W. Park, J. Huang, K. A. Dittmar, Z. X. Lu, Q. Zhou, R. P. Carstens, Y. Xing, MATS: A Bayesian framework for flexible detection of differential alternative splicing from RNA-Seq data. *Nucleic Acids Res.* **40**, e61–e61 (2012).

266. J. W. Park, C. Tokheim, S. Shen, Y. Xing, Identifying differential alternative splicing events from RNA sequencing data using RNASeq-MATS. *Methods Mol. Biol.* **1038**, 171–179 (2013).

267. W. J. Kent, C. W. Sugnet, T. S. Furey, K. M. Roskin, T. H. Pringle, A. M. Zahler, a. D. Haussler, The Human Genome Browser at UCSC. *Genome Res.* **12**, 996–1006 (2002).

268. H. Li, Minimap2: Pairwise alignment for nucleotide sequences. *Bioinformatics*. **34**, 3094–3100 (2018).

269. D. Wyman, A. Mortazavi, TranscriptClean: Variant-aware correction of indels, mismatches and splice junctions in long-read transcripts. *Bioinformatics*. **35**, 340–342 (2019).

270. D. Wyman, G. Balderrama-Gutierrez, F. Reese, S. Jiang, S. Rahmanian, W. Zeng, B. Williams, D. Trout, W. England, S. Chu, R. C. Spitale, A. Tenner, B. Wold, A. Mortazavi, A technology-agnostic long-read analysis pipeline for transcriptome discovery and quantification. *bioRxiv*, 672931 (2019).

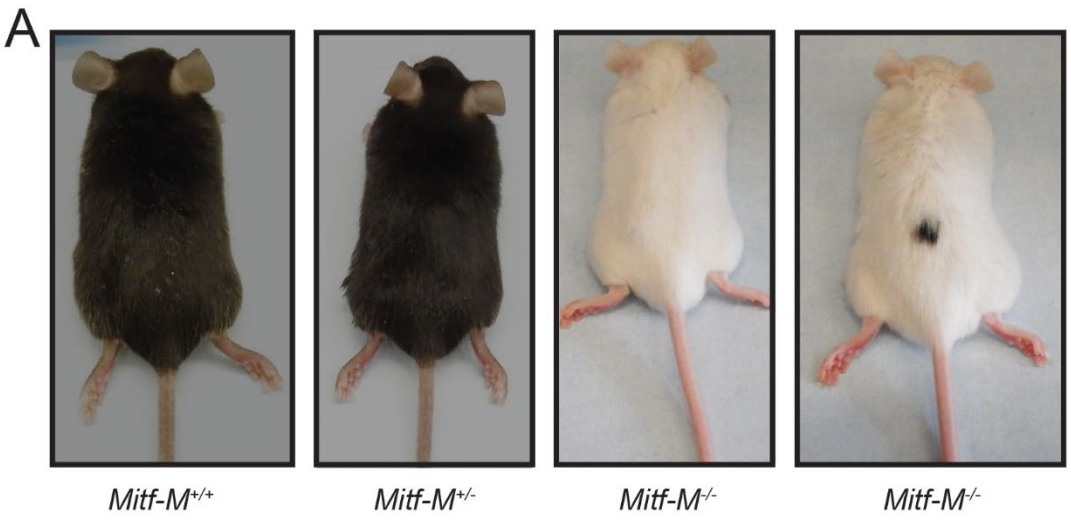
A
Mitf-M+/+
Mitf-M+/-
Mitf-M-/-
Mitf-M-/-

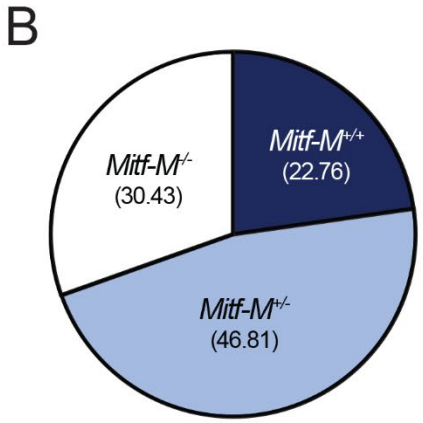
B
Mitf-M-/-
(30.43)
Mitf-M+/+
(22.76)
Mitf-M+/-
(46.81)

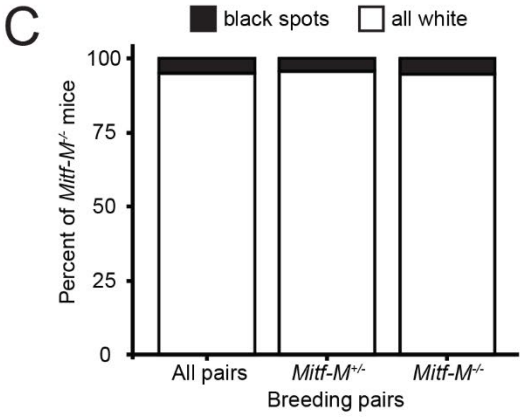
C
black spots
all white
Percent of Mitf-M-/- mice
100
75
50
25
0
All pairs
Mitf-M+/-
Mitf-M-/-
Breeding pairs

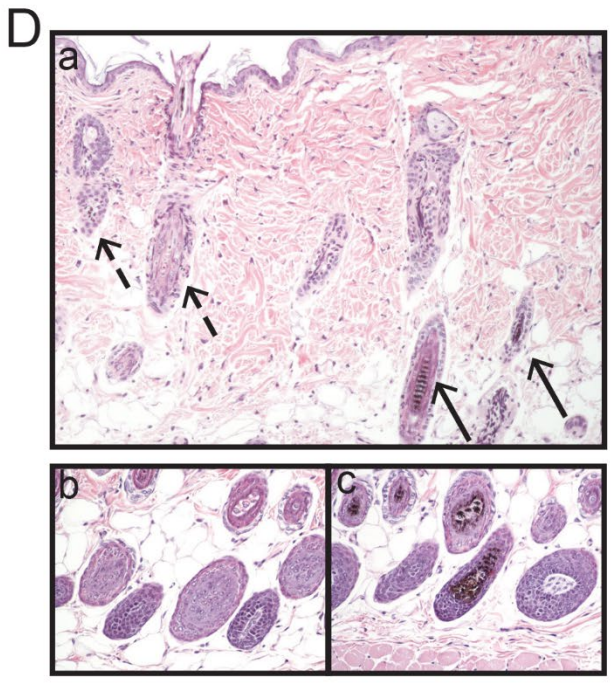
D
a
b
c

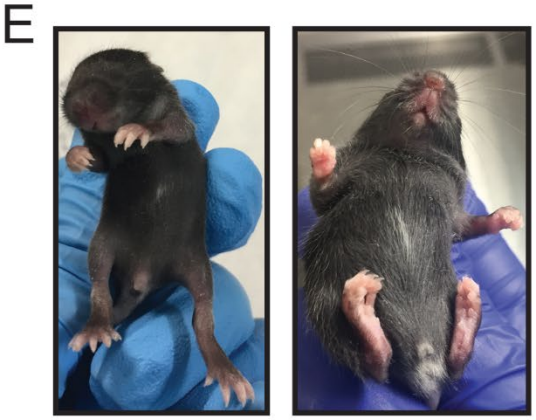
E

Figure 5.1. Spotting occurs in the *Mitf-M* knockout mice. **A)** Representative photographs of littermates including wildtype, *Mitf-M* knockout, and *Mitf-M* knockout with a spot taken at P50. **B)** Distribution of genotypes from heterozygous breeding pairs. **C)** Frequency of spotting in *Mitf-M* knockout pups within the breeding colony from heterozygous pairs (4.20%), homozygous pairs (5.39%), and all breeding pairs combined (4.95%). **D)** Representative hematoxylin & eosin staining of skin from *Mitf-M* knockout spotted mice. (a) highlights border of one spot where unpigmented or lightly pigmented hairs (dashed arrows) are neighboring pigmented hairs (solid arrows), (b) are unpigmented follicles from a sperate mouse found on the same section as pigmented follicles of the spot. **E)** Representative *Mitf-M* heterozygotes with white belly spots.

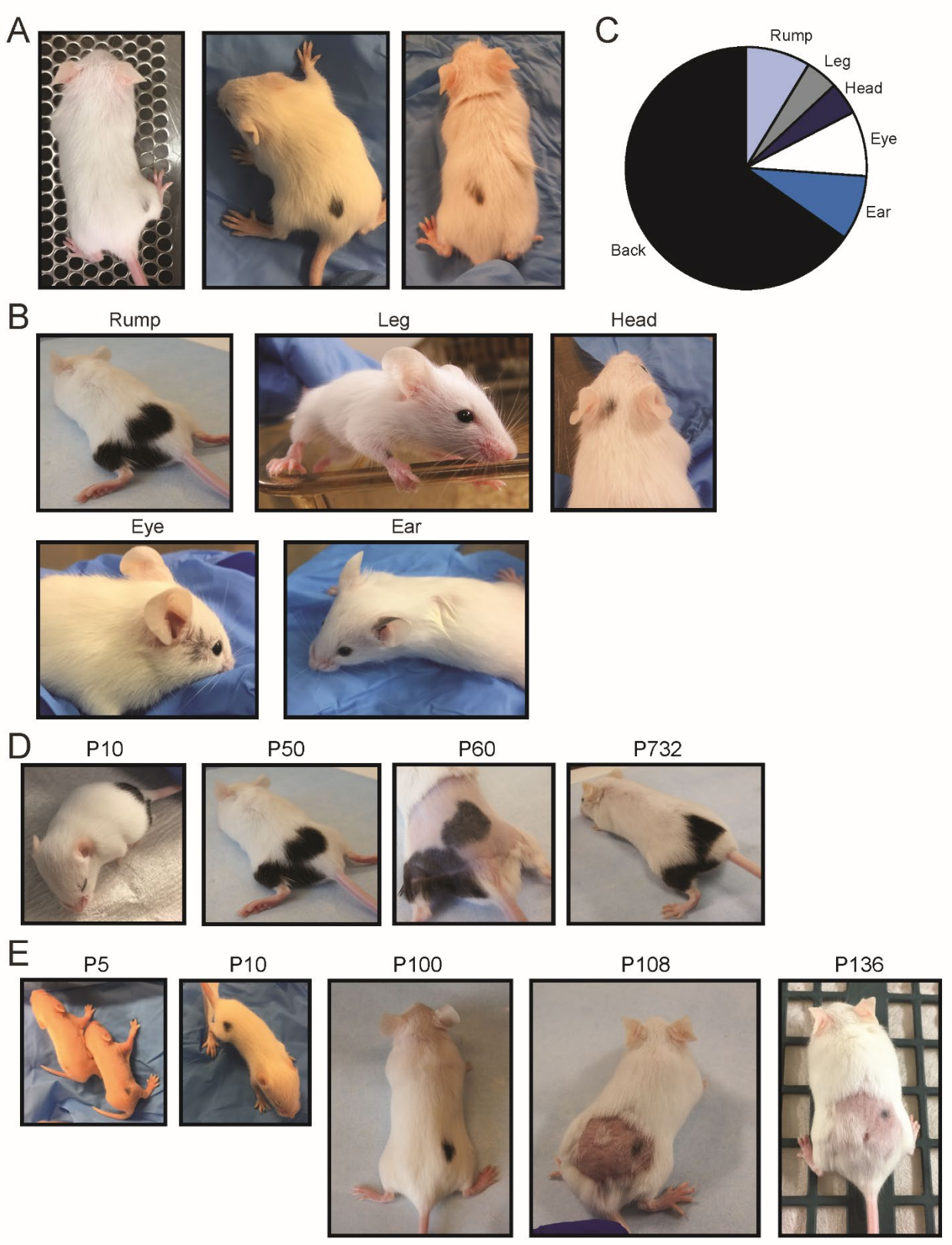
A
C
Rump
Leg
Head
Eye
Ear
Back
B
Rump
Leg
Head
Eye
Ear
D
P10
P50
P60
P732
E
P5
P10
P100
P108
P136

Figure 5.2. Representative images of spotted *Mitf-M* knockout mice. A) Representative images of *Mitf-M* knockout mice with spots along the back (total of 15 mice, 2 had additional spots in other body regions). **B)** Additional spots were occasionally observed on the rump (2 mice), head (1 mouse), ear (2 mice), leg (1 mouse), and around the eye (2 mice). **C)** Frequency of spotting by body region (two mice had discernable spots in two distinct body regions). **D)** Representative images of a mouse with two large spots, one on the back and one on the rump. Images were captured on indicated postnatal days, where P60 image was taken following shave and depilation on P50. **E)** Representative image of another mouse where spots were visible as early as P5. This mouse was shaved and depilated at P100 and reimaged at P108.

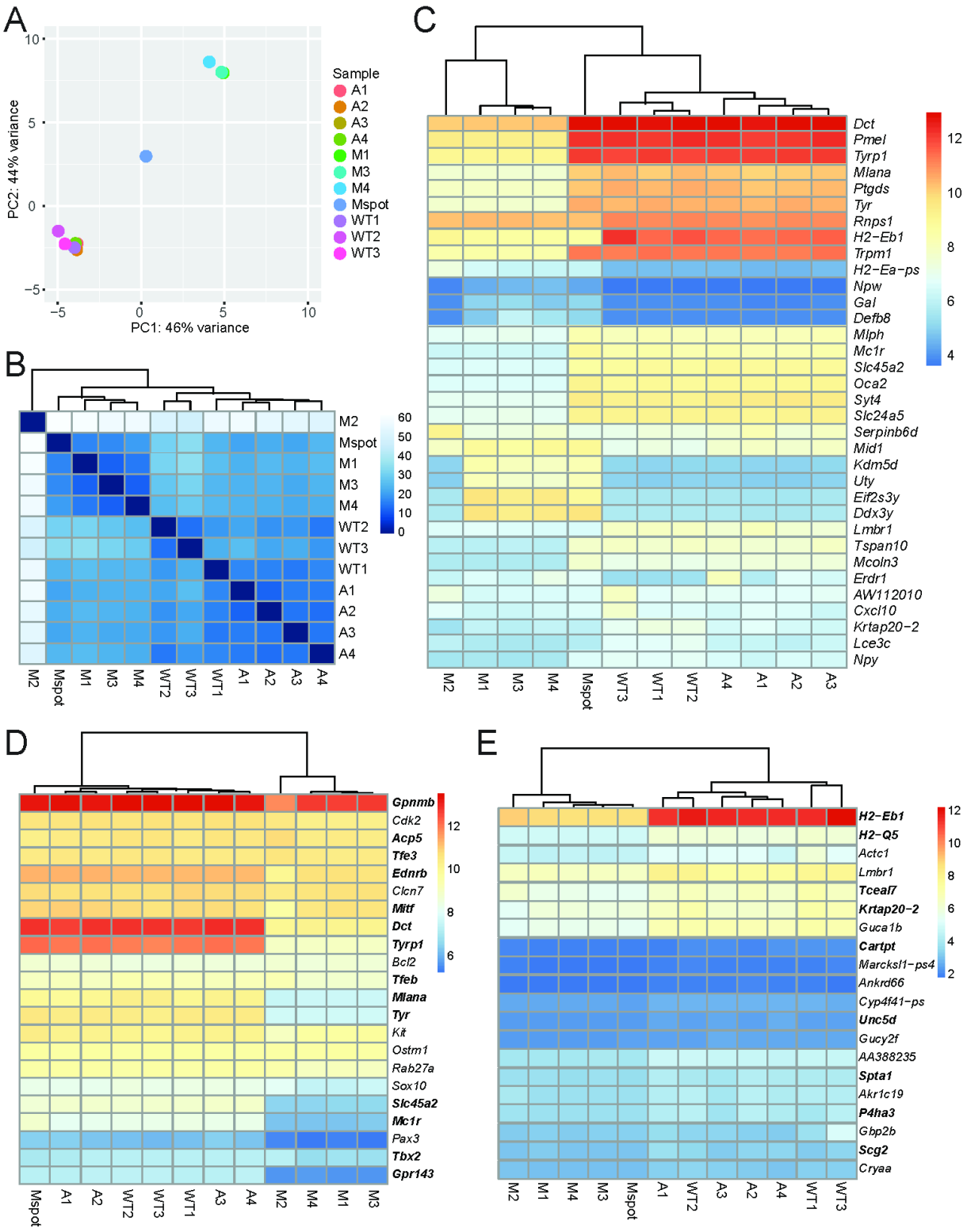
A
PC2: 44% variance
PC1: 46% variance
Sample
A1
A2
A3
A4
M1
M3
M4
Mspot
WT1
WT2
WT3
B
C
Dct
Pmel
Tyrp1
Mlana
Ptgds
Tyr
Rnps1
H2-Eb1
Trpm1
H2-Ea-ps
Npw
Gal
Defb8
Mlph
Mc1r
Slc45a2
Oca2
Syt4
Slc24a5
Serpinb6d
Mid1
Kdm5d
Uty
Eif2s3y
Ddx3y
Lmbr1
Tspan10
Mcoln3
Erdr1
AW112010
Cxcl10
Krtap20-2
Lce3c
Npy
D
Gpnmb
Cdk2
Acp5
Tfe3
Ednrb
Clcn7
Mitf
Dct
Tyrp1
Bcl2
Tfeb
Mlana
Tyr
Kit
Ostm1
Rab27a
Sox10
Slc45a2
Mc1r
Pax3
Tbx2
Gpr143
E
H2-Eb1
H2-Q5
Actc1
Lmbr1
Tceal7
Krtap20-2
Guca1b
Cartpt
Marcksl1-ps4
Ankrd66
Cyp4f41-ps
Unc5d
Gucy2f
AA388235
Spta1
Akr1c19
P4ha3
Gbp2b
Scg2
Cryaa

Figure 5.3. *Mitf-M* knockout spots have partial rescue of wildtype gene expression. A) PCA of RNA sequencing data highlighting similarities between wildtype (WT1-3) and *Mitf-A* knockout (A1-4) samples. *Mitf-M* knockout skin has distinct gene expression (M1-4, M2 was excluded from plot) from wildtype, but skin from the spot has an intermediate gene expression profile. **B)** MA plot highlighting similarities between samples. **C)** Heatmap of the top 20 downregulated and top 10 upregulated genes in *Mitf-M* knockout mice compared to wildtype combined with the top differentially expressed genes in *Mitf-A* knockout mice compared to wildtype, log2 fold change more than 1-fold with padj < 0.05. **D)** Heatmap of known *Mitf* target genes, bolded genes have MITF binding motif detailed in Table 5.5. **E**) Heatmap of top 20 downregulated genes in *Mitf-M* knockout mice compared against all other samples, bolded genes have MITF binding motif detailed in Table 5.5.

A

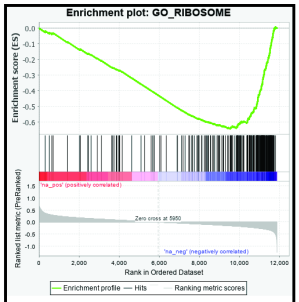

Rps21, Mrps21, Rpl41, Rplp2, Rpl37, Mrpl23, Rps15, Rpl21, Rpl28, Mrps28

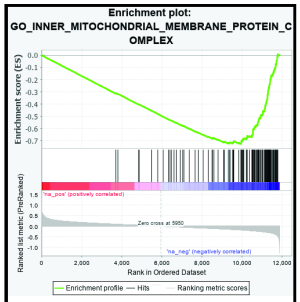

Cox6a2, Romo1, Cox4i2, Ndufa2, Chchd10, Ndufa13, Atp5f1e, Ndufc1, Cox6a1

C

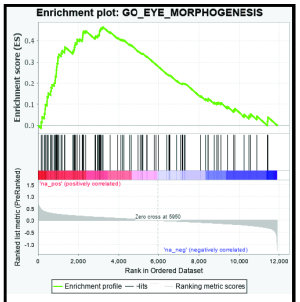

Zeb1, Fbn2, Cep290, Fbn1, Ccdc66, Ptprm, Nipbl, Tenm3, Tspan12, Dll1

B

Enriched Gene Sets for Wildtype and *Mitf-A* knockout

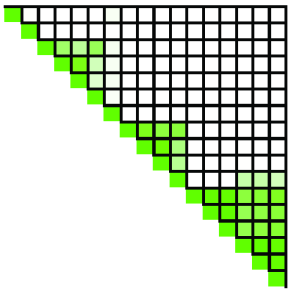

GO_CENTRIOLE
GO_NEURON_PROJECTION_ARBORIZATION
GO_EXTRACELLULAR_MATRIX_STRUCTURAL_CONSTITUENT
GO_EXTRACELLULAR_MATRIX_STRUCTURAL_CONSTITUENT_CONFERRING_TENSILE_STRENGTH
GO_COMPLEX_OF_COLLAGEN_TRIMERS
GO_BASEMENT_MEMBRANE
GO_EYE_MORPHOGENESIS
GO_INNER_MITOCHONDRIAL_MEMBRANE_PROTEIN_COMPLEX
GO_OXIDATIVE_PHOSPHORYLATION
GO_ATP_SYNTHESIS_COUPLED_ELECTRON_TRANSPORT
GO_MITOCHONDRIAL_PROTEIN_COMPLEX
GO_CYTOSOLIC_RIBOSOME
GO_ESTABLISHMENT_OF_PROTEIN_LOCALIZATION_TO_ENDOPLASMIC_RETICULUM
GO_COTRANSLATIONAL_PROTEIN_TARGETING_TO_MEMBRANE
GO_RIBOSOME
GO_RIBOSOMAL_SUBUNIT
GO_STRUCTURAL_CONSTITUENT_OF_RIBOSOME

Figure 5.4. Enriched gene sets in pairwise comparison of wildtype and *Mitf-A* knockout mice. **A)** Enrichment plots for ribosome and inner mitochondrial membrane protein complex gene ontology sets comparing wildtype (positive, red) and *Mitf-A* knockout mice (negative, blue). **B)** Top enriched gene ontology sets using log2 fold change in expression when comparing skin from wildtype (black, n = 3) and *Mitf-A* knockout mice (red, n = 4). Cutoff for gene set enrichment was family-wise error rate $p < 0.25$, false discovery rate $q < 0.1$, nominal $p < 0.05$ with no more than 10 depicted for each comparison. **C)** Enrichment plot for eye morphogenesis gene set comparing wildtype (positive, red) and *Mitf-A* null (negative, blue) mice with list of top 10 depleted markers in *Mitf-A* knockout skin

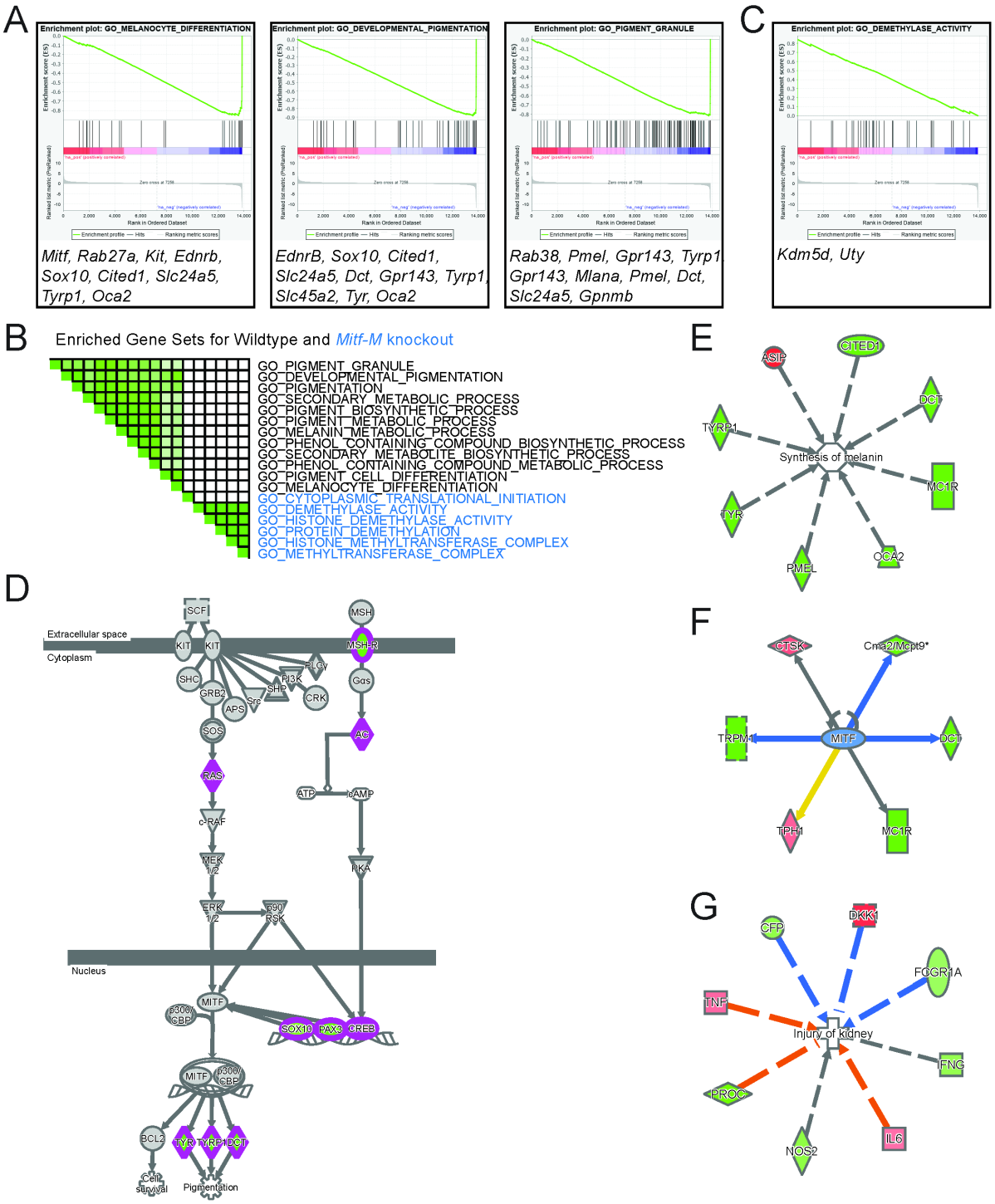
A
Enrichment plot: GO_MELANOCYTE_DIFFERENTIATION
Mitf, Rab27a, Kit, Ednrb, Sox10, Cited1, Slc24a5, Tyrp1, Oca2
Enrichment plot: GO_DEVELOPMENTAL_PIGMENTATION
EdnrB, Sox10, Cited1, Slc24a5, Dct, Gpr143, Tyrp1, Slc45a2, Tyr, Oca2
Enrichment plot: GO_PIGMENT_GRANULE
Rab38, Pmel, Gpr143, Tyrp1 Gpr143, Mlana, Pmel, Dct, Slc24a5, Gpnmb
C
Enrichment plot: GO_DEMETHYLASE_ACTIVITY
Kdm5d, Uty
B
Enriched Gene Sets for Wildtype and Mitf-M knockout
GO_PIGMENT_GRANULE
GO_DEVELOPMENTAL_PIGMENTATION
GO_PIGMENTATION
GO_SECONDARY_METABOLIC_PROCESS
GO_PIGMENT_BIOSYNTHETIC_PROCESS
GO_PIGMENT_METABOLIC_PROCESS
GO_MELANIN_METABOLIC_PROCESS
GO_PHENOL_CONTAINING_COMPOUND_BIOSYNTHETIC_PROCESS
GO_SECONDARY_METABOLITE_BIOSYNTHETIC_PROCESS
GO_PHENOL_CONTAINING_COMPOUND_METABOLIC_PROCESS
GO_PIGMENT_CELL_DIFFERENTIATION
GO_MELANOCYTE_DIFFERENTIATION
GO_CYTOPLASMIC_TRANSLATIONAL_INITIATION
GO_DEMETHYLASE_ACTIVITY
GO_HISTONE_DEMETHYLASE_ACTIVITY
GO_PROTEIN_DEMETHYLATION
GO_HISTONE_METHYLTRANSFERASE_COMPLEX
GO_METHYLTRANSFERASE_COMPLEX
D
Extracellular space
Cytoplasm
Nucleus
SCF
KIT
KIT
MSH
MSH-R
SHC
GRB2
APS
Src
PLCγ
PI3K
SHP
CRK
Gαs
AC
SOS
RAS
ATP
cAMP
c-RAF
MEK 1/2
PKA
ERK 1/2
p90 RSK
MITF
p300/ CBP
SOX10 PAX3 CREB
MITF
p300/ CBP
BCL2
TYR
TYRP1
DCT
Cell survival
Pigmentation
E
ASIP
CITED1
DCT
TYRP1
Synthesis of melanin
MC1R
TYR
PMEL
OCA2
F
CTSK
Cma2/Mcpt9*
TRPM1
MITF
DCT
TPH1
MC1R
G
CFP
DKK1
FGGR1A
TNF
Injury of kidney
IFNG
PROC
NOS2
IL6

Figure 5.5. Enriched gene sets in pairwise comparison of wildtype and *Mitf-M* knockout mice. **A)** Enrichment plots for melanocyte differentiation, developmental pigmentation, and pigment granule gene sets comparing wildtype (positive, red) and *Mitf-M* null (negative, blue) mice, with list of depleted markers in *Mitf-M* null skin. **B)** Enriched gene ontology sets for wildtype (black, n = 3) versus *Mitf-M* knockout mice (blue, n = 4) comparison. Cutoff for gene set enrichment was family-wise error rate $p < 0.25$, false discovery rate $q < 0.1$, nominal $p < 0.05$ with no more than 10 depicted for each comparison. **C)** Enrichment plot for demethylase activity, with list of enriched markers in *Mitf-M* knockout skin. **D)** Diagram of the IPA melanocyte development and pigmentation signaling network, highlighting in green genes that are repressed in the *Mitf-M* knockout mice data set (*Msh-r* (or *Mc1r), Sox10, Pax3, Tyr, Tyrp1,* and *Dct*). Purple outlines indicate genes that were also present in the dataset. **E)** Synthesis of melanin, a representative biological function that is altered based on changes in the gene expression of component genes in *Mitf-M* knockout mice. Gene boxes in green are downregulated in *Mitf-M* knockout mice, while red indicates upregulation. **E)** Predicted inhibition of MITF in *Mitf-M* knockout mouse skin versus wildtype skin based on target gene expression using upstream analysis in IPA. Blue indicates predicted inhibition, green denotes downregulated genes, and red highlights upregulated genes. **F)** Misregulation of genes associated with injury of the kidney in *Mitf-M* knockout skin. Blue indicates predicted inhibition, orange predicts activation, green denotes downregulated genes, and red highlights upregulated genes.

A

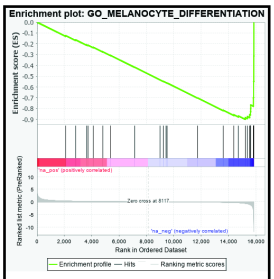

Oca2, Tyrp1, Slc24a5, Cited1, Sox10, Lrmda, Ednrb, Kit, Rab27a, Mitf

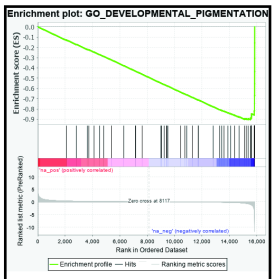

Oca2, Tyr, Slc45a2, Tyrp1, Gpr143, Dct, Slc24a5, Cited1, Sox10, Lrmda

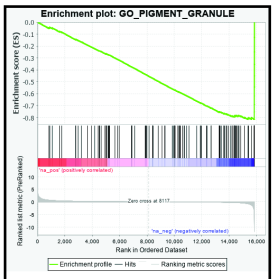

Oca2, Tyr, Slc45A2, Tyrp1, Gpr143, Mlana, Pmel, Dct, Slc24a5, Gpnmb

C

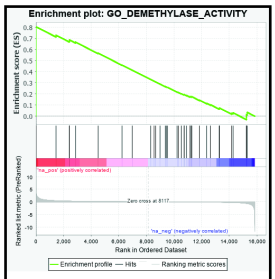

Kdm5d, Uty

B

Enriched Gene Sets for *Mitf-A* knockout and *Mitf-M* knockout

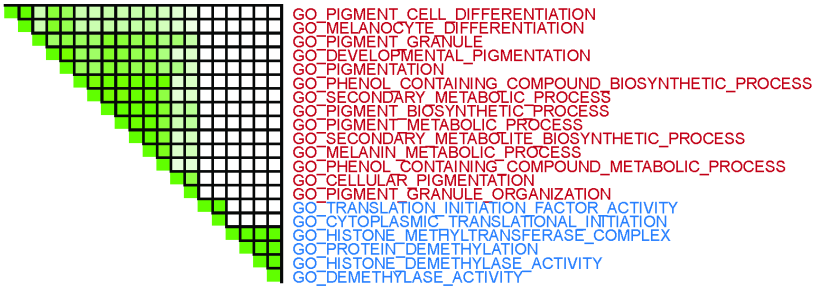

Figure 5.6. Enriched gene sets in comparison of *Mitf-A* knockout mice and *Mitf-M* knockout mice. A). Enrichment plots for melanocyte differentiation, developmental pigmentation, and pigment granule gene sets comparing *Mitf-A* null (positive, red) and *Mitf-M* null (negative, blue) mice, with list of depleted markers in *Mitf-M* null skin. **B)** Enriched gene sets for *Mitf-A* knockout mice (red, n = 4) compared with *Mitf-M* knockout mice (blue, n = 4). Cutoff for gene set enrichment was family-wise error rate $p < 0.25$, false discovery rate $q < 0.1$, nominal $p < 0.05$ with no more than 10 depicted for each comparison. **C)** Enrichment plot for demethylase activity, with list of enriched markers in *Mitf-M* knockout skin compared to *Mitf-A* knockout skin.

A

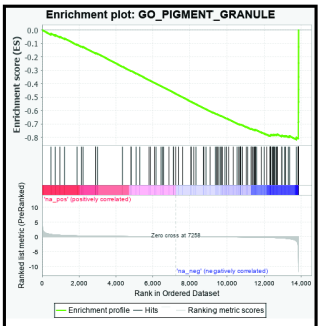

Oca2, Tyr, GPR143, Tyrp1, Slc45a2, Pmel, Mlana, Dct, Slc24a5, Rab38

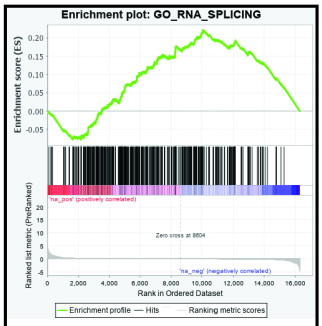

Elavl2, Celf6, Rbm11, Khdrbs2, Rnf113A, Slc39a5, Elavl4, Nova2, Srek1ip1

C

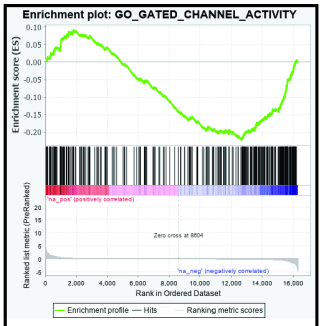

Lrrc26, Chrng, Cnga2, Tmc2 Catsper1, Cngb3, Cnga1, Asic5, Gabra2, Snap25

B

Enriched Gene Sets for *Mitf-M* knockout and *Mitf-M* knockout mouse with spot

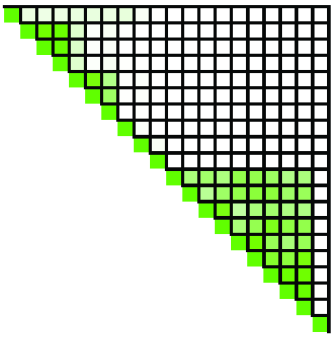

GO_RNA_CATABOLIC_PROCESS
GO_MRNA_PROCESSING
GO_RNA_SPLICING_VIA_TRANSESTERIFICATION_REACTIONS
GO_RNA_SPLICING
GO_RIBONUCLEOPROTEIN_COMPLEX_BIOGENESIS
GO_RIBOSOME_BIOGENESIS
GO_NCRNA_METABOLIC_PROCESS
GO_REGULATION_OF_CELL_CYCLE_PHASE_TRANSITION
GO_CADHERIN_BINDING
GO_PIGMENT_GRANULE
GO_POTASSIUM_CHANNEL_ACTIVITY
GO_CATION_CHANNEL_COMPLEX
GO_MONOVALENT_INORGANIC_CATION_TRANSMEMBRANE_TRANSPORTER_ACTIVITY
GO_METAL_ION_TRANSMEMBRANE_TRANSPORTER_ACTIVITY
GO_VOLTAGE_GATED_CATION_CHANNEL_ACTIVITY
GO_VOLTAGE_GATED_ION_CHANNEL_ACTIVITY
GO_CATION_CHANNEL_ACTIVITY
GO_PASSIVE_TRANSMEMBRANE_TRANSPORTER_ACTIVITY
GO_GATED_CHANNEL_ACTIVITY
GO_G_PROTEIN_COUPLED_RECEPTOR_ACTIVITY

D

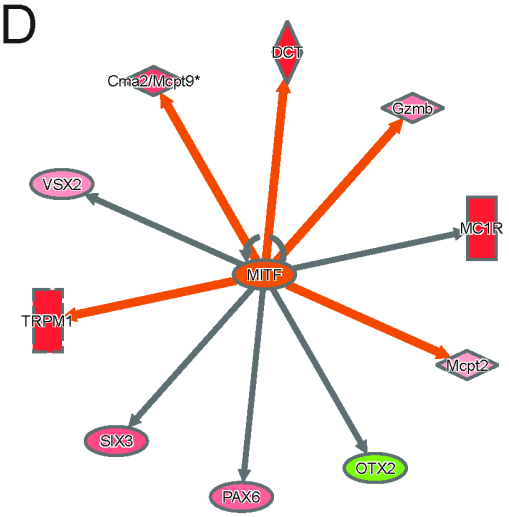

Figure 5.7. Enriched gene sets in comparison of unspotted *Mitf-M* knockout mice to a spotted *Mitf-M* knockout mouse. **A)** Enrichment plot for pigment granule and RNA splicing gene ontology sets comparing unspotted *Mitf-M* knockout mice (positive, red) and skin samples from a spotted *Mitf-M* knockout mouse (negative, blue) with a list of top 10 enriched markers from the spotted mouse. **B)** Top enriched gene sets when comparing black-eyed white *Mitf-M* knockout mice (blue, n = 2) with skin samples from a *Mitf-M* knockout mouse with spots (green, samples included both white and spotted skin). Cutoff for gene set enrichment was family-wise error rate $p < 0.25$, false discovery rate $q < 0.1$, nominal $p < 0.05$ with no more than 10 depicted for each comparison. **C)** Enrichment plot for gated channel activity that is enriched in unspotted mice compared to the spotted mouse. **D)** Predicted activation of MITF activity using IPA upstream regulator analysis. Orange indicates predicted activation, red denotes upregulated genes, and green highlights downregulated genes.

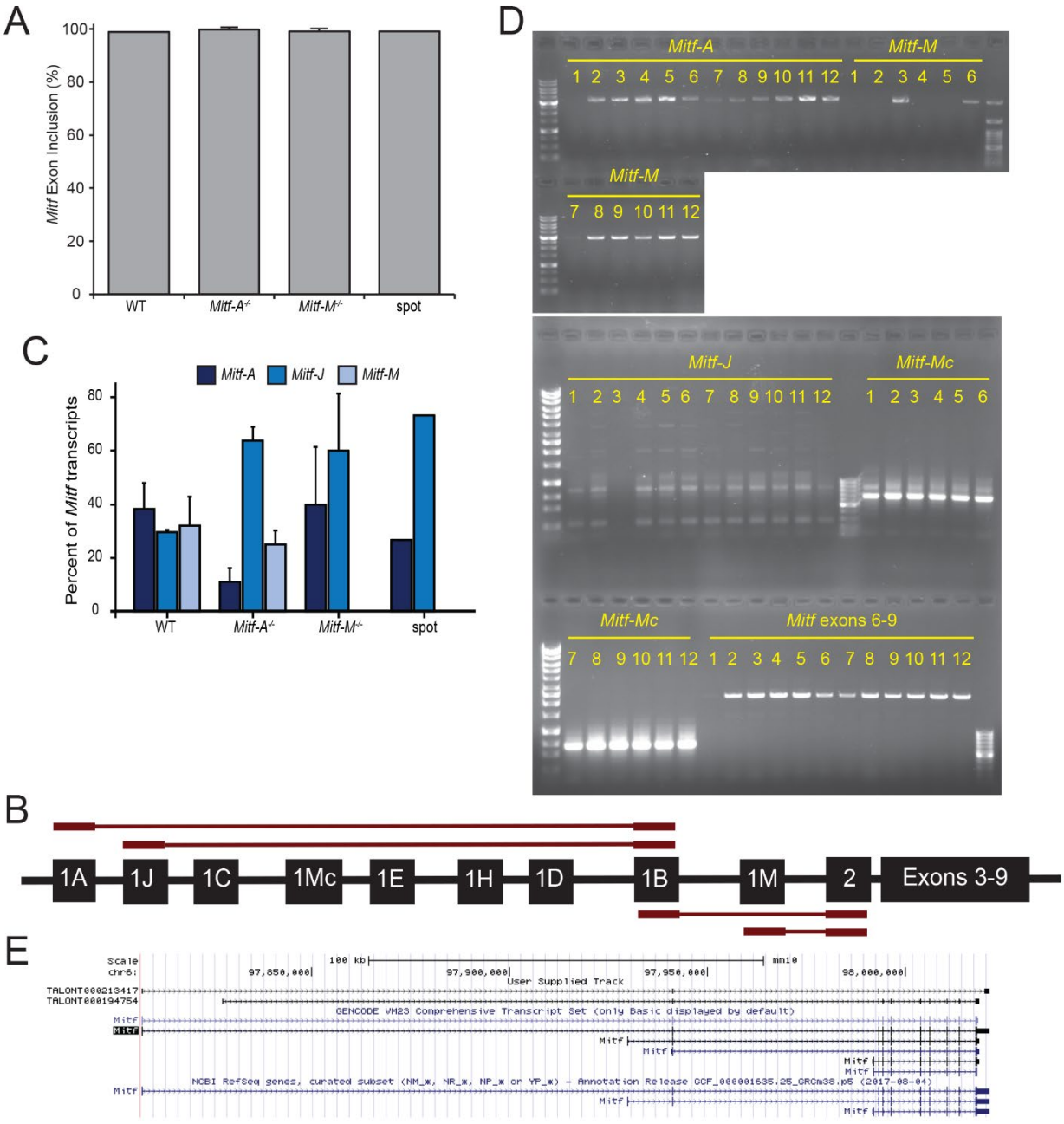
A
Mitf Exon Inclusion (%)
100
80
60
40
20
0
WT
Mitf-A-/-
Mitf-M-/-
spot
C
Mitf-A
Mitf-J
Mitf-M
Percent of Mitf transcripts
80
60
40
20
0
WT
Mitf-A-/-
Mitf-M-/-
spot
D
Mitf-A
1 2 3 4 5 6 7 8 9 10 11 12
Mitf-M
1 2 3 4 5 6
Mitf-M
7 8 9 10 11 12
Mitf-J
1 2 3 4 5 6 7 8 9 10 11 12
Mitf-Mc
1 2 3 4 5 6
Mitf-Mc
7 8 9 10 11 12
Mitf exons 6-9
1 2 3 4 5 6 7 8 9 10 11 12
B
1A
1J
1C
1Mc
1E
1H
1D
1B
1M
2
Exons 3-9
E
Scale
chr6:
100 kb
mm10
97,850,000
97,900,000
97,950,000
98,000,000
User Supplied Track
TALONT000213417
TALONT000194754
GENCODE VM23 Comprehensive Transcript Set (only Basic displayed by default)
Mitf
NCBI RefSeq genes, curated subset (NM_*, NR_*, NP_* or YP_*) - Annotation Release GCF_000001635.25_GRCm38.p5 (2017-08-04)

Figure 5.8. *Mitf* isoform-specific changes in *Mitf* knockout mice. A) Combined percent of inclusion of rare skipped exons (2, 3, 4, or 6) in the *Mitf* gene. Graph depicts mean (WT and spot) or mean ± standard deviation (*Mitf-A*$^{-/-}$ and *Mitf-M*$^{-/-}$). **B)** Overview of read junction counting strategy for individual isoforms of *Mitf*. **C)** *Mitf* isoform abundance in *Mitf* knockout mice, with mean ± standard error shown, n = 2 WT, 4 *Mitf-A* knockouts, 4 *Mitf-M* knockouts, 1 spot from *Mitf-M* knockout. **D)** Full-length PCR products using specified *Mitf* isoform specific primer sets. Full-length transcripts are 3246 bp (*Mitf-A*), 3555 bp (*Mitf-J*), 2993 bp (*Mitf-M*), and 2320 bp (exons 6-9). Samples #1-5 are from *Mitf-M*$^{-/-}$ mice (sample #3 is from a spot), samples #6-8 are from wildtype mice, samples #9-12 are from *Mitf-A*$^{-/-}$ mice. **E)** UCSC GenomeBrowser view of full-length *Mitf* transcripts. TALONT000213417 corresponds to an 1A driven transcript and TALONT000194754 corresponds to a 1J driven transcript.


A
Ruler 1
Consensus
MitfM_transcript
MitfM_spliced_intronM2
MitfMspot_predictedM
Sequence Logo
Ruler 2

Figure 5.9. Predicted aberrant *Mitf-M* sequence from spot of *Mitf-M* knockout mouse. Shown are the canonical *Mitf-M* transcript, the *Mitf-M* transcript with the intron retained through the splice site with exon 2, and the predicted sequence from the spot containing the 18bp CRISPR knockout deletion (bounded by red box) and the intronic splice junction with exon 2. Nucleotides from the exons are capitalized and those from the intron are in lower case. The light blue bar denotes those nucleotides arising from exon 1M, the black bar denotes those from the intron, and blue denotes the start of exon 2. The red shaded boxes highlight all of the in-frame stop codons within the intronic region.

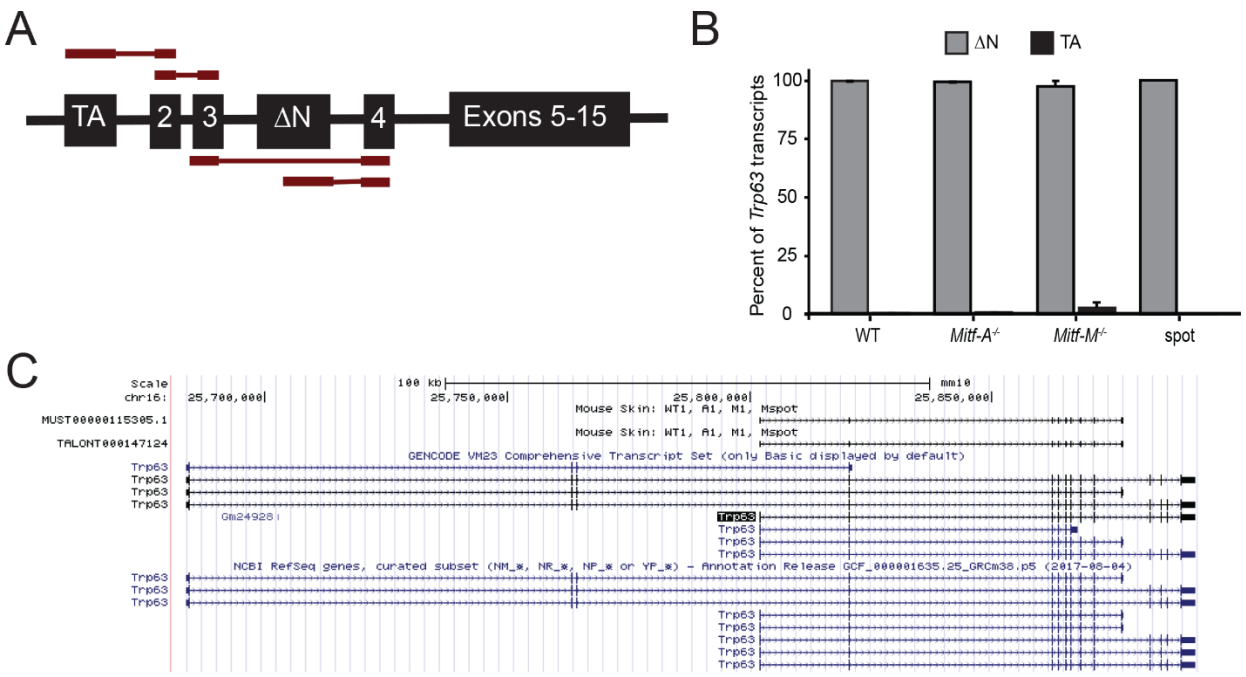
A
TA
2
3
ΔN
4
Exons 5-15
B
ΔN
TA
Percent of Trp63 transcripts
100
75
50
25
0
WT
Mitf-A-/-
Mitf-M-/-
spot
C
Scale
chr16:
25,700,000
25,750,000
25,800,000
25,850,000
100 kb
mm10
MUST00000115305.1
TALONT000147124
Mouse Skin: WT1, A1, M1, Mspot
Mouse Skin: WT1, A1, M1, Mspot
GENCODE VM23 Comprehensive Transcript Set (only Basic displayed by default)
Trp63
Gm24928
NCBI RefSeq genes, curated subset (NM_*, NR_*, NP_* or YP_*) - Annotation Release GCF_000001635.25_GRCm38.p5 (2017-08-04)

Figure 5.10. *Trp63* isoforms are unchanged in *Mitf* knockout mice. A) Depiction of read junctions to distinguish TA and ΔN promoter driven transcripts of *Trp63*. **B)** *Trp63* isoform abundance in wildtype and *Mitf* knockout mice. Mean ± standard error is shown, n = 3 WT, 4 *Mitf-A* knockouts, 4 *Mitf-M* knockouts, 1 spot from *Mitf-M* knockout mouse. **C)** UCSC Genome Browser (http://genome.ucsc.edu) view of full-length *Trp63* transcripts. ENSMUST00000115305.1 corresponds to the known MGI transcript Trp63-204 (and NCBI transcript NM_001127263.1) and TALONT000147124 corresponds to a novel-in-catalog isoform.

Table 5.1. Differentially expressed genes in whole skin by bulk RNA sequencing.

gene	baseMean	log2FoldChange	lfcSE	stat	pvalue	padj	GENENAME	UNIGENE	ENTREZID	A1	A2	A3	A4	M1	M2	M3	M4	Mspot	WT1	WT2	WT3
AA388235	24.4231	-6.7242	0.9414	-7.1432	9.12E-13	4.04E-10	expressed sequence AA388235	Mm.380381	433100	55	47	36	31	0	0	2	0	0	45	44	35
H2-Q5	64.6695	-6.4554	0.5833	-11.0669	1.82E-28	4.37E-25	histocompatibility 2, Q region locus 5	Mm.439648	15016	146	96	90	89	1	2	1	1	2	148	102	101
H2-Eb1	3029.0142	-6.2002	0.3307	-18.7468	2.06E-78	3.46E-74	histocompatibility 2, class II antigen E beta	Mm.22564	14969	4484	5129	4069	3965	71	169	55	55	82	4562	5500	7840
Gbp2b	18.9443	-4.8529	1.0363	-4.6831	2.83E-06	0.0003	guanylate binding protein 2b	Mm.457978	14468	16	3	5	1	2	0	2	1	7	23	9	150
Guca1b	118.0898	-4.4936	0.2919	-15.3946	1.78E-53	9.99E-50	guanylate cyclase activator 1B	Mm.59151	107477	209	205	167	140	17	0	13	10	10	252	210	186
Cartpt	4.5976	-4.0303	1.2011	-3.3555	0.0008	0.0266	CART prepropeptide	Mm.75498	27220	1	3	7	11	0	3	0	0	0	11	6	11
Actc1	40.5842	-3.9126	0.5947	-6.5789	4.74E-11	1.56E-08	actin, alpha, cardiac muscle 1	Mm.686	11464	67	66	47	16	3	13	3	5	7	175	42	53
Ankrd66	3.8930	-3.8428	1.1028	-3.4846	0.0005	0.0187	ankyrin repeat domain 66	Mm.17626	100043332	9	11	5	4	1	0	1	0	0	9	6	2
Gucy2f	5.9640	-3.5477	0.9067	-3.9130	9.12E-05	0.0050	guanylate cyclase 2f	Mm.208511	245650	8	10	14	9	0	0	0	0	4	10	7	9
Cryaa	9.8273	-3.4804	0.6295	-5.5287	3.23E-08	5.78E-06	crystallin, alpha A	Mm.1228	12954	19	12	15	6	1	4	0	2	2	18	23	16
Cyp4f41-ps	6.8167	-3.4721	0.7840	-4.4289	9.47E-06	0.0008	cytochrome P450, family 4, subfamily f, polypeptide 41 pseudogene	Mm.245027	77875	11	14	8	12	3	1	1	0	0	12	14	6
Spta1	16.8937	-3.1647	0.5201	-6.0845	1.17E-09	2.89E-07	spectrin alpha, erythrocytic 1	Mm.200611	20739	38	42	13	28	3	6	3	1	1	26	23	23
Akr1c19	18.1633	-3.1579	0.7864	-4.0158	5.93E-05	0.0036	aldo-keto reductase family 1, member C19	Mm.22832	432720	35	39	11	21	2	15	0	1	1	29	39	29
Marcksl1-ps4	4.0688	-3.1482	1.0049	-3.1330	0.0017	0.0472	MARCKS-like 1, pseudogene 4	Mm.482672	111002	5	4	4	5	0	5	0	0	0	4	10	11
P4ha3	17.6168	-3.0982	0.5959	-5.1989	2.01E-07	2.86E-05	procollagen-proline, 2-oxoglutarate 4-dioxygenase (proline 4-hydroxylase), alpha polypeptide III	Mm.150294	320452	33	42	7	22	5	7	2	2	3	16	38	38
Unc5d	5.8432	-3.0648	0.8834	-3.4695	0.0005	0.0195	unc-5 netrin receptor D	Mm.248433	210801	16	10	8	14	0	1	1	0	2	9	4	6
Krtap20-2	102.5549	-2.7784	0.6085	-4.5657	4.98E-06	0.0005	keratin associated protein 20-2	Mm.459837	622935	145	106	72	84	43	0	31	45	50	270	228	165
Lmbr1	193.1620	-2.7670	0.2480	-11.1578	6.66E-29	1.84E-25	limb region 1	Mm.41572	56873	460	250	174	204	59	55	47	40	56	353	351	298
Scg2	10.7462	-2.7450	0.7625	-3.6001	0.0003	0.0135	secretogranin II	Mm.5038	20254	38	20	3	14	4	3	1	3	1	7	23	16
Tceal7	92.0291	-2.5527	0.5631	-4.5334	5.80E-06	0.0005	transcription elongation factor A (SII)-like 7	Mm.18125	100040972	107	179	72	88	25	84	10	21	12	250	142	129
Nrk	12.2521	-2.5339	0.5239	-4.8364	1.32E-06	0.0002	Nik related kinase	Mm.482319	27206	31	22	18	22	3	2	2	2	4	20	13	10
Lce3c	81.8582	-2.5027	0.3151	-7.9428	1.98E-15	1.59E-12	late cornified envelope 3C	Mm.301748	94060	85	61	76	65	24	59	18	20	44	172	193	161
Gm17660	11.4051	-2.4510	0.5589	-4.3858	1.16E-05	0.0010	predicted gene, 17660	Mm.366664	100271704	18	18	21	11	5	0	0	4	8	17	17	18
Lce3a	39.1589	-2.4476	0.4405	-5.5566	2.75E-08	4.98E-06	late cornified envelope 3A	Mm.387664	545548	75	30	35	31	16	3	10	16	30	83	67	78
Hamp	14.5023	-2.3759	0.7294	-3.2574	0.0011	0.0343	hepcidin antimicrobial peptide	Mm.439939	84506	5	9	13	9	4	23	3	1	3	32	34	35
Lce3b	20.0184	-2.3562	0.4413	-5.3393	9.33E-08	1.48E-05	late cornified envelope 3B	Mm.443421	66344	24	22	21	30	10	0	11	5	10	31	39	35
Agtr2	20.4641	-2.2299	0.3660	-6.0922	1.11E-09	2.80E-07	angiotensin II receptor, type 2	Mm.2679	11609	19	25	17	33	10	9	7	5	10	44	38	28
Siglec1	589.0098	-2.1443	0.2394	-8.9590	3.28E-19	5.52E-16	sialic acid binding Ig-like lectin 1, sialoadhesin	Mm.1374	20612	1145	1097	445	857	169	247	163	161	310	1057	913	653
Gbp8	33.0494	-2.1357	0.5299	-4.0301	5.58E-05	0.0034	guanylate-binding protein 8	Mm.458519	76074	40	46	26	21	10	21	15	19	10	41	21	124
1700097N02Rik	7.5028	-2.0531	0.6430	-3.1929	0.0014	0.0412	RIKEN cDNA 1700097N02 gene	Mm.254797	67522	10	12	11	11	1	5	0	2	6	5	12	15
Wfdc12	35.9048	-2.0059	0.4154	-4.8285	1.38E-06	0.0002	WAP four-disulfide core domain 12	Mm.6433	192200	17	11	15	23	45	116	52	45	69	13	13	20
a	11.2902	-2.0090	0.6139	-3.2728	0.0011	0.0331	nonagouti	Mm.315593	50518	3	7	15	6	17	29	16	10	20	4	4	5
Mgarp	29.4369	-2.0985	0.5058	-4.1492	3.34E-05	0.0023	mitochondria localized glutamic acid rich protein	Mm.273339	67749	5	12	8	14	39	120	36	37	52	18	9	11
Aldh1l2	227.0846	-2.1461	0.3829	-5.6050	2.08E-08	3.90E-06	aldehyde dehydrogenase 1 family, member L2	Mm.263138	216188	140	147	128	98	492	138	412	326	666	123	54	84
Fam196b	16.3153	-2.2119	0.5831	-3.7936	0.0001	0.0073	family with sequence similarity 196, member B	Mm.444796	574403	11	8	7	10	32	5	31	30	50	6	7	5
Lrrtm3	13.5943	-2.4382	0.7269	-3.3544	0.0008	0.0266	leucine rich repeat transmembrane neuronal 3	Mm.431318	216028	9	8	2	4	24	3	35	22	50	8	3	3
D030045P18Rik	24.7244	-2.4448	0.5096	-4.7978	1.60E-06	0.0002	RIKEN cDNA D030045P18 gene	Mm.123343	320363	11	9	7	4	66	15	58	38	70	11	8	7
Rgag1	10.8998	-2.4861	0.6165	-4.0324	5.52E-05	0.0034	NA	NA	NA	20	6	7	5	13	21	17	13	25	4	3	2
Gm11127	8.1456	-2.5408	0.6724	-3.7785	0.0002	0.0076	predicted gene 11127	Mm.484641	100529082	3	2	0	6	8	15	15	23	21	4	2	2
Ptcra	8.1221	-2.7629	0.7159	-3.8593	0.0001	0.0059	pre T cell antigen receptor alpha	Mm.215173	19208	4	1	1	3	23	7	18	20	14	2	3	2
Gm4349	6.3093	-2.8126	0.8791	-3.1995	0.0014	0.0405	SET domain, bifurcated 1 pseudogene	Mm.412052	100043305	0	3	2	6	9	5	15	17	15	3	2	0
Prss41	17.4167	-3.0151	0.6322	-4.7689	1.85E-06	0.0002	protease, serine 41	Mm.328839	71003	5	8	3	3	47	10	49	40	33	7	4	2
Hapln4	28.4042	-3.0442	0.6215	-4.8984	9.66E-07	0.0001	hyaluronan and proteoglycan link protein 4	Mm.152048	330790	9	6	6	5	84	9	77	43	89	9	6	6
Mid1	331.5716	-3.2251	0.3816	-8.4517	2.87E-17	3.02E-14	midline 1	Mm.34441	17318	259	182	182	152	660	208	536	749	1001	96	50	46
Mmp8	8.9479	-3.3834	0.7960	-4.2506	2.13E-05	0.0016	matrix metallopeptidase 8	Mm.16415	17394	6	2	5	0	19	28	11	19	14	1	2	2
Pydc3	7.0976	-3.4273	0.9639	-3.5556	0.0004	0.0152	NA	NA	NA	2	4	2	0	11	6	7	22	33	1	0	3
Serpina3m	35.4891	-3.4616	0.7190	-4.8145	1.48E-06	0.0002	serine (or cysteine) peptidase inhibitor, clade A, member 3M	Mm.395085	20717	5	7	3	9	95	7	99	83	107	2	9	9
G530011O06Rik	36.8555	-3.5053	0.5392	-6.5013	7.96E-11	2.58E-08	RIKEN cDNA G530011O06 gene	Mm.34441	654820	15	37	20	46	51	35	84	64	83	7	7	2
Tpsab1	19.5498	-3.7308	0.8881	-4.2009	2.66E-05	0.0019	tryptase alpha/beta 1	Mm.3301	100503895	21	3	4	0	28	85	21	37	35	6	2	1
Tdo2	17.4552	-3.9813	0.9028	-4.4102	1.03E-05	0.0009	tryptophan 2,3-dioxygenase	Mm.258622	56720	4	2	3	4	43	1	50	35	68	2	2	3
Treml1	3.2370	-4.0825	1.2928	-3.1579	0.0016	0.0445	triggering receptor expressed on myeloid cells-like 1	Mm.90177	71326	3	1	1	2	5	10	6	4	7	1	0	0
Cd1d2	11.4088	-4.2173	0.8659	-4.8704	1.11E-06	0.0001	CD1d2 antigen	Mm.389465	12480	4	1	0	1	16	47	22	17	30	1	0	3
C7	412.1623	-4.8872	0.9524	-5.1313	2.88E-07	3.94E-05	complement component 7	Mm.208034	109828	44	25	22	22	988	14	1605	853	1404	61	12	23
4930426D05Rik	5.2575	-4.9217	1.3006	-3.7843	0.0002	0.0075	RIKEN cDNA 4930426D05 gene	Mm.329311	74644	0	2	1	3	13	6	16	13	8	1	0	0
Gal	28.5692	-5.2895	1.0944	-4.8334	1.34E-06	0.0002	galanin	Mm.4655	14419	0	0	2	2	78	1	94	60	112	2	1	2
Slc38a5	5.0493	-5.9063	1.5510	-3.8081	0.0001	0.0070	solute carrier family 38, member 5	Mm.6055	209837	1	0	1	2	7	0	19	12	21	0	0	0
Npw	19.7771	-6.0848	1.1615	-5.2386	1.62E-07	2.41E-05	neuropeptide W	Mm.291772	381073	2	2	1	0	46	11	59	72	46	1	1	0
Erdr1	123.4191	-8.4137	1.4652	-5.7423	9.34E-09	1.91E-06	erythroid differentiation regulator 1	Mm.76062	170942	31	169	80	542	115	66	81	224	161	0	1	0
Defb8	38.2247	-8.9292	2.8142	-3.1729	0.0015	0.0432	defensin beta 8	Mm.390008	244334	0	0	0	0	46	0	201	124	92	0	0	0
H2-Ea-ps	80.8346	-10.0097	1.2886	-7.7676	8.00E-15	5.61E-12	histocompatibility 2, class II antigen E alpha, pseudogene	Mm.15680	100504404	0	0	0	0	170	439	115	121	147	0	0	0
Uty	186.0187	-11.2121	2.9715	-3.7732	0.0002	0.0077	ubiquitously transcribed tetratricopeptide repeat gene, Y chromosome	Mm.20477	22290	0	0	0	0	633	0	460	436	793	0	0	0
Kdm5d	217.7495	-11.4393	2.9925	-3.8226	0.0001	0.0067	lysine (K)-specific demethylase 5D	Mm.262676	20592	0	0	0	0	769	0	563	521	846	0	0	0
Eif2s3y	522.1089	-12.7010	3.1196	-4.0714	4.67E-05	0.0029	eukaryotic translation initiation factor 2, subunit 3, structural gene Y-linked	Mm.250909	26908	0	0	0	0	1962	0	1368	1729	1257	0	0	0
Ddx3y	590.6037	-12.8788	3.1228	-4.1242	3.72E-05	0.0025	DEAD (Asp-Glu-Ala-Asp) box polypeptide 3, Y-linked	Mm.302938	26900	0	0	0	0	1893	0	1388	1655	2433	0	0	0

Table 5.2. Differentially expressed genes comparing wildtype and *Mitf-A* knockout skin.

gene	baseMean	log2FoldChange	lfcSE	stat	pvalue	padj	GENENAME	UNIGENE	ENTREZID	A1	A2	A3	A4	WT1	WT2	WT3
Lce3c	116.9140	-1.3314	0.1951	-6.8260	8.73E-12	3.60E-08	late cornified envelope 3C	Mm.301748	94060	85	61	76	65	172	193	161
Krtap20-2	151.3161	-1.1814	0.1979	-5.9704	2.37E-09	4.18E-06	keratin associated protein 20-2	Mm.459837	622935	145	106	72	84	270	228	165
Serpinb6d	203.0254	1.1813	0.2645	4.4668	7.94E-06	0.0021	serine (or cysteine) peptidase inhibitor, clade B, member 6d	Mm.249698	238568	444	198	259	196	152	114	85
Mid1	135.5812	1.5564	0.2420	6.4312	1.27E-10	3.13E-07	midline 1	Mm.34441	17318	259	182	182	152	96	50	46
Erdr1	121.4710	9.1896	1.7007	5.4033	6.54E-08	4.49E-05	erythroid differentiation regulator 1	Mm.76062	170942	31	169	80	542	0	1	0

Table 5.3. Differentially expressed genes comparing wildtype and *Mitf-M* knockout skin.

gene	baseMean	log2FoldChange	lfcSE	stat	pvalue	padj	GENENAME	UNIGENE	ENTREZID	M1	M2	M3	M4	WT1	WT2	WT3
Oca2	267.8463	-11.7441	1.0325	-11.3749	5.58E-30	5.09E-27	oculocutaneous albinism II	Mm.137052	18431	0	0	0	0	709	619	569
Tyr	826.3218	-11.3409	0.8484	-13.3669	9.44E-41	1.26E-37	tyrosinase	Mm.238127	22173	3	0	0	0	2244	1926	1686
Slc45a2	266.5037	-9.7069	0.8464	-11.4691	1.89E-30	1.82E-27	solute carrier family 45, member 2	Mm.138278	22293	2	0	1	0	687	602	593
Syt4	331.2448	-9.0191	0.6092	-14.8052	1.36E-49	2.94E-46	synaptotagmin IV	Mm.233846	20983	4	0	0	2	852	729	755
Tyrp1	2419.7091	-8.8008	0.2535	-34.7230	3.55E-264	6.15E-260	tyrosinase-related protein 1	Mm.30438	22178	16	15	9	11	6683	5350	5074
Gpr143	93.7489	-8.7828	1.0285	-8.5392	1.35E-17	8.37E-15	G protein-coupled receptor 143	Mm.5157	18241	0	0	0	2	225	223	212
Mc1r	195.6214	-8.5211	0.6665	-12.7845	2.00E-37	2.48E-34	melanocortin 1 receptor	Mm.324942	17199	1	1	3	0	519	435	426
Trpm1	1504.5278	-7.9756	0.2739	-29.1234	1.81E-186	1.05E-182	transient receptor potential cation channel, subfamily M, member 1	Mm.38875	17364	22	15	7	12	4097	3426	3089
Tspan10	133.2541	-7.9646	0.6774	-11.7579	6.43E-32	7.44E-29	tetraspanin 10	Mm.209875	208634	0	1	3	1	289	344	301
Mlana	763.3997	-7.2428	0.2799	-25.8723	1.36E-147	3.94E-144	melan-A	Mm.138437	77836	15	8	12	12	1590	1873	1859
Mcoln3	78.7193	-6.9379	0.6331	-10.9584	6.06E-28	5.25E-25	mucolipin 3	Mm.114683	171166	0	2	1	3	224	169	160
Pmel	2945.9523	-6.8735	0.2560	-26.8462	9.34E-159	3.24E-155	premelanosome protein	Mm.16756	20431	63	87	41	44	6387	7336	6797
Ptgds	892.2471	-6.6258	0.2048	-32.3526	1.28E-229	1.11E-225	prostaglandin D2 synthase (brain)	Mm.1008	19215	22	22	21	19	2020	2179	2016
H2-Q5	50.0842	-6.5428	0.6987	-9.3636	7.71E-21	5.35E-18	histocompatibility 2, Q region locus 5	Mm.439648	15016	1	2	1	1	148	102	101
AA388235	17.7975	-6.3655	1.0741	-5.9262	3.10E-09	8.53E-07	expressed sequence AA388235	Mm.380381	433100	0	0	2	0	45	44	35
H2-Eb1	2611.7383	-6.1261	0.4227	-14.4931	1.34E-47	2.32E-44	histocompatibility 2, class II antigen E beta	Mm.22564	14969	71	169	55	55	4562	5500	7840
Alx1	9.0811	-6.1169	1.1356	-5.3865	7.19E-08	1.54E-05	ALX homeobox 1	Mm.19287	216285	0	0	0	1	22	17	24
Gpr158	4.7440	-5.9272	1.3543	-4.3765	1.21E-05	0.0014	G protein-coupled receptor 158	Mm.166647	241263	0	0	0	0	19	5	10
Dct	4522.1190	-5.8212	0.2099	-27.7345	2.68E-169	1.16E-165	dopachrome tautomerase	Mm.19987	13190	177	133	185	240	10426	10680	10073
Slc24a5	334.3885	-5.6968	0.2658	-21.4344	6.38E-102	1.58E-98	solute carrier family 24, member 5	Mm.330538	317750	18	8	21	12	840	753	713
Gbp2b	27.4552	-5.6361	1.1544	-4.8822	1.05E-06	0.0002	guanylate binding protein 2b	Mm.457978	14468	2	0	2	1	23	9	150
Gucy2f	3.6766	-5.5571	1.2901	-4.3074	1.65E-05	0.0018	guanylate cyclase 2f	Mm.208511	245650	0	0	0	0	10	7	9
B3galt5	50.2813	-4.9288	0.4908	-10.0430	9.87E-24	7.78E-21	UDP-Gal:betaGlcNAc beta 1,3-galactosyltransferase, polypeptide 5	Mm.154783	93961	2	9	2	2	127	126	89
Guca1b	97.1407	-4.4043	0.6059	-7.2692	3.62E-13	1.65E-10	guanylate cyclase activator 1B	Mm.59151	107477	17	0	13	10	252	210	186
Actc1	40.6080	-3.8934	0.6834	-5.6970	1.22E-08	3.02E-06	actin, alpha, cardiac muscle 1	Mm.686	11464	3	13	3	5	175	42	53
Npy	75.0415	-3.6140	0.3122	-11.5761	5.45E-31	5.90E-28	neuropeptide Y	Mm.154796	109648	18	9	8	17	154	166	157
Cryaa	9.0326	-3.4518	0.7504	-4.5998	4.23E-06	0.0006	crystallin, alpha A	Mm.1228	12954	1	4	0	2	18	23	16
Fabp7	34.2222	-3.3012	0.4404	-7.4963	6.56E-14	3.16E-11	fatty acid binding protein 7, brain	Mm.3644	12140	5	14	5	5	67	61	84
Fstl4	10.1018	-3.2083	0.6721	-4.7733	1.81E-06	0.0003	follistatin-like 4	Mm.44518	320027	2	1	3	3	30	17	16
Wdr95	13.2893	-3.1963	0.5748	-5.5606	2.69E-08	6.39E-06	WD40 repeat domain 95	Mm.136919	381693	2	5	1	4	29	24	29
P4ha3	15.4702	-2.9629	0.6436	-4.6035	4.15E-06	0.0006	procollagen-proline, 2-oxoglutarate 4-dioxygenase (proline 4-hydroxylase), alpha polypeptide III	Mm.150294	320452	5	7	2	2	16	38	38
Gm17660	8.6697	-2.9408	0.8577	-3.4285	0.0006	0.0361	predicted gene, 17660	Mm.366664	100271704	5	0	0	4	17	17	18
Spta1	12.0108	-2.8872	0.5753	-5.0183	5.21E-07	8.78E-05	spectrin alpha, erythrocytic 1	Mm.200611	20739	3	6	3	1	26	23	23
Pax3	41.7798	-2.8228	0.3674	-7.6831	1.55E-14	8.16E-12	paired box 3	Mm.1371	18505	12	20	9	6	91	84	74
Mlph	174.5654	-2.7972	0.2047	-13.6624	1.70E-42	2.46E-39	melanophilin	Mm.105208	171531	51	42	60	45	393	351	294
Lce3a	38.7119	-2.7479	0.4489	-6.1221	9.23E-10	2.81E-07	late cornified envelope 3A	Mm.387664	545548	16	3	10	16	83	67	78
Limbr1	170.1559	-2.7302	0.1927	-14.1662	1.48E-45	2.34E-42	limb region 1	Mm.41572	56873	59	55	47	40	353	351	298
Atp6v0d2	111.9238	-2.6638	0.3578	-7.4442	9.75E-14	4.57E-11	ATPase, H+ transporting, lysosomal V0 subunit D2	Mm.19298	242341	39	17	31	50	254	243	160
Nrk	7.2980	-2.6584	0.6952	-3.8240	0.0001	0.0103	Nik related kinase	Mm.482319	27206	3	2	2	2	20	13	10
Slc24a4	109.4926	-2.6408	0.5235	-5.0446	4.55E-07	7.80E-05	solute carrier family 24 (sodium/potassium/calcium exchanger), member 4	Mm.312448	238384	32	7	48	48	243	227	170
Lce3c	91.3869	-2.5525	0.4026	-6.3361	2.36E-10	7.71E-08	late cornified envelope 3C	Mm.301748	94060	24	59	18	20	172	193	161
Scg2	8.1541	-2.4965	0.7505	-3.3263	0.0009	0.0484	secretogranin II	Mm.5038	20254	4	3	1	3	7	23	16
Gm2115	28.5612	-2.4459	0.3932	-6.2209	4.94E-10	1.53E-07	predicted gene 2115	Mm.44882	100039239	5	16	7	12	54	51	57
Lce3b	18.6943	-2.4098	0.6992	-3.4468	0.0006	0.0342	late cornified envelope 3B	Mm.443421	66344	10	0	11	5	31	39	35
Tceal7	92.2628	-2.3246	0.6127	-3.7939	0.0001	0.0113	transcription elongation factor A (SII)-like 7	Mm.18125	100040972	25	84	10	21	250	142	129
Glrb	88.3949	-2.2931	0.2690	-8.5252	1.53E-17	9.12E-15	glycine receptor, beta subunit	Mm.275639	14658	41	22	35	35	199	153	141
Siglec1	479.0554	-2.2371	0.2164	-10.3394	4.67E-25	3.86E-22	sialic acid binding Ig-like lectin 1, sialoadhesin	Mm.1374	20612	169	247	163	161	1057	913	653
Agtr2	19.8740	-2.2347	0.4186	-5.3380	9.40E-08	1.92E-05	angiotensin II receptor, type 2	Mm.2679	11609	10	9	7	5	44	38	28
Addb	14.6409	-2.0718	0.4802	-4.3140	1.60E-05	0.0017	androglobin	Mm.246573	215772	4	9	8	4	31	28	20
Aldh1l2	233.0700	2.0053	0.4645	4.3167	1.58E-05	0.0017	aldehyde dehydrogenase 1 family, member L2	Mm.263138	216188	492	138	412	326	123	54	84
a	11.9848	2.0453	0.6120	3.3421	0.0008	0.0462	nonagouti	Mm.315593	50518	17	29	16	10	4	4	5
Wfdc12	42.6554	2.0479	0.4656	4.3983	1.09E-05	0.0013	WAP four-disulfide core domain 12	Mm.6433	192200	45	116	52	45	13	13	20
H2-Q1	41.3943	2.1436	0.6459	3.3189	0.0009	0.0491	histocompatibility 2, Q region locus 1	Mm.466882	15006	33	145	41	36	12	8	22
Mqarp	37.6225	2.1825	0.5582	3.9098	9.24E-05	0.0076	mitochondria localized glutamic acid rich protein	Mm.273339	67749	39	120	36	37	18	9	11
D030045P18Rik	29.1353	2.3810	0.5974	3.9854	6.74E-05	0.0058	RIKEN cDNA D030045P18 gene	Mm.123343	320363	66	15	58	38	11	8	7
Rqap1	10.2875	2.4156	0.6317	3.8237	0.0001	0.0103	NA	NA	NA	13	21	17	13	4	3	2
Gm11127	9.6883	2.5139	0.7080	3.5507	0.0004	0.0247	predicted gene 11127	Mm.484641	100529082	8	15	15	23	4	2	2
Ptcra	10.7221	2.8762	0.7616	3.7766	0.0002	0.0119	pre T cell antigen receptor alpha	Mm.215173	19208	23	7	18	20	2	3	2
Haplln4	33.7474	2.9634	0.7396	4.0067	6.16E-05	0.0054	hyaluronan and proteoglycan link protein 4	Mm.152048	330790	84	9	77	43	9	6	6
Mid1	333.9929	3.1009	0.4592	6.7536	1.44E-11	5.56E-09	midline 1	Mm.34441	17318	660	208	536	749	96	50	46
Prss41	22.7698	3.1091	0.7186	4.3267	1.51E-05	0.0017	protease, serine 41	Mm.328839	71003	47	10	49	40	7	4	2
Serpina3m	43.7801	3.4127	0.8505	4.0126	6.01E-05	0.0053	serine (or cysteine) peptidase inhibitor, clade A, member 3M	Mm.395085	20717	95	7	99	83	2	9	9
G530011O06Rik	35.5852	3.4731	0.5465	6.3547	2.09E-10	6.96E-08	RIKEN cDNA G530011O06 gene	Mm.34441	654820	51	35	84	64	7	7	2
Mmp8	11.5245	3.5173	0.7868	4.4701	7.82E-06	0.0010	matrix metallopeptidase 8	Mm.16415	17394	19	28	11	19	1	2	2
Tdo2	19.6182	3.8080	1.0514	3.6219	0.0003	0.0198	tryptophan 2,3-dioxygenase	Mm.258622	56720	43	1	50	35	2	2	3
Tpsab1	24.9993	3.8277	0.7527	5.0852	3.67E-07	6.56E-05	tryptase alpha/beta 1	Mm.3301	100503895	28	85	21	37	6	2	1
Cd1d2	14.8370	4.2328	0.9119	4.6415	3.46E-06	0.0005	CD1d2 antigen	Mm.389465	12480	16	47	22	17	1	0	3
C7	513.2685	4.8171	1.2577	3.8300	0.0001	0.0102	complement component 7	Mm.208034	109828	988	14	1605	853	61	12	23

4930426D05Rik	6.9935	5.0752	1.3193	3.8470	0.0001	0.0096	RIKEN cDNA 4930426D05 gene	Mm.329311	74644	13	6	16	13	1	0	0
Gal	34.3720	5.1561	1.1613	4.4398	9.00E-06	0.0011	galanin	Mm.4655	14419	78	1	94	60	2	1	2
Npw	27.1112	6.1577	1.2097	5.0903	3.57E-07	6.46E-05	neuropeptide W	Mm.291772	381073	46	11	59	72	1	1	0
Erdr1	68.7803	8.4017	1.2788	6.5699	5.03E-11	1.82E-08	erythroid differentiation regulator 1	Mm.76062	170942	115	66	81	224	0	1	0
H2-Ea-ps	117.7462	10.1424	1.2974	7.8176	5.38E-15	3.01E-12	histocompatibility 2, class II antigen E alpha, pseudogene	Mm.15680	100504404	170	439	115	121	0	0	0
Uty	220.8190	11.0491	3.0361	3.6393	0.0003	0.0190	ubiquitously transcribed tetratricopeptide repeat gene, Y chromosome	Mm.20477	22290	633	0	460	436	0	0	0
Kdm5d	267.6727	11.3267	3.0672	3.6928	0.0002	0.0160	lysine (K)-specific demethylase 5D	Mm.262676	20592	769	0	563	521	0	0	0
Ddx3y	710.6804	12.7354	3.2103	3.9671	7.28E-05	0.0062	DEAD (Asp-Glu-Ala-Asp) box polypeptide 3, Y-linked	Mm.302938	26900	1893	0	1388	1655	0	0	0
Eif2s3y	728.1601	12.7705	3.2149	3.9723	7.12E-05	0.0060	eukaryotic translation initiation factor 2, subunit 3, structural gene Y-linked	Mm.250909	26906	1962	0	1368	1729	0	0	0

Table 5.4. Differentially expressed genes comparing *Mitf-A* and *Mitf-M* knockout skin.

gene	baseMean	log2FoldChange	lfcSE	stat	pvalue	padj	GENENAME	UNIGENE	ENTREZID	A1	A2	A3	A4	M1	M2	M3	M4
Oca2	353.9292	-11.8980	1.0253	-11.6042	3.92E-31	3.64E-28	oculocutaneous albinism II	Mm.137052	18431	773	842	643	663	0	0	0	0
Tyr	1014.9314	-11.3907	0.8361	-13.5908	4.54E-42	6.49E-39	tyrosinase	Mm.238127	22173	2208	2481	1770	1932	3	0	0	0
Slc45a2	332.4645	-9.7785	0.8407	-11.6318	2.84E-31	2.78E-28	solute carrier family 45, member 2	Mm.139278	22293	728	744	587	674	2	0	1	0
Syt4	488.6558	-9.3349	0.6003	-15.5512	1.56E-54	2.64E-51	synaptotagmin IV	Mm.233846	20983	1107	1250	858	840	4	0	0	2
Tyrp1	3242.6962	-8.9772	0.2210	-40.6264	0	0	tyrosinase-related protein 1	Mm.30438	22178	7244	7993	5778	5796	16	15	9	11
Gpr143	109.9822	-8.7665	1.0196	-8.5977	8.13E-18	4.20E-15	G protein-coupled receptor 143	Mm.5157	18241	238	266	191	212	0	0	0	2
Mc1r	207.9941	-8.3610	0.6624	-12.6224	1.59E-36	1.97E-33	melanocortin 1 receptor	Mm.324942	17199	421	457	399	419	1	1	3	0
Trpm1	1815.7091	-8.0019	0.2323	-34.4427	5.80E-260	5.39E-256	transient receptor potential cation channel, subfamily M, member 1	Mm.38875	17364	3935	4006	3456	3453	22	15	7	12
Tspan10	138.9078	-7.7761	0.6715	-11.5801	5.20E-31	4.60E-28	tetraspanin 10	Mm.209875	208634	268	292	278	287	0	1	3	1
Mcoln3	112.1810	-7.2054	0.6026	-11.9575	5.93E-33	6.48E-30	mucolipin 3	Mm.114683	171166	258	266	199	200	0	2	1	3
Mlana	766.9808	-7.0039	0.2584	-27.1037	8.90E-162	2.76E-158	melan-A	Mm.138437	77836	1491	1691	1477	1557	15	8	12	12
Pmel	3318.0373	-6.8003	0.2152	-31.5969	4.07E-219	1.89E-215	premelanosome protein	Mm.16756	20431	6912	7243	6374	6410	63	87	41	44
Ptgds	889.5581	-6.3757	0.2024	-31.4960	9.84E-218	3.66E-214	prostaglandin D2 synthase (brain)	Mm.1008	19215	1783	1971	1587	1863	22	22	21	19
H2-Q5	51.4103	-6.3349	0.6831	-9.2742	1.79E-20	1.07E-17	histocompatibility 2, Q region locus 5	Mm.439648	15016	146	96	90	89	1	2	1	1
AA388235	20.5074	-6.9313	1.0466	-6.6495	1.45E-09	3.42E-07	expressed sequence AA388235	Mm.380381	433100	55	47	36	31	0	0	2	0
Alx1	10.7767	-6.1124	1.0854	-5.6316	1.79E-08	3.61E-06	ALX homeobox 1	Mm.19287	216285	20	20	22	24	0	0	0	1
Dct	5228.2898	-5.7916	0.1820	-31.8171	3.76E-222	2.33E-218	dopachrome tautomerase	Mm.19987	13190	10524	11959	9649	10041	177	133	185	240
Gucy2f	5.1424	-5.7786	1.1662	-4.9552	7.22E-07	0.0001	guanylate cyclase 2f	Mm.208511	245650	8	10	14	9	0	0	0	0
Slc24a5	390.9822	-5.6852	0.2330	-24.4038	1.56E-131	4.14E-128	solute carrier family 24, member 5	Mm.330538	317750	802	911	717	726	18	8	21	12
H2-Eb1	2187.3419	-5.6194	0.3304	-17.0064	7.37E-65	1.52E-61	histocompatibility 2, class II antigen E beta	Mm.22564	14969	4484	5129	4069	3965	71	169	55	55
Gpr158	3.8028	-5.3660	1.1733	-4.5736	4.79E-06	0.0006	G protein-coupled receptor 158	Mm.166647	241263	8	12	6	6	0	0	0	0
B3galt5	72.5215	-5.2268	0.4133	-12.6476	1.15E-36	1.53E-33	UDP-Gal:betaGlcNAc beta 1,3-galactosyltransferase, polypeptide 5	Mm.154783	93961	172	146	130	134	2	9	2	2
Gm829	2.3260	-4.6423	1.2564	-3.6948	0.0002	0.0155	predicted gene 829	Mm.331582	329839	6	4	5	4	0	0	0	0
Unc5d	6.0598	-4.5273	1.1141	-4.0638	4.83E-05	0.0046	unc-5 netrin receptor D	Mm.248433	210801	16	10	8	14	0	1	1	0
Guca1b	92.2095	-4.0915	0.4803	-8.5181	1.62E-17	8.15E-15	guanylate cyclase activator 1B	Mm.59151	107477	209	205	167	140	17	0	13	10
Fabp7	40.4301	-3.3368	0.3399	-9.8175	9.47E-23	6.77E-20	fatty acid binding protein 7, brain	Mm.3644	12140	79	89	66	70	5	14	5	5
Nrk	12.3494	-3.3064	0.5725	-5.7758	7.66E-09	1.66E-06	Nik related kinase	Mm.482319	27206	31	22	18	22	3	2	2	2
Pax3	62.4334	-3.2579	0.2993	-10.8857	1.35E-27	1.09E-24	paired box 3	Mm.1371	18505	141	122	109	95	12	20	9	6
Spta1	15.8002	-3.1261	0.5580	-5.6027	2.11E-08	4.17E-06	spectrin alpha, erythrocytic 1	Mm.200611	20739	38	42	13	28	3	6	3	1
Cyp4f41-ps	6.0718	-3.1038	0.7867	-3.9452	7.97E-05	0.0068	cytochrome P450, family 4, subfamily f, polypeptide 41 pseudogene	Mm.245027	77875	11	14	8	12	3	1	1	0
Cited1	13.5786	-3.0364	0.8044	-3.7747	0.0002	0.0119	Cbp/p300-interacting transactivator with Glu/Asp-rich carboxy-terminal domain 1	Mm.2390	12705	33	33	11	26	1	10	0	1
Fstl4	10.4269	-3.0334	0.5911	-5.1320	2.87E-07	4.51E-05	follistatin-like 4	Mm.44518	320027	21	24	19	13	2	1	3	3
Wdr95	13.9566	-2.9819	0.5529	-5.3936	6.90E-08	1.22E-05	WD40 repeat domain 95	Mm.136919	381693	34	21	26	17	2	5	1	4
Npy	57.6154	-2.9589	0.3160	-9.3648	7.62E-21	4.88E-18	neuropeptide Y	Mm.154796	109648	88	131	89	111	18	9	8	17
Actc1	26.1018	-2.9559	0.5726	-5.1620	2.44E-07	3.88E-05	actin, alpha, cardiac muscle 1	Mm.686	11464	67	66	47	16	3	13	3	5
Slc24a4	150.0321	-2.9538	0.4347	-6.7944	1.09E-11	3.31E-09	solute carrier family 24 (sodium/potassium/calcium exchanger), member 4	Mm.312448	238384	343	301	236	224	32	7	48	48
Gm17660	9.4916	-2.8698	0.7249	-3.9591	7.52E-05	0.0065	predicted gene, 17660	Mm.366664	100271704	18	18	21	11	5	0	0	4
Cryaa	7.1423	-2.8444	0.7630	-3.7278	0.0002	0.0140	crystallin, alpha A	Mm.1228	12954	19	12	15	6	1	4	0	2
Mlph	200.0444	-2.8074	0.1564	-17.9513	4.69E-72	1.09E-68	melanophilin	Mm.105208	171531	388	415	317	325	51	42	60	45
Atp6v0d2	135.1121	-2.7664	0.2716	-10.1842	2.33E-24	1.73E-21	ATPase, H+ transporting, lysosomal V0 subunit D2	Mm.19298	242341	245	276	225	222	39	17	31	50
Cma2	5.3860	-2.6361	0.7809	-3.3756	0.0007	0.0407	chymase 2, mast cell	Mm.378966	545055	8	16	8	7	0	3	1	2
Scg2	9.9082	-2.6355	0.7637	-3.4508	0.0006	0.0332	secretogranin II	Mm.5038	20254	38	20	3	14	4	3	1	3
Omg	11.7822	-2.6293	0.5171	-5.0845	3.69E-07	5.62E-05	oligodendrocyte myelin glycoprotein	Mm.93335	18377	20	23	21	19	3	6	2	2
P4ha3	13.9711	-2.5855	0.6241	-4.1429	3.43E-05	0.0034	procollagen-proline, 2-oxoglutarate 4-dioxygenase (proline 4-hydroxylase), alpha polypeptide III	Mm.150294	320452	33	42	7	22	5	7	2	2
Gm2115	33.3778	-2.4999	0.3440	-7.2675	3.66E-13	1.31E-10	predicted gene 2115	Mm.44882	100039239	51	72	55	55	5	16	7	12
1700097N02Rik	6.3843	-2.4266	0.7035	-3.4492	0.0006	0.0333	RIKEN cDNA 1700097N02 gene	Mm.254797	67522	10	12	11	11	1	5	0	2
Adgb	19.5120	-2.3817	0.3897	-6.1114	9.87E-10	2.42E-07	androglobin	Mm.246573	215772	43	35	26	32	4	9	8	4
Lmbr1	153.8380	-2.3424	0.2844	-8.2350	1.80E-16	8.56E-14	limb region 1	Mm.41572	56873	460	250	174	204	59	55	47	40
Glrb	99.5520	-2.2981	0.2107	-10.9052	1.09E-27	9.20E-25	glycine receptor, beta subunit	Mm.275639	14658	181	202	157	143	41	22	35	35
Slfn4	141.7731	-2.2310	0.6234	-3.5787	0.0003	0.0226	schlafen 4	Mm.38192	20558	340	332	45	288	32	118	31	20
Gm10863	10.0658	-2.2151	0.6109	-3.6259	0.0003	0.0194	predicted gene 10863	Mm.483310	100041655	16	22	19	11	7	0	3	4
Siglec1	511.4071	-2.1727	0.2422	-8.9706	2.95E-19	1.71E-16	sialic acid binding Ig-like lectin 1, sialoadhesin	Mm.1374	20612	1145	1097	445	857	169	247	163	161
Dppa3	37.5790	-2.0981	0.6150	-3.4113	0.0006	0.0370	developmental pluripotency-associated 3	Mm.27982	73708	107	42	54	50	27	3	5	21
Igsf11	35.0869	-2.0949	0.3436	-6.0973	1.08E-09	2.60E-07	immunoglobulin superfamily, member 11	Mm.245564	207683	47	76	61	49	8	21	13	11
Slc6a17	166.9767	-2.0198	0.3449	-5.8570	4.71E-09	1.06E-06	solute carrier family 6 (neurotransmitter transporter), member 17	Mm.212867	229706	302	331	233	245	42	130	39	55
Cftr	12.5749	-2.0019	0.4980	-4.0198	5.82E-05	0.0053	cystic fibrosis transmembrane conductance regulator	Mm.15621	12638	33	27	12	14	7	3	6	4
9630028I04Rik	25.3874	2.0361	0.3882	5.2447	1.57E-07	2.58E-05	RIKEN cDNA 9630028I04 gene	Mm.394996	319720	11	12	13	5	45	55	35	27
Btnl2	24.1289	2.3029	0.4402	5.2318	1.68E-07	2.74E-05	butyrophilin-like 2	Mm.441007	547431	15	6	5	8	32	66	29	34
Gm11127	8.9664	2.5183	0.6808	3.6988	0.0002	0.0154	predicted gene 11127	Mm.484641	100529082	3	2	0	6	8	15	15	23
Mgarp	33.6183	2.5869	0.5332	4.8519	1.22E-06	0.0002	mitochondria localized glutamic acid rich protein	Mm.273339	67749	5	12	8	14	39	120	36	37
D030045P18Rik	26.3522	2.6100	0.5420	4.8153	1.47E-06	0.0002	RIKEN cDNA D030045P18 gene	Mm.123343	320363	11	9	7	4	66	15	58	38
Mmp8	11.2032	2.6160	0.6241	4.1919	2.77E-05	0.0026	matrix metallopeptidase 8	Mm.16415	17394	6	2	5	0	19	28	11	19
Ptcra	9.7364	2.9909	0.6937	4.3118	1.62E-05	0.0017	pre T cell antigen receptor alpha	Mm.215173	19208	4	1	1	3	23	7	18	20
Prss41	20.8717	3.0448	0.6091	4.9992	5.76E-07	8.36E-05	protease, serine 41	Mm.328839	71003	5	8	3	3	47	10	49	40
4930426D05Rik	6.8610	3.0539	0.7860	3.8856	0.0001	0.0084	RIKEN cDNA 4930426D05 gene	Mm.329311	74644	0	2	1	3	13	6	16	13
Hapln4	30.5307	3.1235	0.6554	4.7657	1.88E-06	0.0002	hyaluronan and proteoglycan link protein 4	Mm.152048	330790	9	6	6	5	84	9	77	43
Tdo2	18.1688	3.3733	0.8838	3.8168	0.0001	0.0103	tryptophan 2,3-dioxygenase	Mm.258622	56720	4	2	3	4	43	1	50	35
H2-Q1	34.1878	3.6019	0.8971	4.0151	5.94E-05	0.0053	histocompatibility 2, Q region locus 1	Mm.466882	15006	1	5	14	0	33	145	41	36
Serpina3m	39.2813	3.6412	0.7247	5.0248	5.04E-07	7.49E-05	serine (or cysteine) peptidase inhibitor, clade A, member 3M	Mm.395085	20717	5	7	3	9	95	7	99	83

Cd1d2	13.3754	4.1599	0.7815	5.3232	1.02E-07	1.74E-05	CD1d2 antigen	Mm.389465	12480	4	1	0	1	16	47	22	17
C7	458.2571	5.0407	1.0258	4.9138	8.93E-07	0.0001	complement component 7	Mm.208034	109828	44	25	22	22	988	14	1605	853
Npw	24.4400	5.3254	0.8714	6.1113	9.88E-10	2.42E-07	neuropeptide W	Mm.291772	381073	2	2	1	0	46	11	59	72
H2-Bl	3.6225	5.3389	1.3061	4.0876	4.36E-05	0.0042	histocompatibility 2, blastocyst	Mm.477808	14963	0	0	0	0	8	14	4	3
Gal	30.4958	5.8498	1.2187	4.8000	1.59E-06	0.0002	galanin	Mm.4655	14419	0	0	2	2	78	1	94	60
H2-Ea-ps	104.9417	10.1936	1.1368	8.9672	3.04E-19	1.71E-16	histocompatibility 2, class II antigen E alpha, pseudogene	Mm.15680	100504404	0	0	0	0	170	439	115	121
Uty	196.3378	11.0969	2.8895	3.8404	0.0001	0.0096	ubiquitously transcribed tetratricopeptide repeat gene, Y chromosome	Mm.20477	22290	0	0	0	0	633	0	460	436
Kdm5d	237.9991	11.3745	2.9185	3.8974	9.72E-05	0.0080	lysine (K)-specific demethylase 5D	Mm.262676	20592	0	0	0	0	769	0	563	521
Ddx3y	631.8528	12.7831	3.0517	4.1888	2.80E-05	0.0028	DEAD (Asp-Glu-Ala-Asp) box polypeptide 3, Y-linked	Mm.302938	26900	0	0	0	0	1893	0	1388	1655
Eif2s3y	647.3741	12.8181	3.0560	4.1944	2.74E-05	0.0028	eukaryotic translation initiation factor 2, subunit 3, structural gene Y-linked	Mm.250909	26908	0	0	0	0	1962	0	1368	1729

Table 5.5. MITF binding motifs in top differentially expressed genes.

chromosome	start	stop	orientation	BBLS	FDR	BLS	Zscore	NLOD	Refseq	Gene	distance
chr9	22127610	22127617	1	3.2788	0.0321	5.5338	4.2064	1	NM_007388	Acp5	-2985
chr9	22130682	22130689	1	3.6737	0.0332	3.8008	4.2064	1	NM_007388	Acp5	87
chr1	106707094	106707101	1	3.3049	0.0322	3.7728	4.2064	1	NM_009741	Bcl2	-7193
chr1	106708046	106708053	1	2.6846	0.0284	4.4644	4.2064	1	NM_009741	Bcl2	-6241
chr1	106710865	106710872	1	1.9164	0.0258	4.7299	4.2064	1	NM_009741	Bcl2	-3422
chr13	99896859	99896866	1	1.1971	0.0298	1.8461	4.2064	1	NM_013732	Cartpt	-3821
chr14	118057610	118057617	-1	2.1657	0.0260	3.9725	4.2064	1	NM_010024	Dct	-5367
chr14	103850823	103850830	-1	3.3561	0.0329	4.4722	4.2064	1	NM_001136061	Ednrb	-6350
chr6	49028325	49028332	-1	2.8377	0.0296	3.6652	4.2064	1	NM_053110	Gpnmb	-8190
chr6	49035940	49035947	-1	1.7463	0.0262	3.1294	4.2064	1	NM_053110	Gpnmb	-575
chrX	152781641	152781648	-1	1.2610	0.0290	1.8541	4.2064	1	NM_010951	Gpr143	-277
chrX	142196005	142196012	-1	1.5618	0.0270	1.9825	4.2064	1	NM_001007576	Gucy2f	928
chr17	34301834	34301841	-1	1.9704	0.0260	2.9412	4.2064	1	NM_010382	H2-Eb1	-4030
chr17	34306166	34306173	-1	2.5708	0.0280	4.2072	4.2064	1	NM_010382	H2-Eb1	302
chr17	35397080	35397087	1	3.1806	0.0316	4.6021	4.2064	1	NR_051981	H2-Q5	-2984
chr16	89205595	89205602	1	1.8999	0.0258	3.1640	4.2064	1	NM_001163615	Krtap20-2	263
chr8	123399063	123399070	-1	1.8442	0.0257	3.0240	4.2064	1	NM_008559	Mc1r	-8016
chr6	97932797	97932804	1	1.1904	0.0298	1.9306	4.2064	1	NM_001178049	Mitf	-2983
chr7	100286173	100286180	-1	1.2079	0.0295	2.4090	4.2064	1	NM_177161	P4ha3	656
chr1	79448010	79448017	-1	1.3038	0.0284	3.0332	4.2064	1	NM_009129	Scg2	-7923
chr1	79446809	79446816	-1	1.3684	0.0281	2.0268	4.2064	1	NM_009129	Scg2	-6722
chr1	79434042	79434049	1	2.2869	0.0263	3.7484	4.2064	1	NM_009129	Scg2	-6045
chr1	79442325	79442332	-1	2.6294	0.0284	3.6726	4.2064	1	NM_009129	Scg2	-2238
chr1	79442315	79442322	-1	2.4573	0.0273	3.6726	4.2064	1	NM_009129	Scg2	-2228
chr1	79439106	79439113	1	4.1725	0.0341	6.3671	4.2064	1	NM_009129	Scg2	-981
chr15	10996790	10996797	-1	1.4843	0.0276	2.4696	4.2064	1	NM_053077	Slc45a2	-3928
chr15	11003848	11003855	1	1.1026	0.0310	1.3858	4.2064	1	NM_053077	Slc45a2	-3130
chr1	174180921	174180928	1	1.5900	0.0267	3.3961	4.2064	1	NM_011465	Spta1	-8148
chr11	85840420	85840427	1	3.2706	0.0321	5.1887	4.2064	1	NM_009324	Tbx2	-7808
chrX	136220662	136220669	-1	1.8097	0.0263	2.2870	4.2064	1	NM_001127169	Tceal7	-3376
chrX	7764737	7764744	1	1.6667	0.0266	2.8482	4.2064	1	NM_001271491	Tfe3	-699
chr17	47794989	47794996	1	1.8883	0.0258	3.3230	4.2064	1	NM_011549	Tfeb	-9248
chr7	87486312	87486319	1	1.3638	0.0281	1.8742	4.2064	1	NM_011661	Tyr	-7096
chr7	87488229	87488236	1	4.3192	0.0344	4.4885	4.2064	1	NM_011661	Tyr	-5179
chr7	87494566	87494573	-1	6.7336	0.0417	6.9780	4.2064	1	NM_011661	Tyr	-1158
chr7	87493434	87493441	-1	9.0795	0.0350	9.3123	4.2064	1	NM_011661	Tyr	-26
chr4	80839914	80839921	1	3.0072	0.0307	5.4328	4.2064	1	NM_031202	Tyrp1	-5687
chr4	80834901	80834908	-1	4.0925	0.0340	7.2605	4.2064	1	NM_031202	Tyrp1	674
chr8	29210968	29210975	1	2.3290	0.0265	2.9166	4.2064	1	NM_153135	Unc5d	-8665
chr8	29215324	29215331	1	1.1459	0.0305	1.6534	4.2064	1	NM_153135	Unc5d	-4309
chr8	29223938	29223945	-1	4.8260	0.0342	6.2149	4.2064	1	NM_153135	Unc5d	-4305
chr8	29216296	29216303	1	2.2644	0.0262	2.8907	4.2064	1	NM_153135	Unc5d	-3337

Table 5.6. Enriched gene sets in *Mitf-A* knockout skin when comparing to wildtype.

NAME	SIZE	ES	NES	NOM p-val	FDR q-val	FWER p-val	RANK AT MAX	LEADING EDGE
GO_STRUCTURAL_CONSTITUENT_OF_RIBOSOME	147	-0.7239	-3.4818	0	0	0	2279	tags=78%, list=19%, signal=96%
GO_COTRANSLATIONAL_PROTEIN_TARGETING_TO_MEMBRANE	92	-0.7624	-3.4310	0	0	0	1977	tags=79%, list=17%, signal=94%
GO_RIBOSOMAL_SUBUNIT	170	-0.6958	-3.4006	0	0	0	2344	tags=73%, list=20%, signal=90%
GO_MITOCHONDRIAL_PROTEIN_COMPLEX	236	-0.6572	-3.3640	0	0	0	2378	tags=63%, list=20%, signal=77%
GO_ESTABLISHMENT_OF_PROTEIN_LOCALIZATION_TO_ENDOPLASMIC_RETICULUM	102	-0.7380	-3.3556	0	0	0	1977	tags=75%, list=17%, signal=89%
GO_ATP_SYNTHESIS_COUPLED_ELECTRON_TRANSPORT	79	-0.7598	-3.3031	0	0	0	2049	tags=76%, list=17%, signal=91%
GO_CYTOSOLIC_RIBOSOME	89	-0.7457	-3.2991	0	0	0	1977	tags=79%, list=17%, signal=94%
GO_INNER_MITOCHONDRIAL_MEMBRANE_PROTEIN_COMPLEX	113	-0.7256	-3.2795	0	0	0	1940	tags=70%, list=16%, signal=83%
GO_OXIDATIVE_PHOSPHORYLATION	121	-0.6990	-3.2375	0	0	0	1944	tags=66%, list=16%, signal=78%
GO_RIBOSOME	206	-0.6420	-3.2283	0	0	0	2344	tags=66%, list=20%, signal=80%

Table 5.7. Enriched gene sets in wildtype when comparing to *Mitf-A* knockouts

NAME	SIZE	ES	NES	NOM p-val	FDR q-val	FWER p-val	RANK AT MAX	LEADING EDGE
GO_EXTRACELLULAR_MATRIX_STRUCTURAL_CONSTITUENT_CONFERRING_TENSILE_STRENGTH	28	0.7068	2.3914	0	0	0	2261	tags=71%, list=19%, signal=88%
GO_EXTRACELLULAR_MATRIX_STRUCTURAL_CONSTITUENT	109	0.4936	2.2312	0	0.0071	0.013	2331	tags=45%, list=20%, signal=55%
GO_COMPLEX_OF_COLLAGEN_TRIMERS	17	0.7311	2.1636	0	0.0145	0.038	2261	tags=82%, list=19%, signal=102%
GO_BASEMENT_MEMBRANE	78	0.5094	2.1616	0	0.0117	0.041	2331	tags=53%, list=20%, signal=65%
GO_CENTRIOLE	118	0.4702	2.1387	0	0.0155	0.067	3047	tags=43%, list=26%, signal=58%
GO_NEURON_PROJECTION_ARBORIZATION	18	0.6938	2.1269	0	0.0162	0.085	1068	tags=44%, list=9%, signal=49%
GO_EYE_MORPHOGENESIS	96	0.4645	2.0628	0	0.0323	0.19	3219	tags=52%, list=27%, signal=71%

Table 5.8. Enriched gene sets in wildtype when comparing to *Mitf-M* knockout skin.

NAME	SIZE	ES	NES	NOM p-val	FDR q-val	FWER p-val	RANK AT MAX	LEADING EDGE
GO_PIGMENT_METABOLIC_PROCESS	57	-0.8820	-2.5796	0	0	0	37	tags=18%, list=0%, signal=18%
GO_PIGMENT_GRANULE	96	-0.8174	-2.5716	0	0	0	122	tags=10%, list=1%, signal=10%
GO_PIGMENT_BIOSYNTHETIC_PROCESS	46	-0.9306	-2.5621	0	0	0	37	tags=22%, list=0%, signal=22%
GO_PIGMENTATION	88	-0.8120	-2.4914	0	0	0	266	tags=16%, list=2%, signal=16%
GO_DEVELOPMENTAL_PIGMENTATION	44	-0.8833	-2.4408	0	0	0	266	tags=25%, list=2%, signal=25%
GO_SECONDARY_METABOLIC_PROCESS	49	-0.8576	-2.3652	0	0	0	375	tags=27%, list=3%, signal=27%
GO_SECONDARY_METABOLITE_BIOSYNTHETIC_PROCESS	23	-0.9326	-2.3593	0	1.60E-04	0.001	158	tags=43%, list=1%, signal=44%
GO_PHENOL_CONTAINING_COMPOUND_BIOSYNTHETIC_PROCESS	35	-0.8472	-2.3066	0	1.40E-04	0.001	55	tags=29%, list=0%, signal=29%
GO_MELANIN_METABOLIC_PROCESS	19	-0.9497	-2.2766	0	1.24E-04	0.001	37	tags=47%, list=0%, signal=47%
GO_PIGMENT_CELL_DIFFERENTIATION	34	-0.8228	-2.1855	0	0.0035	0.03	790	tags=29%, list=6%, signal=31%
GO_PHENOL_CONTAINING_COMPOUND_METABOLIC_PROCESS	80	-0.7189	-2.1853	0	0.0032	0.03	217	tags=16%, list=2%, signal=16%
GO_MELANOCYTE_DIFFERENTIATION	25	-0.8530	-2.1398	0	8.57E-03	0.088	266	tags=28%, list=2%, signal=28%

Table 5.9. Enriched gene sets in *Mitf-M* knockout skin when comparing to wildtype.

NAME	SIZE	ES	NES	NOM p-val	FDR q-val	FWER p-val	RANK AT MAX	LEADING EDGE
GO_DEMETHYLASE_ACTIVITY	33	0.8439	2.2191	0	0.0027	0.003	3	tags=6%, list=0%, signal=6%
GO_HISTONE_DEMETHYLASE_ACTIVITY	25	0.8886	2.2119	0	0.0018	0.004	3	tags=8%, list=0%, signal=8%
GO_PROTEIN_DEMETHYLATION	29	0.8541	2.1377	0	0.0119	0.038	3	tags=7%, list=0%, signal=7%
GO_CYTOPLASMIC_TRANSLATIONAL_INITIATION	25	0.8586	2.1040	0	0.0179	0.074	0	tags=4%, list=0%, signal=4%
GO_HISTONE_METHYLTRANSFERASE_COMPLEX	76	0.7135	2.1001	0	0.0156	0.081	3	tags=3%, list=0%, signal=3%
GO_METHYLTRANSFERASE_COMPLEX	101	0.6653	2.0717	0	0.0275	0.165	3	tags=2%, list=0%, signal=2%

Table 5.10. Enriched gene sets in *Mitf-A* knockout skin when comparing to *Mitf-M* knockout skin.

NAME	SIZE	ES	NES	NOM p-val	FDR q-val	FWER p-val	RANK AT MAX	LEADING EDGE
GO_PIGMENTATION	97	-0.8478	-2.6056	0	0	0	478	tags=19%, list=3%, signal=19%
GO_PIGMENT_METABOLIC_PROCESS	67	-0.8761	-2.5455	0	0	0	240	tags=16%, list=2%, signal=17%
GO_PIGMENT_BIOSYNTHETIC_PROCESS	55	-0.9172	-2.5343	0	0	0	34	tags=18%, list=0%, signal=18%
GO_PIGMENT_GRANULE	105	-0.8147	-2.4919	0	0	0	478	tags=11%, list=3%, signal=12%
GO_SECONDARY_METABOLIC_PROCESS	53	-0.8650	-2.4568	0	0	0	238	tags=23%, list=2%, signal=23%
GO_DEVELOPMENTAL_PIGMENTATION	47	-0.9039	-2.4413	0	0	0	312	tags=26%, list=2%, signal=26%
GO_SECONDARY_METABOLITE_BIOSYNTHETIC_PROCESS	26	-0.9334	-2.2887	0	0	0	238	tags=38%, list=2%, signal=39%
GO_PIGMENT_CELL_DIFFERENTIATION	36	-0.8766	-2.2882	0	0	0	737	tags=31%, list=5%, signal=32%
GO_PHENOL_CONTAINING_COMPOUND_BIOSYNTHETIC_PROCESS	40	-0.8453	-2.2597	0	1.21E-04	0.001	317	tags=28%, list=2%, signal=28%
GO_MELANIN_METABOLIC_PROCESS	22	-0.9556	-2.2339	0	3.26E-04	0.003	34	tags=41%, list=0%, signal=41%
GO_MELANOCYTE_DIFFERENTIATION	26	-0.9001	-2.2307	0	2.97E-04	0.003	625	tags=38%, list=4%, signal=40%
GO_CELLULAR_PIGMENTATION	50	-0.7845	-2.2293	0	2.72E-04	0.003	478	tags=12%, list=3%, signal=12%
GO_PHENOL_CONTAINING_COMPOUND_METABOLIC_PROCESS	90	-0.7197	-2.1560	0	0.0017	0.02	446	tags=17%, list=3%, signal=17%
GO_PIGMENT_GRANULE_ORGANIZATION	26	-0.8682	-2.1319	0	0.0040	0.05	13	tags=12%, list=0%, signal=12%
GO_CELLULAR_RESPONSE_TO_LIGHT_STIMULUS	115	-0.6495	-2.0495	0	0.0239	0.268	542	tags=11%, list=3%, signal=12%

Table 5.11. Enriched gene sets in *Mitf-M* knockout skin when comparing to *Mitf-A* knockout skin.

NAME	SIZE	ES	NES	NOM p-val	FDR q-val	FWER p-val	RANK AT MAX	LEADING EDGE
GO_TRANSLATION_INITIATION_FACTOR_ACTIVITY	47	0.7974	2.0741	0	0.0219	0.023	0	tags=2%, list=0%, signal=2%
GO_HISTONE_METHYLTRANSFERASE_COMPLEX	83	0.7212	2.0716	0	0.0109	0.023	3	tags=2%, list=0%, signal=2%
GO_PROTEIN_DEMETHYLATION	31	0.8402	2.0666	0	0.0082	0.026	3	tags=6%, list=0%, signal=6%
GO_CYTOPLASMIC_TRANSLATIONAL_INITIATION	28	0.8602	2.0564	0	0.0093	0.039	0	tags=4%, list=0%, signal=4%
GO_HISTONE_DEMETHYLASE_ACTIVITY	27	0.8559	2.0472	0	0.0118	0.061	3	tags=7%, list=0%, signal=7%
GO_DEMETHYLASE_ACTIVITY	36	0.8036	1.9974	0	0.0346	0.205	3	tags=6%, list=0%, signal=6%

Table 5.12. Enriched gene sets in black-eyed white *Mitf-M* knockout skin compared to skin of spotted *Mitf-M* knockout.

NAME	SIZE	ES	NES	NOM p-val	FDR q-val	FWER p-val	RANK AT MAX	LEADING EDGE
GO_G_PROTEIN_COUPLED_RECEPTOR_ACTIVITY	384	-0.2006	-4.4902	0	0	0	2496	tags=35%, list=15%, signal=40%
GO_GATED_CHANNEL_ACTIVITY	307	-0.2214	-4.4737	0	0	0	3628	tags=44%, list=22%, signal=55%
GO_CATION_CHANNEL_ACTIVITY	306	-0.2080	-4.2566	0	0	0	3866	tags=44%, list=24%, signal=57%
GO_VOLTAGE_GATED_ION_CHANNEL_ACTIVITY	180	-0.2602	-4.0633	0	0	0	3685	tags=48%, list=23%, signal=62%
GO_PASSIVE_TRANSMEMBRANE_TRANSPORTER_ACTIVITY	425	-0.1702	-4.0597	0	0	0	3628	tags=39%, list=22%, signal=49%
GO_METAL_ION_TRANSMEMBRANE_TRANSPORTER_ACTIVITY	416	-0.1674	-3.8655	0	0	0	3886	tags=40%, list=24%, signal=51%
GO_MONOVALENT_INORGANIC_CATION_TRANSMEMBRANE_TRANSPORTER_ACTIVITY	356	-0.1683	-3.6902	0	0	0	3866	tags=40%, list=24%, signal=52%
GO_CATION_CHANNEL_COMPLEX	204	-0.2166	-3.6665	0	0	0	3866	tags=45%, list=24%, signal=58%
GO_VOLTAGE_GATED_CATION_CHANNEL_ACTIVITY	128	-0.2574	-3.4139	0	0	0	3607	tags=48%, list=22%, signal=61%
GO_POTASSIUM_CHANNEL_ACTIVITY	114	-0.2743	-3.4138	0	0	0	3997	tags=52%, list=25%, signal=68%

Table 5.13. Enriched gene sets in skin of spotted *Mitf-M* knockout mouse compared to unspotted *Mitf-M* knockout mice.

NAME	SIZE	ES	NES	NOM p-val	FDR q-val	FWER p-val	RANK AT MAX	LEADING EDGE
GO_RIBONUCLEOPROTEIN_COMPLEX_BIOGENESIS	400	0.2546	5.9117	0	0	0	10337	tags=88%, list=63%, signal=235%
GO_MRNA_PROCESSING	475	0.2129	5.4164	0	0	0	10083	tags=83%, list=62%, signal=210%
GO_CADHERIN_BINDING	322	0.2495	5.1356	0	0	0	9377	tags=82%, list=58%, signal=189%
GO_RNA_SPLICING_VIA_TRANSESTERIFICATION_REACTIONS	327	0.2363	5.0615	0	0	0	10083	tags=85%, list=62%, signal=218%
GO_RNA_SPLICING	410	0.2211	5.0569	0	0	0	10083	tags=83%, list=62%, signal=213%
GO_RIBOSOME_BIOGENESIS	277	0.2568	4.8738	0	0	0	9067	tags=81%, list=56%, signal=179%
GO_PIGMENT_GRANULE	105	0.3939	4.6472	0	0	0	6816	tags=81%, list=42%, signal=138%
GO_RNA_CATABOLIC_PROCESS	387	0.1832	4.0888	0	0	0	10690	tags=83%, list=66%, signal=237%
GO_NCRNA_METABOLIC_PROCESS	446	0.1673	4.0794	0	0	0	9007	tags=72%, list=55%, signal=155%
GO_REGULATION_OF_CELL_CYCLE_PHASE_TRANSITION	429	0.1712	3.9851	0	0	0	10315	tags=80%, list=63%, signal=212%

Table 5.14. Identified *Mitf* and *Trp63* transcripts from full-length RNA sequencing of mouse whole skin.

gene_ID	transcript_ID	annot_gene_id	annot_transcript_id	annot_gene_name	annot_transcript_name	n_exons	length	gene_novelty	transcript_novelty	WT1	A1	M1	Mspot
15349	141289	ENSMUSG00000035158.15	TALONT000141289	Mitf	TALONT000141289	1	948	Known	Genomic	2	3	0	3
15349	141905	ENSMUSG00000035158.15	TALONT000141905	Mitf	TALONT000141905	1	961	Known	Genomic	1	0	0	0
15349	142688	ENSMUSG00000035158.15	TALONT000142688	Mitf	TALONT000142688	1	1930	Known	Genomic	1	0	0	0
15349	165597	ENSMUSG00000035158.15	TALONT000165597	Mitf	TALONT000165597	1	1624	Known	Genomic	0	1	0	0
15349	**194754**	**ENSMUSG00000035158.15**	**TALONT000194754**	**Mitf**	**TALONT000194754**	**10**	**2044**	**Known**	**NNC**	**0**	**0**	**1**	**0**
15349	**213417**	**ENSMUSG00000035158.15**	**TALONT000213417**	**Mitf**	**TALONT000213417**	**4**	**1801**	**Known**	**NNC**	**0**	**0**	**0**	**1**
37748	**107892**	**ENSMUSG00000022510.14**	**ENSMUST00000115305.1**	**Trp63**	**Trp63-204**	**9**	**1729**	**Known**	**Known**	**0**	**1**	**4**	**0**
37748	134010	ENSMUSG00000022510.14	TALONT000134010	Trp63	TALONT000134010	10	1839	Known	NNC	1	0	0	0
37748	136371	ENSMUSG00000022510.14	TALONT000136371	Trp63	TALONT000136371	1	1265	Known	Genomic	1	0	0	0
37748	146683	ENSMUSG00000022510.14	TALONT000146683	Trp63	TALONT000146683	11	2392	Known	NIC	1	0	0	0
37748	**147124**	**ENSMUSG00000022510.14**	**TALONT000147124**	**Trp63**	**TALONT000147124**	**9**	**1717**	**Known**	**NIC**	**1**	**1**	**2**	**2**
37748	175371	ENSMUSG00000022510.14	TALONT000175371	Trp63	TALONT000175371	1	1350	Known	Genomic	0	1	3	4
37748	182859	ENSMUSG00000022510.14	TALONT000182859	Trp63	TALONT000182859	1	429	Known	Genomic	0	0	1	0
37748	198119	ENSMUSG00000022510.14	TALONT000198119	Trp63	TALONT000198119	1	455	Known	Genomic	0	0	0	1
37748	198190	ENSMUSG00000022510.14	TALONT000198190	Trp63	TALONT000198190	1	937	Known	Genomic	0	0	0	2

Table 5.15. Primers and PCR conditions

Primer Name	Sequence 5'-3'	Expected size	Assay
Mitf-A For	CGCTCTGGTGTGAGAGTAAAC	WT - 285 bp, KO - 278 bp	genotyping
Mitf-A Rev	TCACCACTCTCATGCTCTTCA		genotyping
Mitf-M1 For	GACTAAGTGGTCTGCGGTGTC	WT - 202 bp , KO - 184 bp	genotyping
Mitf-M2 For	GTCACTACCAGGTGAGCATT	WT - 128 bp	genotyping
Mitf-M Rev	GATCTGTCCCCTTTTCGAATCGG		genotyping
mMitf 1A For	GTTCTGGTCCAAGTCCCAAG	3246 bp	full length PCR
mMitf 1J For	GCATAGTGGGAGAGGAGAGAGA	3555 bp	full length PCR
mMitf 1C For	GGTGACCAGGGAGTGTATCCTA	3186 bp	full length PCR
mMitf 1Mc For	TGGCAGCTTTGAGGATGGA	3208 bp	full length PCR
mMitf 1E For	CCACAGGCTGCTCTTCTGTGT	3198 bp	full length PCR
mMitf 1H For	GGGCTTGCAGAACACCTTAAAGG	3182 bp	full length PCR
mMitf 1D For	GTTGGGACCTGACAGGCTCTGAATACAG	3121 bp	full length PCR
mMitf 1B For	CGATGCAGGTGATGGGTCTCA	3158 bp	full length PCR
mMitf 1M For	TATGGTGCCTTCTTTATGCC	2993 bp	full length PCR
mMitf 6 For	CGTGTATTTTCCCCACAGAGTC	2320 bp	full length PCR
mMitf 9 Rev	CTTTATGCCACACAGGATTCAA		full length PCR

PCR Step	Genotyping (Mitf-A)	Genotyping (Mitf-M)	Full-length PCR
Denaturation	94°C for 2 min	94°C for 2 min	95°C for 5 min
Amplification	94°C for 30 sec	94°C for 30 sec	95°C for 30 sec
	60°C for 30 sec	55°C for 30 sec	60°C for 30 sec
	68°C for 1 min	68°C for 1 min	72°C for 15 min
Final Extension			72°C for 5 min

CHAPTER 6

Summary and Conclusions

Jessica L. Flesher and Anand K. Ganesan

Pigmentation in mice has captivated humans since ancient times where written record describes spotted and waltzing mice in China and Japanese woodcuts depict still common phenotypes (*271*). Breeding of mouse strains continued into the 18th and 19th century by fanciers who were interested in specific patterns and colorations (*272*), leading to the identification of a number of the classical pigmentation loci including agouti (*Asip*), brown (*Tyrp1)*, albinism (*Tyr)*, and pink-eye dilution (*Oca2*) (*88*). While some variation is found in wild mouse species today (*273*, *274*), laboratory mice have provided an unparalleled tool for linking basic melanocyte biology to *in vivo* phenotypes of mammals. From early mutagenesis studies, loci that regulate pigmentation including the microphthalmia locus (*114*) hinted at the genes that weren't cloned until 50 years later (*233*). Over 171 pigmentation associated genes have been cloned while another 207 loci associated with pigment phenotypes in mice have not been cloned to date (*104*). The identification of novel regulators of *in vivo* pigmentation continues to expand the list of pigmentation genes (*57*, *110*, *180*) shedding light on the complexity of melanocyte biology.

Melanosomes contain key protein components that regulate melanin synthesis (TYR, TYRP1, DCT), acidification (OCA2, MATP), and trafficking (RAB27A) (*92*, *174*, *275*). Another component of melanosome biogenesis is the regulation of trafficking to and from endosomal and lysosomal compartments via phosphoinositides (PIs) (*276*). This was first implicated by mouse mutants for *Fig4* and *Vac14* that exhibited dilution of coat color in addition to neurological phenotypes (*106*, *107*), but understanding the role of PIs in melanogenesis is still in its early stages. The work presented here highlights the *in vivo* phenotypes associated with two additional PI binding proteins, PIKFYVE and WIPI1 (Chapters 2-3). PIKFYVE plays multiple roles during melanosome maturation by coordinating transfer between the lysosome and melanosomes (*29*), in addition to labeling TYR and TYRP1 containing vesicles with the appropriate PI for fusion with

the melanosome (*110*). We have identified that phosphorylation of PIs by PIKFYVE is required for proper melanosome maturation and pigmentation of melanocytes and the murine coat (Chapter 2,(*110*)). While the role of WIPI1 has been most extensively studied in autophagy through the delivery of PI(3)P containing ER membranes to the growing phagophore (*181*), WIPI1 also regulates melanin production and melanosome maturation *in vitro* (*112*, *113*). Additionally, we present the subtle *in vivo* phenotype associated with the constitutive loss of *Wipi1* and a proposed role in trafficking membranes and vesicles to the maturing melanosome (Chapter 3). While additional work is necessary, we have developed the tools to understand the defects in melanosome maturation and trafficking associated with loss of *Wipi1 in vivo*.

A major question that still remains is which PIs are required for melanosome maturation. PIKFYVE is the kinase for the production of both PI(5)P and $PI(3,5)P_2$ (*147–149*) and WIPI1 binds to both of those species in addition to PI(3)P (Chapter 3, (*183*)). Myotubularins are a family of PI 3-phosphatases that are responsible for the conversion of $PI(3,5)P_2$ to PI(5)P and PI(3)P to phosphatidylinositol (*277*). A siRNA based screen identified five family members (*MTMR4, MTMR9, MTMR12 MTMR13/SBF2,* and *SBF1*) that decreased pigmentation over 20 percent when knocked down in melanoma cell lines (*113*) and mutations in *FIG4, MTMR2* and *MTMR13/SBF2* lead to subtypes of Charcot-Marie-Tooth disease (*276*). Other diseases associated with vesicle and organelle trafficking exhibit hypopigmentation in addition to more severe neurological and immune symptoms. Mouse mutants played a pivotal role in the identification of the subunits of AP3, BLOC-1, BLOC-2, and BLOC-3, which are mutated in subtypes of Hermansky-Pudlak syndrome (*87*). For example, mutations in the pale ear mouse are found in the *Hps1* gene, while the light ear mouse has a mutation in *Hps4,* two components of the BLOC-3 complex (*96*). While these models can be used to study melanosome maturation and trafficking, new mouse models are

needed to pinpoint the roles of phosphoinositides in regulation of melanosomes. Myotubularin family mutant mice have been generated including the five family members that reduced pigmentation in the siRNA screen (*Mtmr4,* MGI:2180699; *Mtmr9*, MGI:2442842; *Mtmr12*, MGI:2443034; *Mtmr13/Sbf2,* MGI:1921831; *Sbf1,* MGI:1925230) (*115*). Though none have notable pigment phenotypes, future studies crossing to the conditional *Pikfyve* allele may answer whether PI(5)P is required for maturation of melanosomes. Patients with Griscelli syndrome and the corresponding mouse models (*Myo5a, Rab27a,* and *Mlph*) may provide further insight into trafficking defects associated with loss of *Wipi1* (*95*). While we detected accumulation of early stage melanosomes in *Wipi1* knockout mice, by crossing with *Myo5a, Rab27a*, or *Mlph* mutant mice we can understand whether WIPI1 coordinates the trafficking of melanosomes to the periphery of the melanocyte.

As the master regulator of melanocyte cell identity and differentiation, MITF and the microphthalmia locus has long been the focus of pigment cell research. Over 40 mutant *Mitf* mouse alleles (MGI:104554) have contributed to understanding the role of *Mitf in vivo* (*115*, *119*). Mutations fit into two categories, those that alter all isoforms are generally found in the common exons including the basic helix-loop-helix domain and those that alter individual isoforms disrupt the unique first exons and the regulatory regions (*105*). With the identification of conserved unique promoter driven isoforms, an ongoing area of interest are the contributions of individual *Mitf* isoforms and how they are regulated (*117*). We have generated a *Mitf-A* isoform specific knockout mouse. This knockout implicated a partial role for *Mitf-A* in pigmentation of the skin and eye, and determined that *Mitf-A* expression is partially regulated by retinoids (Chapter 4, (*119*)). Loss of *Mitf-M* results in the loss of neural crest derived melanocytes of the skin and eye and, as found in our *Mitf-M* isoform specific knockout mice, alter the size of the adult kidney (Chapter 4, (*119*)).

Additional work identified some potential new targets for MITF-M with MITF binding motifs (Chapter 5). Rare spotting events occur in approximately five percent of *Mitf-M* knockout mice, due to melanocytes escaping the loss of *Mitf-M* (Chapter 5). Intriguingly, these spots seem to result not from the upregulation of other *Tfeb* isoforms and other MiT family members or through the low level of expression of aberrantly spliced *Mitf* isoforms, but possibly compensation by other promotor driven isoforms of *Mitf*. These isoforms are not upregulated in these spots, suggesting that expression of these other isoforms, while necessary for generation of the spots, are not sufficient on their own to form the spots. Identifying the specific mechanism by which the melanocyte gene expression program is reactivated in the spots could lead to a better understanding of the regulation of the pigmentation program in melanocytes.

Mutations in *MITF* have been linked to familial cancers and severe pigmentation disorders including Waardenburg syndrome (*102*), but understanding the regulation of *MITF* and its individual isoforms is ongoing. Retinoid stimulation of *MITF* has sparked interest in the development of novel retinoid compounds to treat pigmentary disorders like vitiligo (*118*). However, the retinoic acid response element is only one of the binding motifs that are unique to *MITF-A* (*119*). Identifying additional compounds that can regulate pigmentation is needed to develop treatments for pigmentary disorders that do not cause severe side effects or worsen the disease (*118*). The identification of the nine promoter driven isoforms was influenced in part due to the tissues and cells from which they were identified: *Mitf-M* (melanocyte), *Mitf-H* (heart), *Mitf-Mc* (Mast cells) (*233*, *278*, *279*). This doesn't provide a complete story, since multiple isoforms have been implicated in tissues including melanocytes, the eye, and kidneys (*119*, *198*, *204*). Within the spot, we found no evidence of activation of *Mitf-M* through alternative splicing, which suggests other isoforms may compensate to trigger melanocyte survival and differentiation

in the absence of *Mitf-M.* Since the spots remain pigmented throughout the lifespan of the mice, the melanocytes appear to have a viable stem cell compartment. Another possibility is that initial activation of Mitf target genes for melanogenesis and melanocyte survival are maintained through super enhancers like the one identified in humans in the *HERC2* locus that regulates *OCA2* expression and contributes to eye color in humans (*280*, *281*). By crossing the *Mitf-M* knockout mice to other *Mitf* mutant alleles to generate compound heterozygotes, we may be able to generate more frequent and robust spotting phenotype to follow up on chromatin immunoprecipitation (ChIP) or ChIP-seq to identify novel super enhancers for melanocytes. The addition of the novel isoform-specific knockout mice to the *Mitf* mutant models will further our understanding of MITF isoforms in development through the study of the spotted phenotype and pigmentation through comparative studies of the subtle role of *Mitf-A* compared to the requirement for *Mitf-M.*

From studies in mice, pigmentation biology has revealed the functional significance of many genes that control skin, hair, and eye color. By combining *in vitro* studies with mouse models, the underlying science goes from what is observed in a dish to the impacts on individual organs and the organism as a whole. My graduate work has added to the field's understanding of the complex role of PIs in melanosome biogenesis and delved into the complexity of *Mitf* isoforms, their unique contributions, and regulation. Next steps include identifying PI phosphatases that coordinate the regulation of PI species in melanocytes, how those same proteins impact melanosome biogenesis and trafficking, and expanding on the role of *Mitf* isoforms in melanocyte development and differentiation. While basic biology requires years to advance to human treatments, the identification of a retinoid receptor binding site within the *Mitf-A* promoter has supported continued research into the use of retinoids to increase pigmentation to prevent skin cancer and treat pigmentary disorders. The contribution of *Pikfyve*, *Wipi1, Mitf*, and the hundreds

of other genes to mouse coat color continues to remind us of the complexity behind something as seemingly simple as skin color.

REFERENCES

29. C. Bissig, P. Croisé, X. Heiligenstein, I. Hurbain, G. M. Lenk, E. Kaufman, R. Sannerud, W. Annaert, M. H. Meisler, L. S. Weisman, G. Raposo, G. Van Niel, The PIKfyve complex regulates the early melanosome homeostasis required for physiological amyloid formation. *J. Cell Sci.* **132**, jcs229500 (2019).

57. N. G. Crawford, D. E. Kelly, M. E. B. Hansen, M. H. Beltrame, S. Fan, S. L. Bowman, E. Jewett, A. Ranciaro, S. Thompson, Y. Lo, S. P. Pfeifer, J. D. Jensen, M. C. Campbell, W. Beggs, F. Hormozdiari, S. W. Mpoloka, G. G. Mokone, T. Nyambo, D. W. Meskel, G. Belay, J. Haut, H. Rothschild, L. Zon, Y. Zhou, M. A. Kovacs, M. Xu, T. Zhang, K. Bishop, J. Sinclair, C. Rivas, E. Elliot, J. Choi, S. A. Li, B. Hicks, S. Burgess, C. Abnet, D. E. Watkins-Chow, E. Oceana, Y. S. Song, E. Eskin, K. M. Brown, M. S. Marks, S. K. Loftus, W. J. Pavan, M. Yeager, S. Chanock, S. A. Tishkoff, Loci associated with skin pigmentation identified in African populations. *Science (80-.).* (2017), doi:10.1126/science.aan8433.

87. Y. Yamaguchi, V. J. Hearing, Melanocytes and their diseases. *Cold Spring Harb. Perspect. Med.* **4**, a017046- (2014).

88. E. S. Russell, A History of Mouse Genetics. *Annu. Rev. Genet.* **19**, 1–29 (1985).

92. H. Shoji, Y. Kiniwa, R. Okuyama, M. Yang, K. Higuchi, M. Mori, A nonsense nucleotide substitution in the oculocutaneous albinism II gene underlies the original pink-eyed dilution allele (Oca2p) in mice. *Exp. Anim.* **64**, 171 (2015).

95. S. L. Bowman, J. Bi-Karchin, L. Le, M. S. Marks, The road to lysosome-related organelles: Insights from Hermansky-Pudlak syndrome and other rare diseases. *Traffic*. **20**, 404–435 (2019).

96. P. W. Chiang, N. Oiso, R. Gautam, T. Suzuki, R. T. Swank, R. A. Spritz, The Hermansky-Pudlak syndrome 1 (HPS1) and HPS4 proteins are components of two complexes, BLOC-3 and BLOC-4, involved in the biogenesis of lysosome-related organelles. *J. Biol. Chem.* **278**, 20332–20337 (2003).

102. V. Pingault, D. Ente, F. Dastot-Le Moal, M. Goossens, S. Marlin, N. Bondurand, Review and update of mutations causing Waardenburg syndrome. *Hum. Mutat.* **31**, 391–406 (2010).

104. L. Montoliu, W. S. Oetting, D. C. Bennett, International Federation of Pigmented Cell Societies, Color Genes. *Eur. Soc. Pigment Cell Res.* (2017), (available at http://www.espcr.org/micemut.html).

105. E. Steingrímsson, N. G. Copeland, N. A. Jenkins, Melanocytes and the ak. *Annu. Rev. Genet.* **38**, 365–411 (2004).

106. C. Y. Chow, Y. Zhang, J. J. Dowling, N. Jin, M. Adamska, K. Shiga, K. Szigeti, M. E. Shy, J. Li, X. Zhang, J. R. Lupski, L. S. Weisman, M. H. Meisler, Mutation of FIG4 causes neurodegeneration in the pale tremor mouse and patients with CMT4J. *Nature*. **448**, 68–72 (2007).

107. N. Jin, C. Y. Chow, L. Liu, S. N. Zolov, R. Bronson, M. Davisson, J. L. Petersen, Y. Zhang, S. Park, J. E. Duex, D. Goldowitz, M. H. Meisler, L. S. Weisman, VAC14

nucleates a protein complex essential for the acute interconversion of PI3P and PI(3,5)P2 in yeast and mouse. *EMBO J.* **27**, 3221–34 (2008).

110. M. C. Liggins, J. L. Flesher, S. Jahid, P. Vasudeva, V. Eby, S. Takasuga, J. Sasaki, T. Sasaki, R. E. Boissy, A. K. Ganesan, PIKfyve regulates melanosome biogenesis. *PLoS Genet.* **14** (2018), doi:10.1371/journal.pgen.1007290.

112. H. Ho, R. Kapadia, S. Al-Tahan, S. Ahmad, A. K. Ganesan, WIPI1 coordinates melanogenic gene transcription and melanosome formation via TORC1 inhibition. *J. Biol. Chem.* **286**, 12509–12523 (2011).

113. A. K. Ganesan, H. Ho, B. Bodemann, S. Petersen, J. Aruri, S. Koshy, Z. Richardson, L. Q. Le, T. Krasieva, M. G. Roth, P. Farmer, M. A. White, Genome-wide siRNA-based functional genomics of pigmentation identifies novel genes and pathways that impact melanogenesis in human cells. *PLoS Genet.* **4** (2008), doi:10.1371/journal.pgen.1000298.

114. P. Hertwig, Neue Mutationen und Kopplungsgruppen bei der Hausmaus. *Z. Indukt. Abstammungs- u. Vererbungsl.* **80**, 220–246 (1942).

115. C. J. Bult, J. A. Blake, C. L. Smith, J. A. Kadin, J. E. Richardson, A. Anagnostopoulos, R. Asabor, R. M. Baldarelli, J. S. Beal, S. M. Bello, O. Blodgett, N. E. Butler, K. R. Christie, L. E. Corbani, J. Creelman, M. E. Dolan, H. J. Drabkin, S. L. Giannatto, P. Hale, D. P. Hill, M. Law, A. Mendoza, M. McAndrews, D. Miers, H. Motenko, L. Ni, H. Onda, M. Perry, J. M. Recla, B. Richards-Smith, D. Sitnikov, M. Tomczuk, G. Tonorio, L. Wilming, Y. Zhu, Mouse Genome Database (MGD) 2019. *Nucleic Acids Res.* (2019), doi:10.1093/nar/gky1056.

117. E. Steingrímsson, All for one, one for all: alternative promoters and Mitf. *Pigment Cell Melanoma Res.* **21**, 412–414 (2008).

118. E. K. Paterson, H. Ho, R. Kapadia, A. K. Ganesan, 9-cis retinoic acid is the ALDH1A1 product that stimulates melanogenesis. *Exp. Dermatol.* **22**, 202–209 (2013).

119. J. L. Flesher, E. K. Paterson-Coleman, P. Vasudeva, R. Ruiz-Vega, M. Marshall, E. Pearlman, G. R. MacGregor, J. Neumann, A. K. Ganesan, Delineating the role of MITF isoforms in pigmentation and tissue homeostasis. *Pigment Cell Melanoma Res.* **33**, 279–292 (2020).

147. D. Sbrissa, O. C. Ikonomov, H. Fenner, A. Shisheva, ArPIKfyve Homomeric and Heteromeric Interactions Scaffold PIKfyve and Sac3 in a Complex to Promote PIKfyve Activity and Functionality. *J. Mol. Biol.* (2008), doi:10.1016/j.jmb.2008.10.009.

148. O. C. Ikonomov, D. Sbrissa, H. Fenner, A. Shisheva, PIKfyve-ArPIKfyve-Sac3 core complex: Contact sites and their consequence for Sac3 phosphatase activity and endocytic membrane homeostasis. *J. Biol. Chem.* (2009), doi:10.1074/jbc.M109.037515.

149. D. Sbrissa, O. C. Ikonomov, Z. Fu, T. Ijuin, J. Gruenberg, T. Takenawa, A. Shisheva, Core protein machinery for mammalian phosphatidylinositol 3,5-bisphosphate synthesis and turnover that regulates the progression of endosomal transport: Novel Sac phosphatase joins the ArPIKfyve-PIKfyve complex. *J. Biol. Chem.* (2007), doi:10.1074/jbc.M611678200.

174. V. Basrur, F. Yang, T. Kushimoto, Y. Higashimoto, K.-I. Yasumoto, J. Valencia, J.

Muller, W. D. Vieira, H. Watabe, J. Shabanowitz, V. J. Hearing, D. F. Hunt, E. Appella, Proteomic Analysis of Early Melanosomes: Identification of Novel Melanosomal Proteins. *J. Proteome Res.* **2**, 69–79 (2003).

180. C. F. Zhang, F. Gruber, C. Ni, M. Mildner, U. Koenig, S. Karner, C. Barresi, H. Rossiter, M. S. Narzt, I. M. Nagelreiter, L. Larue, D. J. Tobin, L. Eckhart, E. Tschachler, Suppression of autophagy dysregulates the antioxidant response and causes premature senescence of melanocytes. *J. Invest. Dermatol.* **135**, 1348–1357 (2015).

181. T. Proikas-Cezanne, Z. Takacs, P. Dönnes, O. Kohlbacher, WIPI proteins: essential PtdIns3P effectors at the nascent autophagosome. *J. Cell Sci.* **128**, 207–17 (2015).

183. T. Proikas-Cezanne, S. Ruckerbauer, Y. D. Stierhof, C. Berg, A. Nordheim, Human WIPI-1 puncta-formation: A novel assay to assess mammalian autophagy. *FEBS Lett.* **581**, 3396–3404 (2007).

198. K. Bharti, W. Liu, T. Csermely, S. Bertuzzi, H. Arnheiter, Alternative promoter use in eye development: The complex role and regulation of the transcription factor MITF. *Development*. **135**, 1169–1178 (2008).

204. A. Phelep, D. Laouari, K. Bharti, M. Burtin, S. Tammaccaro, S. Garbay, C. Nguyen, F. Vasseur, T. Blanc, S. Berissi, F. Langa-Vives, E. Fischer, A. Druilhe, H. Arnheiter, G. Friedlander, M. Pontoglio, F. Terzi, MITF – A controls branching morphogenesis and nephron endowment. *PLoS Genet.* **13**, e1007093 (2017).

233. C. A. Hodgkinson, K. J. Moore, A. Nakayama, E. Steingrímsson, N. G. Copeland, N. A. Jenkins, H. Arnheiter, Mutations at the mouse microphthalmia locus are associated with defects in a gene encoding a novel basic-helix-loop-helix-zipper protein. *Cell*. **74**, 395–404 (1993).

271. K. Paigen, One hundred years of mouse genetics: An intellectual history. I. The classical period (1902-1980). *Genetics* (2003).

272. G. S. Barsh, The genetics of pigmentation: From fancy genes to complex traits. *Trends Genet.* **12**, 299–305 (1996).

273. M. R. Johnson, G. S. Barsh, R. Mallarino, J. MR, B. GS, M. R, Periodic Patterns in Rodentia: Development and Evolution. *Exp. Dermatol.* **28**, 509 (2019).

274. R. Mallarino, C. Henegar, M. Mirasierra, M. Manceau, C. Schradin, M. Vallejo, S. Beronja, G. S. Barsh, H. E. Hoekstra, Developmental mechanisms of stripe patterns in rodents. *Nature*. **539**, 518–523 (2016).

275. B. H. Bin, J. Bhin, S. H. Yang, M. Shin, Y. J. Nam, D. H. Choi, D. W. Shin, A. Y. Lee, D. Hwang, E. G. Cho, T. R. Lee, Membrane-associated transporter protein (MATP) regulates melanosomal pH and influences tyrosinase activity. *PLoS One*. **10** (2015), doi:10.1371/journal.pone.0129273.

276. M. S. Marks, FIG4, Charcot-Marie-Tooth disease, and hypopigmentation: A role for phosphoinositides in melanosome biogenesis? *Pigment Cell Melanoma Res.* **21**, 11–14 (2008).

277. Z. H. Shah, D. R. Jones, L. Sommer, R. Foulger, Y. Bultsma, C. D'Santos, N. Divecha, Nuclear phosphoinositides and their impact on nuclear functions. *FEBS J.* (2013),

doi:10.1111/febs.12543.

278. N. Fuse, K. I. Yasumoto, K. Takeda, S. Amae, M. Yoshizawa, T. Udono, K. Takahashi, M. Tamai, Y. Tomita, M. Tachibana, S. Shibahara, Molecular cloning of cDNA encoding a novel microphthalmia-associated transcription factor isoform with a distinct amino-terminus. *J. Biochem.* **126**, 1043–1051 (1999).

279. C. M. Takemoto, Y. J. Yoon, D. E. Fisher, The identification and functional characterization of a novel mast cell isoform of the microphthalmia-associated transcription factor. *J. Biol. Chem.* **277**, 30244–30252 (2002).

280. M. Visser, M. Kayser, R. J. Palstra, HERC2 rs12913832 modulates human pigmentation by attenuating chromatin-loop formation between a long-range enhancer and the OCA2 promoter. *Genome Res.* **22**, 446–455 (2012).

281. H. Eiberg, J. Troelsen, M. Nielsen, A. Mikkelsen, J. Mengel-From, K. W. Kjaer, L. Hansen, Blue eye color in humans may be caused by a perfectly associated founder mutation in a regulatory element located within the HERC2 gene inhibiting OCA2 expression. *Hum. Genet.* **123**, 177–187 (2008).

BIBLIOGRAPHY

1. T. S. Kupper, R. C. Fuhlbrigge, Immune surveillance in the skin: Mechanisms and clinical consequences. *Nat. Rev. Immunol.* **4**, 211–222 (2004).

2. R. Wong, S. Geyer, W. Weninger, J. C. Guimberteau, J. K. Wong, The dynamic anatomy and patterning of skin. *Exp. Dermatol.* **25**, 92–98 (2016).

3. E. Fuchs, in *Current Topics in Developmental Biology* (2016; https://linkinghub.elsevier.com/retrieve/pii/S0070215315001994), vol. 116, pp. 357–374.

4. M. Cichorek, M. Wachulska, A. Stasiewicz, A. Tymińska, Skin melanocytes: Biology and development. *Postep. Dermatologii i Alergol.* **30**, 30–41 (2013).

5. W. C. Chou, M. Takeo, P. Rabbani, H. Hu, W. Lee, Y. R. Chung, J. Carucci, P. Overbeek, M. Ito, Direct migration of follicular melanocyte stem cells to the epidermis after wounding or UVB irradiation is dependent on Mc1r signaling. *Nat. Med.* **19**, 924–929 (2013).

6. M. Nakamura, M. Fukunaga-Kalabis, Y. Yamaguchi, T. Furuhashi, E. Nishida, H. Kato, T. Mizuno, M. Sugiura, A. Morita, Site-specific migration of human fetal melanocytes in volar skin. *J. Dermatol. Sci.* **78**, 143–148 (2015).

7. J. Hasegawa, Y. Goto, H. Murata, M. Takata, T. Saida, G. Imokawa, Downregulated melanogenic paracrine cytokine linkages in hypopigmented palmoplantar skin. *Pigment Cell Melanoma Res.* (2008), doi:10.1111/j.1755-148X.2008.00492.x.

8. T. Hirobe, H. Enami, Histochemical study of the distribution of epidermal melanoblasts and melanocytes in Asian human skin. *Ski. Res. Technol.* (2019), doi:10.1111/srt.12649.

9. T. Masaki, Y. Wang, J. J. Digiovanna, S. G. Khan, M. Raffeld, S. Beltaifa, T. J. Hornyak, T. N. Darling, C. C. R. Lee, K. H. Kraemer, High frequency of PTEN mutations in nevi and melanomas from xeroderma pigmentosum patients. *Pigment Cell Melanoma Res.* (2014), doi:10.1111/pcmr.12226.

10. K. Wakamatsu, R. Kavanagh, A. L. Kadekaro, S. Terzieva, R. A. Sturm, S. Leachman, Z. Abdel-Malek, S. Ito, Diversity of pigmentation in cultured human melanocytes is due to differences in the type as well as quantity of melanin. *Pigment Cell Res.* (2006), doi:10.1111/j.1600-0749.2006.00293.x.

11. M. L. Lamoreux, V. Delmas, L. Larue, D. C. Bennett, *The Colors of Mice: A Model Genetic Network* (2010).

12. N. Vandamme, G. Berx, From neural crest cells to melanocytes: cellular plasticity during development and beyond. *Cell. Mol. Life Sci.* **76**, 1919–1934 (2019).

13. L. L. Baxter, W. J. Pavan, Pmel17 expression is Mitf-dependent and reveals cranial melanoblast migration during murine development. *Gene Expr. Patterns*. **3**, 703–707 (2003).

14. Y. M. Wilson, K. L. Richards, M. L. Ford-Perriss, J. J. Panthier, M. Murphy, Neural crest cell lineage segregation in the mouse neural tube. *Development*. **131**, 6153–6162 (2004).

15. C. Grimm, M. P. Cuajungco, A. F. J. Van Aken, M. Schnee, S. Jörs, C. J. Kros, A. J. Ricci, S. Heller, A helix-breaking mutation in TRPML3 leads to constitutive activity underlying deafness in the varitint-waddler mouse. *Proc. Natl. Acad. Sci. U. S. A.* **104**, 19583–19588 (2007).

16. J. Vachtenheim, L. Ondrusov, in *Recent Advances in the Biology, Therapy and Management of Melanoma* (InTech, 2013; http://www.intechopen.com/books/recent-advances-in-the-biology-therapy-and-management-of-melanoma/mitf-a-critical-transcription-factor-in-melanoma-transcriptional-regulatory-network).

17. K. Bharti, M. T. T. Nguyen, S. Skuntz, S. Bertuzzi, H. Arnheiter, The other pigment cell: Specification and development of the pigmented epithelium of the vertebrate eye. *Pigment Cell Res.* **19**, 380–394 (2006).

18. M. H. Goldgeier, L. E. Klein, S. Klein-Angerer, The distribution of melanocytes in the leptomeninges of the human brain. *J. Invest. Dermatol.* **82**, 235–238 (1984).

19. S. Colombo, I. Berlin, V. Delmas, L. Larue, in *Melanins and Melanosomes: Biosynthesis, Biogenesis, Physiological, and Pathological Functions* (Wiley-VCH Verlag GmbH & Co. KGaA, Weinheim, Germany, 2011; http://doi.wiley.com/10.1002/9783527636150.ch2), pp. 21–61.

20. E. M. Wolf Horrell, M. C. Boulanger, J. A. D'Orazio, Melanocortin 1 receptor: Structure, function, and regulation. *Front. Genet.* **7**, 95 (2016).

21. R. Cui, H. R. Widlund, E. Feige, J. Y. Lin, D. L. Wilensky, V. E. Igras, J. D'Orazio, C. Y. Fung, C. F. Schanbacher, S. R. Granter, D. E. Fisher, Central Role of p53 in the Suntan Response and Pathologic Hyperpigmentation. *Cell*. **128**, 853–864 (2007).

22. S. Benjannet, N. Rondeau, R. Day, M. Chrétien, N. G. Seidah, PC1 and PC2 are proprotein convertases capable of cleaving proopiomelanocortin at distinct pairs of basic residues. *Proc. Natl. Acad. Sci. U. S. A.* **88**, 3564–3568 (1991).

23. S. A. N. D'Mello, G. J. Finlay, B. C. Baguley, M. E. Askarian-Amiri, Signaling pathways in melanogenesis. *Int. J. Mol. Sci.* **17** (2016), doi:10.3390/ijms17071144.

24. C. Serre, V. Busuttil, J. M. Botto, Intrinsic and extrinsic regulation of human skin melanogenesis and pigmentation. *Int. J. Cosmet. Sci.* **40**, 328–347 (2018).

25. H. Murakami, H. Arnheiter, Sumoylation modulates transcriptional activity of MITF in a promoter-specific manner. *Pigment Cell Res.* (2005), doi:10.1111/j.1600-0749.2005.00234.x.

26. H. E. Seberg, E. Van Otterloo, R. A. Cornell, Beyond MITF: Multiple transcription factors directly regulate the cellular phenotype in melanocytes and melanoma. *Pigment Cell Melanoma Res.* (2017), doi:10.1111/pcmr.12611.

27. A. Sitaram, M. S. Marks, Mechanisms of protein delivery to melanosomes in pigment cells. *Physiology*. **27**, 85–99 (2012).

28. A. M. De Mazière, K. Muehlethaler, E. Van Donselaar, S. Salvi, J. Davoust, J. C. Cerottini, F. Lévy, J. W. Slot, D. Rimoldi, The melanocytic protein Melan-A/MART-1 has

a subcellular localization distinct from typical melanosomal proteins. *Traffic* (2002), doi:10.1034/j.1600-0854.2002.30909.x.

29. C. Bissig, P. Croisé, X. Heiligenstein, I. Hurbain, G. M. Lenk, E. Kaufman, R. Sannerud, W. Annaert, M. H. Meisler, L. S. Weisman, G. Raposo, G. Van Niel, The PIKfyve complex regulates the early melanosome homeostasis required for physiological amyloid formation. *J. Cell Sci.* **132**, jcs229500 (2019).

30. C. Wasmeier, M. Romao, L. Plowright, D. C. Bennett, G. Raposo, M. C. Seabra, Rab38 and Rab32 control post-Golgi trafficking of melanogenic enzymes. *J. Cell Biol.* **175**, 271–81 (2006).

31. A. Gerondopoulos, L. Langemeyer, J. R. Liang, A. Linford, F. A. Barr, BLOC-3 mutated in Hermansky-Pudlak syndrome is a Rab32/38 guanine nucleotide exchange factor. *Curr. Biol.* **22**, 2135–2139 (2012).

32. S. R. G. Setty, D. Tenza, S. T. Truschel, E. Chou, E. V. Sviderskaya, A. C. Theos, M. L. Lamoreux, S. M. Di Pietro, M. M. Starcevic, D. C. Bennett, E. C. Dell'Angelica, G. Raposo, M. S. Marks, BLOC-1 is required for cargo-specific sorting from vacuolar early endosomes toward lysosome-related organelles. *Mol. Biol. Cell*. **18**, 768–780 (2007).

33. M. Starcevic, E. C. Dell'Angelica, Identification of Snapin and three novel proteins (BLOS1, BLOS2, and BLOS3/reduced pigmentation) as subunits of biogenesis of lysosome-related organelles complex-1 (BLOC-1). *J. Biol. Chem.* **279**, 28393–28401 (2004).

34. J. M. Falcón-Pérez, M. Starcevic, R. Gautam, E. C. Dell'Angelica, BLOC-1, a novel complex containing the pallidin and muted proteins involved in the biogenesis of melanosomes and platelet-dense granules. *J. Biol. Chem.* **277**, 28191–28199 (2002).

35. S. L. Ciciotte, B. Gwynn, K. Moriyama, M. Huizing, W. A. Gahl, J. S. Bonifacino, L. L. Peters, Cappuccino, a mouse model of Hermansky-Pudlak syndrome, encodes a novel protein that is part of the pallidin-muted complex (BLOC-1). *Blood*. **101**, 4402–4407 (2003).

36. W. Li, Q. Zhang, N. Oiso, E. K. Novak, R. Gautam, E. P. O'Brien, C. L. Tinsley, D. J. Blake, R. A. Spritz, N. G. Copeland, N. A. Jenkins, D. Amato, B. A. Roe, M. Starcevic, E. C. Dell'Angelica, R. W. Elliott, V. Mishra, S. F. Kingsmore, R. E. Paylor, R. T. Swank, Hermansky-Pudlak syndrome type 7 (HPS-7) results from mutant dysbindin, a member of the biogenesis of lysosome-related organelles complex 1 (BLOC-1). *Nat. Genet.* **35**, 84–89 (2003).

37. C. Delevoye, I. Hurbain, D. Tenza, J.-B. B. Sibarita, S. Uzan-Gafsou, H. Ohno, W. J. C. Geerts, A. J. Verkleij, J. Salamero, M. S. Marks, G. Raposo, AP-1 and KIF13A coordinate endosomal sorting and positioning during melanosome biogenesis. *J. Cell Biol.* **187**, 247–264 (2009).

38. M. K. Dennis, A. R. Mantegazza, O. L. Snir, D. Tenza, A. Acosta-Ruiz, C. Delevoye, R. Zorger, A. Sitaram, W. de Jesus-Rojas, K. Ravichandran, J. Rux, E. V. Sviderskaya, D. C. Bennett, G. Raposo, M. S. Marks, S. R. G. Setty, BLOC-2 targets recycling endosomal tubules to melanosomes for cargo delivery. *J. Cell Biol.* **209**, 563–577 (2015).

39. S. M. Di Pietro, J. M. Falcón-Pérez, E. C. Dell'Angelica, Characterization of BLOC-2, a complex containing the Hermansky-Pudlak syndrome proteins HPS3, HPS5 and HPS6. *Traffic*. **5**, 276–283 (2004).

40. A. C. Theos, A. Martina, I. Hurbain, A. A. Peden, E. V Sviderskaya, A. Stewart, M. S. Robinson, D. C. Bennett, D. F. Cutler, J. S. Bonifacino, M. S. Marks, D. Tenza, J. A. Martina, I. Hurbain, A. A. Peden, E. V Sviderskaya, A. Stewart, M. S. Robinson, D. C. Bennett, D. F. Cutler, J. S. Bonifacino, M. S. Marks, G. Raposo, Functions of adaptor protein (AP)-3 and AP-1 in tyrosinase sorting from endosomes to melanosomes. *Mol. Biol. Cell*. **16**, 5356–72 (2005).

41. M. J. Petris, The Menkes copper transporter is required for the activation of tyrosinase. *Hum. Mol. Genet.* **9**, 2845–2851 (2000).

42. S. R. G. Setty, D. Tenza, E. V. Sviderskaya, D. C. Bennett, G. Raposo, M. S. Marks, Cell-specific ATP7A transport sustains copper-dependent tyrosinase activity in melanosomes. *Nature*. **454**, 1142–1146 (2008).

43. A. Ramkumar, D. Murthy, D. A. Raja, A. Singh, A. Krishnan, S. Khanna, A. Vats, L. Thukral, P. Sharma, S. Sivasubbu, R. Rani, V. T. Natarajan, R. S. Gokhale, Classical autophagy proteins LC3B and ATG4B facilitate melanosome movement on cytoskeletal tracks. *Autophagy*. **13**, 1331–1347 (2017).

44. J. D'Orazio, S. Jarrett, A. Amaro-Ortiz, T. Scott, UV Radiation and the Skin. *Int. J. Mol. Sci.* **14**, 12222–48 (2013).

45. R. E. Boissy, in *Experimental Dermatology, Supplement* (Munksgaard International Publishers, 2003; http://doi.wiley.com/10.1034/j.1600-0625.12.s2.1.x), vol. 12, pp. 5–12.

46. W. J. Yun, E.-Y. Kim, J.-E. Park, S. Y. Jo, S. H. Bang, E.-J. Chang, S. E. Chang, Microtubule-associated protein light chain 3 is involved in melanogenesis via regulation of MITF expression in melanocytes. *Sci. Rep.* **6**, 19914 (2016).

47. R. Micillo, L. Panzella, K. Koike, G. Monfrecola, A. Napolitano, M. D'Ischia, "Fifty shades" of black and red or how carboxyl groups fine tune eumelanin and pheomelanin properties. *Int. J. Mol. Sci.* **17** (2016), doi:10.3390/ijms17050746.

48. T. H. Nasti, L. Timares, MC1R, eumelanin and pheomelanin: Their role in determining the susceptibility to skin cancer. *Photochem. Photobiol.* **91**, 188–200 (2015).

49. F. Van Nieuwpoort, N. P. M. Smit, R. Kolb, H. Van Der Meulen, H. Koerten, S. Pavel, Tyrosine-induced melanogenesis shows differences in morphologic and melanogenic preferences of melanosomes from light and dark skin types. *J. Invest. Dermatol.* **122**, 1251–1255 (2004).

50. S. Schmitz, P. D. Thomas, T. M. Allen, M. J. Poznansky, K. Jimbow, DUAL ROLE OF MELANINS AND MELANIN PRECURSORS AS PHOTOPROTECTIVE AND PHOTOTOXIC AGENTS: INHIBITION OF ULTRAVIOLET RADIATION-INDUCED LIPID PEROXIDATION. *Photochem. Photobiol.* (1995), doi:10.1111/j.1751-1097.1995.tb09883.x.

51. E. Wenczl, N. P. M. Smit, S. S. Pavel, A. A. Schothorst, G. P. Van Der Schans, A. J.

Timmerman, L. Roza, R. M. Kolb, A. J. Timmerman, N. P. M. Smit, S. S. Pavel, A. A. Schothorst, (Pheo)melanin photosensitizes UVA-induced DNA damage in cultured human melanocytes. *J. Invest. Dermatol.* **111**, 678–682 (1998).

52. M. R. Chedekel, S. K. Smith, P. W. Post, A. Pokora, D. L. Vessell, Photodestruction of pheomelanin: role of oxygen. *Proc. Natl. Acad. Sci. U. S. A.* **75**, 5395–5399 (1978).

53. M. D. Morgan, E. Pairo-Castineira, K. Rawlik, O. Canela-Xandri, J. Rees, D. Sims, A. Tenesa, I. J. Jackson, Genome-wide study of hair colour in UK Biobank explains most of the SNP heritability. *Nat. Commun.* **9** (2018), doi:10.1038/s41467-018-07691-z.

54. C. Bonilla, L.-A. Boxill, S. A. M. Donald, T. Williams, N. Sylvester, E. J. Parra, S. Dios, H. L. Norton, M. D. Shriver, R. A. Kittles, The 8818G allele of the agouti signaling protein (ASIP) gene is ancestral and is associated with darker skin color in African Americans. *Hum. Genet.* **116**, 402–406 (2005).

55. M. Reissmann, A. Ludwig, Pleiotropic effects of coat colour-associated mutations in humans, mice and other mammals. *Semin. Cell Dev. Biol.* (2013), doi:10.1016/j.semcdb.2013.03.014.

56. R. L. Lamason, M.-A. A. P. K. Mohideen, J. R. Mest, A. C. Wong, H. L. Norton, M. C. Aros, M. J. Jurynec, X. Mao, V. R. Humphreville, J. E. Humbert, S. Sinha, J. L. Moore, P. Jagadeeswaran, W. Zhao, G. Ning, I. Makalowska, P. M. McKeigue, D. O'Donnell, R. Kittles, E. J. Parra, N. J. Mangini, D. J. Grunwald, M. D. Shriver, V. A. Canfield, K. C. Cheng, Genetics: SLC24A5, a putative cation exchanger, affects pigmentation in zebrafish and humans. *Science (80-.).* **310**, 1782–1786 (2005).

57. N. G. Crawford, D. E. Kelly, M. E. B. Hansen, M. H. Beltrame, S. Fan, S. L. Bowman, E. Jewett, A. Ranciaro, S. Thompson, Y. Lo, S. P. Pfeifer, J. D. Jensen, M. C. Campbell, W. Beggs, F. Hormozdiari, S. W. Mpoloka, G. G. Mokone, T. Nyambo, D. W. Meskel, G. Belay, J. Haut, H. Rothschild, L. Zon, Y. Zhou, M. A. Kovacs, M. Xu, T. Zhang, K. Bishop, J. Sinclair, C. Rivas, E. Elliot, J. Choi, S. A. Li, B. Hicks, S. Burgess, C. Abnet, D. E. Watkins-Chow, E. Oceana, Y. S. Song, E. Eskin, K. M. Brown, M. S. Marks, S. K. Loftus, W. J. Pavan, M. Yeager, S. Chanock, S. A. Tishkoff, Loci associated with skin pigmentation identified in African populations. *Science (80-.).* (2017), doi:10.1126/science.aan8433.

58. D. C. Whiteman, W. J. Pavan, B. C. Bastian, The melanomas: A synthesis of epidemiological, clinical, histopathological, genetic, and biological aspects, supporting distinct subtypes, causal pathways, and cells of origin. *Pigment Cell Melanoma Res.* (2011), , doi:10.1111/j.1755-148X.2011.00880.x.

59. N. G. Jablonski, G. Chaplin, The evolution of human skin coloration. *J. Hum. Evol.* **39**, 57–106 (2000).

60. A. Piotrowska, J. Wierzbicka, M. A. Zmijewski, Vitamin D in the skin physiology and pathology. *Acta Biochim. Pol.* **63**, 17–29 (2016).

61. G. Chaplin, N. G. Jablonski, Vitamin D and the evolution of human depigmentation. *Am. J. Phys. Anthropol.* **139**, 451–461 (2009).

62. G. S. Barsh, What controls variation in human skin color? *PLoS Biol.* (2003), doi:10.1371/journal.pbio.0000027.

63. G. B. Parker, H. Brotchie, R. K. Graham, Vitamin D and depression. *J. Affect. Disord.* **208**, 56–61 (2017).

64. R. Vieth, S. Kimball, A. Hu, P. G. Walfish, Randomized comparison of the effects of the vitamin D3 adequate intake versus 100 mcg (4000 IU) per day on biochemical responses and the wellbeing of patients. *Nutr. J.* **3**, 8 (2004).

65. A. M. Morgan, J. Lo, D. E. Fisher, How does pheomelanin synthesis contribute to melanomagenesis?: Two distinct mechanisms could explain the carcinogenicity of pheomelanin synthesis. *BioEssays*. **35**, 672–676 (2013).

66. B. Anna, Z. Blazej, G. Jacqueline, C. J. Andrew, R. Jeffrey, S. Andrzej, Mechanism of UV-related carcinogenesis and its contribution to nevi/melanoma. *Expert Rev. Dermatol.* **2**, 451–469 (2007).

67. L. B. Alexandrov, S. Nik-Zainal, D. C. Wedge, S. A. J. R. J. R. Aparicio, S. Behjati, A. V. Biankin, G. R. Bignell, N. Bolli, A. Borg, A.-L. L. Børresen-Dale, S. Boyault, B. Burkhardt, A. P. Butler, C. Caldas, H. R. Davies, C. Desmedt, R. Eils, J. E. Eyfjörd, J. A. Foekens, M. Greaves, F. Hosoda, B. Hutter, T. Ilicic, S. Imbeaud, M. Imielinsk, N. Jäger, D. T. W. W. Jones, D. T. W. W. Jones, S. Knappskog, M. Kool, S. R. Lakhani, C. López-Otín, S. Martin, N. C. Munshi, H. Nakamura, P. A. Northcott, M. Pajic, E. Papaemmanuil, A. Paradiso, J. V. Pearson, X. S. Puente, K. Raine, M. Ramakrishna, A. L. Richardson, J. Richter, P. Rosenstiel, M. Schlesner, T. N. Schumacher, P. N. Span, J. W. Teague, Y. Totoki, A. N. J. J. Tutt, R. Valdés-Mas, M. M. van Buuren, L. van 't Veer, A. Vincent-Salomon, N. Waddell, L. R. Yates, J. Zucman-Rossi, P. Andrew Futreal, U. McDermott, P. Lichter, M. Meyerson, S. M. Grimmond, R. Siebert, E. Campo, T. Shibata, S. M. Pfister, P. J. Campbell, M. R. Stratton, T. Shibata, S. M. Pfister, P. J. Campbell, M. R. Stratton, D. Jonas, S. Knappskog, M. Koo, S. R. Lakhani, C. López-Otín, S. Martin, N. C. Munshi, H. Nakamura, P. A. Northcott, M. Pajic, E. Papaemmanuil, A. Paradiso, J. V. Pearson, X. S. Puente, K. Raine, M. Ramakrishna, A. L. Richardson, J. Richter, P. Rosenstiel, M. Schlesner, T. N. Schumacher, P. N. Span, J. W. Teague, Y. Totoki, A. N. J. J. Tutt, R. Valdés-Mas, M. M. van Buuren, L. Van 'T Veer, A. Vincent-Salomon, N. Waddell, L. R. Yates, J. Zucman-Rossi, P. Andrew Futreal, U. McDermott, P. Lichter, M. Meyerson, S. M. Grimmond, R. Siebert, E. Campo, T. Shibata, S. M. Pfister, P. J. Campbell, M. R. Stratton, Signatures of mutational processes in human cancer. *Nature*. **500**, 415–421 (2013).

68. H. L. Kaufman, J. M. Kirkwood, F. S. Hodi, S. Agarwala, T. Amatruda, S. D. Bines, J. I. Clark, B. Curti, M. S. Ernstoff, T. Gajewski, R. Gonzalez, L. J. Hyde, D. Lawson, M. Lotze, J. Lutzky, K. Margolin, D. F. McDermott, D. Morton, A. Pavlick, J. M. Richards, W. Sharfman, V. K. Sondak, J. Sosman, S. Steel, A. Tarhini, J. A. Thompson, J. Titze, W. Urba, R. White, M. B. Atkins, The society for immunotherapy of cancer consensus statement on tumour immunotherapy for the treatment of cutaneous melanoma. *Nat. Rev. Clin. Oncol.* **10**, 588–598 (2013).

69. A. H. Shain, I. Yeh, I. Kovalyshyn, A. Sriharan, E. Talevich, A. Gagnon, R. Dummer, J.

North, L. Pincus, B. Ruben, W. Rickaby, C. D'Arrigo, A. Robson, B. C. Bastian, The genetic evolution of melanoma from precursor lesions. *N. Engl. J. Med.* **373**, 1926–1936 (2015).

70. N. Dhomen, J. S. Reis-Filho, S. da Rocha Dias, R. Hayward, K. Savage, V. Delmas, L. Larue, C. Pritchard, R. Marais, Oncogenic Braf Induces Melanocyte Senescence and Melanoma in Mice. *Cancer Cell*. **15**, 294–303 (2009).

71. D. Dankort, D. P. Curley, R. A. Cartlidge, B. Nelson, A. N. Karnezis, W. E. Damsky, M. J. You, R. A. DePinho, M. McMahon, M. Bosenberg, BrafV600E cooperates with Pten loss to induce metastatic melanoma. *Nat. Genet.* **41**, 544–552 (2009).

72. M. Bosenberg, V. Muthusamy, D. P. Curley, Z. Wang, C. Hobbs, B. Nelson, C. Nogueira, J. W. Horner, R. DePinho, L. Chin, Characterization of melanocyte-specific inducible Cre recombinase transgenic mice. *Genesis*. **44**, 262–7 (2006).

73. L. N. Kwong, J. C. Costello, H. Liu, S. Jiang, T. L. Helms, A. E. Langsdorf, D. Jakubosky, G. Genovese, F. L. Muller, J. H. Jeong, R. P. Bender, G. C. Chu, K. T. Flaherty, J. A. Wargo, J. J. Collins, L. Chin, Oncogenic NRAS signaling differentially regulates survival and proliferation in melanoma. *Nat. Med.* **18**, 1503–1510 (2012).

74. O. A. Ogbechie-Godec, N. Elbuluk, Melasma: an Up-to-Date Comprehensive Review. *Dermatol. Ther. (Heidelb).* (2017), doi:10.1007/s13555-017-0194-1.

75. E. Nicolaidou, A. D. Katsambas, Pigmentation disorders: Hyperpigmentation and hypopigmentation. *Clin. Dermatol.* **32**, 66–72 (2014).

76. F. Boukari, E. Jourdan, E. Fontas, H. Montaudié, E. Castela, J. P. Lacour, T. Passeron, Prevention of melasma relapses with sunscreen combining protection against UV and short wavelengths of visible light: A prospective randomized comparative trial. *J. Am. Acad. Dermatol.* **72**, 189-190.e1 (2015).

77. C. A. Natale, E. K. Duperret, J. Zhang, R. Sadeghi, A. Dahal, K. T. O'Brien, R. Cookson, J. D. Winkler, T. W. Ridky, Sex steroids regulate skin pigmentation through nonclassical membrane-bound receptors. *Elife* (2016), doi:10.7554/eLife.15104.

78. M. Rashighi, J. E. Harris, Vitiligo Pathogenesis and Emerging Treatments. *Dermatol. Clin.* **35**, 257–265 (2017).

79. K. Ezzedine, V. Eleftheriadou, M. Whitton, N. van Geel, Vitiligo. *Lancet (London, England)*. **386**, 74–84 (2015).

80. K. Ezzedine, V. Sheth, M. Rodrigues, V. Eleftheriadou, J. E. Harris, I. H. Hamzavi, A. G. Pandya, Vitiligo is not a cosmetic disease. *J. Am. Acad. Dermatol.* **73**, 883–885 (2015).

81. S. A. Birlea, N. B. Goldstein, D. A. Norris, Repigmentation through Melanocyte Regeneration in Vitiligo. *Dermatol. Clin.* **35**, 205–218 (2017).

82. R. L. Sidman, B. Kosaras, M. Tang, Pigment epithelial and retinal phenotypes in the vitiligo, mivit, mutant mouse. *Investig. Ophthalmol. Vis. Sci.* (1996).

83. J. E. Harris, T. H. Harris, W. Weninger, E. J. Wherry, C. A. Hunter, L. A. Turka, A mouse

model of vitiligo with focused epidermal depigmentation requires IFN-γ for autoreactive CD8+ T-cell accumulation in the skin. *J. Invest. Dermatol.* **132**, 1869–1876 (2012).

84. B. Kamaraj, R. Purohit, Mutational analysis of oculocutaneous albinism: A compact review. *Biomed Res. Int.* **2014**, 905472 (2014).

85. N. Puri, J. M. Gardner, M. H. Brilliant, Aberrant pH of melanosomes in pink-eyed dilution (p) mutant melanocytes. *J. Invest. Dermatol.* **115**, 607–613 (2000).

86. P. Manga, S. Pifko-Hirst, B. K. Zhou, S. J. Orlow, R. E. Boissy, Mislocalization of melanosomal proteins in melanocytes from mice with oculocutaneous albinism type 2. *Exp. Eye Res.* **72**, 695–710 (2001).

87. Y. Yamaguchi, V. J. Hearing, Melanocytes and their diseases. *Cold Spring Harb. Perspect. Med.* **4**, a017046- (2014).

88. E. S. Russell, A History of Mouse Genetics. *Annu. Rev. Genet.* **19**, 1–29 (1985).

89. F. Beermann, S. J. Orlow, M. L. Lamoreux, The Tyr (albino) locus of the laboratory mouse. *Mamm. Genome*. **15**, 749–758 (2004).

90. B. S. Kwon, A. K. Haq, M. Wakulchik, D. Kestler, D. E. Barton, U. Francke, M. L. Lamoreux, J. B. Whitney, R. Halaban, Isolation, chromosomal mapping, and expression of the mouse tyrosinase gene. *J. Invest. Dermatol.* **93**, 589–594 (1989).

91. E. K. Paterson, T. J. Fielder, G. R. MacGregor, S. Ito, K. Wakamatsu, D. L. Gillen, V. Eby, R. E. Boissy, A. K. Ganesan, Tyrosinase depletion prevents the maturation of melanosomes in the mouse hair follicle. *PLoS One*. **10** (2015), doi:10.1371/journal.pone.0143702.

92. H. Shoji, Y. Kiniwa, R. Okuyama, M. Yang, K. Higuchi, M. Mori, A nonsense nucleotide substitution in the oculocutaneous albinism II gene underlies the original pink-eyed dilution allele (Oca2p) in mice. *Exp. Anim.* **64**, 171 (2015).

93. P. Manga, K. Sato, L. Ye, F. Beermann, M. Lynn Lamoreux, S. J. Orlow, Mutational analysis of the modulation of tyrosinase by tyrosinase-related proteins 1 and 2 in vitro. *Pigment Cell Res.* **13**, 364–374 (2000).

94. J. M. Newton, O. Cohen-Barak, N. Hagiwara, J. M. Gardner, M. T. Davisson, R. A. King, M. H. Brilliant, Mutations in the human orthologue of the mouse underwhite gene (uw) underlie a new form of oculocutaneous albinism, OCA4. *Am. J. Hum. Genet.* **69**, 981–988 (2001).

95. S. L. Bowman, J. Bi-Karchin, L. Le, M. S. Marks, The road to lysosome-related organelles: Insights from Hermansky-Pudlak syndrome and other rare diseases. *Traffic*. **20**, 404–435 (2019).

96. P. W. Chiang, N. Oiso, R. Gautam, T. Suzuki, R. T. Swank, R. A. Spritz, The Hermansky-Pudlak syndrome 1 (HPS1) and HPS4 proteins are components of two complexes, BLOC-3 and BLOC-4, involved in the biogenesis of lysosome-related organelles. *J. Biol. Chem.* **278**, 20332–20337 (2003).

97. L. Feng, A. B. Seymour, S. Jiang, A. To, A. A. Peden, E. K. Novak, L. Zhen, M. E. Rusiniak, E. M. Eicher, M. S. Robinson, M. B. Gorin, R. T. Swank, The β3A subunit gene (Ap3b1) of the AP-3 adaptor complex is altered in the mouse hypopigmentation mutant pearl, a model for Hermansky-Pudlak syndrome and night blindness. *Hum. Mol. Genet.* **8**, 323–330 (1999).

98. R. Gautam, S. Chintala, W. Li, Q. Zhang, J. Tan, E. K. Novak, S. M. Di Pietro, E. C. Dell'Angelica, R. T. Swank, The Hermansky-Pudlak Syndrome 3 (Cocoa) Protein Is a Component of the Biogenesis of Lysosome-related Organelles Complex-2 (BLOC-2). *J. Biol. Chem.* **279**, 12935–12942 (2004).

99. J. Kaplan, I. De Domenico, D. M. V. Ward, Chediak-Higashi syndrome. *Curr. Opin. Hematol.* **15**, 22–29 (2008).

100. S. K. Fistarol, P. H. Itin, Disorders of pigmentation. *J. Ger. Soc. Dermatology*. **8**, 187–202 (2010).

101. R. Mayor, E. Theveneau, The neural crest. *Dev.* **140**, 2247–2251 (2012).

102. V. Pingault, D. Ente, F. Dastot-Le Moal, M. Goossens, S. Marlin, N. Bondurand, Review and update of mutations causing Waardenburg syndrome. *Hum. Mutat.* **31**, 391–406 (2010).

103. M. D. Saleem, Biology of human melanocyte development, Piebaldism, and Waardenburg syndrome. *Pediatr. Dermatol.* **36**, 72–84 (2019).

104. L. Montoliu, W. S. Oetting, D. C. Bennett, International Federation of Pigmented Cell Societies, Color Genes. *Eur. Soc. Pigment Cell Res.* (2017), (available at http://www.espcr.org/micemut.html).

105. E. Steingrímsson, N. G. Copeland, N. A. Jenkins, Melanocytes and the Microphthalmia Transcription Factor Network. *Annu. Rev. Genet.* **38**, 365–411 (2004).

106. C. Y. Chow, Y. Zhang, J. J. Dowling, N. Jin, M. Adamska, K. Shiga, K. Szigeti, M. E. Shy, J. Li, X. Zhang, J. R. Lupski, L. S. Weisman, M. H. Meisler, Mutation of FIG4 causes neurodegeneration in the pale tremor mouse and patients with CMT4J. *Nature*. **448**, 68–72 (2007).

107. N. Jin, C. Y. Chow, L. Liu, S. N. Zolov, R. Bronson, M. Davisson, J. L. Petersen, Y. Zhang, S. Park, J. E. Duex, D. Goldowitz, M. H. Meisler, L. S. Weisman, VAC14 nucleates a protein complex essential for the acute interconversion of PI3P and PI(3,5)P2 in yeast and mouse. *EMBO J.* **27**, 3221–34 (2008).

108. O. C. Ikonomov, D. Sbrissa, K. Delvecchio, Y. Xie, J. P. Jin, D. Rappolee, A. Shisheva, The phosphoinositide kinase PIKfyve is vital in early embryonic development: Preimplantation lethality of PIKfyve-/- embryos but normality of PIKfyve+/- mice. *J. Biol. Chem.* (2011), doi:10.1074/jbc.M111.222364.

109. S. Takasuga, Y. Horie, J. Sasaki, G.-H. H. Sun-Wada, N. Kawamura, R. Iizuka, K. Mizuno, S. Eguchi, S. Kofuji, H. Kimura, M. Yamazaki, C. Horie, E. Odanaga, Y. Sato, S. Chida, K. Kontani, A. Harada, T. Katada, A. Suzuki, Y. Wada, H. Ohnishi, T. Sasaki, Critical roles of type III phosphatidylinositol phosphate kinase in murine embryonic

visceral endoderm and adult intestine. *Proc. Natl. Acad. Sci. U. S. A.* **110**, 1726–31 (2013).

110. M. C. Liggins, J. L. Flesher, S. Jahid, P. Vasudeva, V. Eby, S. Takasuga, J. Sasaki, T. Sasaki, R. E. Boissy, A. K. Ganesan, PIKfyve regulates melanosome biogenesis. *PLoS Genet.* **14** (2018), doi:10.1371/journal.pgen.1007290.

111. T. Proikas-Cezanne, S. Waddell, A. Gaugel, T. Frickey, A. Lupas, A. Nordheim, WIPI-1alpha (WIPI49), a member of the novel 7-bladed WIPI protein family, is aberrantly expressed in human cancer and is linked to starvation-induced autophagy. *Oncogene*. **23**, 9314–9325 (2004).

112. H. Ho, R. Kapadia, S. Al-Tahan, S. Ahmad, A. K. Ganesan, WIPI1 coordinates melanogenic gene transcription and melanosome formation via TORC1 inhibition. *J. Biol. Chem.* **286**, 12509–12523 (2011).

113. A. K. Ganesan, H. Ho, B. Bodemann, S. Petersen, J. Aruri, S. Koshy, Z. Richardson, L. Q. Le, T. Krasieva, M. G. Roth, P. Farmer, M. A. White, Genome-wide siRNA-based functional genomics of pigmentation identifies novel genes and pathways that impact melanogenesis in human cells. *PLoS Genet.* **4** (2008), doi:10.1371/journal.pgen.1000298.

114. P. Hertwig, Neue Mutationen und Kopplungsgruppen bei der Hausmaus. *Z. Indukt. Abstammungs- u. Vererbungsl.* **80**, 220–246 (1942).

115. C. J. Bult, J. A. Blake, C. L. Smith, J. A. Kadin, J. E. Richardson, A. Anagnostopoulos, R. Asabor, R. M. Baldarelli, J. S. Beal, S. M. Bello, O. Blodgett, N. E. Butler, K. R. Christie, L. E. Corbani, J. Creelman, M. E. Dolan, H. J. Drabkin, S. L. Giannatto, P. Hale, D. P. Hill, M. Law, A. Mendoza, M. McAndrews, D. Miers, H. Motenko, L. Ni, H. Onda, M. Perry, J. M. Recla, B. Richards-Smith, D. Sitnikov, M. Tomczuk, G. Tonorio, L. Wilming, Y. Zhu, Mouse Genome Database (MGD) 2019. *Nucleic Acids Res.* (2019), doi:10.1093/nar/gky1056.

116. H. Arnheiter, The discovery of the microphthalmia locus and its gene, Mitf. *Pigment Cell Melanoma Res.* **23**, 729–735 (2010).

117. E. Steingrímsson, All for one, one for all: alternative promoters and Mitf. *Pigment Cell Melanoma Res.* **21**, 412–414 (2008).

118. E. K. Paterson, H. Ho, R. Kapadia, A. K. Ganesan, 9-cis retinoic acid is the ALDH1A1 product that stimulates melanogenesis. *Exp. Dermatol.* **22**, 202–209 (2013).

119. J. L. Flesher, E. K. Paterson-Coleman, P. Vasudeva, R. Ruiz-Vega, M. Marshall, E. Pearlman, G. R. MacGregor, J. Neumann, A. K. Ganesan, Delineating the role of MITF isoforms in pigmentation and tissue homeostasis. *Pigment Cell Melanoma Res.* **33**, 279–292 (2020).

120. G.-E. Costin, V. J. Hearing, Human skin pigmentation: melanocytes modulate skin color in response to stress. *FASEB J.* (2007), doi:10.1096/fj.06-6649rev.

121. G. Raposo, M. S. Marks, Melanosomes - Dark organelles enlighten endosomal membrane transport. *Nat. Rev. Mol. Cell Biol.* (2007), doi:10.1038/nrm2258.

122. A. H. Wei, W. Li, Hermansky-Pudlak syndrome: Pigmentary and non-pigmentary defects and their pathogenesis. *Pigment Cell Melanoma Res.* (2013), doi:10.1111/pcmr.12051.

123. C. Wasmeier, A. N. Hume, G. Bolasco, M. C. Seabra, Melanosomes at a glance. *J. Cell Sci.* **121**, 3995–3999 (2008).

124. F. Giordano, C. Bonetti, E. M. Surace, V. Marigo, G. Raposo, The ocular albinism type 1 (OA1) G-protein-coupled receptor functions with MART-1 at early stages of melanogenesis to control melanosome identity and composition. *Hum. Mol. Genet.* (2009), doi:10.1093/hmg/ddp415.

125. B. Watt, G. van Niel, G. Raposo, M. S. Marks, PMEL: a pigment cell-specific model for functional amyloid formation. *Pigment Cell Melanoma Res.* **26**, 300–15 (2013).

126. Y. Yamaguchi, V. J. Hearing, Physiological factors that regulate skin pigmentation. *BioFactors* (2009), doi:10.1002/biof.29.

127. C. Bissig, L. Rochin, G. van Niel, PMEL amyloid fibril formation: The bright steps of pigmentation. *Int. J. Mol. Sci.* **17**, 1438 (2016).

128. A. Slominski, D. J. Tobin, S. Shibahara, J. Wortsman, Melanin pigmentation in mammalian skin and its hormonal regulation. *Physiol. Rev.* **84**, 1155–1228 (2004).

129. H. Y. Park, M. Kosmadaki, M. Yaar, B. A. Gilchrest, Cellular mechanisms regulating human melanogenesis. *Cell. Mol. Life Sci.* **66**, 1493–506 (2009).

130. Z. Erpapazoglou, M. Dhaoui, M. Pantazopoulou, F. Giordano, M. Mari, S. Léon, G. Raposo, F. Reggiori, R. Haguenauer-Tsapis, A dual role for K63-linked ubiquitin chains in multivesicular body biogenesis and cargo sorting. *Mol. Biol. Cell* (2012), doi:10.1091/mbc.E11-10-0891.

131. G. van Niel, S. Charrin, S. Simoes, M. Romao, L. Rochin, P. Saftig, M. S. Marks, E. Rubinstein, G. Raposo, The Tetraspanin CD63 Regulates ESCRT-Independent and -Dependent Endosomal Sorting during Melanogenesis. *Dev. Cell* (2011), doi:10.1016/j.devcel.2011.08.019.

132. S. T. Truschel, S. Simoes, S. R. G. Setty, D. C. Harper, D. Tenza, P. C. Thomas, K. E. Herman, S. D. Sackett, D. C. Cowan, A. C. Theos, G. Raposo, M. S. Marks, ESCRT-I function is required for Tyrp1 transport from early endosomes to the melanosome limiting membrane. *Traffic* (2009), doi:10.1111/j.1600-0854.2009.00955.x.

133. M. S. Marks, Organelle biogenesis: En BLOC exchange for RAB32 and RAB38. *Curr. Biol.* (2012), doi:10.1016/j.cub.2012.10.005.

134. G. Di Paolo, P. De Camilli, Phosphoinositides in cell regulation and membrane dynamics. *Nature*. **443**, 651–657 (2006).

135. D. Poccia, B. Larijani, Phosphatidylinositol metabolism and membrane fusion. *Biochem. J.* (2009), doi:10.1042/BJ20082105.

136. S. Martin, C. B. Harper, L. M. May, E. J. Coulson, F. A. Meunier, S. L. Osborne, Inhibition of PIKfyve by YM-201636 Dysregulates Autophagy and Leads to Apoptosis-

Independent Neuronal Cell Death. *PLoS One* (2013), doi:10.1371/journal.pone.0060152.

137. M. Vicinanza, V. I. Korolchuk, A. Ashkenazi, C. Puri, F. M. Menzies, J. H. Clarke, D. C. Rubinsztein, PI(5)P regulates autophagosome biogenesis. *Mol. Cell*. **57**, 219–234 (2015).

138. C. J. Ferguson, G. M. Lenk, M. H. Meisler, Defective autophagy in neurons and astrocytes from mice deficient in PI(3,5)P2. *Hum. Mol. Genet.* (2009), doi:10.1093/hmg/ddp460.

139. S. H. Min, A. Suzuki, T. J. Stalker, L. Zhao, Y. Wang, C. McKennan, M. J. Riese, J. F. Guzman, S. Zhang, L. Lian, R. Joshi, R. Meng, S. H. Seeholzer, J. K. Choi, G. Koretzky, M. S. Marks, C. S. Abrams, Loss of PIKfyve in platelets causes a lysosomal disease leading to inflammation and thrombosis in mice. *Nat. Commun.* (2014), doi:10.1038/ncomms5691.

140. Y. Lin-Moshier, M. V. Keebler, R. Hooper, M. J. Boulware, X. Liu, D. Churamani, M. E. Abood, T. F. Walseth, E. Brailoiu, S. Patel, J. S. Marchant, The Two-pore channel (TPC) interactome unmasks isoform-specific roles for TPCs in endolysosomal morphology and cell pigmentation. *Proc. Natl. Acad. Sci. U. S. A.* (2014), doi:10.1073/pnas.1407004111.

141. X. P. Dong, D. Shen, X. Wang, T. Dawson, X. Li, Q. Zhang, X. Cheng, Y. Zhang, L. S. Weisman, M. Delling, H. Xu, PI(3,5)P2 controls membrane trafficking by direct activation of mucolipin Ca2+ release channels in the endolysosome. *Nat. Commun.* (2010), doi:10.1038/ncomms1037.

142. X. Li, S. ichiroh Saitoh, T. Shibata, N. Tanimura, R. Fukui, K. Miyake, Mucolipin 1 positively regulates TLR7 responses in dendritic cells by facilitating RNA transportation to lysosomes. *Int. Immunol.* (2015), doi:10.1093/intimm/dxu086.

143. J. de Lartigue, H. Polson, M. Feldman, K. Shokat, S. A. Tooze, S. Urbé, M. J. Clague, PIKfyve regulation of endosome-linked pathways. *Traffic* (2009), doi:10.1111/j.1600-0854.2009.00915.x.

144. A. S. Nicot, H. Fares, B. Payrastre, A. D. Chisholm, M. Labouesse, J. Laporte, The phosphoinositide kinase PIKfyve/Fab1p regulates terminal lysosome maturation in Caenorhabditis elegans. *Mol. Biol. Cell* (2006), doi:10.1091/mbc.e05-12-1120.

145. X. Cai, Y. Xu, A. K. Cheung, R. C. Tomlinson, A. Alcázar-Román, L. Murphy, A. Billich, B. Zhang, Y. Feng, M. Klumpp, J. M. Rondeau, A. N. Fazal, C. J. Wilson, V. Myer, G. Joberty, T. Bouwmeester, M. A. Labow, P. M. Finan, J. A. Porter, H. L. Ploegh, D. Baird, P. De Camilli, J. A. Tallarico, Q. Huang, PIKfyve, a class III PI Kinase, is the target of the small molecular IL-12/IL-23 inhibitor apilimod and a player in toll-like receptor signaling. *Chem. Biol.* (2013), doi:10.1016/j.chembiol.2013.05.010.

146. A. C. Rutherford, C. Traer, T. Wassmer, K. Pattni, M. V. Bujny, J. G. Carlton, H. Stenmark, P. J. Cullen, The mammalian phosphatidylinositol 3-phosphate 5-kinase (PIKfyve) regulates endosome-to-TGN retrograde transport. *J. Cell Sci.* (2006), doi:10.1242/jcs.03153.

147. D. Sbrissa, O. C. Ikonomov, H. Fenner, A. Shisheva, ArPIKfyve Homomeric and Heteromeric Interactions Scaffold PIKfyve and Sac3 in a Complex to Promote PIKfyve Activity and Functionality. *J. Mol. Biol.* (2008), doi:10.1016/j.jmb.2008.10.009.

148. O. C. Ikonomov, D. Sbrissa, H. Fenner, A. Shisheva, PIKfyve-ArPIKfyve-Sac3 core complex: Contact sites and their consequence for Sac3 phosphatase activity and endocytic membrane homeostasis. *J. Biol. Chem.* (2009), doi:10.1074/jbc.M109.037515.

149. D. Sbrissa, O. C. Ikonomov, Z. Fu, T. Ijuin, J. Gruenberg, T. Takenawa, A. Shisheva, Core protein machinery for mammalian phosphatidylinositol 3,5-bisphosphate synthesis and turnover that regulates the progression of endosomal transport: Novel Sac phosphatase joins the ArPIKfyve-PIKfyve complex. *J. Biol. Chem.* (2007), doi:10.1074/jbc.M611678200.

150. C. J. Ferguson, G. M. Lenk, M. H. Meisler, PtdIns(3,5)P2 and autophagy in mouse models of neurodegeneration. *Autophagy*. **6**, 170–1 (2010).

151. C. Bissig, I. Hurbain, G. Raposo, G. van Niel, PIKfyve activity regulates reformation of terminal storage lysosomes from endolysosomes. *Traffic* (2017), doi:10.1111/tra.12525.

152. L. S. Godwin, J. T. Castle, J. S. Kohli, P. S. Goff, C. J. Cairney, W. N. Keith, E. V. Sviderskaya, D. C. Bennett, *Curr. Protoc. Cell Biol.*, in press, doi:10.1002/0471143030.cb0108s63.

153. M. J. Karnovsky, A formaldehyde-glutaraldehyde fixative of high osmolality for use in electron microscopy. *J. Cell Biol.* **27**, 1965 (1965).

154. S. N. Zolov, D. Bridges, Y. Zhang, W.-W. W. Lee, E. Riehle, R. Verma, G. M. Lenk, K. Converso-Baran, T. Weide, R. L. Albin, A. R. Saltiel, M. H. Meisler, M. W. Russell, L. S. Weisman, In vivo, Pikfyve generates PI(3,5)P2, which serves as both a signaling lipid and the major precursor for PI5P. *Proc. Natl. Acad. Sci. U. S. A.* **109**, 17472–7 (2012).

155. A. Shisheva, D. Sbrissa, O. Ikonomov, Plentiful PtdIns5P from scanty PtdIns(3,5)P2 or from ample PtdIns? PIKfyve-dependent models: Evidence and speculation (response to: DOI 10.1002/bies.201300012). *BioEssays*. **37**, 267–77 (2015).

156. A. Shisheva, PtdIns5P: News and views of its appearance, disappearance and deeds. *Arch. Biochem. Biophys.* (2013), doi:10.1016/j.abb.2013.07.023.

157. G. M. Lenk, C. J. Ferguson, C. Y. Chow, N. Jin, J. M. Jones, A. E. Grant, S. N. Zolov, J. J. Winters, R. J. Giger, J. J. Dowling, L. S. Weisman, M. H. Meisler, Pathogenic mechanism of the FIG4 mutation responsible for charcot-marie-tooth disease CMT4J. *PLoS Genet.* (2011), doi:10.1371/journal.pgen.1002104.

158. H. Ozeki, S. Ito, K. Wakamatsu, A. J. Thody, Spectrophotometric characterization of eumelanin and pheomelanin in hair. *Pigment Cell Res.* (1996), doi:10.1111/j.1600-0749.1996.tb00116.x.

159. E. K. Nishimura, S. R. Granter, D. E. Fisher, Mechanisms of hair graying: Incomplete melanocyte stem cell maintenance in the niche. *Science (80-.).* (2005), doi:10.1126/science.1099593.

160. M. D. Muzumdar, B. Tasic, K. Miyamichi, N. Li, L. Luo, L. Li, L. Luo, A global double-fluorescent cre reporter mouse. *Genesis*. **45**, 593–605 (2007).

161. G. H. E. Kim, R. M. Dayam, A. Prashar, M. Terebiznik, R. J. Botelho, PIKfyve inhibition

interferes with phagosome and endosome maturation in macrophages. *Traffic* (2014), doi:10.1111/tra.12199.

162. M. C. Kerr, J. T. H. Wang, N. A. Castro, N. A. Hamilton, L. Town, D. L. Brown, F. A. Meunier, N. F. Brown, J. L. Stow, R. D. Teasdale, Inhibition of the PtdIns(5) kinase PIKfyve disrupts intracellular replication of Salmonella. *EMBO J.* (2010), doi:10.1038/emboj.2010.28.

163. G. Odorizzi, M. Babst, S. D. Emr, Fab1p Ptdlns(3)P 5-kinase function essential for protein sorting in the multivesicular body. *Cell* (1998), doi:10.1016/S0092-8674(00)81707-9.

164. N. Jin, M. J. Lang, L. S. Weisman, Phosphatidylinositol 3,5-bisphosphate: Regulation of cellular events in space and time. *Biochem. Soc. Trans.* (2016), doi:10.1042/BST20150174.

165. P. Whitley, B. J. Reaves, M. Hashimoto, A. M. Riley, B. V. L. Potter, G. D. Holman, Identification of mammalian Vps24p as an effector of phosphatidylinositol 3,5-bisphosphate-dependent endosome compartmentalization. *J. Biol. Chem.* (2003), doi:10.1074/jbc.M306864200.

166. A. Shisheva, PIKfyve: Partners, significance, debates and paradoxes. *Cell Biol. Int.* (2008), doi:10.1016/j.cellbi.2008.01.006.

167. N. W. Bellono, E. V. Oancea, Ion transport in pigmentation. *Arch. Biochem. Biophys.* (2014), doi:10.1016/j.abb.2014.06.020.

168. X. Feng, Y. Huang, Y. Lu, J. Xiong, C. -On Wong, P. Yang, J. Xia, D. Chen, G. Du, K. Venkatachalam, X. Xia, M. X. Zhu, Drosophila TRPML forms PI(3,5)P2-activated cation channels in both endolysosomes and plasma Membrane. *J. Biol. Chem.* (2014), doi:10.1074/jbc.M113.506501.

169. N. W. Bellono, I. E. Escobar, E. V. Oancea, N. W. Bellono, E. V. Oancea, R. H. Michell, V. L. Heath, M. A. Lemmon, S. K. Dove, C. Y. Chow, X. P. Dong, X. Wang, X. P. Dong, D. Shen, M. Samie, C. Cang, X. Cheng, C. Cang, B. Bekele, D. Ren, P. Sulem, Y. Lin-Moshier, P. J. Calcraft, S. J. Pitt, A. Kosiniak-Kamysz, J. M. Kocarnik, I. Palmisano, K. Cortese, N. W. Bellono, I. E. Escobar, A. J. Lefkovith, M. S. F. I. G. 4. Marks, E. V. Oancea, M. Ruas, A. Sitaram, F. A. Ran, J. Ancans, A. J. Thody, R. Halaban, J. Ancans, E. V. Sviderskaya, M. S. F. I. G. 4. Marks, B. E. Steinberg, E. V. Sviderskaya, S. R. G. Setty, N. W. Bellono, L. G. Kammel, A. L. Zimmerman, E. V. Oancea, A melanosomal two-pore sodium channel regulates pigmentation. *Sci. Rep.* **6**, 26570 (2016).

170. A. L. Ambrosio, J. A. Boyle, A. E. Aradi, K. A. Christian, S. M. Di Pietro, TPC2 controls pigmentation by regulating melanosome pH and size. *Proc. Natl. Acad. Sci. U. S. A.* **113**, 5622–5627 (2016).

171. P. Sulem, D. F. Gudbjartsson, S. N. Stacey, A. Helgason, T. Rafnar, M. Jakobsdottir, S. Steinberg, S. A. Gudjonsson, A. Palsson, G. Thorleifsson, S. Pálsson, B. Sigurgeirsson, K. Thorisdottir, R. Ragnarsson, K. R. Benediktsdottir, K. K. Aben, S. H. Vermeulen, A. M. Goldstein, M. A. Tucker, L. A. Kiemeney, J. H. Olafsson, J. Gulcher, A. Kong, U. Thorsteinsdottir, K. Stefansson, Two newly identified genetic determinants of pigmentation in Europeans. *Nat. Genet.* (2008), doi:10.1038/ng.160.

172. H. Xu, M. Delling, L. Li, X. Dong, D. E. Clapham, Activating mutation in a mucolipin transient receptor potential channel leads to melanocyte loss in varitint-waddler mice. *Proc. Natl. Acad. Sci. U. S. A.* (2007), doi:10.1073/pnas.0709096104.

173. G. Raposo, M. S. Marks, D. F. Cutler, Lysosome-related organelles: driving post-Golgi compartments into specialisation. *Curr. Opin. Cell Biol.* **19**, 394–401 (2007).

174. V. Basrur, F. Yang, T. Kushimoto, Y. Higashimoto, K.-I. Yasumoto, J. Valencia, J. Muller, W. D. Vieira, H. Watabe, J. Shabanowitz, V. J. Hearing, D. F. Hunt, E. Appella, Proteomic Analysis of Early Melanosomes: Identification of Novel Melanosomal Proteins. *J. Proteome Res.* **2**, 69–79 (2003).

175. A. Kawase, T. Kushimoto, Y. Kawa, K. Ohsumi, H. Nishikawa, T. Kawakami, M. Mizoguchi, Y. Soma, Proteomic analysis of immature murine melanocytes at different stages of maturation: A crucial role for calreticulin. *J. Dermatol. Sci.* **49**, 43–52 (2008).

176. C. I. Popescu, C. Paduraru, R. A. Dwek, S. M. Petrescu, Soluble tyrosinase is an endoplasmic reticulum (ER)-associated degradation substrate retained in the ER by calreticulin and BiP/GRP78 and not calnexin. *J. Biol. Chem.* **280**, 13833–13840 (2005).

177. B. K. Zhou, R. E. Boissy, S. Pifko-Hirst, D. J. Moran, S. J. Orlow, Lysosome-associated membrane protein-1 (LAMP-1) is the melanocyte vesicular membrane glycoprotein band II. *J. Invest. Dermatol.* **100**, 110–114 (1993).

178. P. W. Lane, E. L. Green, Pale ear and light ear in the house mouse: Mimic mutations in linkage groups XII and xvii. *J. Hered.* **58**, 17–20 (1967).

179. H. Ho, A. K. Ganesan, The pleiotropic roles of autophagy regulators in melanogenesis. *Pigment Cell Melanoma Res.* **24**, 595–604 (2011).

180. C. F. Zhang, F. Gruber, C. Ni, M. Mildner, U. Koenig, S. Karner, C. Barresi, H. Rossiter, M. S. Narzt, I. M. Nagelreiter, L. Larue, D. J. Tobin, L. Eckhart, E. Tschachler, Suppression of autophagy dysregulates the antioxidant response and causes premature senescence of melanocytes. *J. Invest. Dermatol.* **135**, 1348–1357 (2015).

181. T. Proikas-Cezanne, Z. Takacs, P. Dönnes, O. Kohlbacher, WIPI proteins: essential PtdIns3P effectors at the nascent autophagosome. *J. Cell Sci.* **128**, 207–17 (2015).

182. H. E. J. Polson, J. de Lartigue, D. J. Rigden, M. Reedijk, S. Urbé, M. J. Clague, S. A. Tooze, Mammalian Atg18 (WIPI2) localizes to omegasome-anchored phagophores and positively regulates LC3 lipidation. *Autophagy*. **6**, 506–22 (2010).

183. T. Proikas-Cezanne, S. Ruckerbauer, Y. D. Stierhof, C. Berg, A. Nordheim, Human WIPI-1 puncta-formation: A novel assay to assess mammalian autophagy. *FEBS Lett.* **581**, 3396–3404 (2007).

184. A. R. Hellström, B. Watt, S. S. Fard, D. Tenza, P. Mannström, K. Narfström, B. Ekesten, S. Ito, K. Wakamatsu, J. Larsson, M. Ulfendahl, K. Kullander, G. Raposo, S. Kerje, F. Hallböök, M. S. Marks, L. Andersson, Inactivation of Pmel alters melanosome shape but has only a subtle effect on visible pigmentation. *PLoS Genet.* **7**, e1002285 (2011).

185. I. T. Aydin, E. Hummler, N. P. M. Smit, F. Beermann, Coat color dilution in mice because

of inactivation of the melanoma antigen MART-1. *Pigment Cell Melanoma Res.* **25**, 37–46 (2012).

186. W. K. Silvers, *The Coat Colors of Mice* (1979).

187. M. Grimmel, C. Backhaus, T. Proikas-Cezanne, WIPI-Mediated Autophagy and Longevity. *Cells* (2015), doi:10.3390/cells4020202.

188. M. I. Wilson, H. C. Dooley, S. A. Tooze, WIPI2b and Atg16L1: setting the stage for autophagosome formation. *Biochem. Soc. Trans.* **42**, 1327–1334 (2014).

189. K. Hirosaki, T. Yamashita, I. Wada, H. Y. Jin, K. Jimbow, Tyrosinase and tyrosinase-related protein 1 require Rab7 for their intracellular transport. *J. Invest. Dermatol.* **119**, 475–480 (2002).

190. S. S. Joshi, B. Tandukar, L. Pan, J. M. Huang, F. Livak, B. J. Smith, T. Hodges, A. A. Mahurkar, T. J. Hornyak, CD34 defines melanocyte stem cell subpopulations with distinct regenerative properties. *PLoS Genet.* **15**, e1008034 (2019).

191. S. Preibisch, S. Saalfeld, P. Tomancak, Globally optimal stitching of tiled 3D microscopic image acquisitions. *Bioinformatics* (2009), doi:10.1093/bioinformatics/btp184.

192. R. V. Davuluri, Y. Suzuki, S. Sugano, C. Plass, T. H.-M. Huang, The functional consequences of alternative promoter use in mammalian genomes. *Trends Genet.* **24**, 167–177 (2008).

193. W. Davis, R. M. Schultz, Developmental change in TATA-box utilization during preimplantation mouse development. *Dev. Biol.* **218**, 275–283 (2000).

194. J. R. Landry, D. L. Mager, B. T. Wilhelm, Complex controls: The role of alternative promoters in mammalian genomes. *Trends Genet.* **19**, 640–648 (2003).

195. S. Kim, S. S. A. An, Role of p53 isoforms and aggregations in cancer. *Med. (United States)*. **95**, e3993 (2016).

196. N. Arsic, G. Gadea, E. L. Lagerqvist, M. Bußon, N. Cahuzac, C. Brock, F. Hollande, V. Gire, J. Pannequin, P. Roux, The p53 isoform Δ133p53β promotes cancer stem cell potential. *Stem Cell Reports*. **4**, 531–540 (2015).

197. C. Bertolotto, F. Lesueur, S. Giuliano, T. Strub, M. De Lichy, K. Bille, P. Dessen, B. D'Hayer, H. Mohamdi, A. Remenieras, E. Maubec, A. De La Fouchardière, V. Molinié, P. Vabres, S. Dalle, N. Poulalhon, T. Martin-Denavit, L. Thomas, P. Andry-Benzaquen, N. Dupin, F. Boitier, A. Rossi, J. L. Perrot, B. Labeille, C. Robert, B. Escudier, O. Caron, L. Brugières, S. Saule, B. Gardie, S. Gad, S. Richard, J. Couturier, B. T. Teh, P. Ghiorzo, L. Pastorino, S. Puig, C. Badenas, H. Olsson, C. Ingvar, E. Rouleau, R. Lidereau, P. Bahadoran, P. Vielh, E. Corda, H. Blanché, D. Zelenika, P. Galan, F. Aubin, B. Bachollet, C. Becuwe, P. Berthet, Y. Jean Bignon, V. Bonadona, J. L. Bonafe, M. N. Bonnet-Dupeyron, F. Cambazard, J. Chevrant-Breton, I. Coupier, S. Dalac, L. Demange, M. D'Incan, C. Dugast, L. Faivre, L. Vincent-Fétita, M. Gauthier-Villars, B. Gilbert, F. Grange, J. J. Grob, P. Humbert, N. Janin, P. Joly, D. Kerob, C. Lasset, D. Leroux, J. Levang, J. M. Limacher, C. Livideanu, M. Longy, A. Lortholary, D. Stoppa-Lyonnet, S. Mansard, L. Mansuy, K. Marrou, C. Matéus, C. Maugard, N. Meyer, C. Nogues, P.

Souteyrand, L. Venat-Bouvet, H. Zattara, V. Chaudru, G. M. Lenoir, M. Lathrop, I. Davidson, M. F. Avril, F. Demenais, R. Ballotti, B. Bressac-De Paillerets, A SUMOylation-defective MITF germline mutation predisposes to melanoma and renal carcinoma. *Nature*. **480**, 94–98 (2011).

198. K. Bharti, W. Liu, T. Csermely, S. Bertuzzi, H. Arnheiter, Alternative promoter use in eye development: The complex role and regulation of the transcription factor MITF. *Development*. **135**, 1169–1178 (2008).

199. S. Amae, N. Fuse, K. Yasumoto, S. Sato, I. Yajima, H. Yamamoto, T. Udono, Y. K. Durlu, M. Tamai, K. Takahashi, S. Shibahara, Identification of a novel isoform of microphthalmia-associated transcription factor that is enriched in retinal pigment epithelium. *Biochem. Biophys. Res. Commun.* **247**, 710–5 (1998).

200. V. Pogenberg, M. H. Ögmundsdóttir, K. Bergsteinsdóttir, A. Schepsky, B. Phung, V. Deineko, M. Milewski, E. Steingrímsson, M. Wilmanns, Restricted leucine zipper dimerization and specificity of DNA recognition of the melanocyte master regulator MITF. *Genes Dev.* **26**, 2647–2658 (2012).

201. C. Levy, M. Khaled, D. E. Fisher, MITF: master regulator of melanocyte development and melanoma oncogene. *Trends Mol. Med.* **12**, 406–414 (2006).

202. H. T. Michael, C. Graff-Cherry, S. Chin, C. Rauck, A. D. Habtemichael, P. Bunda, T. Smith, M. M. Campos, K. Bharti, H. Arnheiter, G. Merlino, C. P. Day, Partial rescue of ocular pigment cells and structure by inducible ectopic expression of Mitf-M in MITF-deficient mice. *Investig. Ophthalmol. Vis. Sci.* **59**, 6067–6073 (2018).

203. K. Bharti, M. Gasper, J. Ou, M. Brucato, K. Clore-Gronenborn, J. Pickel, H. Arnheiter, A regulatory loop involving PAX6, MITF, and WNT signaling controls retinal pigment epithelium development. *PLoS Genet.* **8**, e1002757 (2012).

204. A. Phelep, D. Laouari, K. Bharti, M. Burtin, S. Tammaccaro, S. Garbay, C. Nguyen, F. Vasseur, T. Blanc, S. Berissi, F. Langa-Vives, E. Fischer, A. Druilhe, H. Arnheiter, G. Friedlander, M. Pontoglio, F. Terzi, MITF – A controls branching morphogenesis and nephron endowment. *PLoS Genet.* **13**, e1007093 (2017).

205. L. Cong, F. A. Ran, D. Cox, S. Lin, R. Barretto, Multiplex genome engineering using CRISPR/Cas systems. *Mult. genome Eng. using Cris. Syst.* **339**, 819–823 (2013).

206. C. Trapnell, L. Pachter, S. L. Salzberg, TopHat: Discovering splice junctions with RNA-Seq. *Bioinformatics*. **25**, 1105–1111 (2009).

207. C. Trapnell, D. G. Hendrickson, M. Sauvageau, L. Goff, J. L. Rinn, L. Pachter, Differential analysis of gene regulation at transcript resolution with RNA-seq. *Nat. Biotechnol.* **31**, 46–53 (2013).

208. M. I. Love, W. Huber, S. Anders, Moderated estimation of fold change and dispersion for RNA-seq data with DESeq2. *Genome Biol.* **15**, 550 (2014).

209. R. Edgar, M. Domrachev, A. E. Lash, Gene Expression Omnibus: NCBI gene expression and hybridization array data repository. *Nucleic Acids Res.* **30**, 207–210 (2002).

210. J. T. Robinson, H. Thorvaldsdóttir, W. Winckler, M. Guttman, E. S. Lander, G. Getz, J. P. Mesirov, Integrative genomics viewer. *Nat. Biotechnol.* **29**, 24–26 (2011).

211. H. Thorvaldsdóttir, J. T. Robinson, J. P. Mesirov, Integrative Genomics Viewer (IGV): High-performance genomics data visualization and exploration. *Brief. Bioinform.* **14**, 178–192 (2013).

212. K. D. Haltaufderhyde, E. Oancea, Genome-wide transcriptome analysis of human epidermal melanocytes. *Genomics*. **104**, 482–489 (2014).

213. T. Koressaar, M. Remm, Enhancements and modifications of primer design program Primer3. *Bioinformatics*. **23**, 1289–1291 (2007).

214. A. Untergasser, I. Cutcutache, T. Koressaar, J. Ye, B. C. Faircloth, M. Remm, S. G. Rozen, Primer3-new capabilities and interfaces. *Nucleic Acids Res.* **40**, e115 (2012).

215. K. Daily, V. R. Patel, P. Rigor, X. Xie, P. Baldi, MotifMap: Integrative genome-wide maps of regulatory motif sites for model species. *BMC Bioinformatics*. **12**, 495 (2011).

216. X. Xie, P. Rigor, P. Baldi, MotifMap: A human genome-wide map of candidate regulatory motif sites. *Bioinformatics*. **25**, 167–174 (2009).

217. T. Udono, K. I. Yasumoto, K. Takeda, S. Amae, K. I. Watanabe, H. Saito, N. Fuse, M. Tachibana, K. Takahashi, M. Tamai, S. Shibahara, Structural organization of the human microphthalmia-associated transcription factor gene containing four alternative promoters. *Biochim. Biophys. Acta - Gene Struct. Expr.* **1491**, 205–219 (2000).

218. M. L. Harris, T. D. Fufa, J. W. Palmer, S. S. Joshi, D. M. Larson, A. Incao, D. E. Gildea, N. S. Trivedi, A. N. Lee, C. P. Day, H. T. Michael, T. J. Hornyak, G. Merlino, W. J. Pavan, A direct link between MITF, innate immunity, and hair graying. *PLoS Biol.* **16**, e2003648 (2018).

219. A. A. Mills, B. Zheng, X. J. Wang, H. Vogel, D. R. Roop, A. Bradley, p63 is a p53 homologue required for limb and epidermal morphogenesis. *Nature*. **398**, 708–713 (1999).

220. A. Yang, R. Schweitzer, D. Sun, M. Kaghad, N. Walker, R. T. Bronson, C. Tabin, A. Sharpe, D. Caput, C. Crum, F. McKeon, p63 is essential for regenerative proliferation in limb, craniofacial and epithelial development. *Nature*. **398**, 714–718 (1999).

221. H. Aoki, Y. Yamada, A. Hara, T. Kunisada, W. J. Pavan, H. Arnheiter, Two distinct types of mouse melanocyte: differential signaling requirement for the maintenance of non-cutaneous and dermal versus epidermal melanocytes. *Development*. **136**, 2511–21 (2009).

222. G. Allenby, M. T. Bocquel, M. Saunders, S. Kazmer, J. Speck, M. Rosenberger, A. Lovey, P. Kastner, J. F. Grippo, P. Chambon, A. A. Levin, Retinoic acid receptors and retinoid X receptors: Interactions with endogenous retinoic acids. *Proc. Natl. Acad. Sci. U. S. A.* **90**, 30–34 (1993).

223. J. Reichrath, T. Munssinger, A. Kerber, C. Rochette-Egly, P. Chambon, F. A. Bahmer, H. P. Baum, In situ detection of retinoid-X receptor expression in normal and psoriatic human skin. *Br. J. Dermatol.* **133**, 168–175 (1995).

224. X. Du, K. Tabeta, N. Mann, K. Crozat, S. Mudd, B. Beutler, An essential role for Rxr alpha in the development of Th2 responses. *Eur. J. Immunol.* **35**, 3414–23 (2005).

225. M. Reinisalo, J. Putula, E. Mannermaa, A. Urtti, P. Honkakoski, Regulation of the human tyrosinase gene in retinal pigment epithelium cells: The significance of transcription factor orthodenticle homeobox 2 and its polymorphic binding site. *Mol. Vis.* **18**, 38–54 (2012).

226. H. Grüneberg, The relations of microphthalmia and white in the mouse. *J. Genet.* **51**, 359–362 (1953).

227. J. K. McBee, K. Palczewski, W. Baehr, D. R. Pepperberg, Confronting complexity: The interlink of phototransduction and retinoid metabolism in the vertebrate retina. *Prog. Retin. Eye Res.* **20**, 469–529 (2001).

228. K. B. Laursen, V. Kashyap, J. Scandura, L. J. Gudas, An alternative retinoic acid-responsive Stra6 promoter regulated in response to retinol deficiency. *J. Biol. Chem.* **290**, 4356–4366 (2015).

229. N. L. Wicks, J. W. Chan, J. A. Najera, J. M. Ciriello, E. Oancea, UVA phototransduction drives early melanin synthesis in human melanocytes. *Curr. Biol.* **21**, 1906–11 (2011).

230. M. Li, H. Chiba, X. Warot, N. Messaddeq, C. Gérard, P. Chambon, D. Metzger, RXRα ablation in skin keratinocytes results in alopecia and epidermal alterations. *Development*. **128**, 675–688 (2001).

231. G. Wildhardt, B. Zirn, L. M. Graul-Neumann, J. Wechtenbruch, M. Suckfüll, A. Buske, A. Bohring, C. Kubisch, S. Vogt, G. Strobl-Wildemann, M. Greally, O. Bartsch, D. Steinberger, Spectrum of novel mutations found in waardenburg syndrome types 1 and 2: Implications for molecular genetic diagnostics. *BMJ Open*. **3**, e001917 (2013).

232. C. Grill, K. Bergsteinsdó ttir, M. H. Ögmundsdó ttir, V. Pogenberg, A. Schepsky, M. Wilmanns, V. Pingault, E. Steingrímsson, MITF mutations associated with pigment deficiency syndromes and melanoma have different effects on protein function. *Hum. Mol. Genet.* **22**, 4357–4367 (2013).

233. C. A. Hodgkinson, K. J. Moore, A. Nakayama, E. Steingrímsson, N. G. Copeland, N. A. Jenkins, H. Arnheiter, Mutations at the mouse microphthalmia locus are associated with defects in a gene encoding a novel basic-helix-loop-helix-zipper protein. *Cell*. **74**, 395–404 (1993).

234. K. I. Watanabe, K. Takeda, K. I. Yasumoto, T. Udono, H. Saito, K. Ikeda, T. Takasaka, K. Takahashi, T. Kobayashi, M. Tachibana, S. Shibahara, Identification of a distal enhancer for the melanocyte-specific promoter of the MITF gene. *Pigment Cell Res.* **15**, 201–211 (2002).

235. I. Yajima, S. Sato, T. Kimura, K. I. Yasumoto, S. Shibahara, C. R. Goding, H. Yamamoto, An L1 element intronic insertion in the black-eyed white (Mitf(mi-bw)) gene: The loss of a single Mitf isoform responsible for the pigmentary defect and inner ear deafness. *Hum. Mol. Genet.* **8**, 1431–1441 (1999).

236. H. Hozumi, K. Takeda, Y. Yoshida-Amano, Y. Takemoto, R. Kusumi, U. Fukuzaki-Dohi, A. Higashitani, H. Yamamoto, S. Shibahara, Impaired development of melanoblasts in the

black-eyed white Mitf mi-bw mouse, a model for auditory-pigmentary disorders. *Genes to Cells*. **17**, 494–508 (2012).

237. K. Takeda, H. Hozumi, K. Nakai, M. Yoshizawa, H. Satoh, H. Yamamoto, S. Shibahara, Insertion of long interspersed element-1 in the Mitf gene is associated with altered neurobehavior of the black-eyed white Mitfmi-bwmouse. *Genes to Cells*. **19**, 126–140 (2014).

238. J. Maruotti, T. Thein, D. J. Zack, N. Esumi, MITF-M, a "melanocyte-specific" isoform, is expressed in the adult retinal pigment epithelium. *Pigment Cell Melanoma Res.* **25**, 641–644 (2012).

239. B. A. Moore, M. J. Roux, L. Sebbag, A. Cooper, S. G. Edwards, B. C. Leonard, D. M. Imai, S. Griffey, L. Bower, D. Clary, K. C. K. Lloyd, Y. Hérault, S. M. Thomasy, C. J. Murphy, A. Moshiri, A population study of common ocular abnormalities in C57BL/6N rd8 mice. *Investig. Ophthalmol. Vis. Sci.* **59**, 2252–2261 (2018).

240. M. J. Mattapallil, E. F. Wawrousek, C. C. Chan, H. Zhao, J. Roychoudhury, T. A. Ferguson, R. R. Caspi, The Rd8 mutation of the Crb1 gene is present in vendor lines of C57BL/6N mice and embryonic stem cells, and confounds ocular induced mutant phenotypes. *Invest. Ophthalmol. Vis. Sci.* **53**, 2921–2927 (2012).

241. U. F. O. Luhmann, L. S. Carvalho, S. M. kleine Holthaus, J. A. Cowing, S. Greenaway, C. J. Chu, P. Herrmann, A. J. Smith, P. M. G. Munro, P. Potter, J. W. B. Bainbridge, R. R. Ali, The severity of retinal pathology in homozygous Crb1rd8/rd8 mice is dependent on additional genetic factors. *Hum. Mol. Genet.* **24**, 128–141 (2015).

242. S. Hofstetter, F. Seefried, I. M. Häfliger, V. Jagannathan, T. Leeb, C. Drögemüller, A non-coding regulatory variant in the 5′-region of the MITF gene is associated with white-spotted coat in Brown Swiss cattle. *Anim. Genet.* **50**, 27–32 (2019).

243. J. Henkel, C. Lafayette, S. A. Brooks, K. Martin, L. Patterson-Rosa, D. Cook, V. Jagannathan, T. Leeb, Whole-genome sequencing reveals a large deletion in the MITF gene in horses with white spotted coat colour and increased risk of deafness. *Anim. Genet.* **50**, 172–174 (2019).

244. L. Andersson, Genome-wide association analysis in domestic animals: A powerful approach for genetic dissection of trait loci. *Genetica*. **136**, 341–349 (2009).

245. L. L. Baxter, L. Hou, S. K. Loftus, W. J. Pavan, Spotlight on spotted mice: a review of white spotting mouse mutants and associated human pigmentation disorders. *Pigment cell Res.* **17**, 215–24 (2004).

246. C. Thaung, Novel ENU-induced eye mutations in the mouse: models for human eye disease. *Hum. Mol. Genet.* (2002), doi:10.1093/hmg/11.7.755.

247. K. Stelzner, No Title. *Mouse News Lett.* **31**, 40 (1964).

248. K. Stelzner, No Title. *Mouse News Lett.* **34**, 41 (1966).

249. H. Sweet, Recessive spotting mutation mapped to the Mitf<mi> locus on chromosome 6. *Mouse News Lett.* **94**, 145 (1996).

250. B. Wen, Y. Chen, H. Li, J. Wang, J. Shen, A. Ma, J. Qu, K. Bismuth, J. Debbache, H. Arnheiter, L. Hou, Allele-specific genetic interactions between Mitf and Kit affect melanocyte development. *Pigment Cell Melanoma Res.* **23**, 441–447 (2010).

251. K. Takeda, H. Hozumi, K. Ohba, H. Yamamoto, S. Shibahara, Regional Fluctuation in the Functional Consequence of LINE-1 Insertion in the Mitf Gene: The Black Spotting Phenotype Arisen from the Mitfmi-bw Mouse Lacking Melanocytes. *PLoS One*. **11**, e0150228 (2016).

252. S. Müller-Röver, B. Handjiski, C. van der Veen, S. Eichmüller, K. Foitzik, I. A. McKay, K. S. Stenn, R. Paus, A comprehensive guide for the accurate classification of murine hair follicles in distinct hair cycle stages. *J. Invest. Dermatol.* **117**, 3–15 (2001).

253. L. Hou, W. J. Pavan, Transcriptional and signaling regulation in neural crest stem cell-derived melanocyte development: do all roads lead to Mitf? *Cell Res.* **18**, 1163–1176 (2008).

254. K. S. Hoek, N. C. Schlegel, O. M. Eichhoff, D. S. Widmer, C. Praetorius, S. O. Einarsson, S. Valgeirsdottir, K. Bergsteinsdottir, A. Schepsky, R. Dummer, E. Steingrimsson, Novel MITF targets identified using a two-step DNA microarray strategy. *Pigment Cell Melanoma Res.* **21**, 665–676 (2008).

255. K. S. Stenn, R. Paus, Controls of hair follicle cycling. *Physiol. Rev.* **81**, 449–494 (2001).

256. M. V Plikus, C. M. Chuong, Macroenvironmental regulation of hair cycling and collective regenerative behavior. *Cold Spring Harb. Perspect. Med.* **4**, a015198 (2014).

257. J. M. Shin, J. W. Ko, C. W. Choi, Y. Lee, Y. J. Seo, J. H. Lee, C. D. Kim, Deficiency of Crif1 in hair follicle stem cells retards hair growth cycle in adult mice. *PLoS One*. **15**, e0232206 (2020).

258. M. Yang, E. Liu, L. Tang, Y. Lei, X. Sun, J. Hu, H. Dong, S. M. Yang, M. Gao, B. Tang, Emerging roles and regulation of MiT/TFE transcriptional factors. *Cell Commun. Signal.* **16** (2018), doi:10.1186/s12964-018-0242-1.

259. A. M. Bolger, M. Lohse, B. Usadel, Trimmomatic: A flexible trimmer for Illumina sequence data. *Bioinformatics*. **30**, 2114–2120 (2014).

260. D. Kim, J. M. Paggi, C. Park, C. Bennett, S. L. Salzberg, Graph-based genome alignment and genotyping with HISAT2 and HISAT-genotype. *Nat. Biotechnol.* **37**, 907–915 (2019).

261. Y. Liao, G. K. Smyth, W. Shi, FeatureCounts: An efficient general purpose program for assigning sequence reads to genomic features. *Bioinformatics*. **30**, 923–930 (2014).

262. A. Subramanian, P. Tamayo, V. K. Mootha, S. Mukherjee, B. L. Ebert, M. A. Gillette, A. Paulovich, S. L. Pomeroy, T. R. Golub, E. S. Lander, J. P. Mesirov, Gene set enrichment analysis: A knowledge-based approach for interpreting genome-wide expression profiles. *Proc. Natl. Acad. Sci. U. S. A.* **102**, 15545–15550 (2005).

263. V. K. Mootha, C. M. Lindgren, K. F. Eriksson, A. Subramanian, S. Sihag, J. Lehar, P. Puigserver, E. Carlsson, M. Ridderstråle, E. Laurila, N. Houstis, M. J. Daly, N. Patterson, J. P. Mesirov, T. R. Golub, P. Tamayo, B. Spiegelman, E. S. Lander, J. N. Hirschhorn, D.

Altshuler, L. C. Groop, PGC-1α-responsive genes involved in oxidative phosphorylation are coordinately downregulated in human diabetes. *Nat. Genet.* **34**, 267–273 (2003).

264. S. Shen, J. W. Park, Z. X. Lu, L. Lin, M. D. Henry, Y. N. Wu, Q. Zhou, Y. Xing, rMATS: Robust and flexible detection of differential alternative splicing from replicate RNA-Seq data. *Proc. Natl. Acad. Sci. U. S. A.* **111**, E5593–E5601 (2014).

265. S. Shen, J. W. Park, J. Huang, K. A. Dittmar, Z. X. Lu, Q. Zhou, R. P. Carstens, Y. Xing, MATS: A Bayesian framework for flexible detection of differential alternative splicing from RNA-Seq data. *Nucleic Acids Res.* **40**, e61–e61 (2012).

266. J. W. Park, C. Tokheim, S. Shen, Y. Xing, Identifying differential alternative splicing events from RNA sequencing data using RNASeq-MATS. *Methods Mol. Biol.* **1038**, 171–179 (2013).

267. W. J. Kent, C. W. Sugnet, T. S. Furey, K. M. Roskin, T. H. Pringle, A. M. Zahler, a. D. Haussler, The Human Genome Browser at UCSC. *Genome Res.* **12**, 996–1006 (2002).

268. H. Li, Minimap2: Pairwise alignment for nucleotide sequences. *Bioinformatics*. **34**, 3094–3100 (2018).

269. D. Wyman, A. Mortazavi, TranscriptClean: Variant-aware correction of indels, mismatches and splice junctions in long-read transcripts. *Bioinformatics*. **35**, 340–342 (2019).

270. D. Wyman, G. Balderrama-Gutierrez, F. Reese, S. Jiang, S. Rahmanian, W. Zeng, B. Williams, D. Trout, W. England, S. Chu, R. C. Spitale, A. Tenner, B. Wold, A. Mortazavi, A technology-agnostic long-read analysis pipeline for transcriptome discovery and quantification. *bioRxiv*, 672931 (2019).

271. K. Paigen, One hundred years of mouse genetics: An intellectual history. I. The classical period (1902-1980). *Genetics* (2003).

272. G. S. Barsh, The genetics of pigmentation: From fancy genes to complex traits. *Trends Genet.* **12**, 299–305 (1996).

273. M. R. Johnson, G. S. Barsh, R. Mallarino, J. MR, B. GS, M. R, Periodic Patterns in Rodentia: Development and Evolution. *Exp. Dermatol.* **28**, 509 (2019).

274. R. Mallarino, C. Henegar, M. Mirasierra, M. Manceau, C. Schradin, M. Vallejo, S. Beronja, G. S. Barsh, H. E. Hoekstra, Developmental mechanisms of stripe patterns in rodents. *Nature*. **539**, 518–523 (2016).

275. B. H. Bin, J. Bhin, S. H. Yang, M. Shin, Y. J. Nam, D. H. Choi, D. W. Shin, A. Y. Lee, D. Hwang, E. G. Cho, T. R. Lee, Membrane-associated transporter protein (MATP) regulates melanosomal pH and influences tyrosinase activity. *PLoS One*. **10** (2015), doi:10.1371/journal.pone.0129273.

276. M. S. Marks, FIG4, Charcot-Marie-Tooth disease, and hypopigmentation: A role for phosphoinositides in melanosome biogenesis? *Pigment Cell Melanoma Res.* **21**, 11–14 (2008).

277. Z. H. Shah, D. R. Jones, L. Sommer, R. Foulger, Y. Bultsma, C. D'Santos, N. Divecha, Nuclear phosphoinositides and their impact on nuclear functions. *FEBS J.* (2013), doi:10.1111/febs.12543.

278. N. Fuse, K. I. Yasumoto, K. Takeda, S. Amae, M. Yoshizawa, T. Udono, K. Takahashi, M. Tamai, Y. Tomita, M. Tachibana, S. Shibahara, Molecular cloning of cDNA encoding a novel microphthalmia-associated transcription factor isoform with a distinct amino-terminus. *J. Biochem.* **126**, 1043–1051 (1999).

279. C. M. Takemoto, Y. J. Yoon, D. E. Fisher, The identification and functional characterization of a novel mast cell isoform of the microphthalmia-associated transcription factor. *J. Biol. Chem.* **277**, 30244–30252 (2002).

280. M. Visser, M. Kayser, R. J. Palstra, HERC2 rs12913832 modulates human pigmentation by attenuating chromatin-loop formation between a long-range enhancer and the OCA2 promoter. *Genome Res.* **22**, 446–455 (2012).

281. H. Eiberg, J. Troelsen, M. Nielsen, A. Mikkelsen, J. Mengel-From, K. W. Kjaer, L. Hansen, Blue eye color in humans may be caused by a perfectly associated founder mutation in a regulatory element located within the HERC2 gene inhibiting OCA2 expression. *Hum. Genet.* **123**, 177–187 (2008).